Développement de modèles animaux de maladies génétiques des systèmes cardiovasculaire et musculaire chez le poisson-zèbre

Caroline Ramspacher

UNIVERSITÉ DE STRASBOURG

ÉCOLE DOCTORALE DES SCIENCES DE LA VIE ET DE LA SANTE

Institut de Génétique et de Biologie Moléculaire et Cellulaire (IGBMC)

THÈSE présentée par :

Caroline RAMSPACHER

soutenue le : **05 septembre 2014**

pour obtenir le grade de : **Docteur de l'université de Strasbourg**

Discipline/ Spécialité : Sciences de la Vie et de la Santé

Développement de modèles animaux de maladies génétiques des systèmes cardiovasculaire et musculaire chez le poisson-zèbre

Developing new models of cardiovascular and muscular genetic diseases in zebrafish

THÈSE dirigée par :
Docteur VERMOT Julien — CR1, Université de Strasbourg

RAPPORTEURS :
Professeur PAULIN Denise — Professeur émérite, UPMC - Paris 6
Docteur JUST Steffen — Assistent Professor, University Hospital Ulm

---

AUTRES MEMBRES DU JURY :
Professeur MANDEL Jean-Louis — Professeur au Collège de France-PH, Université de Strasbourg

Aknowledgments/Remerciements

First, I would like to thank the members of my jury, Professor Denise Paulin, Doctor Steffen Just and Professor Jean-Louis Mandel for accepting to evaluate my PhD work. En particulier, je voudrais remercier Denise Paulin qui a fait le déplacement jusqu'à Strasbourg déjà à l'occasion de ma mi-thèse et avec qui j'ai eu le plaisir d'échanger plusieurs fois au courant de ma thèse.

Il n'est scientifiquement pas prouvé que le poisson développe l'intelligence mais il stimule incontestablement l'imagination du pêcheur. (Anonyme)

Je voudrais ensuite remercier Julien, mon directeur de thèse, pour m'avoir permis de réaliser ma thèse dans son équipe, sur un sujet, certes aux limites des problématiques du labo, mais pour moi passionnant. Merci Julien pour ta confiance et pour l'indépendance que tu m'as laissée au cours de ces quatre années. J'ai énormément appris, changé, murit peut-être, grâce à ce projet et à ta supervision. Merci enfin d'avoir accepté d'emmené mon manuscrit de thèse jusqu'en Grèce, je crois que ça lui a fait du bien de voir du pays ! ;)

Je dois un des plus gros MERCI de ces pages à mon collaborateur Karim. Tout d'abord pour les innombrables et passionnantes discussions scientifiques « musculaires » et « desmin…iennes ? », idées échangées, théorie (plus ou moins folles) imaginées. Mais surtout pour avoir toujours été là pour moi, pour avoir été une oreille attentive et un point de repère au cours de ces quatre années. Merci aussi d'avoir partagé tes talents de graphistes !

Je voudrais ensuite remercier mes autres collaborateurs. Pour le projet desmine : Jocelyn Laporte qui a suivi le projet desmin depuis le début et avec qui j'ai pu échanger de manière constructive sur cette problématique, les autres membres de l'équipe Laporte « composante poisson », Ursula, Lavanya, Catherine, pour leur aide technique et nos échanges de bons protocoles. Merci également à Alain Lilienbaum et Patrick Vicart, pour les idées échangées sur le projet et ses perspectives. Pour le projet GCN2, je tiens à remercier Florent Soubrier et son équipe pour leur aide dans la conception du projet et pour certains de ses aspects techniques, en particulier merci à Virginie et Caroline, avec qui nous avons encore un peu de travail !

I would like to thank also my international collaboratorsas well, in particular Le for sharing the Flip-Trap lines with us and for her constructive feed-back on the project and on the manuscript. Thanks to Mickael Liebling, Dave Wu and Scott Fraser for sharing analysis tools.

Je voudrais ensuite remercier les plateformes de l'IGBMC avec qui j'ai eu le plaisir de travailler. Merci à Anne, Benoit et Laurent de la plateforme de criblage, les tests sur les « petits poissons » resteront des moments mémorables de ma thèse ! Merci à Claire et Céline de la plateforme de séquençage et à Betty et Leslie de la plateforme de culture cellulaire pour l'entretien des PAC2, ainsi qu'à l'ensemble des services communs, Maité, Evelyne, Sylviane, Elisabeth et toutes celles et ceux qui rendent la vie de chercheur bien plus facile à l'IGBMC.

Un merci tout particulier aux membres de la plateforme d'imagerie, en particulier Coralie et Nadia, pour avoir bien galéré avec moi surtout sur « les cœurs », Didier pour m'avoir installé des systèmes d'imagerie des fois exotiques mais surtout Marc et Pascal, pour votre aide plus que précieuse au quotidien, votre réactivité et votre patience, mais surtout pour les franches rigolades lors des longues après-midi d'Imaris. Je sais, vous allez tout de même dire que je suis mauvaise langue… ;)

Et bien sur un grand coup de chapeau à Sandrine et Sylvie, qui font tourner l'animalerie poisson comme des chefs ! Vous faites un boulot super et je suis extrêmement reconnaissante pour toute l'aide et les services que vous nous rendez en prenant soin de nos petits protégés.

Des poissons qui sont dans une même marmite, on ne peut tirer qu'un même bouillon. (Proverbe malgache)

Coming to my friends, I would like to thank warmly all the members of the labo Vermot! You are fantastic people, we had so much fun (and cakes) and you made my days in the lab just HAPPY!! Merci d'abord à Stéphane, pour m'avoir appris énormément depuis l'été 2009, pour m'avoir aidée avec de nombreux problèmes techniques et tout simplement pour être pour nous tous le petit papa de ce labo. Familie Roth, c'est vraiment nous !! Merci Emilie, de m'avoir montré la voie dans cette thèse

et partagé un peu de ta combativité légendaire ! Emily, thanks for being such an adorable, sweet and caring lab mate! I am and will stay extremely proud to be called your lab sister!! Thanks as well for all the fabulous cakes, of course! Rita, I miss you so much! Thanks for all the fun we had together playing at night in the lab, and thanks for bringing Maurice into our lives!! And don't forget: Wake me up when it's all over!! Once, ~~in Milan~~, in Illkirch, I met this guy and… he had a suit!!! Thanks Mister (sorry Doctor) Francesco Boselli for bringing so much fun in the lab! And I definitively just love your stories!!! Finally thank you Pedro, for all the crazy talks at lunch time and I hope Marylène will be as cool as you are! Je voudrais également remercier les anciens membres du labo, Jacky, avec qui j'ai adoré jouer à la poufi de labo et Halina pour sa bonne humeur et son sourire même dans les spirales de la loose. Merci également aux étudiants qui sont passés par là, en particulier Fleur et Jacub pour avoir supporté ma supervision. A particular thank to Charlie, who helped me to analyze the last GCN2 results and for your careful proofreading of this manuscript.

Quand les gros poissons se battent, les crevettes doivent se tenir tranquilles. (Proverbe créole)

Parce qu'ici les crevettes c'est nous!! Merci mes IGBMC'girls! Laure, Sylvia, Charlène, Camille, Gabi, Miriam, Aurore, Morgane ! Chacune à votre façon, vous avez rendu ces quatre années plus rythmées, gourmandes, rigolotes, faites de confidences, de coups de gueules, de pleurs, de rire, de jolis évènements et de potins !! Juste plus cools quoi !! Spéciale casse-dé-dit à Sylvia pour avoir partagé cette période extraordinaire de l'écriture avec moi, de la bibliothèque au Do-Mac, des recettes de cuisine alsaciennes à ces fameux petits emballés violets !!

Merci aux autres personnes de l'IGBMC avec qui j'ai partagé des moments supers, les membres du SPB de manière général, les warriors de la bibliothèque et toute l'équipe Téléthon. Un merci tout spécial à Ziad et Samia, qui ont subi ma crise de « mi-thèse » un fameux vendredi aprem, à cause d'un Western-Blot.

Un homard, c'est autre chose qu'un poisson ! Vivre dans une carapace, autrement dit avoir ses os autour de soi, quel changement radical cela doit être dans la façon de comprendre la vie. (Raymond Queneau)

Mes G-stars, Laurent, Pauline et Caroline, le temps des homards est loin derrière nous maintenant ! Même si nos thèses respectives nous ont un peu éloignés, vous restez dans mon cœur et dans mes meilleurs souvenirs de labo. Je suis super contente d'être la première d'entre nous à finir cette étape et j'ai hâte de venir voir vos thèses aux quatre coins de la France et de l'Europe.

Si les poissons sont muets, les poissonnières sont bavardes pour eux. (Georg Christoph Lichtenberg)

Ma chère meute, Clara, Morgane, Amélie, Aurore, Anaïs, Manue, Claire, Héloïse, vous m'avez énormément apporté ces dernières années. Vous êtes des amies exemplaires et nos week-ends ont été un immense bol d'air frais pour moi à chaque fois.

Un grand merci également à Cha, que j'ai retrouvé ces dernières années, qui a souvent attendu des nouvelles, parce que j'étais overbookée au labo. Merci pour ta patience, pour ton sourire, ta sincérité et pour tous ces bons moments !

Finalement, mes vieilles Tepus, Betty, Caro, Julie et Véra, depuis 15 ans maintenant on partage tous les moments de nos vies, des plus difficiles aux plus heureux, des plus futiles aux plus sérieux. Cette thèse n'est qu'une page de plus à cette longue histoire. Merci d'avoir toujours été là, vous êtes ma deuxième famille !

Le paysan entre deux avocats est comme le poisson entre deux chats. (Proverbe espagnol)
Parce que ces dernière années, c'est moi qui me suit souvent retrouvée entre les avocats. Merci à vous ainsi qu'au Kettelser et Cie, Alex, Célia, etc. de m'avoir acceptée avec mes histoires bizarres de poissons à nourrir le dimanche matin et les jours fériés quand vous faisiez encore la fête. Et pour tous les barbec loupés de cet été, ne vous inquiétez pas ce n'est que partie remise.

Je voudrais en profiter aussi pour remercier les Graptons et Cie, alsaciens et berrichons, qui m'ont accueillie à bras ouverts et qui ont toujours montré beaucoup d'intérêt à propos de ma thèse et de mes petits poissons malades.

Poisson rouge : animal de compagnie qui, par rapport au chat, présente l'avantage de moins s'acharner sur les rideaux du salon. (Marc Escayrol)
Mon petit Kiwi, tu as été un de mes plus gros réconforts cette dernière année. Merci pour ta douceur, tes bêtises, qui me font toujours rire et tes bisous.

Petit poisson deviendra grand. (Jean de La Fontaine)
Un merci tout particulier à toute ma famille, qui m'a soutenue tout au long de ces années. Merci de m'avoir fait travailler mon « résumé de thèse grand publique » en écoutant avec beaucoup d'intérêt l'avancement de mes travaux lors des multiples repas de familles.

Merci à mes parents bien sûr, à Céline et à Olivier, qui ont respecté mes choix, même si le « retour sur investissement » n'est pas prévu pour tout de suite. Merci pour votre soutien inconditionnel, pour tous vos conseils et pour le modèle que vous êtes pour moi. Docteur Ramspacher ou pas, je serai toujours votre Cajoline !

Mamama, j'ai commencé ma thèse tu étais là, et puis tu es partie et finalement, les mois puis les années passent et je me rends compte que tu n'es jamais loin… Et puis, c'est toi qui l'as dit : « Docteur, ça, ça reste ! ». Qui l'eut cru que ça serait moi, finalement !

« L'amour est un poisson d'avril. » (Joseph-Guillaume Barthe)
Pour moi effectivement, c'est un poisson d'avril ! Merci, mon cœur, d'avoir été là pour moi ces dernières années. Même si tu m'as traitée de cloporte et de cheval de traie ces derniers temps, je te suis extrêmement reconnaissante de tout ce que tu as fait pour moi, des bons petits plats, aux sacrifices de vacances etc. Deux concours et une thèse plus tard, on est et on restera la meilleure des équipes ! <3

Les larmes sont pour le coeur ce que l'eau est pour les poissons. (Gustave Flaubert)…

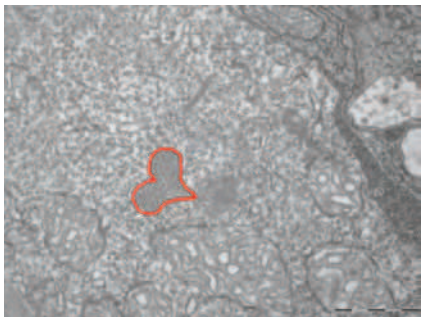

List of publications

- Pulse propagation by a capacitive mechanism drives embryonic blood flow. **(Manuscript 3)**

Anton H, Harlepp S, Ramspacher C, Wu D, Monduc F, Bhat S, Liebling M, Paoletti C, Charvin G, Freund JB, Vermot J.
Development. 2013 Nov;140(21):4426-34. doi: 10.1242/dev.096768. Epub 2013 Oct 2.

- Endothelial cilia mediate low flow sensing during zebrafish vascular development.

Goetz JG, Steed E, Ferreira RR, Roth S, Ramspacher C, Boselli F, Charvin G, Liebling M, Wyart C, Schwab Y, Vermot J.
Cell Rep. 2014 Mar 13;6(5):799-808. doi: 10.1016/j.celrep.2014.01.032. Epub 2014 Feb 20.

- Regulation of ß1 Integrin-KLF2-Egfl7-mediated angiogenesis by CCM proteins.

Marc Renz, Cécile Otten, Franziska Rudolph, Yuan Zhu, Gwénola Boulday, Johan Duchene, Michaela Mickoleit, Ann-Christin Dietrich, Caroline Ramspacher, Emily Steed, Julien Vermot, Jan Huisken, Elisabeth Tournier-Lasserve, Ute Felbor, Ulrich Sure, and Salim Abdelilah-Seyfried
(submitted to Developmental Cell)

- Developmental alterations in heart biomechanics and skeletal muscle function in desmin mutants suggest an early pathological root for desminopathies. **(Manuscript 2)**

Caroline Ramspacher, Coralie Spiegelhalter, Le Trinh, Federico Tessadori, Jeroen Bakkers, Jocelyn Laporte, Karim Hnia, Julien Vermot
(submitted)

- Desmin in muscle and associated diseases: beyond the structural function (Review). **(Manuscript 1)**

Karim Hnia*, Caroline Ramspacher*, Julien Vermot, Jocelyn Laporte
(* equal contribution)
(in preparation for Cell and Tissue Research)

- GCN2 (eif2ak4), a gene involved in pulmonary veno-occlusive disease, controls venous angiogenesis in zebrafish. **(Manuscript 4)**

Caroline Ramspacher, Virginie Monceau, Stephane Roth, Emily Steed, Florent Soubrier, Julien Vermot
(in preparation)

List of oral and poster communications

Oral communications:

- Printemps de la Cardiologie, Bordeaux, 11-14 avril 2012

Title : Développement de modèles de cardiomyopathies chez le poisson zèbre
Autors : Caroline Ramspacher, Karim Hnia, Jocelyn Laporte and Julien Vermot

- Intermediate Filaments in Neuromuscular Disorders workshop, Nice, 6 juillet 2014

Title: Zebrafish models for new insights into desmin function and aggregation in desminopathies
Autors: Caroline Ramspacher, Coralie Spiegelhalter, Nadia Messaddeq, Le Trinh, Jocelyn Laporte, Mohammed Karim Hnia, Julien Vermot

Poster communications :

- BOLD/ZF-HEALTH workshop 'Cutting edge technologies in biomedical research', Karlsruhe, 4-6 mai 2011

Title: Generating and characterizing knock-out zebrafish for *desmin a* and *klf2a*, two genes implicated in cardiovascular development
Autors: Caroline Ramspacher, Julien Vermot

- Symposium "Cardiovascular development and applications", Paris, 7-8 décembre 2011

Title: Characterization of *desmina* null zebrafish embryos
Autors: Caroline Ramspacher, Karim Hnia, Jocelyn Laporte and Julien Vermot

- Printemps de la Cardiologie, Bordeaux, 11-14 avril 2012

Title : Développement de modèles de cardiomyopathie chez le poisson zèbre
Autors : Caroline Ramspacher, Karim Hnia, Jocelyn Laporte and Julien Vermot

- 8th European Zebrafish Meeting, Barcelona, 9-13 juillet 2013

Title: Developing models of desminopathies in zebrafish suitable for drug screening
Autors: Caroline Ramspacher, Karim Hnia, Le Trinh and Julien Vermot

Table of contents

Introduction

Results

Chapter 1: Characterizing novel zebrafish models for new insights into desmin function and aggregation in desminopathies

Chapter II: Validating zebrafish use and generating models for vascular pathologies including hypertension and PVOD

Discussion

APPENDIX

List of figures

List of tables

List of abbreviations

2'OMe: 2'O-methylphosphorothioate oligoribonucleotides
AC: arterial calcification
AD: Alzheimer disease
AH: arterial hypertension
AKAP: A-kinase anchor protein
ALPM: anterior lateral plate mesoderm
ALS: amyotrophic lateral sclerosis
amhc: atrial myosin heavy chain
AS: arterial stiffness
AV: atrio-ventricular
AVC: atrio-ventricular canal
AVMs: cerebral arteriovenous malformation
AZ: S1555 or AZD8055 (autophagy inhibitor, Selleckchem)
BA: basilar artery
BAG3: BCL2-associated athanogene 3
BCA: basal communicating artery
Bmp: bone morphogenetic protein
C/EBP: CCAAT-enhancer binding protein
CARE: C/EBP activating transcription factor response element
CASA: chaperone-assisted autophagy
CCM: cerebral cavernous malformations
CLEM: correlative light and electron microscopy
CMA: chaperone mediated autophagy
cmlc2: cardiac myosin light chain 2
CNVs: copy number variants
CRISPR/Cas9: Clustered Regularly Interspaced Short Palindromic Repeats/ Cluster associated 9
CTD: connective tissue disease
DA: dorsal aorta
DDIT4: DNA-damage-inducible transcript 4 protein
DGC: dystroglycan complex
DMD: Duchenne muscular dystrophy
Doxy: doxycycline
ds: double stranded
EIF2AK4: Eukaryotic Translation Initiation Factor 2 Alpha Kinase 4
ENU: N-ethyl-N-nitrosourea
ETS: E26 transformation-specific
FDA: food and drug administration
FGF: fibroblast growth factor
fli: friend leukemia integration
flk: fetal liver kinase
GCN2: general control nonderepressible 2
HD: Huntington disease
Hh: hedgehog
HHT2: hemorrhagic telangiectasia type 2
IF: intermediate filament
iPSCs: induced pluripotent stem cells
ISR: Integrate Stress Response

ISV: intersomitic vessels
KD: knock-down
KI: knock-in
klf: krüppel like factor
KO: knock-out
LDA: lateral dorsal aortae
LGMD: limb-girdle muscular dystrophy
MFM: myofibrillar myopathy
MRFs: Myogenic Regulatory factors
MTJ: myotendinous junction
myl: myosin light chain polypeptide
NAC: N-acetyl-L-cysteine
NHEJ: non-homologous end joining
NMJ: neuromuscular junction
PAH : pulmonary arterial hypertension
PAO: pre-amyloid oligomers
PCH: pulmonary capillary hemangiomatosis
PCV: posterior cardinal vein
PD: Parkinson's disease
PHBCs: primordial hindbrain channels
PKA: protein kinase A
PKD2: polycystic kidney disease 2
PMBC: primordial midbrain channel
PVOD: pulmonary venous occlusive disease
SACs: stretch-activated cation channels
scl: stem cell leukemia
SHG: second harmonic generation
shh: sonic hedgehog
SNP: single nucleotide polymorphism
SR: sarcoplasmic reticulum
TAC transverse aortic constriction
TALEN: transcription activator-like effector nuclease
TEM: transmission electron microscopy
TGFβ: transforming growth factor beta
tnnt2: cardiac troponin t2
TRP: transient receptor potential
UPS: ubiquitin-proteasome system
vegf: vascular endothelial growth factor
vmhc : ventricle myosin heavy chain
VSMC: vascular smooth muscle cells
WES: whole exome sequencing
WGS: whole genome sequencing
WT: wild-type
ZIRC: Zebrafish International Resource Center

Introduction

I/ Zebrafish as a model in the context of human diseases modeling

A. A “new” model to suit the need of current challenges in human genetics

1) Current challenges in human genetics

Recent technological advances in the last 5 years have placed the field of translational medicine in a rapidly moving period. Massively parallel, high-throughput, next-generation sequencing techniques have enabled whole exome and whole genome sequencing (WES/WGS), giving a hyper-accelerated pace to the identification of genes implicated in human pathologies. In particular, the reduced costs following these technological progresses enable the use of sequencing from the bench to bedside, altering patient care (Biesecker et al., 2014; Fraser et al., 2014). This opens the possibilities for “personalized medicine”, which proposes a better understanding of the molecular causes of diseases and their genomic environment, and specific and personalized treatments options. Nevertheless these new techniques raise new questions from economical to ethical considerations including for their implementation in clinics, the support of their cost, the establishment and evaluation of relevant biomarkers. Another ethical issue concerns the patient, because the knowledge of its whole genome raises the possibility that it could contain mutations or predispositions to previously unknown diseases (Katsanis and Katsanis, 2013).

WES/WGS leads to the finding of rare alleles defined as a minor allele frequency of less than 0.5% (Tennessen et al., 2012). Dissecting the contribution of these alleles and of different candidate genes to the clinical phenotypes constitutes a significant difficulty for the attribution of a precise genomic defect to a disease. In fact, functional interpretation of genetic information and assignment of the predictive clinical value to a genotype represents a major problem in medical genetics. Computational algorithms to understand a mutation's impact, based on evolutionary, biophysical and structural properties of proteins, are more and more used but their predictive ability remains limited (Davis et al., 2014). Therefore validation of a gene's implication in disease and the related mechanism needs to be carried out through other methods, usually through the use of cell culture or animal models. Cellular *in vitro* models are extensively used for clinical and biomedical research for their simplicity of use and homology to patient tissues. More and more, induced pluripotent stem cells (iPSCs) disease models are generated and studied. iPSCs are reprogrammed from adult somatic cells with a defined set of pluripotency factors (Takahashi et al., 2007). They enable the generation of autologous patient-specific stem cells recapitulating precisely the patient mutation in its overall genomic environment. They represent a nice model for the understanding of cellular and molecular disease mechanisms, drug screening and eventually cell therapy (Salani et al., 2012). Nevertheless, they lack functional aspects of whole organs and do not permit to study complex interactions in disease pathology or treatments. Later in this manuscript, we will discuss animal models of diseases principally. Mouse is the most common animal model to determine the causal link between genotype variation and phenotypic manifestations. Nevertheless, some studies are not compatible with the use of mouse models, for

example in cases when the murine phenotype is not completely representative of the disease phenotype in human (e.g. Alzheimer's disease mouse model (Webster et al., 2014)). Some genetic particularities like copy number variants (CNVs) and epistatic interactions are moreover challenging to study and model in mice and only a few examples have been described so far (Bryk et al., 2014; Lindsay et al., 2001). Furthermore, the use of mammals raises the concern of ethics for animal experimentation. Finally, the rise of personalized medicine raises the question of the possibility of personalized models with a sufficient high-throughput for testing of specific patient mutations. In these cases some alternative models have to be considered.

Another challenge is the development of novel therapies. New pharmacological treatments need to be continuously developed for a large range of diseases with a current lack of, or poor, treatment. Moreover, some treatments can lead to secondary effects, effects limited to a category of patients or on a subtype of symptoms. Furthermore, many therapeutic strategies currently control the symptoms but only slightly delay the progression of the disease. Thus there is a constant need for ameliorating existing drugs or developing new ones. For that, drug screening approaches are more and more developed, using cultured cells or small animal models. They enable to identify new compounds but importantly they also permit to discover new function of existing drugs for use in another (sometimes completely different) pathological context. This approach is particularly interesting from an economical point of view because these drugs are already approved. This saves time and money in clinical trials and in translation of the research into an industrial product, which can be a limiting point in new drug release (Pober et al., 2001). Besides the pharmaceutical approach, additional therapeutic approaches include the development of new strategies such as gene therapies and cell therapies. Typical examples of gene therapy include the adeno-associated and lentivirus based delivery of micro-dystrophin and mini-utrophin in Duschenne muscular dystrophy (DMD) mdx model mice, non-human primate models and Golden Retriever Muscular Dystrophy (GRMD) dog models (Cerletti et al., 2003; Rodino-Klapac et al., 2007; Koo et al., 2011). Moreover, morpholino-oligonucleotides (MO) or 2'O-methylphosphorothioate oligoribonucleotides (2'OMe) based antisense-mediated exon-skipping techniques were developed and tested in GRDM (Benedetti et al., 2013) and human patients (Kinali et al., 2009). Cell therapy, using satellite or mesoangioblast cells and miRNA-based translation inhibition (Berardi et al., 2014), is currently raising new hope, in particular in the context of DMD.

2) Diversity of animal models

a) Numerous animal models are available

The first record of animal models' use in science is dated from the 4th to 3rd century BC. Aristote (384-322 BC) was the first to observe differences between animal models by experimental surgery and Erasistratus of Alexandra (302-258 BC) carried the first physiology research studying the function of the heart and respiratory systems in living pigs. The first anatomy textbook by Galen (129-200) was completely based on animal dissections (pig and apes) as the dissection of human cadavers was forbidden by religious and legal authorities (Chow et al., 2008). Since then, the use of animal models

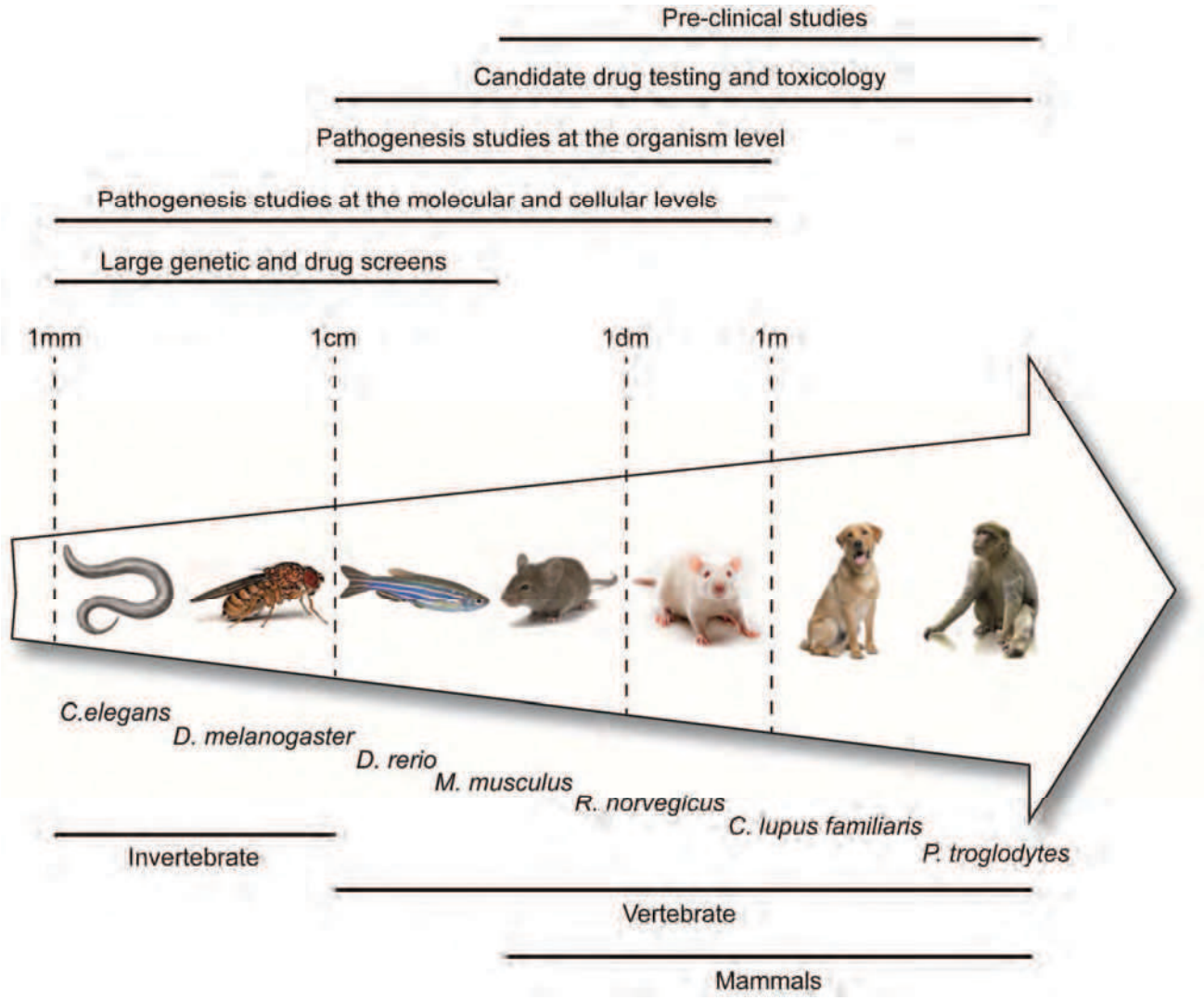

Figure 1: Scheme presenting the most common model animals in the context of biomedical research and disease modelling and the principal type of studies they are used in.

has been essential for virtually every medical breakthrough in human and animal health. Evolving more and more from observational to experimental studies, the work on animals enables a better understanding of biological mechanism and physiology in normal or pathological conditions and for the development of safe new medical treatments.

Despite various genome sizes and organism complexity, there is a high genetic conservation from the primitive eukaryotes to mammals. Moreover, cellular mechanism and pathways are highly homologous, enabling the study of most of human physiology, in normal and pathological conditions, in model animals. Model animals include mice, rats, bird, rabbits, guinea pigs, sheep, fish, frog, pigs, dogs, cats and primates, among others (Figure 1). Despite their variety, 95% of animal models used are mice and rats. Less than 1% includes big animals like cats, dogs or non-human primates. For the establishment of a disease model, both spontaneous models, presenting naturally the animal equivalent of a human disease (for example, spontaneous models for Duchenne muscular dystrophy exist in mice (mdx model), golden retriever and cats) (Wells et al., 2005) and genetically engineered models, in which a specific condition is recapitulated artificially in an animal, are used.
The use of animals in research raises ethical issues. Nevertheless, replacement methods like computer model, tissue and cell culture are not sufficient to recapitulate the extreme complexity of a living system at the whole organism level. Animal testing remains a necessity and stays unequivocal for public health authorities for the testing and the approval of novel therapies.

b) Choosing the right animal model

The first concern when choosing an animal model is the relevance of the species for the studied character or pathology. In particular, the chosen animal should maintain at least a specifically relevant biomarker for a specific pathology. The similarity between the organ affected in the model animal and human is important to ensure the model mimics the pathology closely and has more chances of a sufficient predictability and transferability. For that, a cross-species phylogenic investigation, for conservation of organ functionality, studied mechanism and gene function is necessary. In this context, a “specialization” of animal models for certain pathologies is established, like the use of rat for the study of primary liver cancer, pig for cardiovascular grafts and rabbit for bone fracture, for example (Chow et al., 2008).
The design of the experiments needed and the experience of the experimenter are also to be taken into account (Table 1). Some obvious technical constraints, for example the possibility of genetic modifications, often guide the model choice toward the models with the most potential. The mouse model, in which many techniques allowing gene knock-out (KO), replacement and mutagenesis were developed throughout the years, offers many possibilities for testing gene function. Moreover, inbred or naturally immunosuppressed animals can be used in the case of transplant or immunological studies and are not available in all species. The relevance of a species can also reside in the availability of previous comparable studies which enables researchers to rely on an experimental background and envisage more easily the outcome.

	C. elegans	D. melano-gaster	D. rerio	M. musculus	R. norve-gicus	H. Sapiens
Usual name	C. elegans	Drosophila	Zebrafish	Mouse	Rat	Human
Percent identity with Homosapiens	43%	61%	70%	80%	90%	-
Genome size	9.7×10^{7}bp	1.3×10^{8}bp	1.4×10^{9}bp	2.5×10^{9}bp	$2{,}8X10^{9}$ bp	$3{,}3X10^{9}$ bp
Number of genes	20 541	13 937	26 459	23 148	22 940	20 805
Practical attributes						
Husbandry demands	$	$	$	$$$	$$$	
Cost per animal	$	$	$	$$$	$$$	
Characterized inbred strains	+	+	+	++++	+++	
Outbred laboratory strains	+	+	+++	++	++	
Germline/embryonic cryopreservation	Yes	No	Yes	Yes	Yes	
Lifespan	2 weeks	0.3 years	2–3 years	1.3–3 years	2,5-3 years	
Generation interval	5.5 days	2 weeks	3 months	6–8 weeks	2 months	
Number of offspring	300 larva	10–20 eggs	> 200 embryos/clutch	10–12 pups/litter	6-12 pups/litter	
Embryonic development	ex vivo	ex vivo	ex vivo	in utero	in utero	
Molecular biology tools						
Transgenesis	++++	+++	++++	+++	+++	
Gene targeting	++++	+++	++	++++	+	
Conditional gene targeting	+	++	+	++++	+	
Transient in vivo assays	+++	++	++++	+	+	
Allelic series from TILLING	+++	+++	++++	++	+	
Affordability of large scale screens	++++	++++	+++	+	-	
Cell biology tools						
Cell lines and tissue culture	+	++	+	++++	+	
Antibody reagents	+	++	+	++++	++	
In situ probes	+	+++	++++	+++	++	
Disease process						
Birth defects	+	++	++++	++++	++++	
Adult-onset	++	+	+	++++	++++	
Behavioral	++	++	++	++	+++	
Aging	+++	++	++	++	+	
Metabolic	++	++	+++	+++	+++	

Table 1: General attributes of animal models and interest in the context of human disease modelling.

Attributes are categorized using -: not relevant or not a strength; $, $$, $$$ and +, ++, +++: relative cost ($) and strength (+) of the model in each category; ++++ being outstanding strength of the model. Table adapted from Davis et al., 2014 and Lieschke and Currie 2007.

Then, the choice of a model is largely dependent on the number of samples required. For large scale drug screens for example, small animals including invertebrates (or cell culture) will be preferred. In relation with the number of animal chosen, the availability and cost of animals and of their maintenance are crucial (Table 1). Finally, the 3R ethical rule has to be considered and replacement, in particular of higher vertebrates, envisaged when possible.

3) General presentation of the zebrafish model

Zebrafish or *Brachydanio rerio* (Figure 2) is a vertebrate from the Teleosteis infraclass. Originally living in the freshwaters of the tropical south-west Asia, the small-sized zebrafish (3cm in length for an adult fish) is a common aquarium species. In the late 1960s, George Streisinger first used it as a model animal for embryogenesis and development studies because of its “desirable attributes” including easy maintenance, short generation time, large clutches and synchronous *ex vivo* development (Davis et al., 2014). It has a diploid genome containing 25 chromosomes without heteromorphic sexual chromosomes. The zebrafish genome has a size of around 1.4 billion nucleotide base pairs, corresponding to a little less than half of the human genome. Despite this small size, the zebrafish genome counts more than 26000 protein-coding genes (compared to 20805 protein coding genes in the human genome) (Pickart et al., 2014). There is a human ortholog for 69% of these genes, while 71% of human genes have at least one zebrafish ortholog (Howe et al., 2013). After divergence from mammals (between 360 and 450 million years ago), the zebrafish genome is thought to have undergone a whole genome duplication event, explaining its high redundancy and the fact that approximately 15% of the human genes have more than one ortholog in zebrafish (Howe et al., 2013). Paralogs can have either redundant functionalities or retain specifically one of the functions of their human ortholog.

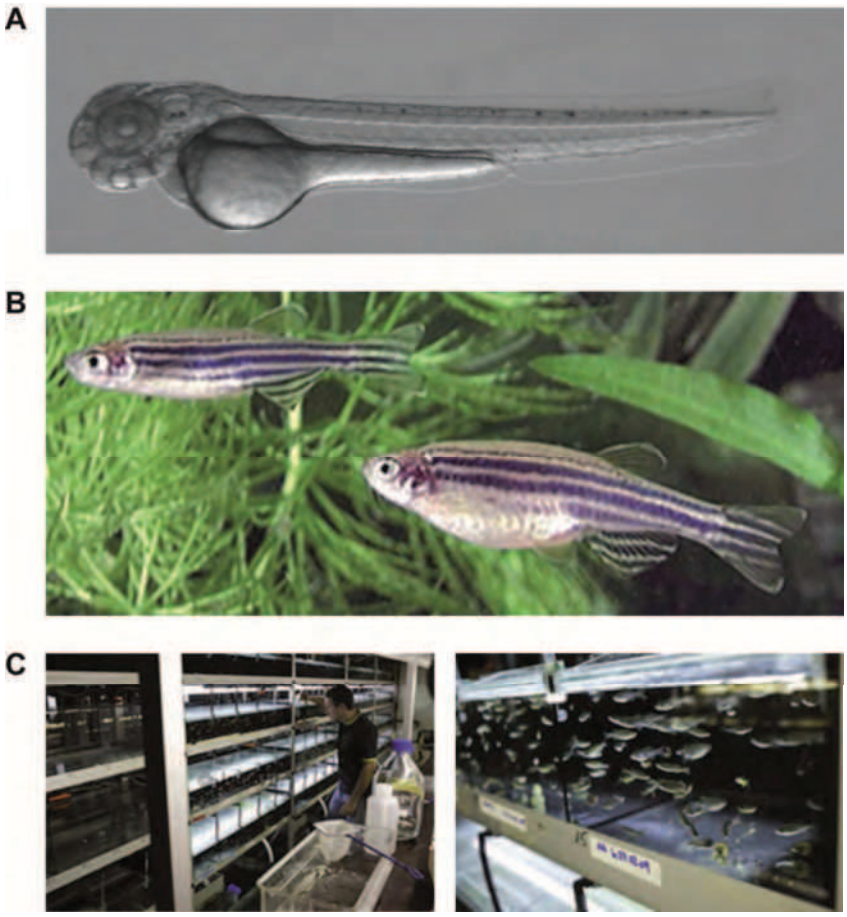

Figure 2: Presentation of zebrafish or *Danio rerio*

(A) Side view of a 48hpf zebrafish embryo. (B) Adult zebrafish. The upper fish is a male; the lower fish is a female. Source Philippe Mourrain, Stanford Report, 2007. (C) Zebrafish facility set-up at IGBMC. Source: Inserm.

B. Variety of use of the zebrafish model in the context of human diseases

1) Use of zebrafish for identification or validation of candidate genes

The zebrafish was extensively used in the context of forward genetic screens for the identification of new genes implicated in developmental or pathological conditions. The concept of these screens is to induce random mutations throughout the genome and, after appropriate breading steps, to select germ line mutations, and to screen the resulting animals for a phenotypic readout of interest. Finally, the mutated gene is identified using gene mapping techniques and increasingly next generation sequencing (Lawson et al., 2011). Random mutagenesis projects including gamma-rays (Chakrabarti et al., 1983) and more commonly N-ethyl-N-nitrosourea (ENU) -induced mutagenesis (Mullins et al., 1994) gave rise to thousands of mutants with embryonic phenotype, which enabled to incriminate genes in previously unknown functions and pathways. This approach brought fundamental new insights in understanding developmental processes as somitogenesis (Van Eeden et al., 1996) or cardiovascular development (Stainier et al., 1996), for example, and contributed to the identification of new genes implicated in congenital or genetic diseases. For instance, zebrafish enabled to identify the implication of *sec23a* (*crusher*^{m299} mutant) in cranio-lenticulo-sutural dysplasia (Lang et al., 2006). Nevertheless, such screens present limits to find candidates for inherited human diseases because they might produce the same allele than implicated in patients, the alleles with dominant-negative inheritance or gain of function effect will be lost in the breeding steps, there is a possible compensation by the second version of the same gene present in the fish due to genome duplication and a phenotypic readout within the time period considered in the screen is needed (Davis et al., 2014).

Large genome wide association studies including WES/WGS have proposed candidate genes for an increasing number of genetic pathologies in humans. Nevertheless, the distinction between a pathogenic allele and a benign polymorphism is difficult, in particular when there are an insufficient number of relatives in the family for precise mapping. The ease of depleting a candidate gene in zebrafish was extensively used for confirmation of loss-of-function effects of mutations. In particular the use of MO-based antisense knock-down (KD) is particularly suited for this use. MO is a powerful approach for a rapid screening for candidate gene validation, genome annotation and disease modeling (Summerton et al., 1999). MOs are typically oligomers of around 25 morpholine bases that are complementary in sequence to their target region. Their phosphorodiamidate backbone confers to them a high affinity with RNA. They generate a transient partial or full KD of the targeted gene expression, either by fixing the translation start-site and consequently blocking the initiation of translation or by targeting a splice site, leading to the excision of the previous exon or insertion of the following intron, leading in most cases to the production of an invalid protein. The efficacy of the morpholino is limited to 3-5 days only and limits the time window of the experiment, limiting concomitantly their application to processes and diseases with manifestations within this period. Moreover, a special care has to be taken to ensure specificity of the MO targeting and avoid off-targets and toxicity (Bill et al., 2009). This includes the use of several morpholinos with distinct targets for

HUMAN PATHOLOGY

ZEBRAFISH MODEL

A1

CCM

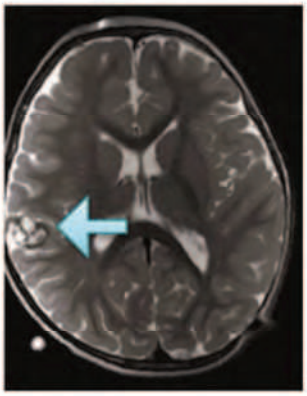

A2

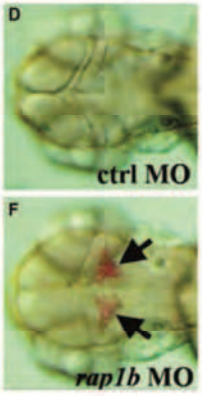

B1

AVM

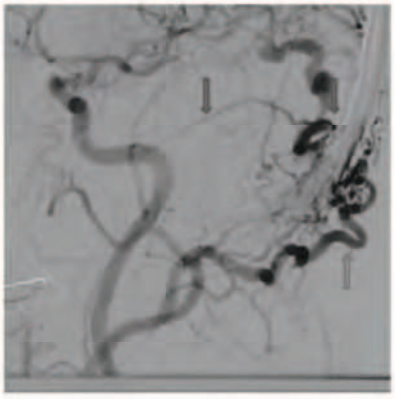

B2

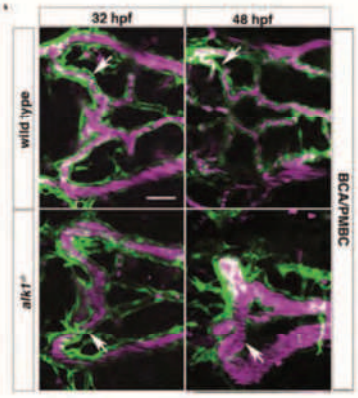

C1

DCM

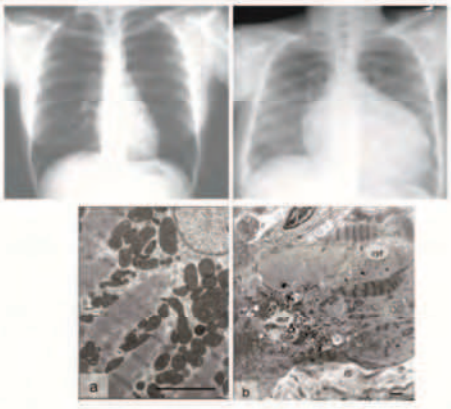

C2

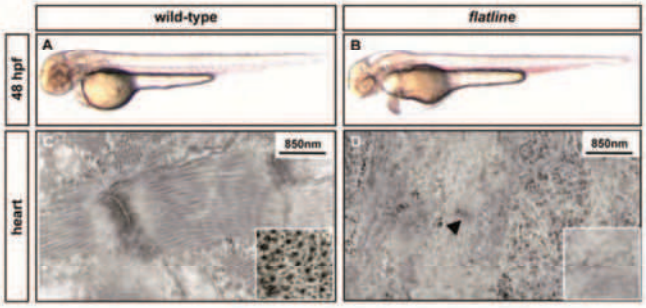

D1

DMD

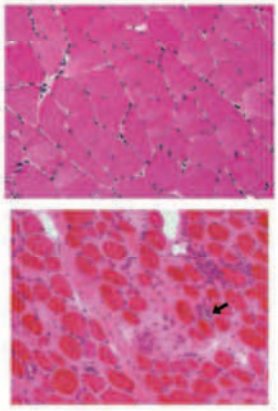

D2

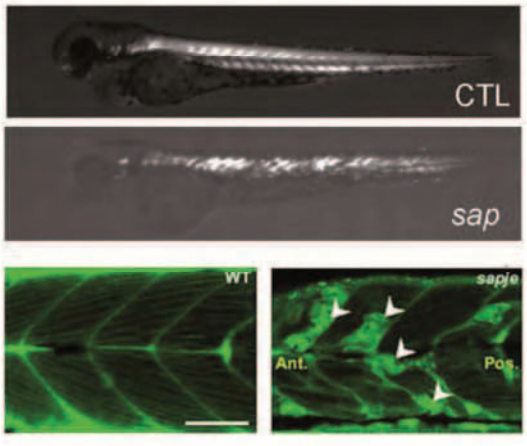

each candidate gene, the specific rescue of the invalidated gene function by injection of the corresponding mRNA and comparison with mutants, when available. Despite these drawbacks, MO KD is a very reliable and rapid approach for functional assessment to narrow a relatively large set of candidate genes from screens. It was used in many examples including the validation of 11 genes out of 68 loci identified by genome-wide association study implicated in the regulation of megakaryopoiesis and platelet formation (Gieger et al., 2011).

Examples showing the use of MO for validation of candidate genes are numerous. An interesting one consists of the recent identification of *CCDC78* mutation as the cause of a unique type of congenital myopathy, which was identified in a three-generation dominant pedigree. Clinical signs presented progressive distal weakness and excessive fatigue and muscle biopsy revealed central nuclei, core-like lesions and desmin- and actin-positive protein accumulation. A combination of single nucleotide polymorphisms (SNPs) linkage and WES revealed the inclusion of an in-frame intron in *CCDC78* in patients. This mutation was modeled precisely in zebrafish using a splice site MO leading to the inclusion of the same exon and mirrored the same findings observed in patient biopsy (Majczenko et al., 2012).

2) Use of zebrafish for disease modelling

a) Morpholino oligonucleotide (MO)-based knock down (KD)

As described in I.B.1) MO antisense KD is a powerful technique for gene depletion. Not only, this method can be used for validation of candidate genes, but the resulting embryos can be analyzed as model of loss of function diseases. Moreover MO dosing can be adjusted to mimic an heterozygous loss-of function mutation. MO KD can be used in combination with mRNA injections (Niederriter et al. 2013), in particular using human mRNA, to validate the redundancy of the gene function across species or using a mutated version of the human gene to study the gain of function of the particular mutation and generate a humanized model of the disease.
Examples are very numerous and include models of dilated cardiomyopathy based on the MO KD of the heat shock protein cochaperone *BCL2-associated athanogene 3* (*bag3*) (Norton et al., 2011) and of *cardiac troponin t2* (*tnnt2)* (Huang et al., 2009) and numerous models of myopathies including MO against *myotubularin* (*mtm1*) (Dowling et al., 2009), *nebulin* (*neb*) (Telfer et al., 2012) and *selenoprotein N* (*sepn1*) (Jurynec et al., 2008).

b) Mutant models

Despite the fact that specific knock-in (KI) is now possible in zebrafish, mutant disease models count almost exclusively KO models. They are especially informative for studies of loss of function effects linked with the corresponding gene mutation in patients.

As discussed in I.B.1), numerous zebrafish mutants were generated through random mutagenesis and can be further used as KO disease models. The largest random mutagenesis project is carried out by

(see figure on previous page)

Figure 3: Example of human disease models of the vascular, cardiac and muscular systems in zebrafish

A. Model of arteriovenous malformations (AVMs) (adapted from Walcott et al., 2014 and Corti et al., 2011). A1: AVMs patient angiogram of carotid artery in the late arterial phase shows arterial branches (red arrow) is directly connected to a venous branch (blue arrow) through a high flow fistula (purple arrow). A2: In WT embryo, a transient connection connects the basal communicating artery (BCA) and the primordial midbrain channel (PMBC) at 32hpf but regresses at 48hpf (white arrows). In *alk1-/-* embryos, this connection is retained at 48hpf forming a BCA-to-PMBC connection. *Tg(kdrl:GFP)*^{la116} highlight endothelial cells (green) and *Tg(gata:dsRed)*^{sd2} highlight the erythrocytes (purple)

B. Model of Cerebral cavernous malformation (CCM) (adapted from Walcott et al., 2014). B1: Magnetic resonance imaging from a patient shows CCM in the right frontal lobe (blue arrow). B2: Zebrafish morphant embryos for *rap1b*, encoding for an effector protein of CCM1, have a disrupted CCM pathway and present intracranial hemorrhage similar to human lesions.

C. Model of dilated cardiomyopathy (DCM). (C1) Upper panel: X-ray radiograph of the thorax of control (left) and dilated cardiomyopathy (right) patients. Sources: Université de Lyon and http://www.heartupdate.com/. Lower panel: Electron micrograph from control myocardium with regular arrangement of sarcomeres (left) and failing myocardium from dilated cardiomyopathy patient (right) exhibiting areas free of contractile material filled with nonspecific cytoplasm (cyt) and numerous autophagic vacuoles (aut). The interstitial space (IS) is widened. Bars represent 5 µm. Source: Hein et al., 2009. (C2) Upper panel: Side view of 48hpf WT and *smyd1*$^{-/-}$ (*flatline* mutants). Mutant fish present a large pericardial oedema. Lower panel: Electron micrograph of sections through myocardium of wild-type and *flatline* mutants at 48 hpf. Mutant embryos lack sarcomeric structures and only premature sarcomeric structures can be detected (arrowhead). Source: Just et al., 2011.

D. Model of Duchenne muscular dystrophy (DMD). (D1) Haemotoxylin and eosin-stained histological transverse sections of skeletal muscles from control (upper panel) and DMD (lower panel) patients. Sources: http://neuromuscular.wustl.edu/ and pathpedia.com. (D2) Upper panel: Side view of 48hpf WT (upper image) and *sapje* mutant (lower image) zebrafish under birefringence conditions. Disrupted muscle fibers are seeable in the mutant tail muscles. Source: Telfer et al., 2012. Lower panel: BODIPY Ceramide staining in WT (left) and *sapje* zebrafish mutants (right) show dystrophic and degenerating muscle fiber in the mutant. Source: Webb et al., 2012.

the Wellcome Trust Sanger institute in Cambridge and entitled “The Zebrafish Mutation Project” (Kettleborough et al., 2013) (http://www.sanger.ac.uk/Projects/D_rerio/zmp/). The aim of this project is to generate a free and opened bank of mutants for all the zebrafish genes available to the zebrafish community. As of June 2014, 11 892 mutated genes were available (corresponding to 45% of the zebrafish genome) with a total of 24 088 alleles and can be ordered directly through the Zebrafish International Resource Center (ZIRC).

For example, zebrafish homologs of genes implicated in cerebral cavernous malformations (CCM), *CCM1*, *CCM2* and *CCM3* have been identified as *santa*, *valentine* and *pcdc10* respectively and extensively studied (Stainier et al., 1996, Yoruk et al., 2012, Gore et al., 2008). KD or KO of these genes was obtained either through genome editing or morpholino injection and showed impaired cardiovascular development, with dilated cardiomyopathy and trunk and head vasculature defects, including thin-walled vessels and hemorrhage (Figure3A).

Another example is the use of a zebrafish model to better understand the rare cases of hereditary forms of cerebral arteriovenous malformation (AVMs) implicated in human syndromes like hereditary hemorrhagic telangiectasia type 2 (HHT2). AVMs correspond to vascular abnormalities with direct communication between arteries and veins without intervening capillary bed. A single nucleotide polymorphism in the gene encoding for activin receptor-like kinase 1 (*alk1*), a TGFβ family type I receptor of the BMP (bone morphogenetic protein) signaling pathway, was linked with many AVMs cases including HHT2 patients. *Alk1* was then mutated in different animal models, including mice,e but an *in vivo* approach and whole cranial circulation imaging was lacking (Walcott et al., 2014). In this context, zebrafish *alk1* mutants were validated as models of AVMs, presenting abnormal artery-vein junctions in the cranial vasculature and high output cardiac failure already observed in patients. Importantly, the simple and well patterned organization of the zebrafish developing cranial vasculature enabled us to attribute these abnormal connections to the persistence of normally transient developmental connections (Corti et al., 2011) (Figure 3B).

Moreover, many examples of zebrafish mutations in genes affected in human hereditary myopathies and cardiomyopathies were identified by large-scale screen (Figure 3C, D). Examples are presented in Table 2. Many of them enabled us to obtain new insights into the pathological mechanism of the modeled disease.

More recently, directed mutagenesis became possible in zebrafish with the help of nuclease-based techniques including Zinc Finger-Nucleases (ZFN) (Meng et al., 2008, Doyon et al., 2008), Transcription Activator-Like Effector Nuclease (TALEN) (Bedell et al., 2012) and Clustered Regularly Interspaced Short Palindromic Repeats/ Cluster associated 9 (CRISPR/Cas9) (Hwang et al., 2013). These technologies are based on the insertion of a double-stranded cut in genomic DNA by a nuclease domain at a locus of interest specifically recognized by the associated DNA binding motif. This motif is peptidic in the case of ZFN and TALEN but RNA-based in the case of CRISPR/Cas9. The

Human disease	Implicated gene	Associated zebrafish gene	Mutant name	Reference
Cardiomyopathy models				
DCM and HCM	TNNT2	*tnnt2a*	*silent heart*	Sehnert et al. 2002
DCM	TTN	*ttna*	*pickwick*	Xu et al., 2002
DCM	ILK	*ilk*	*lost-contact/main-squeeze*	Stainier et al., 1996; Bendig et al., 2006
DCM	LAMA4	*lama4*	*laminin alpha 4*	Knöll et al., 2007
DCM	NEXN	*nexn*	*nexilin*	Hassel et al., 2009
DCM	MLC-1	*cmlc1*	*lazy susan*	Meder et al., 2009
DCM	SMYD1	*smyd1b*	*flatline*	Just et al., 2011
Myopathy models				
Multiple forms of congenital myopathies	RYR1	*ryr1b*	*relatively relaxed*	Hirata et al., 2007
Pierson syndrome	LAMB2	*lamb2*	*softy*	Jacoby et al., 2009
Dystrophy models				
DMD	DMD	*dmd*	*sapje and sapje-like*	Bassett et al., 2003; Guyon et al., 2009
MDC1A (muscular dystrophy congenital 1A) and LGMD	LAMA2	*lama2*	*candyfloss and cl501*	Hall et al., 2007; Gupta et al., 2012
Limb-girdle muscular dystrophy	DAG1	*dag1*	*dag1*	Gupta et al., 2011
Other muscular diseases				
ARTHROGRYPOSIS, DISTAL, TYPE 2B; DA2B	TNNI2A.4	*tnni2a.4*	*tnni2a.4*	Ferrante et al., 2011

Table 2: Zebrafish mutant models of muscle diseases

cut will later be subjected to the error-prone repair mechanism of the cell, which likely lead to an insertion or a deletion perturbing the reading frame and therefore to a shortened and unfunctional protein product. At the moment, experience from the zebrafish community and from our hands give advantage to the TALEN approach in term of KO efficiency and lack of off targets compared to CRISPR/Cas9 (Fu et al., 2013). Moreover, the TALEN method was shown to be powerful enough to generate a biallelic mutation at the targeted loci enabling us to directly analyze the effects of the somatic mutation in the injected embryos as a more specific and less toxic alternative to MO (Bedell et al., 2012). For example, CRISPR/Cas9 was used to target the *etsrp* and *gata5* loci, recapitulating respectively the vasculature phenotypes and the cardiac bifida phenotype observed previously (Chang et al., 2013).

KI using either TALEN or CRISPR/Cas9 and either homologous or non-homologous repair of the generated DNA break was only recently made possible in zebrafish (Zu et al., 2013, Auer et al., 2014) and represents outstanding new possibilities in term of genetic disease modeling in the near future. This method enables to directly and specifically enter a disease-mimicking mutation in the zebrafish ortholog gene for the generation of stable humanized zebrafish model of diseases.

c) Transgenic and mRNA injection overexpression models

The use of transgenic or mRNA injection-based approaches enable the study of dominant and gain-of-function effects in zebrafish. Normal or mutated human versions of the gene of interest can be overexpressed and directly mimic effects in patients. The simplicity and rapidity of mRNA injection enables us to test and compare the influence of several mutations within the same gene. Transgenesis is highly efficient in zebrafish. Based on the use of Tol2 transposons for better transgene integration (Kawakami, 1998), usual transgenesis conditions lead to more than 50% efficiency in zebrafish. Moreover, some Cre-lox regulated transgenic models are available and a zebrafish Cre-zoo project grouping CreER(T2)-driver lines was launched recently (http://crezoo.crt-dresden.de) (Jungke et al., 2013). Transgenic models are often used for their stability in time compared to MO or mRNA, which are transient. An interesting example of the use of a transgenic model was obtained expressing the human 4-repeat *TAU* under the *eno2* promoter, as model of Alzheimer's disease. Tau accumulation comparable to neurofibrillary tangles was found within neuronal bodies axons in neurons in adult zebrafish (Bai et al., 2007).

For more rapid and high throughput overexpression, mRNA injection directly in the one-cell stage embryo was extensively used. A famous example is the use of mRNA overexpression to CNVs associated pathologies. CNVs correspond to the variable number of copies of each gene that can be found in a genome. Following structural rearrangements, duplication, transposition or deletion of some chromosomal regions, which can range in size from a few thousands to millions of base pairs, can occur and lead to imbalance of normal gene expression. They can have both a *de novo* and recurrent apparition. Some CNVs have been associated with diseases. Historically, only few animal models of CNVs related diseases could be generated (Lindsay et al., 2001) due to lack of genetic tools for high-

throughput invalidation or overexpression of genes. The zebrafish has emerged recently as a powerful tool to understand CNVs pathologic effect, using a combination of MO- and mRNA-based overexpression to model respectively deletion or duplication of all the genes present in the region. A well-characterized redundant pathogenic CNV consists of a 600-kb deletion on 16p11.2, encompassing 29 annotated genes. It has been significantly and reproducibly associated with a range of neurocognitive defects, including epilepsy and autism whereas the reciprocal duplication has been associated with autism and schizophrenia. A systematic zebrafish KD and mRNA-based overexpression of each of the 29 genes in the 16p11.2 region was performed and *kctd13* was found to be the main driver of the neuroanatomical phenotypes linked with the disease (Golzio et al., 2012).

Another interesting example of the use of mRNA injection to study diseases is found in a study revealing mutations in the co-chaperone *DNAJB6* as a cause of limb-girdle muscular dystrophy (LGMD) in several families worldwide. mRNA of *DNAJB6* with patient mutations were coinjected with WT and mutated mRNA of the member of the chaperone-assisted autophagy (CASA) complex, myofibrillar myopathy-causing protein, BCL2-associated athanogene 3 (BAG3). This experiment showed interaction between DNAJB6 and BAG3 and the implication of CASA in the pathogenesis of LGMD (Sarparanta et al., 2012).

d) Other models

Some other but more sporadic methods were used for the generation of disease models in zebrafish. In particular, engraftment of disease cells onto a zebrafish host was extensively used for cancer modelling (as reviewed in Blackburn and Langenau, 2014).

Exposure to physical or chemical agents (ex toxins, carcinogens, teratogens) is used for example to induce heart injury by abdominal incision and ventricular freezing using liquid nitrogen (Chablais et al., 2011; Jopling et al., 2010). Indeed, zebrafish is extensively used for regeneration studies in myocardium as a model of heart attack but in trunk and fin as well. Other studies used drugs like glafenine, a nonsteroidal anti-inflamatory drug, to induce injury of intestinal epithelium (Goldsmith et al., 2013).

Some spontaneous models exist in zebrafish. In particular, zebrafish can serve as a model for infectious diseases with natural pathogens. The most famous example is *Mycobacterium marinum* zebrafish infection, which enabled to provide new insight into human tuberculosis pathophysiology (Meeker et al., 2008). This pathogen is a close genetic relative of *Mycobacterium tuberculosis* and produces comparable inflammatory granulomas in fish to that observed in the lung of tuberculosis patients. Studies from zebrafish showed the susceptibility of patients to tuberculosis is dependant on the genotypic combination of alleles for the inflammatory response factor LTA4H, with homozygous patients having more chances to succumb to the disease due to either hyper or hypo-immune response (Tobin et al., 2012).

3) Use of zebrafish for drug discovery, drug testing and toxicology assays

Large scale drug screens are feasible only in small, largely available animal models like invertebrate models. Nevertheless, the homology between these models or cultured cells and a complex physiological mechanism is often poor and lacks relevant functional outcome measures for translation in a pathological context. The zebrafish offers the ideal combination of invertebrate advantages and vertebrate biological relevance and is more and more used in large drug and toxicology screens.

Chemical and drug delivery in the zebrafish embryo is possible by simple passive diffusion from its aquatic medium. Nevertheless, other alternative methods are available, including direct injection into the yolk sac, injection to the cardinal vein located ventrally to the heart along the yolk, non-systemic injection into the abdominal wall or by microgavage from the larvae stage. Intra-peritoneal injections and oral delivery using gluten as a carrier material were developed as well as for drug administration in adult fish. (Pickart et al., 2013).

Moreover, automated phenotyping procedures and softwares have been developed by the zebrafish community to assess automatically a large range of parameter from images taken in 96-well plates. (Peravali et al., 2011).

Zebrafish was used for the identification of new drugs by high throughput drug screening performed in the context of DMD using the dystrophin-null *sapje* and *sapje-like* mutants (Kawahara et al., 2011). After performing a drug screen of the 1120 chemical compounds of the Prestwick chemical library (composed of Food and Drug Administration (FDA) approved drugs) in pools of eight chemicals, they separately screened compounds of the pools for which the treated fish had a reduced perturbation of birefringence signal. Birefringence signal is a label free method based on light polarity allowing to easily image the organization of the skeletal muscles of the fish tail and is a common marker of muscle integrity in zebrafish. Seven compounds that preserved muscle integrity were identified and finally one of them, a phosphodiesterase inhibitor, was shown to extend the survival of treated fish and restore muscle integrity after long term treatment. The same drug was found to ameliorate DMD in human and mouse proving the suitability of zebrafish for drug development (Adamo et al., 2010; Percival et la., 2012).

There is also a growing interest in using zebrafish for teratology and toxicology studies. Many known side effects were studied and modeled in zebrafish. For example, it was shown that the overdose of analgesic and anti-pyretic medication Acetaminophen can cause hepatotoxicity in zebrafish, similar to the acute liver failure in humans (North et al., 2010). Many private biotech and pharmaceutical companies are now developing zebrafish-based toxicology screening services. Additionally, the U.S. Environmental Protection Agency recently added a zebrafish developmental assay (currently based only on death and major structural defects) to its Computational Toxicology Research Program to help elucidate the toxicity of potentially hazardous chemicals (Padilla et al., 2011).

C. Considerations while using the zebrafish for human disease modeling

1) Example of specific advantages for the use in the human genetic field

Beside its completely annotated genome, zebrafish benefits largely from resources developed by the community including an anatomical atlas (Kimmel et al., 1995) and anatomical landmarks for staging, a web-based integrated resource (ZFIN) including an histological and cytological characterization of tissues and organs microanatomy (Zebrafish Phenome project) and available analysis of expression pattern of genes with *in situ* hybridization and DNA microarray, helping for a rapid validation of the presence of a target gene expression in the tissue of interest. All this documentation is of particular importance for cross species comparison and facilitates a direct comparison with changes subsequent to pathology.

The optical clarity of embryos, due to the absence or the possibility to inhibit pigmentation, coupled with their ideal size for imaging, allows real-time imaging of developing pathologies. The development of pigmentation mutant lines like the *casper* line enables us to extend this property for adult imaging (White et al., 2008).Therefore, anatomic, cellular and molecular phenomena can be observed directly live, in particular in combination with the use of transgenic lines largely available for a broad range of cell lines or organs of interest. This permits for example the *in vivo* monitoring of small molecules signaling in live conditions through transgenic reporter expression, like Gcamp for Ca^{2+} imaging (Muto et al., 2011) or H_2O_2, for example, in the process of wound healing (Niethammer et al., 2009). Recently, imaging of the whole brain activity was performed using the Gcamp reporter, reaching more than 80% of all neurons at single-cell resolution (Ahrens et al., 2013).

The small size of zebrafish embryos allows them to receive oxygen from their medium through passive diffusion for the first 5 days of development. This enables to test usually embryonic lethal pathologies or mutations in particular affecting heart function and the development of the cardiovascular system. Moreover, during study at early live stage, no feeding is necessary because the yolk provides all the nutrients needed, which facilitates maintenance during an experiment, in particular in high-throughput conditions (Gut et al., 2012). It enables stable nutritive conditions from one embryo to the other, which is important in the context of metabolic diseases studies for example. Finally, using embryos has the ethical advantage of reducing concerns about pain and suffering as the neurological development is not yet advanced. The use of the zebrafish before 5dpf is therefore recognized by both the United States and the European Union as a “replacement” strategy for ethical animal experimentation (Pickart et al., 2014).

Another zebrafish property, which is particularly relevant for diseases modelling, resides in its answer to diseases with an innate and adaptive immune system typical of other vertebrates and functional from the second day (Novoa et al., 2012).

Finally, the large clutch size of zebrafish increases the possible number of replicates for an experiment and therefore the statistical power. In parallel, it increases the capacity to investigate complex and rare biologic phenomena such as sporadic and idiosyncratic diseases.

2) Examples of limitation of the zebrafish model in the context of disease modeling

Although zebrafish have rapid initial development of organ systems, sexual maturity requires approximately three months delaying the outcome of new generations. Moreover despite its rapid development, the timing of development of different organs is not uniform and sometimes not comparable to what observed in mammals. Therefore, the relevant stage-specific markers need to be assessed rigorously to verify the compatibility of the study (Pickart et al., 2014).

Adult-onset disorders (such as Alzheimer or Parkinson's disease) or slow progression degenerative phenotypes (such as fronto-temporal dementia) represent a challenge to model in an embryonic system and work with adult fish is more complicated and only starting to be explored. Therefore only a few protocols are available (Davis et al., 2014).

Some vertebrate structures, such as the mammalian lung, do not have a sufficiently orthologous structure in the zebrafish embryo and make some specific studies impossible.

Then, due to the genome duplication event that occurred in Teleosteis, the homologs for human disease genes do not always exist and *vice-versa* (e.g. collagen III implicated in Ehlers-Danlos syndrome, one of the most common genetic vascular disease, has no equivalent in zebrafish). As a consequence, it is important to verify the phylogenic conservation of candidate genes and their redundancy before assessing their implication in diseases.

Finally, some technical limitations remain while using the zebrafish. For example, it is difficult to perform transplant experiments because of the lack of many isogenic zebrafish strains. Blood collection is still complicated and inefficient as well (only 2µL collected per week and per fish) (Zang et al., 2013) and can be limiting for example in the context of diabetes or obesity studies (Pickart et al., 2014).

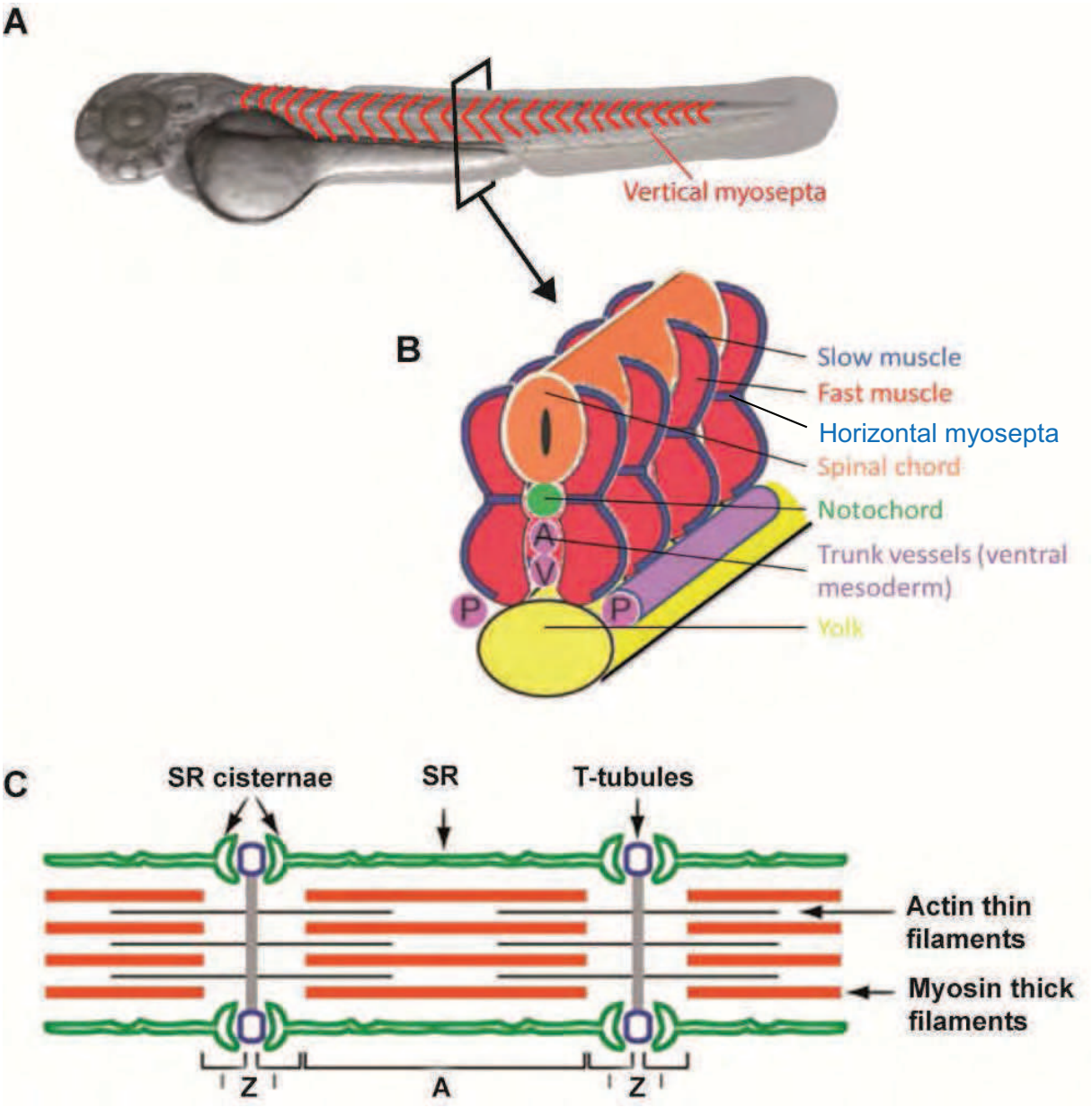

Figure 4: Organization of the skeletal muscle in zebrafish embryos.

(A) Side view of a 48hpf WT zebrafish embryo showing the somatic organization of skeletal muscles of its tail. Vertical myosepta, corresponding to the separation between somites are homolog to myotendinous junctions and are highlighted in red. (B) The organization of a zebrafish embryo somatic muscle is represented. Fast-twitch muscles (red) have a central position in the somite while slow-twitch muscles have a peripheral position. (C) Sarcomere ultrastructure in zebrafish skeletal muscles. Source: Lin et al., 2012. Note the high similarity with mammal sarcomeres organization, despite the presence of a single row of T-tubules along the Z-line while two are observed in higher vertebrates. SR=sarcoplasmic reticulum.

D. Description of the zebrafish muscular and cardiovascular systems

1) Development and organization of the zebrafish muscular system

Skeletal muscle is the largest and the most prominent organ in zebrafish, corresponding to approximately 80% of the fish body mass, compared to 50% of the body mass in human. Beside its obvious role for locomotion, skeletal muscle has a fundamental role in metabolic homeostasis, because muscle acts as a source of energy and participates to its storage (Sanger et al., 2009). The zebrafish skeletal muscle has a somatic organization (Figure 4A), with a specific localization of mononucleated longitudinal slow muscle fiber at the periphery and multinucleated oblique fast muscle fibers at the center of the somites (Figure 4B). Slow-twitch muscle fibers, or type I fibers, are adapted to lower contraction velocity with high mitochondria level, enabling a high oxygen intake and ATP generation. They are typically used in endurance efforts. Fast-twitch muscle fibers, or type II fibers, are better adapted to generate a strong and fast, but shorter, effort. With high contraction velocity and fewer mitochondria, they fatigue more rapidly. The content in fast *vs.* slow fibers in species depends on the adaptation to a particular environment. In fish, the proportion of fast muscles is higher to allow them to escape quickly from predators (Jackson et al., 2013). Nevertheless, the fiber content is highly variable throughout lifetime and depends on exercise, stimulation, mechanical loading and diseases. The partition between somites is referred to as the vertical myoseptum and corresponds to the zone where the differentiated muscle fibers anchor. These structures are composed of connective tissue and are homologous to the myotendinous junctions (MTJ) in mammals. Zebrafish myocyte organization is highly similar to mammals (Sanger et al., 2009) despite the presence of a single row of T-tubule along the Z-line at the sarcomere level, in contrast to a double row per sarcomere in the mammalian skeletal muscles (Figure 4C).

Development of skeletal muscles in zebrafish begins with the commitment of mesodermal cells to the muscle lineage. Contrary to higher vertebrates, myogenesis in zebrafish begins in the adaxial cells before somite formation. Adaxial cells form a subpopulation of the presomitic mesoderm located immediately adjacent to the notochord. Muscle progenitor commitment is dependent on a family of basic helix-loop-helix transcription factors called Myogenic Regulatory factors (MRFs). The first to be expressed in adaxial cells and marking the beginning of muscle progenitors specification is *myoD*. *MyoD* expressing cells elongate and migrate radially and form the precursors of the superficial slow fibers. Within the slow-twitch fiber lineage, the first cells to migrate are the *Engrailed*-expressing Muscle Pioneers, which elongate along the somite during somite formation and later separate the dorsal and ventral domains of the myotome forming the horizontal myoseptum. Slow-muscle fibers specification additionally requires *hedgehog* (*Hh*) signaling (Hirsinger et al., 2004) (Figure 5A). The specification of fast muscle fibers occurs later, after the formation of somites, in a regionalized fashion. Median fast muscle fibers derive from a second wave of *myoD* expressing cells in the posterior half of each newly formed somite (Figure 5B), while the lateral fast muscle fibers derive from *Pax3/7* expressing dermomyotomal cells (Stellabotte et al., 2007) (Figure 5C). Fast muscle progenitors mature and fuse with each other to form multinucleated fibers. *MyoD*-dependent fast muscle

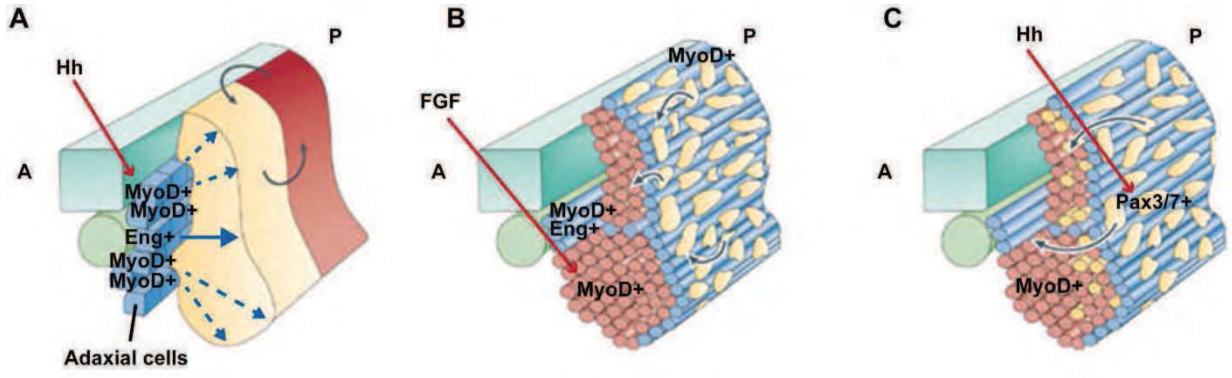

Figure 5: Development of skeletal muscles in zebrafish

Adapted from Bryson-Richardson and Currie, 2008. (A) **First wave: Differentiation of slow muscle fibers.** A first wave of *Hh* signaling dependent *MyoD* expression in the adaxial cells (blue square cells) enables the specification of slow-muscle cells precursors (blue) and their subsequent migration. The first slow muscle cells to migrate are the *Eng*-positive muscle pioneers, which migrate horizontally and form the horizontal myosepta. The presomitic mesoderm, separated in two zones: the anterior zone, which will give rise to the dermomyotome (yellow) and the posterior part which will give rise to the first wave of differentiating fast-muscle cells (red), undergoes rotation during somitogenesis. (B) **Second wave: Differentiation of fast muscle fibers from posterior somatic mesodermal cells.** After differentiation of the slow fibers, the fast fibers differentiate under the laterally migrating slow muscle cells (blue) upon FGF dependant myoD expression in the central mesodermal cells (red). (C) **Third wave: Differentiation of fast muscle fibers from dermomyotomal cells.** More lateral fast muscle cells derive from Hh mediated Pax3/7 expression in the dermomyotomal cells (yellow). In all figure parts, the neural tube is dark green and the notochord is light green. A, anterior; P, posterior.

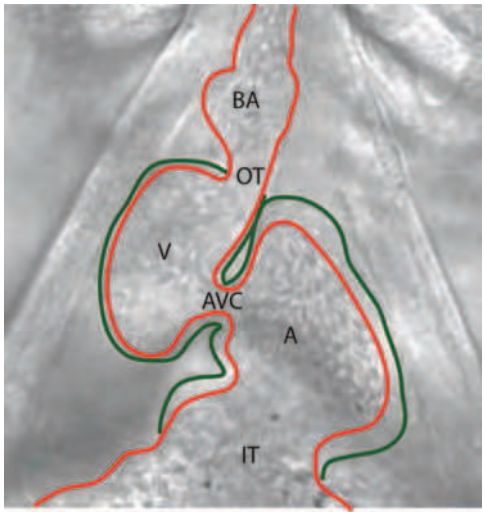

Figure 6: Organization of the zebrafish embryonical heart at 72hpf.

The heart is composed of two layers of cells, the contractile myocardium (green) and the non-contractile endocardium (red). Regions of the heart include (in the direction of blood flow): the inflow track (IT), the atrium (A), the atrio-ventricular canal (AVC), the ventricle (V), the outflow track (OT) and the bulbus arteriosus (BA).

specification is *Hh*-independent contrary to slow fibers specification but relies on *fibroblast growth factor* (*fgf*) signaling while *Pax3/7*-dependant specification is *Hh*-dependent (Groves et al., 2005; Stellabote et al., 2007). Muscle development coincides with somite formation. There is therefore a delay of the muscle cell maturation between anterior somites, which develop first, and the younger posterior somites.

The first spontaneous contraction is observed at 17hpf in the fish. At 21hpf, embryos begin to move spontaneously, coiling in their chorions (Weinberg et al., 1996). This premature muscle function depends on the first established slow muscle fibers while the fast muscle fibers are still maturating. Zebrafish skeletal muscle is fully differentiated at 48hpf.

2) Development and organization of the zebrafish cardiac system

The heart of zebrafish is homologous to the human one, except that it has only two cardiac chambers: the atrium and the ventricle. The heart wall is composed of two main tissues: the myocardium, which is the contractile external layer of the heart, and the endocardium, which is not contractile. The heart is composed of an entry or inflow tract (IT), which enables the blood to accumulate before entry in the atrium, and an outflow tract (OT), which permits the exit of the red blood cells from the ventricle to the fish head (Figure 6).

As in higher vertebrates, the heart is the first organ to form and to be functional in zebrafish embryos. Cardiac development begins with cardiac cell specification at the blastula stage around 5hpf (Stainier et al., 1993). At this stage, endocardial progenitor cells were identified throughout the marginal zone of the blastula. Myocardial progenitors arise bilaterally in the lateral marginal zone, atrial precursors being located slightly more ventrally than ventricular precursors (Keegan et al., 2004) (Figure 7A). The pool of myocardial progenitors was shown to be restricted by retinoic acid signalling (Keegan et al., 2005). During gastrulation, the cardiac progenitor cells migrate dorsally toward the midline into the anterior lateral plate mesoderm (ALPM) (Figure 7B). Further cardiogenic differentiation requires the highly conserved *Nodal* and *Bmp*-dependant activation of the homeobox containing transcription factor *Nkx2.5* (Bakkers, 2011). This activation was shown to be indirect through the expression of *gata5*. In zebrafish, *Nkx2.5* expression is initiated at the 1 to 3-somite stage.

Myocardial differentiation additionally requires *Hand2* expression downstream or in parallel to *Nkx2.5*. From 14 somites, the expression of *myosin light chain polypeptide* (*myl*) *7* (or *cardiac myosin light chain 2* (*cmlc2*)) is detected in an increasing number of myocardial progenitors. Specification of atrial and ventricular cardiomyocytes occurs concomitantly with a progressive expression of *ventricle myosin heavy chain* (*vmhc*) in the medial cells and, slightly later, the expression of *atrial myosin heavy chain* (*amhc*) in the lateral cells until the 26 somite stage (22hpf) (De Pater et al., 2009).

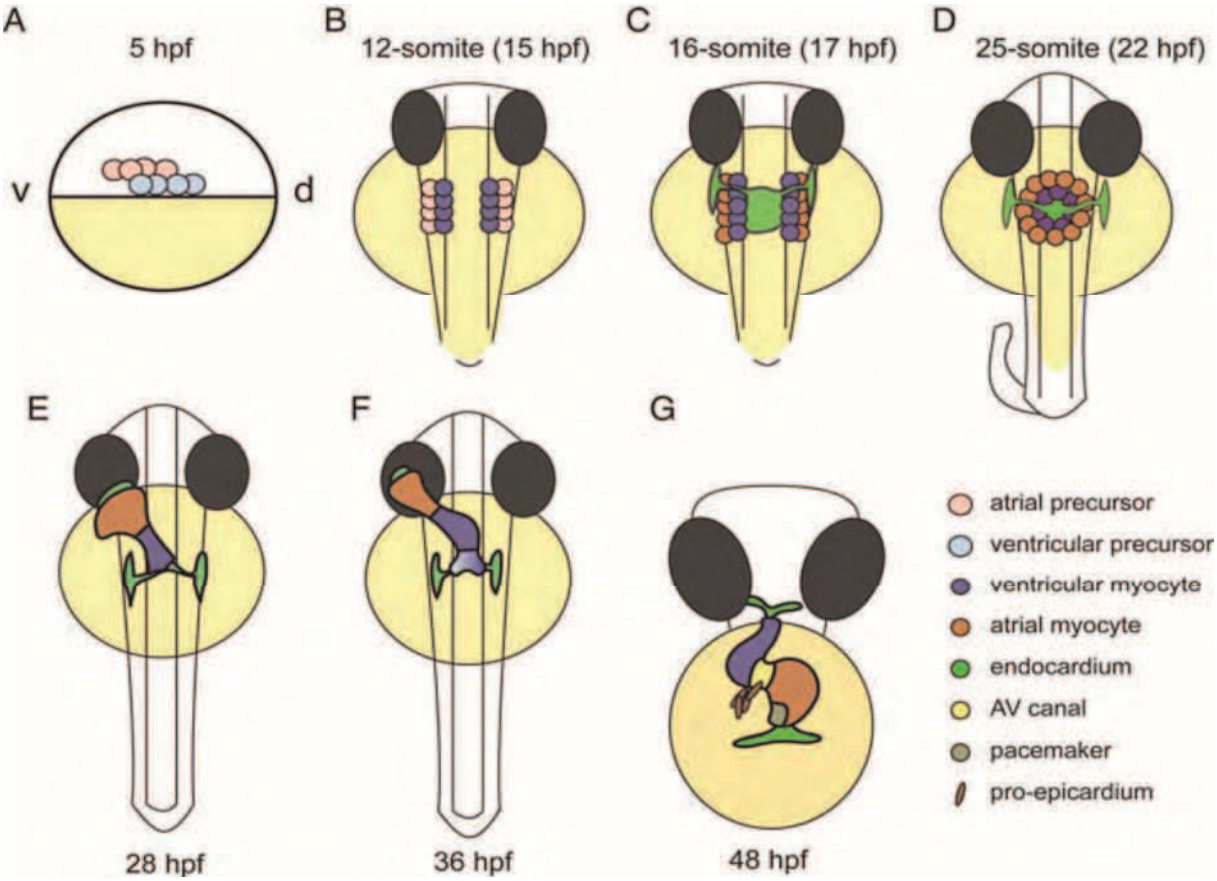

Figure 7: Development of the zebrafish heart

From Bakkers, 2011. (A) At 5hpf the blastula (white) covers approximately 50% of the large yolk cell (yellow). At this stage, cardiac progenitor cells are located bilaterally in the lateral marginal zone. Atrial progenitor cells (pink) are located more ventrally than the ventricle progenitor cells (light blue). During gastrulation, the cardiac progenitor cells move dorsally towards the mid-line to end up in the anterior later plate mesoderm (ALPM). Cardiogenic differentiation is initiated in the future ventricle myocardial cells (purple) by the expression of cardiac myosins at the 12-somite stage. During mid- and late-somite stages, the myocardial tissue expands by continuous cardiogenic differentiation into more lateral regions of the ALPM by the cardiogenic differentiation of future atrial myocytes (brown; venous differentiation). Whilst the endocardial cells (light green) have already migrated from the ALPM towards the mid-line, myocardial cells follow this behaviour slightly later. When the bilateral heart fields fuse at the mid-line, they form a cardiac disc structure with the endocardial cells within the hole at the centre, ventricular myocytes at the circumference and atrial myocytes at the periphery of the disc (D). Cardiac morphogenesis transforms the cardiac disc into a cardiac tube. The endocardium forms the inner lining of the myocardial tube. (E) At 28hpf, the linear heart tube has formed, with the venous pole located at the anterior left and the arterial pole fixed at the mid-line. (F) Cardiogenic differentiation continues at the arterial pole, and as a result new cardiomyocytes are added to this region (purple gradient). At 36hpf, cardiac looping has started, with a displacement of the ventricle towards the mid-line, and the constriction at the position of the AV canal is first visible (F). The heart tube continuous to loop and forms an S-shaped loop (G). Ellipsoid extra-cardiac pro-epicardial cells (brown) are located near the AV canal (yellow), from where they start to cover the myocardium with an epicardial layer. The pacemaker is present in the inner curvature of the atrium near the venous pole (dark green).

Endocardial precursor cells are present in the ALPM in a separate region to the myocardial precursors and migrate to the embryonic midline slightly before the myocardial progenitors (Figure 7C). When the bilateral heart fields fuse, they form a cardiac disc structure (Figure 7D) with endocardial cells in the middle, ventricular myocytes surrounding them and atrial myocytes at the periphery of the disc. Cardiac morphogenesis starts with ventricular myocytes forming a cone, due to involution of the tissue at the right side. Atrial myocytes are therefore subjected to a rotation movement toward the anterior left and endocardial cells are positioned within the lumen of the cardiac tube (Smith et al., 2008) (Figure 7E). These processes form a linear heart tube and are controlled by *Nodal* and *Bmp* expression (Bakkers et al., 2011). While uncoordinated myocyte contractions can already be observed during the formation of the heart tube, the first coordinated heart beats are observed at 24hpf, originally peristaltic. The functional heart continues to extend and to orient its venous pole (future atrium) to the anterior left and the arterial pole (future ventricle) in the mid-line. As the heart develops, the rate of contractions increases and the contraction pattern becomes sequential with alternative contractions of the atrium and the ventricle. This more efficient pattern of contraction was associated with a contraction delay at the atrio-ventricular (AV) boundary (or AV delay). AV delay was attributed to a differential orientation of the atrio-ventricular canal (AVC) cardiomyocytes referred to as slow-conducting myocardium in opposition to fast-conducting myocardium in both chambers (Bakkers, 2011). Both endocardium-derived signals, including expression of *notch1b* and *neuregulin* (Milan et al., 2006) and myocardial signals, including *wnt* signalling/*bmp4* and *foxn4* controlled *tbx2b* expression (Chi et al., 2008; Verhoeven et al., 2011) were shown to be implicated in this differential organisation.

A second wave of myocardial differentiation occurs at the arterial pole after the linear heart tube is formed and functional around 30hpf. This second phase can be interpreted as the homologous mechanism of anterior or second heart field development observed in amniotes (Kelly and Buckingham, 2002; Bakkers, 2011). The molecular mechanism of this differentiation event is not resolved yet but includes the participation of *fgf* signalling (Marques et al., 2008). *Isl1* (Cai et al., 2003) and *bmp* signalling (Marques and Yelon, 2009), which are potential candidates for arterial pole differentiation.

Around 36hpf, bending of the heart tube occurs (Figure 7F) with a displacement of the ventricle to the right side. The different rate of rotation of the two extremities of the tube triggers a torsion force, which induces cardiac looping in the reverse direction to the bending. During the looping, chamber ballooning occurs, accompanied by cellular rearrangement and reorientation and this forms distinguishable chambers with marked inner and outer curvatures (Auman et al., 2007) (Figure 7G).

Using optogenetic tools, the pacemaker region, or sino-atrial node, of the zebrafish embryonic heart was localised in the inner curvature of the atrium and corresponds to the secondarily added myocardial region (Arrenberg et al., 2010). This was further confirmed using transgenic lines for the node cell markers *isl1* and *tbx2b* (Tessadori et al., 2012).

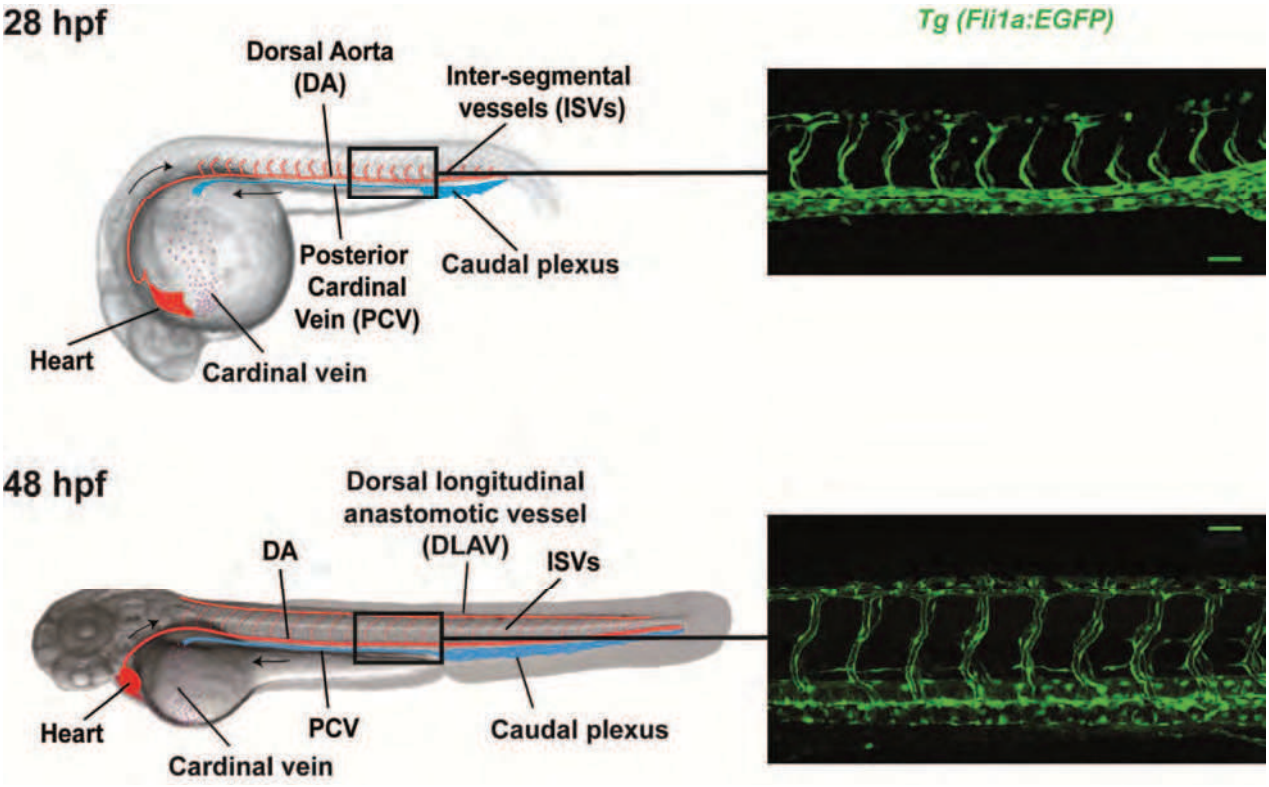

Figure 8: Organization of the zebrafish developing trunk vasculature at 28 and 48 hpf.

Left panel: Side view of a zebrafish embryo at 28hpf (adapted from Jacky Goetz) and 48hpf with the trunk vascular system highlighted. Right panel: Maximal projections of Z-stacks confocal images of the endothelium specific *Tg(Fli1a:EGFP)* transgenic fish line at 28 and 48 hpf. Scale bar=50µm.

From 3dpf, some cardiomyocytes delaminate from the original ventricular myocardium to form the trabecular layer (Gupta and Poss, 2012). Cardiac trabeculae are highly organized sheet-like muscular structures, which enhance cardiac contractility and intra-ventricular conduction. They form as a result of a two-step extrusion and expansion mechanism of differentiated cardiomyocytes into the lumen of the ventricular chambers (Liu et al., 2010; Staudt et al., 2014).

Further rearrangements of the heart, including blood flow dependant AVC valve formation (from 36 to 105 hpf) (Beis et al., 2005; Scherz et al., 2008; Vermot et al., 2009), epicardium formation (from 48 to 96hpf) (Bakkers, 2011, Peralta et al., 2013) and cortical wall formation and perfusion (Gupta and Poss, 2012) (from 6wpf) occur at later stages and won't be described here.

3) Development and organization of the zebrafish vascular system

The zebrafish cardiovascular system consists of a closed circulatory system, composed of the blood vessels, the blood and the heart. The role of the circulatory system involves the transport of oxygen and nutrients to the diverse tissues and the collection of the waste products to be eliminated there. It plays a crucial role for hormonal communication and deployment of the immune response as well.
A complete anatomical description of the zebrafish' early vasculature with a precise nomenclature of vessels is available (Isogai et al., 2001) (Figure 8). Anatomy of the developing vasculature, processes to establish the vascular network and molecular mechanisms are highly similar to those described in higher vertebrates and human.

a) Establishment of the zebrafish embryonic trunk vasculature

In zebrafish, endothelial and hematopoietic precursors derive from a common precursor and develop in close association in the intermediate cell mass derived from the ventral mesoderm (Detrich et al., 1995, Vogeli et al., 2006). Common genes' expression is required for both cell types specification including *stem cell leukemia* (*scl*) and *fetal liver kinase-1/vascular endothelial growth factor (vegf) receptor 2* (*flk1/vegfr2*) (Kabrun et al., 1997). Lineage-restriction of the first endothelial precursor cells or angioblast appears during mid-gastrula and expression of endothelial-specific genes begins during early somitogenesis (Fouquet et al., 1997). Specification of endothelial cells requires expression of members of the E26 transformation-specific (ETS) (including *friend leukemia integration* (*fli*) *1a and 1b*, *ets1* and *ets1-related protein* (*etsrp*)), Forkhead (FOX) and Krüppel-like factor (KLF) families of transcription factors (as reviewed in Gore et al., 2012).

After specification, angioblasts migrate to the embryonic midline and concomitantly acquire their arterial or venous fate (see paragraph I/C.3)c). Angioblasts' migration depends both on the presence of the ventral endoderm and on the hypochord mediated expression of *vegf*. The two main axial vessels: the dorsal aorta (DA) and the posterior cardinal vein (PCV) form through vasculogenesis, defined as *de novo* assembly of vessels from free angioblast progenitors. They are fully functional at the time of circulation onset around 24hpf (Figure 9A).

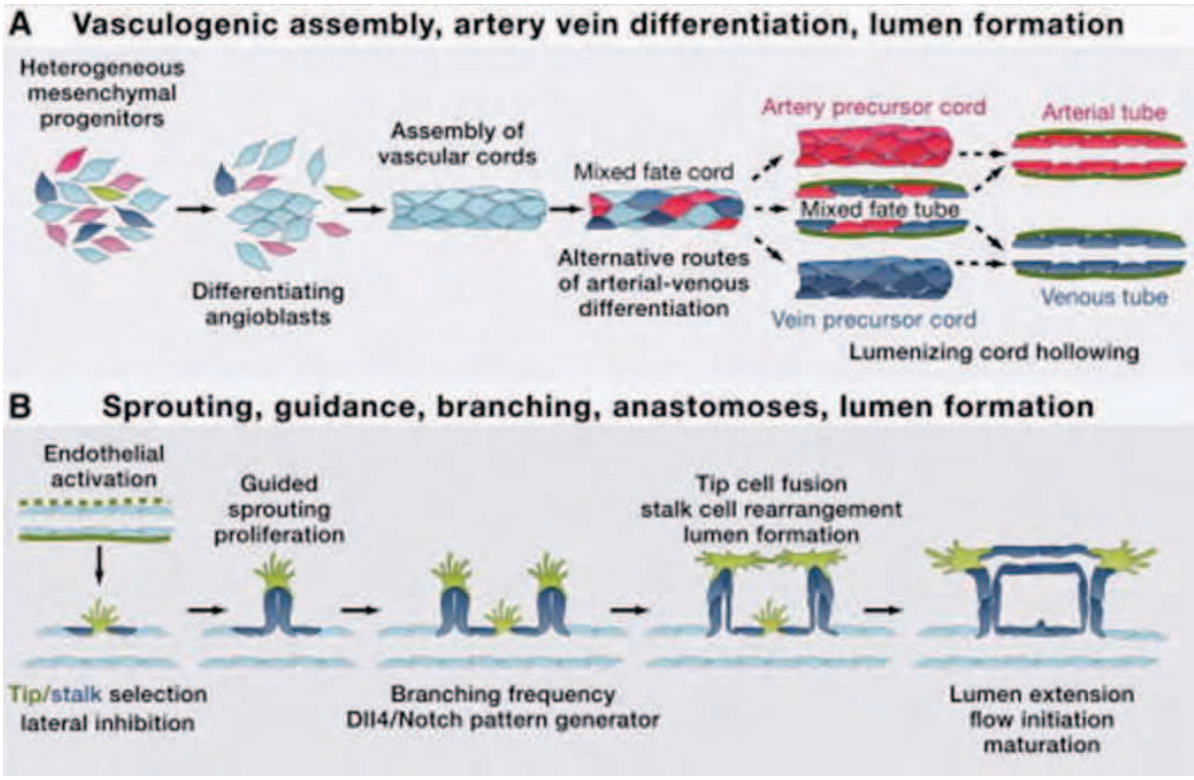

Figure 9: Development of the zebrafish trunk vasculature

From Potente et al., 2011. (A) The first step of the trunk vasculature development in zebrafish consist in the vasculogenesis of the two main vessels: the dorsal aorta (DA) and the posterior cardinal vein (PCV). Angioblasts differentiate into endothelial cells, which form cords, acquire a lumen, and are prespecified to arterial or venous phenotypes. See mechanism in Figure 11. (B) Further development occurs by angiogenesis with intersegmental vessels sprouting going through the steps of: tip/stalk cell selection, tip cell navigation and stalk cell proliferation, branching coordination; stalk elongation, tip cell fusion, lumen formation and perfusion and vessel maturation.

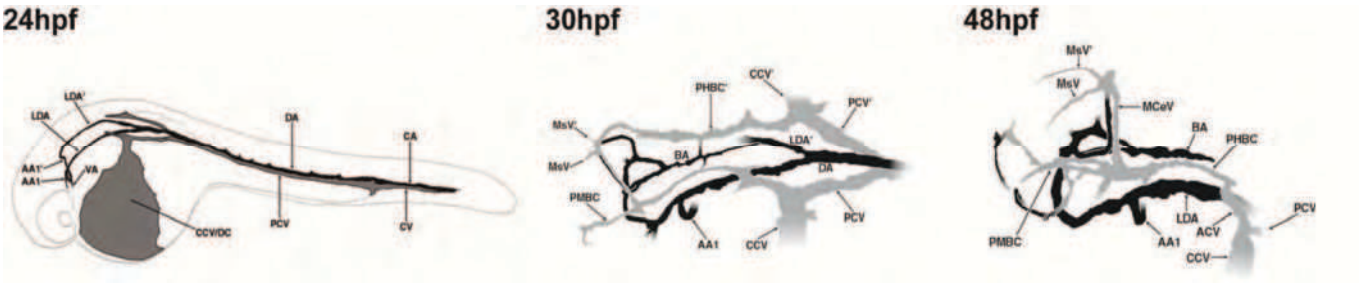

Figure 10: Early organisation of the zebrafish cranial vasculature

Adapted from Isogai et al., 2001. Drawings of the vasculature of zebrafish embryos at 24hpf forming the first vascular loop and of the cranial vasculature of zebrafish at 30 and 48hpf. LDA: lateral dorsal aorta, AA: aortic arch, VA: ventral aorta, CCV: common cardinal vein, PCV, posterior cardinal vein, CV: caudal vein, CA: caudal artery, DA: dorsal aorta, PHBC: primordial hindbrain channel, BA, basilar artery, MsV: mesencephalic vein, PMBC: primordial mid brain channel, MCeV: middle cerebral vein; ACV: anterior (rostral) cardinal vein.

Subsequent vessel formation takes place through angiogenesis, defined as the formation of new vessels by sprouting from or remodeling of a preexisting vessel. Intersegmental vessels (ISVs) are sprouting from the dorsal side of the DA and grow dorsally along the intersomitic space. Migration of these angiogenic cells depends on the specification of two types of cells: the “tip cell”, presenting a highly protrusive profile with numerous filopodia-like structures, guides the migration and typically 3 to 5 more proximal “stalk cells”, maintain the structure forming the vessel. While reaching the dorso-lateral surface of the neural tube, the forming vessels branch and interconnect with their neighboring ISVs to form the dorsal longitudinal anastomotic vessel (DLAV). Blood flow perfuses ISVs after their interconnection and possibly determines the arterial or venous identity of each vessel (Isogai et al., 2003). Molecular mechanisms involved in ISVs sprouting include *vegf* and *notch* signaling pathways (Potente et al., 2011) (Figure 9B).

b) Formation of the zebrafish cranial vasculature

The zebrafish contributes more and more to our understanding in brain vessels development and cerebrovascular pathologies (Walcott et al., 2014). Its cranial vasculature begins to form concomitantly to the trunk vasculature by a similar process of vasculogenesis. The paired lateral dorsal aortae (LDA) are formed by migration and coalescence of two distinct populations of angioblasts migrating from the ALPM around 20hpf. The LDA later fuse with the DA via a Y-shaped junction formed by angiogenesis. The primordial hindbrain channels (PHBCs) are the first primordial vein to develop bilaterally into the embryo head by vasculogenesis. The basilar artery (BA) then assembles between the PHBCs and slightly later the central arteries (CtAs) interconnect the BA and the PHBC (Gore et al., 2012). Further establishment of a complex cranial network is achieved by angiogenesis. The zebrafish has a well-conserved initial cranial vascular plan from one embryo to another, which is not the case for other developing vertebrates, in particular humans (Isogai et al., 2001) (Figure 10).
The formation of the cranial vasculature implicates the *vegf* pathway, *alk1* (Roman et al., 2002) and chemokine signaling including the receptor *cxcr4a* (Gore et al., 2012).

c) Arterial-venous specification

Arteries and vein are both functionally and structurally different. Arterial vessels are subjected to high pressurized blood coming out of the heart. To encompass this function, they acquire a larger diameter and an extensive surrounding supporting system composed of smooth muscle cells and extracellular matrix components. Venous vessels on their side support lower pressure blood returning to the heart and possess specialized valves structures to maintain a proper directional flow. Studies of the last decades showed that cells from the endothelial lineage acquire an arterial or venous fate very early and are consequently both functionally and molecularly distinct already before vasculogenesis (Swift and Weinstein, 2009).

The first family of gene, which was described to be differentially expressed in arterial compared to venous progenitor cells, is the Ephrin (Eph) subclass of receptor tyrosine kinase (Wang et al., 1998). *ephB2* is expressed in arterial cells but absent from the venous cells whereas *ephB4*, encoding for a

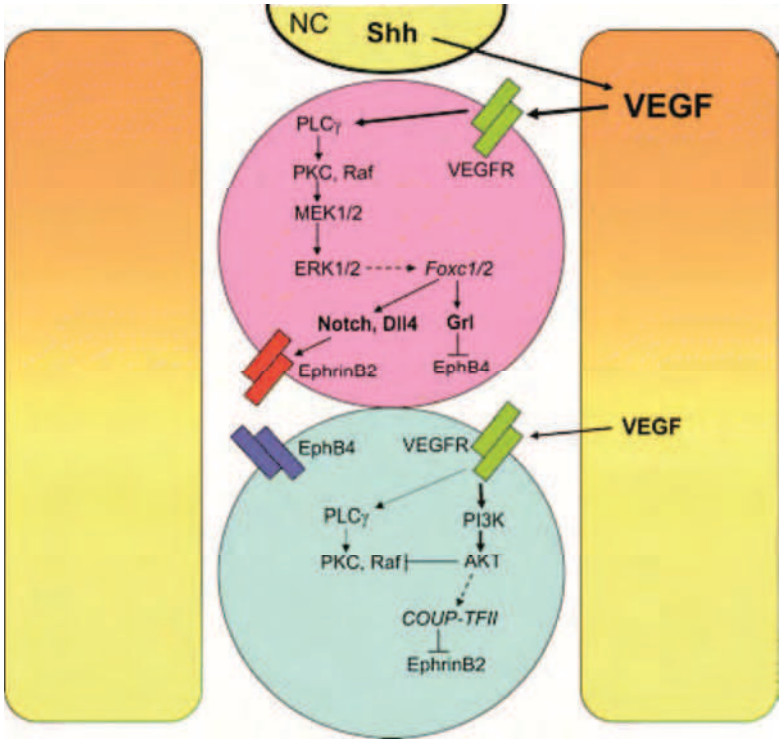

Figure 11: Mechanism of arterial-venous specification during vasculogenesis in the zebrafish trunk.

From Hong et al., 2008 . Shh, expressed in the notochord (NC) induces VEGF expression in nearby somites (yellow gradient). By a process yet to be fully determined, VEGF activates the PLCγ-ERK/MAPK pathway only in the dorsal angioblasts (pink circle), which will develop into aortic endothelial cells. ERK activation results in Notch activation (indicated by Notch and Dll4 expression) via the transcriptional factors Foxc1/2. Notch signaling induces arterial differentiation (indicated by the arterial marker EphrinB2 expression). In the arterial progenitor cells, Grl, induced by Foxc1/2, blocks venous differentiation (indicated by the venous marker EphB4 expression). In the ventral angioblasts (blue circle), VEGF activates the PI3K/AKT pathway, which inhibits the PLCγ-ERK/MAPK pathway, possibly by a direct inhibition of Raf by AKT. AKT signaling is hypothesized to induce expression of COUP-TFII, which blocks arterial differentiation (also EphB2 expression). In this model, a gradient of VEGF along the dorsal–ventral axis is postulated to govern whether VEGF receptor activates PI3K or ERK signaling. For simplicity, the artery–vein specification is depicted here as occurring following the midline convergence of endothelial progenitors, but evidence suggests that this occurs earlier in zebrafish embryos.

receptor of EphB2, is specifically expressed in veins. This specific pattern of expression is present before vessel lumenization and is therefore independent from blood circulation. More upstream signaling pathways for arterial fate determination were studied in zebrafish and include the *sonic hedgehog* (*shh*), *vegf* and *notch* signaling. *Notch* signaling promotes arterial specification and inhibits venous specification during vascular development (Lawson et al., 2001). *Shh* acts upstream of *notch*, through the induction of a *vegf* gradient in the somite surrounding the developing vasculature. Strong levels of Vegf then activates *notch* in the forming DA region. The further specification of DA and PCV include downstream *vegf* signaling effectors like Phospholipase C gamma-1 (Plcg1), the venous specific COUP-TFII, PI3 kinase, Erk and the receptor protein tyrosine phosphatase Dep1 as depicted in Figure 11 (Swift and Weinstein, 2009).

Hemodynamic forces variations applied to the vasculature participate to the reinforcement of the arterial or venous fate of a vessel (Le Noble et al., 2005), and consolidate blood vessel structure by stabilizing the endothelial cell contacts (Potente et al., 2011).

II/ Zebrafish as a model of myofibrillar myopathy and cardiomyopathy: example of desminopathies

Myofibrillar myopathies (MFM) are a group of rare neuromuscular disorders characterized by progressive muscle weakness involving both proximal and distal muscles. Some affected individuals also experience sensory symptoms, muscle stiffness, aching, or cramps. Peripheral neuropathy or cardiomyopathy may also be present. Mostly, MFM begin to develop in mid-adulthood, but features of the condition can appear anytime between infancy and late adulthood. MFM are characterized by their common cellular manifestation including myofibrillar dissolution, Z-disk streaming, ectopic expression of proteins and accumulation of desmin-rich protein aggregates in the subsarcolemmal and pronuclear regions (Selcen, 2011).

We focused in particular on primary desminopathy, a MFM linked with mutation in the desmin gene, encoding a muscle specific intermediate filament (IF) protein.

This part of my thesis introduction corresponds to a review that I recently wrote with Karim Hnia (Laporte team, IGBMC). After discussing IF in general, we describe the muscle-specific member of the IF family: desmin. Desmin mutation was shown to lead to desminopathy, a MFM presenting a large range of clinical manifestations that we described in a second part. Finally we described the different model animals of desminopathy generated so far.

In this review, I was more particularly in charge of writing the part III about desminopathies pathophysiology and model animals for the study of desminopathies.

Manuscript 1: Desmin in muscle and associated diseases: beyond the structural function

Karim Hnia, Caroline Ramspacher, Julien Vermot, Jocelyn Laporte

(in preparation for Cell and Tissue Research)

Desmin in muscle and associated diseases: beyond the structural function

Karim Hnia[1,2,3,4,$,*] , Caroline Ramspacher[1,2,3,4, $], Julien Vermot[1,2,3,4], Jocelyn Laporte[1,2,3,4,*]

1Institut de Génétique et de Biologie Moléculaire et Cellulaire, Illkirch, France
2Centre National de la Recherche Scientifique, UMR7104, Illkirch, France
3Institut National de la Santé et de la Recherche Médicale, U964, Illkirch, France
4Université de Strasbourg, Illkirch, France
$ Equal contribution
* To whom correspondence should be addressed: hnia@igbmc.fr, laporte@igbmc.fr

Abstract: Desmin is a muscle-specific type III intermediate filament essential for proper muscle function. Mutation affecting desmin expression or promoting its aggregation promote skeletal (desmin related myopathies, DRM) or cardiac muscle (desmin related cardiomyopathy, DRCM), phenotype or both. Thus, desminopathy could have variable phenotypes ranging from progressive skeletal muscle weakness to cardiomyopathy and conduction defects. Patient muscle displayed intracellular accumulation of misfolded proteins and presence of desmin-positive insoluble granulofilamentous aggregates leading to a large spectrum of molecular alterations. Increasing evidences show that desmin function is not limited to the structural and mechanical integrity of cells. This novel perception is strongly supported especially by the fact that many of the diseases associated with desmin aggregates could not easily be related to structural functions, but rather pointed toward involvement of desmin filaments in a broader spectrum of functions, such as organelle function and signalling. Here we reviewed desmin functions and related diseases affecting striated muscles and we detailed emergent cellular function of desmin based on reported phenotypes and hallmarks in patients and animal models. We have summarized protein partners of desmin and the ensued function providing by that an overview of how this structural network could serve as a signal transduction platform for subset of molecular events necessary for proper muscle function.

I- Intermediate filaments: classification, structure and biochemical properties

Intermediate filament (IF) protein family encompass 70 members encoded by a large group of genes that are commonly implicated in human diseases accounting for at least 94 different disease entities (Eriksson et al., 2009). The IF family have been subdivided into five distinct types on the basis of their primary structure, assembly properties and their developmental tissue-specific expression pattern. IFs type I and II composed by keratins form obligatory heteropolymers in epithelial cells. By contrast, the type III IF proteins, which include desmin, syncoilin, vimentin and GFAP (glial fibrillary acidic protein), form homopolymers. The type IV group includes the three neurofilaments (NF) subunits (NF-L (light), NF-M (Middle) and NF-H (heavy)), α-internexin, nestin, synamin α and β. The group V is composed by the nuclear IF proteins, which is the oldest type of filaments in term of evolution and is composed by the lamin subfamily (Lamin A, B1, B2, C1 and C2). The last group (group VI) includes the two eye lens IFs or "beaded filaments" proteins CP49 (phakinin) and filensin (CP115) (Coulombe and Wong, 2004) (Figure 1A). Cytoplasmic IF proteins have common secondary structures, which consist of a central α-helical rod domain flanked by non-α-helical domains of variable size. The rod domain forms the core structure of 10-nm filaments. Two segments of the rod domain, the 1A subdomain, which is located in its amino-terminal region, and the 2B subdomain in the carboxy-terminal end, are the most conserved regions among the different types of IF. The non α-helical domains share little homology among different types of IF, but are similar within a given type. The amino terminal domain is essential for IF assembly whereas, the carboxy-terminal domain might be involved in lateral interaction and the organization of IF network (Goldman et al., 2012) (Figure 1A). These non-α-helical domains have numerous phosphorylation sites that are involved in regulating their properties as well as assembly/disassembly and subcellular organization (Eriksson et al., 2004). The first is the most studied process for IF as it could be performed in "autarky" (self-assembly of IF to functional filaments starting from purified protein). IF assembly takes place in a three-step process, in which, first, 8 tetramers rapidly associate laterally to form unit-length filaments (ULFs). These ULFs are approximately 16 nm in diameter and 60 nm in length. The ULFs then anneal end-to-end to generate loosely packed filaments that are several hundred nm long. These filaments start to compact for further elongation by stochastically reducing their diameter. The loosely packed filaments undergo an internal reorganization or compaction that propagates throughout the filament to yield mature intermediate filaments (Herrmann et al., 2009; Schopferer et al., 2009) (Figure 1B).

Cellular function: IFs are highly dynamic structures and increasing evidences show that IFs function is not restricted to maintain the structural and mechanical integrity of cells. This recent perception is strongly supported especially by the fact that many of the diseases associated with mutations in the genes encoding IF proteins and aberrations in IF proteins could not easily be related to structural functions, but rather pointed toward involvement in a broader spectrum of functions, such as organelle maintenance, signalling, and/or regulating transcription (Chang et al., 2009; Chang and Goldman, 2004; Schofield and Bernard, 2013). Indeed subsequent studies shed the light on cellular processes that involves IFs in adhesion, migration and signal transduction (Chung et al., 2013; Windoffer et al.,

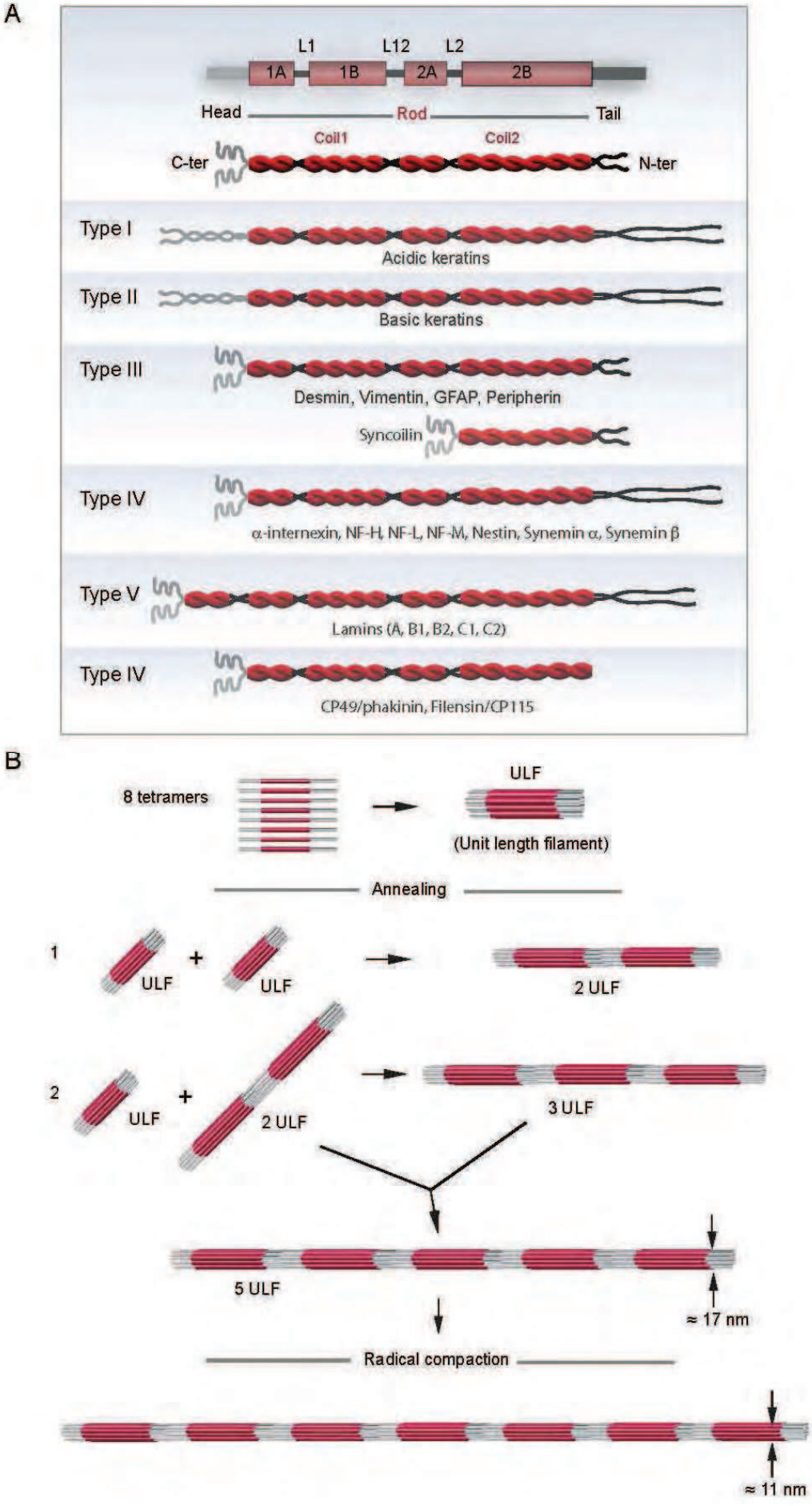
A
L1
L12
L2
1A
1B
2A
2B
Head
Rod
Tail
Coil1
Coil2
C-ter
N-ter
Type I
Acidic keratins
Type II
Basic keratins
Type III
Desmin, Vimentin, GFAP, Peripherin
Syncoilin
Type IV
α-internexin, NF-H, NF-L, NF-M, Nestin, Synemin α, Synemin β
Type V
Lamins (A, B1, B2, C1, C2)
Type IV
CP49/phakinin, Filensin/CP115
B
8 tetramers
ULF
(Unit length filament)
Annealing
1
ULF
ULF
2 ULF
2
ULF
2 ULF
3 ULF
5 ULF
≈ 17 nm
Radical compaction
≈ 11 nm

2011). Ample evidences showed that IFs act as scaffold for and as functional determinant of signalling molecules such as kinases, phosphatases or as a regulator of ion channels (Schofield and Bernard, 2013; Dingli et al.,2012). In many cases post-translational modifications such as phosphorylation, glycosylation or others act as regulators of the IF-related signalling functions, as they regulate IFs interactions with individual signalling proteins and affect the dynamic properties of IFs (Snider and Omary, 2014). An example of an IF-kinase interaction is the interaction of vimentin with the RAF-1/RhoA signalling pathway, which, through Rho-binding kinases (ROKs), is involved in mediating actin dynamics and focal adhesion formation. Activated ROKα phosphorylates vimentin, which leads to filament collapse and consequent release of ROKα from the vimentin IFs and its translocation to the periphery of the cell. Thus, the presence and organization of vimentin affects the outcome of RhoA-mediated signalling (Sin et al., 1998) (Gregor et al., 2014). IFs can influence cell fate by directly controlling death receptor complexes. In particular, K8/K18 filaments have been described to protect liver hepatocytes during apoptosis-promoting stress conditions, either by regulating the targeting of death receptors at the cell surface or by controlling the formation of the death-inducing signalling complex (DISC) through protein sequestration and thereby controlling downstream signalling (Gilbert et al., 2008).

II- Desmin: The muscle IF-specific protein

In contrast to smooth muscles, cardiac and skeletal muscles are both striated (physical result of the overlapping patterns of actin and myosin filaments). Fibers from skeletal muscle are multinucleated and result from fusion of many mononucleated myoblasts, whereas cardiac muscle is composed of individual cardiomyocytes that are oligonucleated and derive from a single precursor. Cardiomyocytes plasma membranes (sarcolemma) are connected mechanically and electrically through highly specialized cell–cell junctions, the intercalated disks. The last are composed of three types of cell-cell contacts, adherent junctions, desmosomes and gap junctions. Skeletal muscles have two specialized cell–cell junctions, neuromuscular junctions (NMJ), where they are innervated by motor neurons, and myotendinous junctions (MTJ), where they attach to the tendons. IFs associate with the sarcolemma of both cardiac and skeletal muscle at structures termed “costameres”, present at the membrane overlying Z-disks and M-bands. The IF cytoskeleton of mature muscle is composed predominantly of type III IF proteins, especially desmin (Lazarides and Hubbard, 1976). The non-muscle-specific IF proteins, synemin and paranemin are co-expressed and form copolymers with desmin (Granger and Lazarides, 1980; Breckler and Lazarides, 1982). Opposite the atypical type III IF syncoilin binds α-dystrobrevin, a component of the dystrophin-associated protein complex (DAPC) and desmin (Newey et al., 2001). The majority of these IFs are typically localized around the α-actinin-rich Z-disks and are situated in the costameres at the sarcolemma as well. Nestin, originally identified as a brain stem cell-specific IF protein, can also copolymerize with type III IF proteins (Steinert et al., 1999). It is present in early cardiac and skeletal muscles, but is only retained at significant levels in adult skeletal muscle at

(see figure on previous page)

Manuscript 1/Figure 1: Structural organisation of intermediate filament (IF) proteins and their classification.

The tripartite structure of IFs, consisting of a highly conserved α-helical central rod domain flanked by non-α-helical head and tail domains. The rod domain consists of heptad repeats that are the signature of α-helical proteins. The heptads are interrupted by short linker sequences (L1, L12 and L2), which result in four α-helical segments: 1A, 1B, 2A and 2B form. The central rod domain is highly conserved in vertebrate IF proteins, with the exception of the nuclear lamins, which contain six extra heptads in the 1B segment. The variability of IF proteins lies in the length and sequence of the head and tail domains.IFs have been classified into five distinct types on the basis of their sequence identity and tissue distribution. The type-I and -II sequence-homology groups contain the keratins of epithelial cells. Heterodimers are formed with one keratin of each type(one acidic and one basic). Type-III IFs include vimentin, desmin, glial fibrillary acidic protein (GFAP), synemin, peripherin, and syncoilin. The neurofilament (NF) triplet proteins (NF-L, NF-M and NF-H), α-internexin and nestin comprise the type-IV intermediate filaments. The type-III and type-IV IFs can form heterodimers with each other. Nuclear lamin A and its splice variant, lamin C, together with lamin B1 and B2 constitute the type-V IFs. The type V IFs encompasses the cytoplasmic lens IF CP49/phakinin and Filensin/CP115.

the NMJ and MTJ (Kachinsky et al., 1994). Adult striated muscle also contains IFs of the cytokeratin family and specifically keratins 8 (K8) and 19 (K19), which form heteropolymers *in vitro*. Like desmin and its associated proteins, K8 and K19 associate with the periphery of Z-disks in the interior of muscle fibres and are present at the sarcolemma (Stone et al., 2005; Ursitti et al., 2004).

II-1- Desmin in myogenesis and developing muscle

Myogenesis and muscle regeneration: The predominant type III protein in myoblasts is vimentin, known to be down-regulated with development (Farrell et al., 1990). During myoblast elongation and fusion, desmin becomes integrated within the pre-existing vimentin filaments and forms longitudinal strands. Upon maturation of myotubes these strands are transformed to transversely organized filaments, localized in between the myofibrils at the level of the Z-discs (Barbet et al., 1991). Earlier studies have demonstrated that desmin deficiency blocks myoblast fusion and myotube formation both in differentiating C2C12 myoblasts and in embryoid bodies (Schultheiss et al., 1991). Myogenesis can be divided into several phases including cell commitment, exit from the cell cycle, initiation of differentiation, cell recognition and alignment, cell adhesion and fusion (Bentzinger et al., 2012). Desmin could actively participate in one or more of these processes or could be directly involved in myoblast fusion. Furthermore ectopic expression of desmin in the lens of mice causes partial plasma membrane fusion (Dunia et al., 1990). Fusion between two cells can take place only between desmin positive cells, however, additional reports using bone marrow stem cells to generate myogenic cells, suggest that, at least in this case, only one of the cells requires desmin for fusion (Camargo et al., 2003). Furthermore, it was reported that absence of desmin resulted in a delayed and modified regeneration and an accumulation of adipocytes, when desmin KO muscle was subjected to notexin treatment (Meyer and Lieber, 2012). This was associated with a persistence of small diameter muscle fibres containing N-CAM and developmental myosin isoforms, markedly disorganised NMJ and absence in some cases of post-junctional folds. These data suggested that desmin is essential for terminal muscle regeneration, maturation of muscle fibers and maintenance of the complex folded structure of the NMJ postsynaptic apparatus (Meyer and Lieber, 2012).

Development: As several IFs proteins (synemin, vimentin etc.), desmin is well expressed in developing muscles (Kuisk et al., 1996). It is one of the earliest known myogenic markers both in heart and somites (Herrmann et al., 1989). In contrast to most muscle-specific genes, desmin is also expressed at low levels in satellite cells and replicating myoblasts (Allen et al., 1991). During development, desmin expression precedes all the other muscle-specific structural genes and the mHLH transcription factors myoD, myogenin and MRF4, with the exception of Myf5 (Li and Capetanaki, 1993). This suggests that desmin may have a modulating role in myogenic commitment and differentiation. The IF protein nestin, which initially was found in neuroepithelial stem cells, is also apparent in embryonic muscle cells (Hockfield and McKay, 1985; Sejersen and Lendahl, 1993). It is transiently co-expressed with desmin and vimentin in developing skeletal and heart muscles, but it becomes postnatally down-

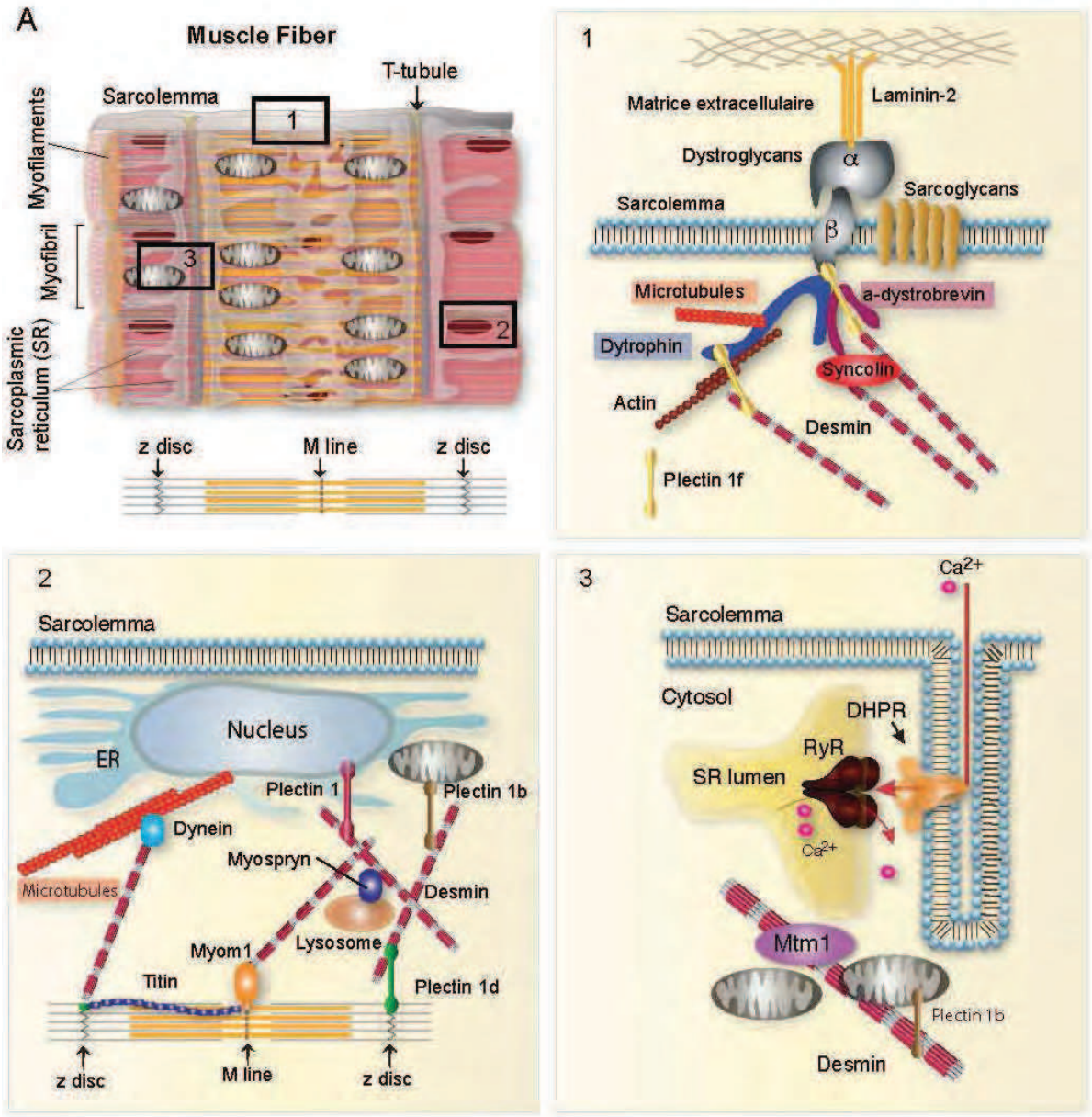

Manuscript 1/ Figure 2: Desmin IF as a cellular organizer involved in plethora of other cellular events.

A. Schematic representation of muscle fibres organization showed compacted myofibres surrounded by the sarcoplasmic reticulum (SR) network. The last is connected to the sarcolemma (plasma membrane) via its intra-fibrillar extension (T-tubule) to form a triad (2 SR sacules connected to one T-tubule). Box 1 to 3 pointed different region of the muscle fibres where desmin IFs scaffolds membranous compartments and organelles. Box 1 shows IFs associated with costameres through dystrobrevin and syncoilin, two proteins from the Dystrophin-Associated Protein Complex (DAPC). The last bridges extracellular matrix to the contractile apparatus and is composed by dystrophin and its associated transmembrane glycosylated proteins (dystroglycans and sarcoglycans). The plectin 1f is a cytolinker that bridges desmin IF and the dystrophin and its associated proteins dystrobrevin and β-dystroglycan. Box 2 shows desmin lattice connecting the nucleus (via the cytolinker plectin 1) and other organelles such as mitochondria (via the cytolinker plectin 1b) or lysosome (via the desmin associated protein myospryn). In the other hand, desmin filament connects the sarcomere via titin and myospryn at the M-band and plectin 1d at the Z-disc. Box 3 pinpoints the possible link of desmin to SR via the phosphoinositide phosphatase myotubularin (MTM1), while the link between desmin and mitochondria via the plectin 1b is established. MTM1 with desmin also co-fractionate with mitochondrial suggesting that MTM1 could also link desmin filaments to mitochondria.

regulated (Sejersen and Lendahl, 1993; Carlsson et al., 1999). The expression of desmin at early stages of embryogenesis suggested an important role for desmin in muscle differentiation (Lazarides, 1982). This was also supported by the fact that a total inhibition of skeletal and smooth muscle development is observed in cultured desmin null mutant embryoid cells (Weitzer et al., 1995). However, the results obtained in mice lacking the desmin gene, which develop normal muscles, show that desmin is not essential either for proliferation and differentiation of myotubes or for the subsequent myofibrillar organization (Capetanaki et al., 1997). Initial study on desmin KO model reported no overexpression of vimentin (Li et al., 1997), however, additional reports have showed that distribution of plectin was unaffected, whereas synemin and paranemin were partly affected (Carlsson et al., 2000). Further investigations are needed to determine which IFs could compensate for the lack of desmin during skeletal and cardiac muscle development. In the same line, the regulatory mechanisms (signalling, post-translational modification, etc.) involving desmin IF in muscle development are not well characterized so far.

II-2- Desmin in adult skeletal muscle and regeneration

In mature striated muscle, desmin IFs form a 3D scaffold that seems to extend across the entire diameter of the myofibril. Desmin IFs surround the Z-disks, interconnecting them to each other and to the sarcolemma, at the level of costameres and at intercalated disks in the case of cardiac muscle (Capetanaki et al., 2007) (Figure 2A). Desmin filaments also link the entire contractile apparatus to different membranous compartments and organelles, including the nucleus, mitochondria, lysosomes (Capetanaki et al., 2007) and potentially the sarcoplasmic reticulum (SR) (Amoasii et al., 2013; Hnia et al., 2011). Connection to many organelles could be materialized by the physical link that desmin could establish with the plectins isoforms (Castanon et al., 2013). Such interactions could control mitochondria dynamics, nuclei positioning and sarcolemma homeostasis (Winter and Wiche, 2013) (Figure 2A). Consequently, nuclei shape and positioning, as well as link to the sarcomeres are altered in desmin-null mice (Capetanaki et al., 1997).

Upon myoblast fusion, each newly incorporated nucleus is actively moved to the center of the immature myotube (Cadot et al., 2012; Kelly and Zacks, 1969). Following many fusion events, the myotube will mature into a myofiber, when desmin IF are transformed to transversely organized filaments. This maturation process is also identified by the development of a dense myofibril network throughout the cell. However, this maturation process also correlates with the second type of nuclear movement during which nuclei are moved from the center of the myofiber to the periphery (Capers, 1960) and the third movement in which the distance between adjacent nuclei is maximized (Bruusgaard et al., 2003). Later the establishment of specialized regions at the sarcolemma for the future NMJ required a final movement of myonuclei (either individuals or as clusters) (Englander and Rubin, 1987). This last movement to the NMJ is an active process, and these nuclei have unique transcriptional profiles and different levels of nuclear membrane proteins compared to the majority of

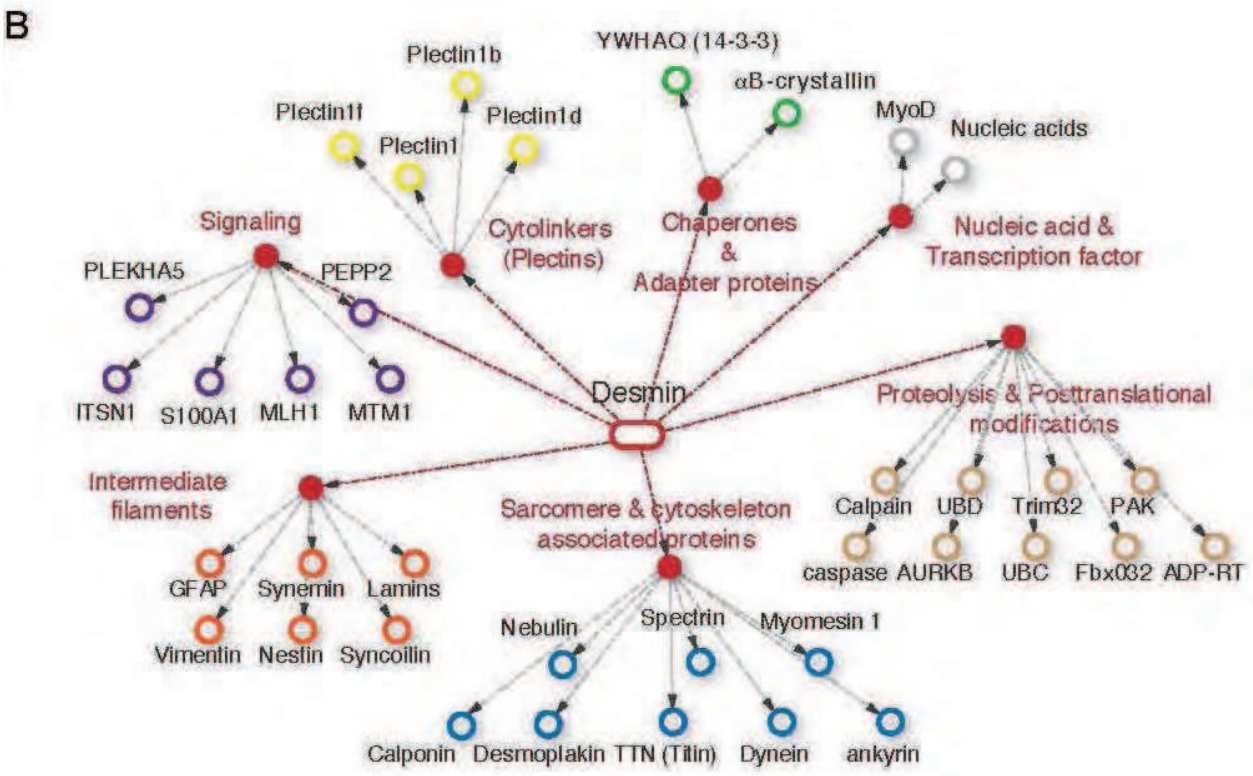

Manuscript 1/ Figure 2: Desmin IF as a cellular organizer involved in plethora of other cellular events.

B. Physical interaction map of desmin based on published data and collection of data on interaction databases (BioGrid, MINT, STRING) shows desmin binding to different proteins such as cytolinkers and chaperones or protein involved in signalling or sarcomere and cytoskeleton regulation.

the muscle nuclei (Sanes et al., 1991). In addition, positioning of these nuclei is essential for synaptic transmission (Jevsek et al., 2006) and the absence of nuclei clustered at the NMJ is hallmark of neuromuscular disease (Grady et al., 2005). It is not clear whether the movement of the nuclei to the periphery and the assembly of the myofibril network are functionally linked to desmin transversal organization and/or whether one process is dependent on the other.

Yet, the coincident nature of these two events and the prevalence of aberrant nuclear and desmin network positioning in individuals with muscle disease, suggest that the peripheral localization of nuclei, maximizing the internuclear distance, and the correct distribution of desmin IF are important factors in nuclei positioning and consequently in muscle growth.

II-3- Desmin partners and ensued function

Clues about novel function of IF desmin polymers have arisen recently from the identification of proteins that are able to bind to desmin dynamically and the assessment of these interactions in the context of animal models. Many of these proteins, including organelles associating proteins, members of membrane complexes, chaperones as well as proteins implicated in posttranslational modifications, function in signalling networks that are important for proper skeletal or cardiac muscle function (Capetanaki et al., 2007; Costa et al., 2004) (Figure 2B). The basic premise of the architectural role of desmin filaments becomes enriched with these new finding which could rephrase certain considerations about desmin function. The idea that desmin could serve as a platform for signalling events could be promising to elucidate molecular clues and events linked to desmin misfolding/aggregation. Here we will address the list of desmin interactors and the biological function that ensue from those partnerships. Based on reported physical interactions in the literature and protein-protein interaction databases (BioGRID, MINT, GeneMANIA) (Stark et al., 2006; Mostafavi et al., 2008), we established the interaction network of desmin IF (Figure 2B). A part the binding capacity to other members of the IF family, desmin could interact with proteins implicated in several cellular processes such as the organization of sarcomere and cytoskeleton, proteolysis and posttranslational modifications, link of cytoskeleton and organelles (cytolinkers) and signalling as well as adapter proteins and chaperones. In this part, we will detail two categories of desmin protein partners, the IF proteins and the signalling proteins. The other categories of partners were detailed and discussed in previous reviews (Clemen et al., 2013; Costa et al., 2004; Winter et al., 2014).

II-3-1 IF interaction partners

Desmin could bind or may co-polymerize other type III IF (vimentin, syncoilin, GFAP) (Schultheiss et al., 1991; Newey et al., 2001; Guma et al., 2001), type VI IF proteins (synemin and nestin) (Granger and Lazarides, 1980; Kachinsky et al., 1994) and type V IFs (lamins) (Cartaud et al., 1995). Co-polymerization of desmin with type III IFs may co-exist in some cell types or during a time point of the development. For example Desmin is co-expressed with vimentin in myoblast or in mature muscle cells (Schultheiss et al., 1991). GFAP can polymerize with desmin *in vitro*, but only a few cell types co-

express both proteins at the same time such as myofibroblast (with additional expression of vimentin) (Guma et al., 2001). Nestin is typically expressed in stem cells from the central nervous system, but is also present with desmin in muscle ligaments and probably in MTJ (Kachinsky et al., 1994). Synemin, initially purified as a desmin-associated molecule (Granger and Lazarides, 1980), is present in higher level striated muscle and may bridge desmin to both myofibrillar Z-lines via its binding site to α-actinin and to costameres via its interaction with vinculin/α7B-integrin complex (Sun et al., 2008). Like desmin, syncoilin is highly expressed in skeletal and cardiac muscles. Syncoilin is found throughout the sarcolemma, but is enriched at the NMJ and MTJ and around the nucleus (Moorwood, 2008). Syncoilin binds α-dystrobrevin, a component of the DAPC meaning that it bridges desmin IF to the sarcolemma (Blake and Martin-Rendon, 2002; Poon et al., 2002) (Figure 2B). Interestingly, in mice null for desmin, syncoilin is lost from all of its normal cellular locations and entirely redistributed to the soluble fraction of the cell, indicating that its normal location and association with the cytoskeleton are desmin-dependent (Howman et al., 2003). The association of syncoilin with both the DAPC and the desmin IF network suggests that it could play a role in the transduction of signals between these two entities. For example, it is known that IF networks are dynamic and can be modulated in response to cell signalling, particularly related to mechanical and non-mechanical stress (Mohamed and Boriek, 2012). There is also some evidence that DAPC may be involved in mechanotransduction (Kumar et al., 2004). Therefore, syncoilin might help to convey mechanical stress signalling from the DAPC to the desmin IF network, allowing it to respond accordingly. In addition α-dystrobrevin could bind signalling protein such as syntrophins/nNOS suggesting that desmin/syncoilin/α-dystrobrevin complex may serve as a platform for a local signal transduction through the sarcolemma (Constantin; Mizuno et al., 2001).

II-3-2- Signalling proteins

• Cardiomyopathy associated 5 (CMYA5) or myospryn: CMYA5 also called myospryn or TRIM76, is a protein member of the tripartite motif (TRIM) superfamily mainly expressed in cardiac and skeletal muscle (Benson et al., 2004; Tsoupri and Capetanaki, 2013). CMYA5 was found to bind desmin by yeast-two-hybrid (Y2H) and confirmed by biochemical analysis (Kouloumenta et al., 2007). Desmin N-terminus binds CMYA5 via its SPRY domain and both proteins colocalize at the periphery of the nucleus in mice cardiomyocytes. In the absence of desmin, myospryn loses its sharp perinuclear localization (Kouloumenta et al., 2007). Myospryn also colocalize with markers for compartments of ER and Golgi sorting machinery (KDEL receptor and TGN38, respectively) suggesting that myospryn resides closer to membrane structures of the endoplasmic reticulum and potentially the ER-Golgi intermediate compartment (Kouloumenta et al., 2007). In adult muscle, the two proteins colocalize, predominantly at intercalated disks in cardiac muscle and at the Z-line in the connection between sarcolemma and costamere (Kouloumenta et al., 2007). Additional function was attributed to CMYA5 as it binds the dystrobrevin-binding protein dysbindin, a component of the biogenesis of lysosome-related organelles complex 1 (BLOC-1). Physical link between desmin and BLOC-1, dysbindin and pallidin, occurs most probably through myospryn (Benson et al., 2004; Kouloumenta et al., 2007). These findings suggest a potential role of desmin IFs and their associated proteins in vesicle trafficking

and organelle biogenesis and/or positioning. It is plausible to speculate that Desmin/CMYA5 interaction with lysosomal machinery required local signal transduction. Indeed *in vitro* study suggested that CMYA5 might be phosphorylated by protein kinase A (PKA) (Reynolds et al., 2007). PKA signalling pathway is a universal mechanism of signal transduction and of particular importance for muscle function (Reynolds et al., 2008). CMYA5 was proposed to be part of the A kinase anchoring proteins (AKAP) family mimicking other desmin associated protein such as synemin (Russell et al., 2006) and suggesting that desmin IF could be considered as a platform for local signal transduction probably to maintain organelle homeostasis and dynamics or to regulate protein involved in their function. On the other hand, CMYA5 could also interact with the calcium–calmodulin-regulated protein phosphatase calcineurin at the Z-disc/costamere region (Kielbasa et al., 2011). Because of its important and diverse role in muscle physiology, calcineurin is subjected to stringent regulation and could dephosphorylate several key proteins such as dystrophin in specific context (Walsh et al., 1995). Overall, Desmin/CMYA5 interaction is likely to coordinate the activity of specific kinases and phosphatases particularly in response to changes in muscle activity or damages.

• S100A1/B1: S100A1 and S100B1 are members of the calcium (Ca^{2+})-binding S100 protein family and represent the most abundant S100 isoforms in cardiac and at lower level in skeletal muscle (Volkers et al., 2010; Prosser et al., 2011). Early studies revealed distinct expression patterns of S100A1 in healthy and diseased cardiac tissue from animal models and humans (Most et al., 2007). Further elaborate investigations uncovered S100A1 protein as a basic requirement for striated muscle Ca^{2+} handling integrity (Volkers et al., 2010). S100A1 binds desmin and regulates the formation of desmin polymers *in vitro* in the presence of micromolar level of Ca^{2+} (Garbuglia et al., 1999). S100A1 also co-localizes with Ryanodine receptor (RyR) in both heart and skeletal muscle (RyR1, RyR2 respectively) and decreases RyR Ca^{2+} transients via a Ca^{2+}-dependent S100A1-RyR interaction (Prosser et al., 2008). Importantly, S100A1 competes directly with Calmodulin (CaM) for the same binding site on RyR1 and RyR2 (Prosser et al., 2008). Because Ca^{2+}-CaM binding to RyR inhibits RyR-induced calcium release in both skeletal and cardiac myocytes, the simplest model for S100A1-dependent activation of RyR involves competing away a well-established RyR inhibitor (i.e. CaM). Alternatively, it cannot be ruled out that the S100A1-RyR interaction stabilizes active RyR and that CaM-dependent inhibition of the RyR occurs by CaM displacing S100A1. In addition S100A1 could also binds the SR Ca^{2+} ATPase SERCA (Remppis et al., 2002). Overall, it is plausible to speculate that the interaction of desmin with S100A1 could indirectly regulate Ca^{2+} channel activity (RyR1, SERCA). Desmin may sequester S100A1 protein in sarcomere favouring CaM inhibition effect on RyR1. However, further investigations are needed to decipher the exact mechanism by which desmin could influence Ca^{2+} homeostasis in adult and developing muscles.

• Pleckstrin homology (PH) domain-containing protein family A member 5 (PLEKHA5) or phosphatidylinositol-three-phosphate-binding PH-domain protein-2 (PEPP2): PLEKHA5 or the PEPP2 is PH domains protein well known to bind membrane phosphoinositides (PI3P, PI4P, PI5P, and PI(3,5)P2) with different specificities (Yamada et al., 2012). Initially identified in brain, it was proposed

that PEPP2 might play an important role in brain development through a potential role in vesicle trafficking (Zou and Zhong, 2012). Bandyopadhyay et al. applied a systematic experimental (Y2H) and computational approach (interaction databases) to map 2,269 interactions between human MAPK-related proteins and other cellular machinery (Bandyopadhyay et al., 2010). PEPP2 was found to interact with desmin with high confidence. Interestingly the same screen identified also PEPP2 interaction with plectin 1, a desmin binding protein belonging to the plectin cytolinker family (Bandyopadhyay et al., 2010). Plectin anchor desmin to several organelle and cell compartments suggesting that PEPP2-desmin interaction could be involved in organelle dynamics. Given the binding capacity of PEPP2 toward specific phosphoinositides mostly enriched in the endosomal machinery, it is possible that PEPP2-desmin-plectin 1 interaction might control sorting or motility of such organelles.

• Myotubularin (MTM1): MTM1 missing in the X-linked form of centronuclear myopathy (XLCNM), was found to bind desmin *in vitro* and *in vivo* in skeletal muscle but integrally this interaction is not conserved in cardiac muscle, suggesting that MTM1-desmin complex may have specific functional significance in skeletal muscle (Hnia et al., 2011). MTM1 is a phosphoinositide phosphatase that metabolizes two phosphorylated entities of this lipid second messenger: (PtdIns3P) and PtdIns(3,5)P2 into PtdIns and PtdIns5P, respectively (Maehama et al., 2001). MTM1 shares the C(X)5R signature motif with the protein tyrosine phosphatase/dual specificity phosphatase family (PTP/DSP) and was initially suggested to be involved in membrane trafficking (Taylor et al., 2000). In skeletal muscle MTM1 colocalizes partially with desmin IF at the periphery of the Z-line (within the I band) (Hnia et al., 2011). MTM1 colocalizes with the sarcoplasmic reticulum markers RyR1 and triadin and defect in Ca^{2+} homeostasis and related EC-coupling machinery defects were observed in Mtm1 KO mouse muscle (Amoasii et al., 2013). Interestingly MTM1 could co-fractionate with desmin in the mitochondrial fraction from skeletal muscle homogenates suggesting that MTM1-desmin interaction might play a role in mitochondrial dynamics or localization (Hnia et al., 2011). Indeed, XLCNM patient and Mtm1 KD mouse muscle cells have decreased mitochondrial dynamics and motility as well as ER/SR shape emphasising a potential role of MTM1-desmin couple in mitochondrial-SR/ER contacts (Amoasii et al., 2013) (Figure 2A).

• Intersectin 1 (ITSN1): ITSN1 belongs to the intersectin family of scaffold proteins linking endocytosis and signal transduction pathways. Members of this protein family contain multiple protein interaction domains (SH3 repetitive domains), each capable of binding various ligands, which can be signalling proteins or components of the endocytic machinery (Tsyba et al., 2011). Growing evidence supports a model in which ITSNs regulate biochemical pathways at specific sites within cells such as actin polymerization or receptor tyrosine kinase ubiquitination (Humphries et al., 2014; Okur et al., 2014). Desmin as well as syncoilin were found by Y2H screen using ITSN1 as bait (Wong et al., 2012). These data revealed also several other protein partners of ITSN1 involved in endocytosis and the regulation of the Rab and Arf GTPase pathways. As ITSN1 is thought to play a pathological role in Down syndrome or Alzheimer's disease, the endocytic pathway anomalies observed in brain of individual patients are reminiscent of the deleterious effects of ITSN1 overexpression on endocytosis (Keating et

al., 2006). ITSN1 might link desmin to the endocytic machinery or recruit signalling proteins such as GEF or Rab GAPases to a specific compartment of the cell.

• MutL Homolog 1 (MLH1): MLH1 is a component of the post-replicative DNA mismatch repair system (MMR) found to interact with desmin by a bacterial two-hybrid system (Brieger et al., 2010). MLH1 exhibits relationships to three interacting pairs of proteins involved in cytoskeletal and filament organization: Thymosin beta 4 and actin gamma, cathepsin B and annexin A2 as well as spectrin alpha and Desmin (Brieger et al., 2010). Coimmunoprecipitation and colocalization experiments validated the interaction of MLH1 with desmin (Brieger et al., 2010). In the same study the authors confirmed that siRNA knockdown of MLH1 showed functional impact of MLH1-Actin interaction on filament organization but they do not access experimentally on desmin filaments. They propose that dysregulation of MLH1 plays an essential role in cytoskeleton dynamics. Further experimental data are needed to address the functional impact of MHL1-desmin interaction in physiological conditions. Of interest, like other IF, desmin specifically binds single strand DNA and RNA *in vitro* via the non-α-helical head domain, which contains 12 arginine residue (charged positively) and lacks negatively charged residue (Tolstonog et al., 2002). In addition to that, desmin was showed to interact with MyoD and regulate its transcriptional activity (Li et al., 1994). Overall, desmin could link nuclear matrix with its bound heterochromatin, which could invoke a role of desmin IF in gene expression regulation (Cartaud et al., 1995). Further research will be required to fully elucidate the mechanisms.

Altogether, it seems that desmin and its associated proteins form a cellular scaffold that could fine-tune mechanochemical signalling and trafficking processes and thus regulate the function of critical homeostatic and survival mechanisms of the mammalian cell. Nevertheless the exact molecular mechanism that ensues for the majority of these associations remains unknown.

III- Desminopathies: genetics and physiopathology

III-1- Genetics and etiology

Yet desminopathy incidence and prevalence are not clear due to lack of detailed epidemiological studies, it can be considered as a rare disease with less than 5 affected individuals in 10000 (Clemen et al., 2013). The dominant inheritance is the most frequent in familial desminopathies and corresponds to gain of function of the mutated desmin leading to aggregates formation (Goldfarb et al., 2008). Autosomal recessive inheritance was observed in five families (Clemen et al.). In two cases, the mutations lead to loss of function and subsequent absence of desmin protein. Also few cases of *de novo* mutations were reported (Clemen et al., 2013). Most frequently, mutations found in the desmin gene (2q35) were missense mutations (van Spaendonck-Zwarts et al., 2011). Few splice site mutations leading to the loss of exon 3 were reported (p.Asp214_Glu245del) (Munoz-Marmol et al., 1998). Small in frame deletions of one, three or seven AA were described in a small number of patients and a larger deletion of 22 bases in exon 6 leading to a premature stop codon was identified in one family (van

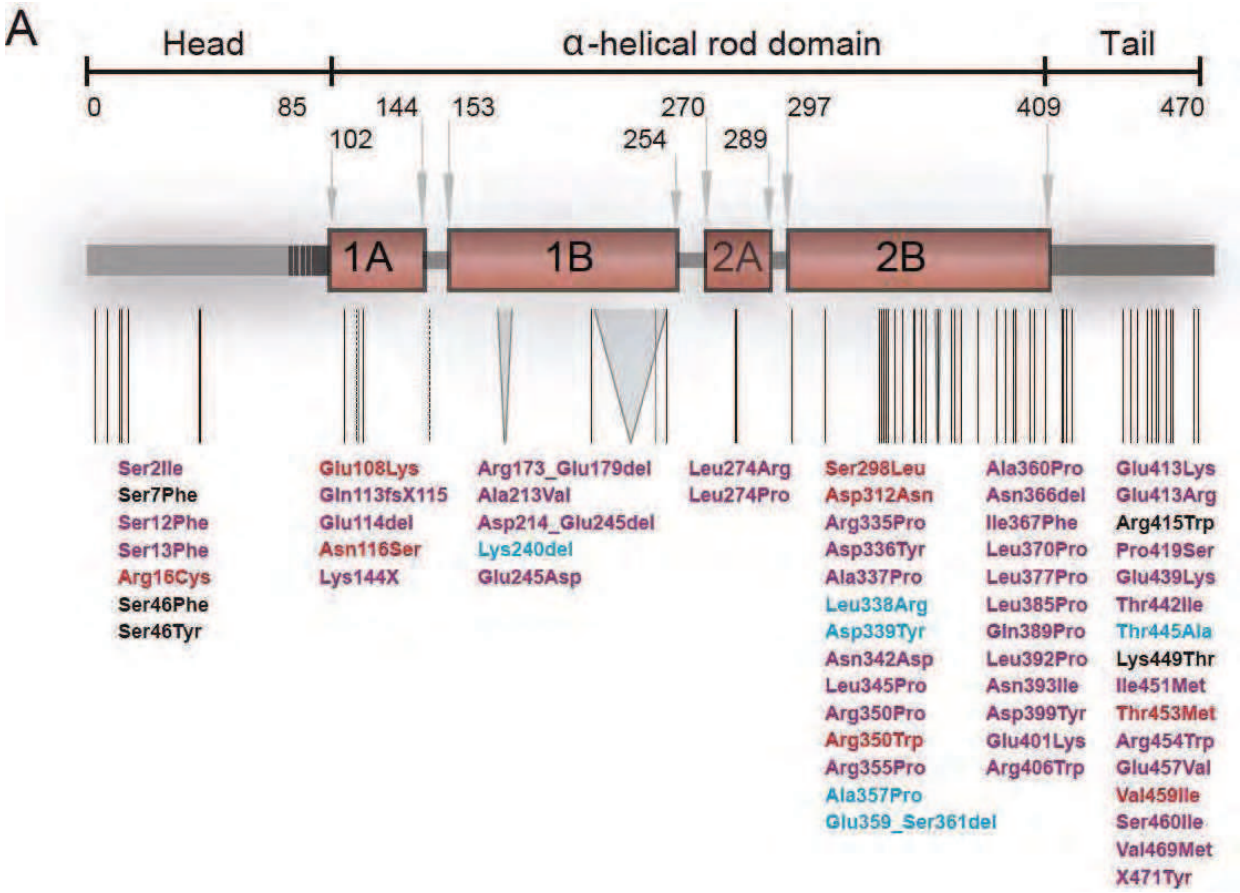

Manuscript 1/ Figure 3: Mutation map of the desmin gene and pathophysiology of desminopathies.

A. Desmin mutation spread the entire gene but majority are found in the α-helical-rod 2B and in the tail domains. Mutations are subdivided in 3 groups depending of their related phenotype: skeletal muscle (in blue), cardiac muscle (in red) and both skeletal and cardiac muscle (in purple).

Spaendonck-Zwarts et al., 2011). Mutations spread the entire desmin gene and were found in both the head and tail domains as well as in the four domains composing the central conserved α-helical region. However, a cluster of mutations could be observed in exon 6 corresponding to the end of the 2B coil domain (Clemen et al., 2013). The updated list (until June 2014) of mutations is summarized in Figure 3A. *DES* mutations are subdivided into 3 groups depending on their related phenotype: specific skeletal muscle phenotype, specific cardiac phenotype and both skeletal muscle and cardiac phenotypes (Figure 3A).

III-2- Pathophysiology

Desminopathy phenotypes are highly variable including skeletal muscle weakness, cardiomyopathy and cardiac conduction disease, respiratory insufficiency and smooth muscle defects (Figure 3B). The age of onset of the disease is highly variable as well varying from birth to the late 80s but generally occurs during the 30s.

III-2-1- Skeletal muscle involvement

Desmin-related myopathy is associated with a highly variable progressive skeletal myopathy in 74% of desmin mutation carriers (van Spaendonck-Zwarts et al., 2011). The distal muscle impairment generally precedes the proximal muscle impairment with muscle weakness in lower then upper limbs (Figure 3B). Muscle weakness can later spread to truncal, neck flexor, facial and bulbar muscles. Desmin mutations lead as well to desmin-related limb girdle muscular dystrophy and scapuloperoneal syndrome type Kaeser distal myopathy (Walter et al., 2007). A recognizable imaging pattern of muscle involvement has been reported for desminopathy diagnostic with sensitivity to detect desminopathy of 100% and specificity of 95% in the studied cohort (Fischer et al., 2008). Some muscles including peroneal muscles and semitendinosus are globally the most seriously and often the earliest affected. Tibialis anterior, soleus, gastrocnemius, gluteus maximus, sartorius and gracilis muscles are affected later. The adductor magnus, bicept femoris and semimembranosus are the last involved and with lesser extent. Respiratory muscle weakness, present in 26% of patients, is a common feature of advanced desminopathy and often leads to patient's death. It is hypothesized that functional dual-oriented desmin is necessary to dissipate the mechanical energy needed in the diaphragm for both longitudinal and transverse force transmission (Boriek et al., 2001). Analysis of patient biopsies showed irregularly shaped muscle fibres with abnormal regions containing amorphous deposits or intracellular inclusion bodies. Abnormal mitochondrial enzyme staining is a hallmark for desminopathies (Reimann et al., 2003). Classical myopathy features are observed including variation of fibres size, atrophic fibres and internal nuclei (Olive et al., 2004). Electron microscopy shows accumulation of dense granulofilamentous material located in the subsarcolemmal, interfibrillar or perinuclear region (Claeys et al., 2008). Z-disc deformities, autophagy structures, and focal grouping of mitochondria are frequently present as well (Claeys et al., 2008).

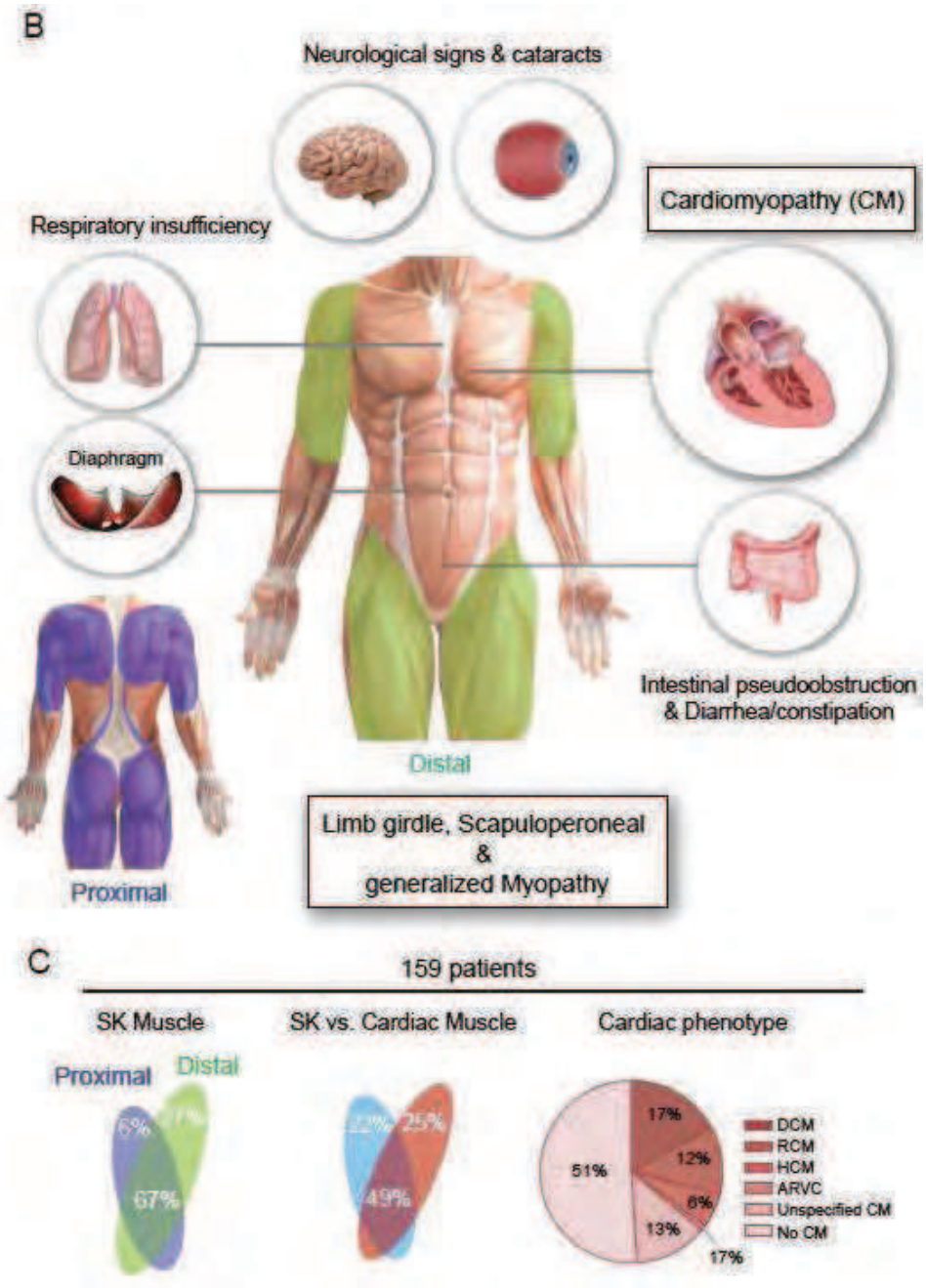

Manuscript 1/ Figure 3: Mutation map of the desmin gene and pathophysiology of desminopathies.

B. Apart the major striated muscle phenotype, we could note additional phenotypes in desmin-related disease such as neurological signs and gastric/intestinal problems. Nevertheless the major phenotype is muscular with distal muscle impairment that generally precedes the proximal muscle impairment. Desmin mutations lead as well to desmin-related limb girdle muscular dystrophy and scapuloperoneal syndrome type Kaeser distal myopathy. The cardiac phenotype is common and frequent in desminopathies reaching 74% of patients. **C.** Meta-analysis study on 159 patients showed that both distal and proximal skeletal muscle phenotypes are present in the majority of patients. These desminopathies patients develop cardiac phenotype as well as 49% have both. Within patients with cardiac phenotype, 17% have dilated cardiomyopathy (DCM), however no cardiomyopathy (CM) was detected in 51%. Hypertrophic cardiomyopathy (HCM), restrictive cardiomyopathy (RCM) or arrhythmogenic right ventricular cardiomyopathy (ARVC) are also noted but in less extent. (van Spaendonck-Zwarts et al., 2011)

III-2-2- Cardiac involvement in desminopathies

Among the 67 mutations in the desmin gene 12 mutations have been identified to specifically affect heart function. In particular, 2 mutations in the tail domain of Desmin (p.Ile451Met and p.Val459Ile) and a mutation in the 2B domain (p.Asp312Asn) have been found to specifically lead to cardiomyopathy without any skeletal muscle phenotype (Li et al., 1999; Taylor et al., 2007). Moreover, several reported cases of desmin-related myopathies could evolve to a cardiac involvement (Olive et al., 2004). Generally, 74% of all desminopathy patients present cardiomyopathy including mostly dilated (DCM), hypertrophic (HCM), restrictive (RCM) or arrhythmogenic right ventricle (ARVC) cardiomyopathies in respectively 17, 12, 6 and 1% of patients depending on the site and nature of the implicated mutation (Figure 3C). Cardiac conduction defects (CCD) was observed in 62% of patients, two thirds of them having cardiomyopathy (van Spaendonck-Zwarts et al., 2011). The most frequent manifestation of CCD is atrioventricular block (47% of cases) and requires urgent implantation of pacemaker. Similar to skeletal muscle, cardiac muscle showed desmin-positive aggregates as well as granulofilamentous and electron dense-amorphous materials in intermyofibrillar, subsarcolemmal and perinuclear regions (Claeys et al., 2008). Cardiomyocytes hypertrophy and disarray as well as misshaped nuclei and degenerated mitochondria are frequent pathological signs (Goldfarb and Dalakas, 2009).

III-2-3- Other pathological involvement

Smooth muscle involvement is not a major feature of desminopathy. Nevertheless, some manifestations has been reported such as intestinal involvement with chronic diarrhea or constipation (Bar et al., 2007) or with intestinal pseudo-obstruction (Ariza et al., 1995), swallowing difficulties (Goldfarb et al., 1998) and cataract (Olive et al., 2004) (Figure 3B). Patients with desmin mutation are at risk to develop respiratory problems. Indeed, meta-analysis of desminopathy showed that 26% of carriers have respiratory insufficiency (van Spaendonck-Zwarts et al., 2011).

III-3- Animal models for desmin-related disease

III-3-1- Desmin knock-out (KO) mice

Two desmin KO mice (Des-/-) models from two different groups were described in 1996-97 (Li et al., 1997; Milner et al., 1996). Des-/- developed and reproduced normally and display no obvious anatomical defects suggesting desmin-independence of myofibrillogenesis. No evidence of compensation by other IF proteins like vimentin or nestin was found by immunofluorescence. After birth, degradation was observed in skeletal, smooth and cardiac muscles and was shown to be more severe in weight-bearing muscles like soleus or continually used muscles like diaphragm, heart and aortic vessel wall. Excessive mitochondria clumping in skeletal and cardiac muscles and extensive mitochondria proliferation in myocardium often accompanied by swollen and disintegrating mitochondria, were observed at very early stage, before other structural effects become obvious (Milner et al., 2000). Mitochondrial respiration *in situ* is significantly altered in Des-/- in cardiac and soleus muscles (Milner et al., 2000) despite an increased creatine kinase activity linked with an

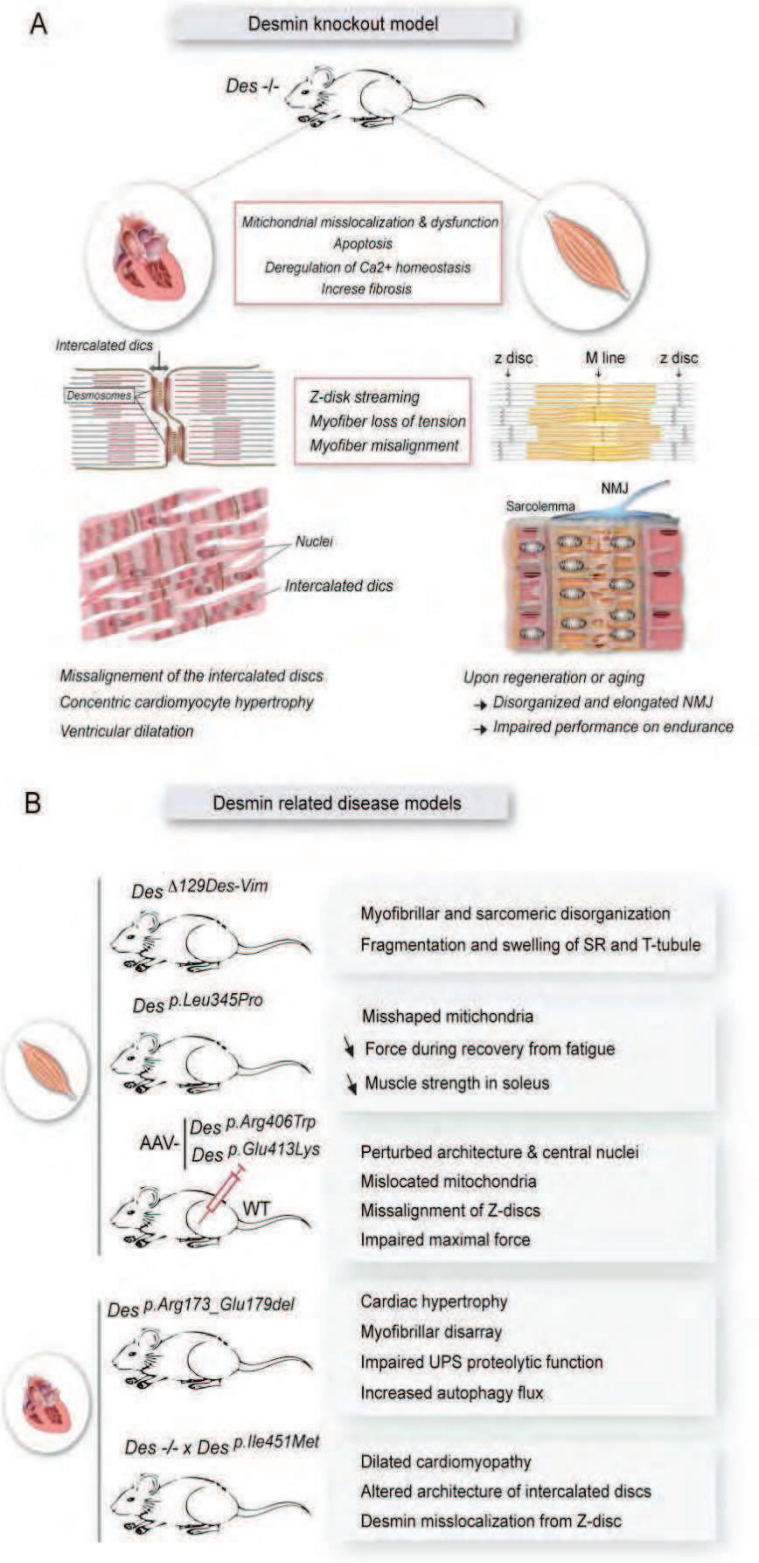

Manuscript 1/ Figure 4: Desmin animal models and associated phenotypes.

A. Desmin knockout mice (Des-/-) present affected cardiac and skeletal muscles with histological and molecular alterations that could be common to striated muscles or specific to skeletal or cardiac muscle. The cardiac phenotype is slightly more prominent than the skeletal muscle one, which is more obvious upon regeneration or aging. **B.** Desmin related diseases models generated for skeletal or cardiac phenotype and reported phenotypes showed common histological (myofibril disorganization and misshaped mitochondria) and physiological signs (decrease muscle function).

increased capacity of energy production and lower amount of cytochrome c in Des-/- heart mitochondria (Milner et al., 2000; Linden et al., 2001). Heart mitochondrial proteome of Des-/- mice was assessed and showed differences in most metabolic pathways in particular ketone body and acetate metabolism, NADH shuttle proteins, amino-acid metabolism proteins and respiratory enzymes. Apoptosis, calcium homeostasis and fibrosis pathways proteins were found perturbed as well (Fountoulakis et al., 2005). These perturbations in mitochondria localization and function can be explained by a lack of desmin-mediated association of the mitochondria with the microtubule associated plus-end directed motor, kinesin, shown to be mislocalized (Linden et al., 2001) and to the reduced capacity of mitochondria to resist to calcium exposure in absence of desmin (Weisleder et al., 2004a).

In skeletal muscles, sarcomere aligned normally until 2 months of age and presented normal distribution of sarcomeric proteins (α-actinin, tropomyosin etc.) (Milner et al., 1996) (Figure 4A). Progressively, skeletal muscles showed Z-disk streaming, myofiber loss of tension and misalignment and myofibrils became fragile and prone to breakage upon mechanical stress. Loss of association of desmin interactants synemin and paranemin with the Z-disk but not with the MTJ and NMJ were observed (Carlsson et al., 2000). After degeneration of the myofibers, a cycle of regeneration was observed but was often aberrant with subsarcolemmal accumulation of mitochondria, disorganization of muscle fibers and a relative increase of slow compared to fast myosin heavy chain, showing a role for desmin in maintenance of structural integrity in loaded skeletal muscles (Li et al., 1997). Upon regeneration or aging, NMJ appeared disorganized and elongated with acetylcholinesterase diffuse staining and reduced overall activity in the muscle cells (Agbulut et al., 2001). Consequently, Des-/- mouse were weaker and fatigue more easily showing impaired performance on endurance running tests (Haubold et al., 2003) (Figure 4A). Also, morphological abnormalities were observed in the diaphragm, which appeared thinner and showed misalignment of muscle fibres and abnormal sarcomeres with no clear demarcation between A and I bands (Li et al., 1997)

In cardiac muscle, myofiber loss of tension and disorganization were visible from the third week and gradually increased with age (Milner et al., 1996). Des-/- mice contained degenerating cardiomyofibers from 5 days post-partum. From 10 days post-partum onwards, an accumulation of macrophages, fibrosis and calcification was observed preferentially in the inter-ventricular septum and the free wall of the right ventricle. Perturbation of the intercalated discs, disruption of the sarcolemma and supercontraction of myofibrils were described as well (Thornell et al., 1997) (Figure 4A). Des-/- mice develop concentric cardiomyocyte hypertrophy accompanied later by ventricular dilatation and perturbed systolic function. The molecular phenotype of pressure overload hypertrophy was observed with overexpression of biomarkers like the α-skeletal actin and repression of SERCA-2A (Li et al., 1999). MRI imaging of desmin-null mice heart showed reduced left and right ventricular ejection fractions and cardiac output. The left ventricle mass was significantly increased and the mice exhibited segmental wall thinning and akinesia suggesting myocardial necrosis (Sprinkart et al., 2012). Electrophysiology studies showed that Des-/- mice present a reduced atrial but prolonged ventricular

refractory period and an enhanced inducibility of atrial fibrillation but lower susceptibility to ventricular arrhythmias. Ventricular conduction was showed to be slower than in control animals (Sprinkart et al., 2012). Finally, re-localization of bcl2 from the inner membrane of mitochondria to its outer membrane and to the cytoplasm in Des-/- mice was observed indicating apoptotic conditions (Linden et al., 2001). Overexpression of bcl2 in desmin null heart was shown to rescue most of the previously described phenotypes, in particular mitochondrial defects and myocardial lesions and fibrosis (Weisleder et al., 2004b). Loose organization of smooth muscle cells in the aortic vessel was observed as well (Li et al., 1997; Milner et al., 1996).

III-3-2- Zebrafish knockdown (KD) models

In zebrafish, the function of desmin is not well characterized. *In situ* hybridization and immunofluorescence studies showed localization of desmin in skeletal muscles and myocardium with enrichment at Z-bands and intercalated disks at embryonic (Costa et al., 2008) and adult (Camara-Pereira et al., 2009) stages. Two versions of the desmin gene are present in zebrafish, *desmina* (*desma*) (Loh et al., 2000) and *desminb* (*desmb*). Desma and Desmb share respectively 81% and 83% similarity with the human desmin protein. *Desma* KD embryos were generated using morpholino antisense oligonucleotide (MO) injection and show strong phenotypes including huge cardiac oedema, tail deformity and dramatic effect on heart rate (Vogel et al., 2009). A recent study shows defects in interfilament spacing using X-ray diffraction in 50% *desma* and *desmb* KD in 4 to 6 dpf larvae. Mechanical properties of skeletal muscles, including active force and response to stretch during active contraction were found to be lower in the context of desmin KD (Li et al., 2013). Phenotype and contraction of the heart was not assessed in this zebrafish model so far. Also, today, there is no fish model that phenocopy major desmin related diseases, with accumulation of protein aggregates.

III-3-3- Desmin-related myopathy models

The first desminopathy model was generated in 1996 substituting the last 129 aa of the hamster desmin by the last 13aa of hamster vimentin under the control of the hamster desmin promoter (Raats et al., 1996). This Delta129Des-Vim model presented an only weak expression of the transgene in all muscle types. Strong diffuse desmin staining was observed in skeletal muscles and only occasionally in heart. Desmin positive dots were present only in few skeletal muscle cells. The expression of the transgene mostly lead to a dominant negative effect on the desmin network resulting in no gross alteration of the myofibrillar and sarcomeric organization but disorganization of the transverse and longitudinal sarcoplasmic tubular system including fragmentation and swelling (Raats et al., 1996) (Figure 4B).

Kostareva et al. reported in 2008 a DRM mouse model with overexpression of the HA-tagged mutated mouse desmin with the p.Leu345Pro missense mutation reported in 28 patients (Kostareva et al., 2008). With an only low expression of the transgenic desmin in the model (corresponding to 5% of the WT desmin in the insoluble fraction and 17,4% of the soluble fraction), no difference in the pattern or intensity of desmin staining and no desmin aggregates were observed (Kostareva et al., 2008). No sign

of myofibrillar or sarcomeric disturbance or misalignment were observed but mitochondria presented reduced cristae density with circular membranes structures due to vacuolization of their matrix and mitochondrial Ca^{2+} increase. This led to a lower relative force during recovery from fatigue, reduced muscle strength in soleus muscle, thickening of the left ventricular wall and increased fibrosis in the heart (Kostareva et al., 2008) (Figure 4B).

Two transitory models of desminopathy were generated recently by injection of AAV carrying p.Arg406Trp and p.Glu413Lys mutated versions of mice desmin (Joanne et al., 2013) (Figure 4B). Ectopic expression of p.Arg406Trp Desmin lead to its accumulation in the perinuclear region, while p.Glu413Lys mutant accumulated in the subsarcolemmal compartment of injected muscle. Muscle fibers had a perturbed architecture with central nuclei, mislocated mitochondria and increased muscle regeneration. Perturbation of the alignment of Z-discs was observed at the sites of desmin accumulation. The affected muscles showed impaired maximal force generation capacity in both models (Joanne et al., 2013).

III-3-4- Desmin related cardiomyopathy models

The DesD7 transgenic mouse, a desmin mutation induced desmin related cardiomyopathy model, was published in 2001 (Wang et al., 2001). This model expressed the mouse desmin transgene with a 7AA deletion (p.Arg173_Glu179del), corresponding to a known mutation in patients of DRM, under the control of the myocardial specific α-myosin heavy chain promoter. Heterozygous DesD7 (p.Arg173_Glu179del) mice displayed characteristic electron dense granular filamentous desmin aggregates in the cardiomyocytes perinuclear region and intermyofibrillar space. Additional analysis revealed myofibrillar disarray and cardiac hypertrophy (with compensation at adult age) (Wang et al., 2001) (Figure 4B). Crossbreeding with ubiquitin-proteasome system (UPS) reporter mice ($GFPdgn^{tg}$) showed that UPS proteolytic function is impaired at the level of the entry of ubiquitinated proteins into the 20s proteasome in DesD7 mice (Liu et al., 2006). Crossbreeding with autophagy reporter mice ($GFP\text{-}LC3^{tg}$) showed that autophagy flux is increased and accompanied with upregulation of p62 in DesD7 cardiomyocytes (Zheng et al., 2011).

A second DRCM model carrying p.Ile451Met mutation under the control of the cardiac α-MHC promoter was reported in 2008 (Mavroidis et al., 2008). Mice expressed a truncated desmin deleted of 20-30 AA at the N-terminal part. After breeding with desmin KO mice (Mavroidis et al., 2008), mice did not show formation of aggregates. However, desmin Z-disc localization was lost. Despite a maintained association with desmin, the intercalated disks had an altered architecture, resembling other examples of dilated cardiomyopathy (Mavroidis et al., 2008) (Figure 4B).

Concluding remarks and outlook

It is obvious that desmin play a central role the integration of structure and function of striated muscle. Desmin IF participate to the generation of effective inter- and intracellular network that support highly efficient physiological functions promoting cell survival. At least, two decades have led to a number of important insights into the mechanisms by which desmin regulates number of cellular processes such as organelle positioning, stability and organization of the sarcolemma, integration of mechanotransduction signals etc. Desmin IFs appear to position mitochondria in area of high-energy demand or Ca^{2+} cycling. Desmin-mitochondria link can also influence the mitochondrial proteome, apoptotic program and fusion/fission events, suggesting that desmin could serve as a signalling platform allowing integrating signals from outside to inside organelles such as mitochondria. Importantly, posttranslational modifications (PTMs) could probably impact on desmin-organelle crosstalk underlying the complexity of how desmin IFs regulate cellular events. The increasing number of desmin partners leads us to emphasize additional role of intermediate filaments in regulating different aspects of muscle function. Indeed, some of those partners are involved in processes such as lipid signalling, DNA repair, endocytosis as well as Ca^{2+} homeostasis. The idea that desmin IF plays such a broad role in the physiology of striated muscle is intriguing and challenging for muscle biologist, with potentially significant implication for understanding myopathies, dilated cardiomyopathies and heart failure. Unravelling the molecular mechanisms by which desmin interaction with other proteins could impact IFs aggregation in pathological context could pave the way for future drug design.

References

Agbulut, O., Li, Z., Perie, S., Ludosky, M.A., Paulin, D., Cartaud, J., and Butler-Browne, G. (2001). Lack of desmin results in abortive muscle regeneration and modifications in synaptic structure. Cell Motil Cytoskeleton 49, 51-66.

Allen, R.E., Rankin, L.L., Greene, E.A., Boxhorn, L.K., Johnson, S.E., Taylor, R.G., and Pierce, P.R. (1991). Desmin is present in proliferating rat muscle satellite cells but not in bovine muscle satellite cells. J Cell Physiol 149, 525-535.

Amoasii, L., Hnia, K., Chicanne, G., Brech, A., Cowling, B.S., Muller, M.M., Schwab, Y., Koebel, P., Ferry, A., Payrastre, B., et al. (2013) Myotubularin and PtdIns3P remodel the sarcoplasmic reticulum in muscle in vivo. J Cell Sci 126, 1806-1819.

Ariza, A., Coll, J., Fernandez-Figueras, M.T., Lopez, M.D., Mate, J.L., Garcia, O., Fernandez-Vasalo, A., and Navas-Palacios, J.J. (1995). Desmin myopathy: a multisystem disorder involving skeletal, cardiac, and smooth muscle. Hum Pathol 26, 1032-1037.

Bandyopadhyay, S., Chiang, C.Y., Srivastava, J., Gersten, M., White, S., Bell, R., Kurschner, C., Martin, C., Smoot, M., Sahasrabudhe, S., et al. (2010)A human MAP kinase interactome. Nat Methods 7, 801-805.

Bar, H., Goudeau, B., Walde, S., Casteras-Simon, M., Mucke, N., Shatunov, A., Goldberg, Y.P., Clarke, C., Holton, J.L., Eymard, B., et al. (2007). Conspicuous involvement of desmin tail mutations in diverse cardiac and skeletal myopathies. Hum Mutat 28, 374-386.

Barbet, J.P., Thornell, L.E., and Butler-Browne, G.S. (1991). Immunocytochemical characterisation of two generations of fibers during the development of the human quadriceps muscle. Mech Dev 35, 3-11.

Benson, M.A., Tinsley, C.L., and Blake, D.J. (2004). Myospryn is a novel binding partner for dysbindin in muscle. J Biol Chem 279, 10450-10458.

Bentzinger, C.F., Wang, Y.X., and Rudnicki, M.A. (2012) Building muscle: molecular regulation of myogenesis. Cold Spring Harb Perspect Biol 4.

Blake, D.J., and Martin-Rendon, E. (2002). Intermediate filaments and the function of the dystrophin-protein complex. Trends Cardiovasc Med 12, 224-228.

Boriek, A.M., Capetanaki, Y., Hwang, W., Officer, T., Badshah, M., Rodarte, J., and Tidball, J.G. (2001). Desmin integrates the three-dimensional mechanical properties of muscles. Am J Physiol Cell Physiol 280, C46-52.

Breckler, J., and Lazarides, E. (1982). Isolation of a new high molecular weight protein associated with desmin and vimentin filaments from avian embryonic skeletal muscle. J Cell Biol 92, 795-806.

Brieger, A., Adryan, B., Wolpert, F., Passmann, S., Zeuzem, S., and Trojan, J. (2010) Cytoskeletal scaffolding proteins interact with Lynch-Syndrome associated mismatch repair protein MLH1. Proteomics 10, 3343-3355.

Bruusgaard, J.C., Liestol, K., Ekmark, M., Kollstad, K., and Gundersen, K. (2003). Number and spatial distribution of nuclei in the muscle fibres of normal mice studied in vivo. J Physiol 551, 467-478.

Cadot, B., Gache, V., Vasyutina, E., Falcone, S., Birchmeier, C., and Gomes, E.R. (2012) Nuclear movement during myotube formation is microtubule and dynein dependent and is regulated by Cdc42, Par6 and Par3. EMBO Rep 13, 741-749.

Camara-Pereira, E.S., Campos, L.M., Vannier-Santos, M.A., Mermelstein, C.S., and Costa, M.L. (2009). Distribution of cytoskeletal and adhesion proteins in adult zebrafish skeletal muscle. Histol Histopathol 24, 187-196.

Camargo, F.D., Green, R., Capetanaki, Y., Jackson, K.A., and Goodell, M.A. (2003). Single hematopoietic stem cells generate skeletal muscle through myeloid intermediates. Nat Med 9, 1520-1527.

Capers, C.R. (1960). Multinucleation of skeletal muscle in vitro. J Biophys Biochem Cytol 7, 559-566.

Capetanaki, Y., Bloch, R.J., Kouloumenta, A., Mavroidis, M., and Psarras, S. (2007). Muscle intermediate filaments and their links to membranes and membranous organelles. Exp Cell Res 313, 2063-2076.

Capetanaki, Y., Milner, D.J., and Weitzer, G. (1997). Desmin in muscle formation and maintenance: knockouts and consequences. Cell Struct Funct 22, 103-116.

Carlsson, L., Li, Z., Paulin, D., and Thornell, L.E. (1999). Nestin is expressed during development and in myotendinous and neuromuscular junctions in wild type and desmin knock-out mice. Exp Cell Res 251, 213-223.

Carlsson, L., Li, Z.L., Paulin, D., Price, M.G., Breckler, J., Robson, R.M., Wiche, G., and Thornell, L.E. (2000). Differences in the distribution of synemin, paranemin, and plectin in skeletal muscles of wild-type and desmin knock-out mice. Histochem Cell Biol 114, 39-47.

Cartaud, A., Jasmin, B.J., Changeux, J.P., and Cartaud, J. (1995). Direct involvement of a lamin-B-related (54 kDa) protein in the association of intermediate filaments with the postsynaptic membrane of the Torpedo marmorata electrocyte. J Cell Sci 108 (Pt 1), 153-160.

Castanon, M.J., Walko, G., Winter, L., and Wiche, G. (2013) Plectin-intermediate filament partnership in skin, skeletal muscle, and peripheral nerve. Histochem Cell Biol 140, 33-53.

Chang, L., Barlan, K., Chou, Y.H., Grin, B., Lakonishok, M., Serpinskaya, A.S., Shumaker, D.K., Herrmann, H., Gelfand, V.I., and Goldman, R.D. (2009). The dynamic properties of intermediate filaments during organelle transport. J Cell Sci 122, 2914-2923.

Chang, L., and Goldman, R.D. (2004). Intermediate filaments mediate cytoskeletal crosstalk. Nat Rev Mol Cell Biol 5, 601-613.

Chung, B.M., Rotty, J.D., and Coulombe, P.A. (2013)Networking galore: intermediate filaments and cell migration. Curr Opin Cell Biol 25, 600-612.

Claeys, K.G., Fardeau, M., Schroder, R., Suominen, T., Tolksdorf, K., Behin, A., Dubourg, O., Eymard, B., Maisonobe, T., Stojkovic, T., et al. (2008). Electron microscopy in myofibrillar myopathies reveals clues to the mutated gene. Neuromuscul Disord 18, 656-666.

Clemen, C.S., Herrmann, H., Strelkov, S.V., and Schroder, R. (2013) Desminopathies: pathology and mechanisms. Acta Neuropathol 125, 47-75.

Constantin, B. (2014) Dystrophin complex functions as a scaffold for signalling proteins. Biochim Biophys Acta 1838, 635-642.

Costa, M.L., Escaleira, R., Cataldo, A., Oliveira, F., and Mermelstein, C.S. (2004). Desmin: molecular interactions and putative functions of the muscle intermediate filament protein. Braz J Med Biol Res 37, 1819-1830.

Costa, M.L., Escaleira, R.C., Jazenko, F., and Mermelstein, C.S. (2008). Cell adhesion in zebrafish myogenesis: distribution of intermediate filaments, microfilaments, intracellular adhesion structures and extracellular matrix. Cell Motil Cytoskeleton 65, 801-815.

Coulombe, P.A., and Wong, P. (2004). Cytoplasmic intermediate filaments revealed as dynamic and multipurpose scaffolds. Nat Cell Biol 6, 699-706.

Dingli, F., Parys, J.B., Loew, D., Saule, S., and Mery, L. (2012) Vimentin and the K-Ras-induced actin-binding protein control inositol-(1,4,5)-trisphosphate receptor redistribution during MDCK cell differentiation. J Cell Sci 125, 5428-5440.

Dunia, I., Pieper, F., Manenti, S., van de Kemp, A., Devilliers, G., Benedetti, E.L., and Bloemendal, H. (1990). Plasma membrane-cytoskeleton damage in eye lenses of transgenic mice expressing desmin. Eur J Cell Biol 53, 59-74.

Englander, L.L., and Rubin, L.L. (1987). Acetylcholine receptor clustering and nuclear movement in muscle fibers in culture. J Cell Biol 104, 87-95.

Eriksson, J.E., Dechat, T., Grin, B., Helfand, B., Mendez, M., Pallari, H.M., and Goldman, R.D. (2009). Introducing intermediate filaments: from discovery to disease. J Clin Invest 119, 1763-1771.

Eriksson, J.E., He, T., Trejo-Skalli, A.V., Harmala-Brasken, A.S., Hellman, J., Chou, Y.H., and Goldman, R.D. (2004). Specific in vivo phosphorylation sites determine the assembly dynamics of vimentin intermediate filaments. J Cell Sci 117, 919-932.

Farrell, F.X., Sax, C.M., and Zehner, Z.E. (1990). A negative element involved in vimentin gene expression. Mol Cell Biol 10, 2349-2358.

Fischer, D., Kley, R.A., Strach, K., Meyer, C., Sommer, T., Eger, K., Rolfs, A., Meyer, W., Pou, A., Pradas, J., et al. (2008). Distinct muscle imaging patterns in myofibrillar myopathies. Neurology 71, 758-765.

Fountoulakis, M., Soumaka, E., Rapti, K., Mavroidis, M., Tsangaris, G., Maris, A., Weisleder, N., and Capetanaki, Y. (2005). Alterations in the heart mitochondrial proteome in a desmin null heart failure model. J Mol Cell Cardiol 38, 461-474.

Garbuglia, M., Verzini, M., Sorci, G., Bianchi, R., Giambanco, I., Agneletti, A.L., and Donato, R. (1999). The calcium-modulated proteins, S100A1 and S100B, as potential regulators of the dynamics of type III intermediate filaments. Braz J Med Biol Res 32, 1177-1185.

Gilbert, S., Ruel, A., Loranger, A., and Marceau, N. (2008). Switch in Fas-activated death signaling pathway as result of keratin 8/18-intermediate filament loss. Apoptosis 13, 1479-1493.

Goldfarb, L.G., and Dalakas, M.C. (2009). Tragedy in a heartbeat: malfunctioning desmin causes skeletal and cardiac muscle disease. J Clin Invest 119, 1806-1813.

Goldfarb, L.G., Olive, M., Vicart, P., and Goebel, H.H. (2008). Intermediate filament diseases: desminopathy. Adv Exp Med Biol 642, 131-164.

Goldfarb, L.G., Park, K.Y., Cervenakova, L., Gorokhova, S., Lee, H.S., Vasconcelos, O., Nagle, J.W., Semino-Mora, C., Sivakumar, K., and Dalakas, M.C. (1998). Missense mutations in desmin associated with familial cardiac and skeletal myopathy. Nat Genet 19, 402-403.

Goldman, R.D., Cleland, M.M., Murthy, S.N., Mahammad, S., and Kuczmarski, E.R. (2012) Inroads into the structure and function of intermediate filament networks. J Struct Biol 177, 14-23.

Grady, R.M., Starr, D.A., Ackerman, G.L., Sanes, J.R., and Han, M. (2005). Syne proteins anchor muscle nuclei at the neuromuscular junction. Proc Natl Acad Sci U S A 102, 4359-4364.

Granger, B.L., and Lazarides, E. (1980). Synemin: a new high molecular weight protein associated with desmin and vimentin filaments in muscle. Cell 22, 727-738.

Gregor, M., Osmanagic-Myers, S., Burgstaller, G., Wolfram, M., Fischer, I., Walko, G., Resch, G.P., Jorgl, A., Herrmann, H., and Wiche, G. (2014) Mechanosensing through focal adhesion-anchored intermediate filaments. FASEB J 28, 715-729.

Guma, F.C.R., Mello, T.G., Mermelstein, C.S., Fortuna, V.A., Wofchuk, S.T., Gottfried, C., Guaragna, R.M., Costa, M.L., and Borojevic, R. (2001). Intermediate filaments modulation in an in vitro model of the hepatic stellate cell activation or conversion into the lipocyte phenotype. Biochem Cell Biol 79, 409-417.

Haubold, K.W., Allen, D.L., Capetanaki, Y., and Leinwand, L.A. (2003). Loss of desmin leads to impaired voluntary wheel running and treadmill exercise performance. J Appl Physiol (1985) 95, 1617-1622.

Herrmann, H., Fouquet, B., and Franke, W.W. (1989). Expression of intermediate filament proteins during development of Xenopus laevis. II. Identification and molecular characterization of desmin. Development 105, 299-307.

Herrmann, H., Strelkov, S.V., Burkhard, P., and Aebi, U. (2009). Intermediate filaments: primary determinants of cell architecture and plasticity. J Clin Invest 119, 1772-1783.

Hnia, K., Tronchere, H., Tomczak, K.K., Amoasii, L., Schultz, P., Beggs, A.H., Payrastre, B., Mandel, J.L., and Laporte, J. (2011) Myotubularin controls desmin intermediate filament architecture and mitochondrial dynamics in human and mouse skeletal muscle. J Clin Invest 121, 70-85.

Hockfield, S., and McKay, R.D. (1985). Identification of major cell classes in the developing mammalian nervous system. J Neurosci 5, 3310-3328.

Howman, E.V., Sullivan, N., Poon, E.P., Britton, J.E., Hilton-Jones, D., and Davies, K.E. (2003). Syncoilin accumulation in two patients with desmin-related myopathy. Neuromuscul Disord 13, 42-48.

Humphries, A.C., Donnelly, S.K., and Way, M. (2014) Cdc42 and the Rho GEF intersectin-1 collaborate with Nck to promote N-WASP-dependent actin polymerisation. J Cell Sci 127, 673-685.

Jevsek, M., Jaworski, A., Polo-Parada, L., Kim, N., Fan, J., Landmesser, L.T., and Burden, S.J. (2006). CD24 is expressed by myofiber synaptic nuclei and regulates synaptic transmission. Proc Natl Acad Sci U S A 103, 6374-6379.

Joanne, P., Chourbagi, O., Hourde, C., Ferry, A., Butler-Browne, G., Vicart, P., Dumonceaux, J., and Agbulut, O. (2013) Viral-mediated expression of desmin mutants to create mouse models of myofibrillar myopathy. Skelet Muscle 3, 4.

Kachinsky, A.M., Dominov, J.A., and Miller, J.B. (1994). Myogenesis and the intermediate filament protein, nestin. Dev Biol 165, 216-228.

Keating, D.J., Chen, C., and Pritchard, M.A. (2006). Alzheimer's disease and endocytic dysfunction: clues from the Down syndrome-related proteins, DSCR1 and ITSN1. Ageing Res Rev 5, 388-401.

Kelly, A.M., and Zacks, S.I. (1969). The histogenesis of rat intercostal muscle. J Cell Biol 42, 135-153.

Kielbasa, O.M., Reynolds, J.G., Wu, C.L., Snyder, C.M., Cho, M.Y., Weiler, H., Kandarian, S., and Naya, F.J. (2011) Myospryn is a calcineurin-interacting protein that negatively modulates slow-fiber-type transformation and skeletal muscle regeneration. FASEB J 25, 2276-2286.

Kostareva, A., Sjoberg, G., Bruton, J., Zhang, S.J., Balogh, J., Gudkova, A., Hedberg, B., Edstrom, L., Westerblad, H., and Sejersen, T. (2008). Mice expressing L345P mutant desmin exhibit morphological and functional changes of skeletal and cardiac mitochondria. J Muscle Res Cell Motil 29, 25-36.

Kouloumenta, A., Mavroidis, M., and Capetanaki, Y. (2007). Proper perinuclear localization of the TRIM-like protein myospryn requires its binding partner desmin. J Biol Chem 282, 35211-35221.

Kuisk, I.R., Li, H., Tran, D., and Capetanaki, Y. (1996). A single MEF2 site governs desmin transcription in both heart and skeletal muscle during mouse embryogenesis. Dev Biol 174, 1-13.

Kumar, A., Khandelwal, N., Malya, R., Reid, M.B., and Boriek, A.M. (2004). Loss of dystrophin causes aberrant mechanotransduction in skeletal muscle fibers. FASEB J 18, 102-113.

Lazarides, E. (1982). Intermediate filaments: a chemically heterogeneous, developmentally regulated class of proteins. Annu Rev Biochem 51, 219-250.

Lazarides, E., and Hubbard, B.D. (1976). Immunological characterization of the subunit of the 100 A filaments from muscle cells. Proc Natl Acad Sci U S A 73, 4344-4348.

Li, D., Tapscoft, T., Gonzalez, O., Burch, P.E., Quinones, M.A., Zoghbi, W.A., Hill, R., Bachinski, L.L., Mann, D.L., and Roberts, R. (1999). Desmin mutation responsible for idiopathic dilated cardiomyopathy. Circulation 100, 461-464.

Li, H., and Capetanaki, Y. (1993). Regulation of the mouse desmin gene: transactivated by MyoD, myogenin, MRF4 and Myf5. Nucleic Acids Res 21, 335-343.

Li, H., Choudhary, S.K., Milner, D.J., Munir, M.I., Kuisk, I.R., and Capetanaki, Y. (1994). Inhibition of desmin expression blocks myoblast fusion and interferes with the myogenic regulators MyoD and myogenin. J Cell Biol 124, 827-841.

Li, M., Andersson-Lendahl, M., Sejersen, T., and Arner, A. (2013) Knockdown of desmin in zebrafish larvae affects interfilament spacing and mechanical properties of skeletal muscle. J Gen Physiol 141, 335-345.

Li, Z., Mericskay, M., Agbulut, O., Butler-Browne, G., Carlsson, L., Thornell, L.E., Babinet, C., and Paulin, D. (1997). Desmin is essential for the tensile strength and integrity of myofibrils but not for myogenic commitment, differentiation, and fusion of skeletal muscle. J Cell Biol 139, 129-144.

Linden, M., Li, Z., Paulin, D., Gotow, T., and Leterrier, J.F. (2001). Effects of desmin gene knockout on mice heart mitochondria. J Bioenerg Biomembr 33, 333-341.

Liu, J., Chen, Q., Huang, W., Horak, K.M., Zheng, H., Mestril, R., and Wang, X. (2006). Impairment of the ubiquitin-proteasome system in desminopathy mouse hearts. FASEB J 20, 362-364.

Loh, S.H., Chan, W.T., Gong, Z., Lim, T.M., and Chua, K.L. (2000). Characterization of a zebrafish (Danio rerio) desmin cDNA: an early molecular marker of myogenesis. Differentiation 65, 247-254.

Maehama, T., Taylor, G.S., and Dixon, J.E. (2001). PTEN and myotubularin: novel phosphoinositide phosphatases. Annu Rev Biochem 70, 247-279.

Mavroidis, M., Panagopoulou, P., Kostavasili, I., Weisleder, N., and Capetanaki, Y. (2008). A missense mutation in desmin tail domain linked to human dilated cardiomyopathy promotes cleavage of the head domain and abolishes its Z-disc localization. FASEB J 22, 3318-3327.

Meyer, G.A., and Lieber, R.L. (2012) Skeletal muscle fibrosis develops in response to desmin deletion. Am J Physiol Cell Physiol 302, C1609-1620.

Milner, D.J., Mavroidis, M., Weisleder, N., and Capetanaki, Y. (2000). Desmin cytoskeleton linked to muscle mitochondrial distribution and respiratory function. J Cell Biol 150, 1283-1298.

Milner, D.J., Weitzer, G., Tran, D., Bradley, A., and Capetanaki, Y. (1996). Disruption of muscle architecture and myocardial degeneration in mice lacking desmin. J Cell Biol 134, 1255-1270.

Mizuno, Y., Thompson, T.G., Guyon, J.R., Lidov, H.G., Brosius, M., Imamura, M., Ozawa, E., Watkins, S.C., and Kunkel, L.M. (2001). Desmuslin, an intermediate filament protein that interacts with alpha -dystrobrevin and desmin. Proc Natl Acad Sci U S A 98, 6156-6161.

Mohamed, J.S., and Boriek, A.M.(2012) Loss of desmin triggers mechanosensitivity and up-regulation of Ankrd1 expression through Akt-NF-kappaB signaling pathway in smooth muscle cells. FASEB J 26, 757-765.

Moorwood, C. (2008). Syncoilin, an intermediate filament-like protein linked to the dystrophin associated protein complex in skeletal muscle. Cell Mol Life Sci 65, 2957-2963.

Most, P., Remppis, A., Pleger, S.T., Katus, H.A., and Koch, W.J. (2007). S100A1: a novel inotropic regulator of cardiac performance. Transition from molecular physiology to pathophysiological relevance. Am J Physiol Regul Integr Comp Physiol 293, R568-577.

Mostafavi, S., Ray, D., Warde-Farley, D., Grouios, C., and Morris, Q. (2008). GeneMANIA: a real-time multiple association network integration algorithm for predicting gene function. Genome Biol 9 Suppl 1, S4.

Munoz-Marmol, A.M., Strasser, G., Isamat, M., Coulombe, P.A., Yang, Y., Roca, X., Vela, E., Mate, J.L., Coll, J., Fernandez-Figueras, M.T., et al. (1998). A dysfunctional desmin mutation in a patient with severe generalized myopathy. Proc Natl Acad Sci U S A 95, 11312-11317.

Newey, S.E., Howman, E.V., Ponting, C.P., Benson, M.A., Nawrotzki, R., Loh, N.Y., Davies, K.E., and Blake, D.J. (2001). Syncoilin, a novel member of the intermediate filament superfamily that interacts with alpha-dystrobrevin in skeletal muscle. J Biol Chem 276, 6645-6655.

Okur, M.N., Russo, A., and O'Bryan, J.P. (2014) Receptor tyrosine kinase ubiquitylation involves the dynamic regulation of Cbl-Spry2 by intersectin 1 and the Shp2 tyrosine phosphatase. Mol Cell Biol 34, 271-279.

Olive, M., Goldfarb, L., Moreno, D., Laforet, E., Dagvadorj, A., Sambuughin, N., Martinez-Matos, J.A., Martinez, F., Alio, J., Farrero, E., et al. (2004). Desmin-related myopathy: clinical, electrophysiological, radiological, neuropathological and genetic studies. J Neurol Sci 219, 125-137.

Poon, E., Howman, E.V., Newey, S.E., and Davies, K.E. (2002). Association of syncoilin and desmin: linking intermediate filament proteins to the dystrophin-associated protein complex. J Biol Chem 277, 3433-3439.

Prosser, B.L., Hernandez-Ochoa, E.O., and Schneider, M.F. (2011) S100A1 and calmodulin regulation of ryanodine receptor in striated muscle. Cell Calcium 50, 323-331.

Prosser, B.L., Wright, N.T., Hernandez-Ochoa, E.O., Varney, K.M., Liu, Y., Olojo, R.O., Zimmer, D.B., Weber, D.J., and Schneider, M.F. (2008). S100A1 binds to the calmodulin-binding site of ryanodine receptor and modulates skeletal muscle excitation-contraction coupling. J Biol Chem 283, 5046-5057.

Raats, J.M., Schaart, G., Henderik, J.B., van der Kemp, A., Dunia, I., Benedetti, E.L., Pieper, F.R., Ramaekers, F.C., and Bloemendal, H. (1996). Muscle-specific expression of a dominant negative desmin mutant in transgenic mice. Eur J Cell Biol 71, 221-236.

Reimann, J., Kunz, W.S., Vielhaber, S., Kappes-Horn, K., and Schroder, R. (2003). Mitochondrial dysfunction in myofibrillar myopathy. Neuropathol Appl Neurobiol 29, 45-51.

Remppis, A., Most, P., Loffler, E., Ehlermann, P., Bernotat, J., Pleger, S., Borries, M., Reppel, M., Fischer, J., Koch, W.J., et al. (2002). The small EF-hand Ca2+ binding protein S100A1 increases contractility and Ca2+ cycling in rat cardiac myocytes. Basic Res Cardiol 97 Suppl 1, I56-62.

Reynolds, J.G., McCalmon, S.A., Donaghey, J.A., and Naya, F.J. (2008). Deregulated protein kinase A signaling and myospryn expression in muscular dystrophy. J Biol Chem 283, 8070-8074.

Reynolds, J.G., McCalmon, S.A., Tomczyk, T., and Naya, F.J. (2007). Identification and mapping of protein kinase A binding sites in the costameric protein myospryn. Biochim Biophys Acta 1773, 891-902.

Russell, M.A., Lund, L.M., Haber, R., McKeegan, K., Cianciola, N., and Bond, M. (2006). The intermediate filament protein, synemin, is an AKAP in the heart. Arch Biochem Biophys 456, 204-215.

Sanes, J.R., Johnson, Y.R., Kotzbauer, P.T., Mudd, J., Hanley, T., Martinou, J.C., and Merlie, J.P. (1991). Selective expression of an acetylcholine receptor-lacZ transgene in synaptic nuclei of adult muscle fibers. Development 113, 1181-1191.

Schofield, A.V., and Bernard, O. (2013) Rho-associated coiled-coil kinase (ROCK) signaling and disease. Crit Rev Biochem Mol Biol 48, 301-316.

Schopferer, M., Bar, H., Hochstein, B., Sharma, S., Mucke, N., Herrmann, H., and Willenbacher, N. (2009). Desmin and vimentin intermediate filament networks: their viscoelastic properties investigated by mechanical rheometry. J Mol Biol 388, 133-143.

Schultheiss, T., Lin, Z.X., Ishikawa, H., Zamir, I., Stoeckert, C.J., and Holtzer, H. (1991). Desmin/vimentin intermediate filaments are dispensable for many aspects of myogenesis. J Cell Biol 114, 953-966.

Sejersen, T., and Lendahl, U. (1993). Transient expression of the intermediate filament nestin during skeletal muscle development. J Cell Sci 106 (Pt 4), 1291-1300.

Sin, W.C., Chen, X.Q., Leung, T., and Lim, L. (1998). RhoA-binding kinase alpha translocation is facilitated by the collapse of the vimentin intermediate filament network. Mol Cell Biol 18, 6325-6339.

Snider, N.T., and Omary, M.B. (2014). Post-translational modifications of intermediate filament proteins: mechanisms and functions. Nat Rev Mol Cell Biol 15, 163-177.

Sprinkart, A.M., Block, W., Traber, F., Meyer, R., Paulin, D., Clemen, C.S., Schroder, R., Gieseke, J., Schild, H., and Thomas, D. (2012). Characterization of the failing murine heart in a desmin knock-out model using a clinical 3 T MRI scanner. Int J Cardiovasc Imaging 28, 1699-1705.

Stark, C., Breitkreutz, B.J., Reguly, T., Boucher, L., Breitkreutz, A., and Tyers, M. (2006). BioGRID: a general repository for interaction datasets. Nucleic Acids Res 34, D535-539.

Steinert, P.M., Chou, Y.H., Prahlad, V., Parry, D.A., Marekov, L.N., Wu, K.C., Jang, S.I., and Goldman, R.D. (1999). A high molecular weight intermediate filament-associated protein in BHK-21 cells is nestin, a type VI intermediate filament protein. Limited co-assembly in vitro to form heteropolymers with type III vimentin and type IV alpha-internexin. J Biol Chem 274, 9881-9890.

Stone, M.R., O'Neill, A., Catino, D., and Bloch, R.J. (2005). Specific interaction of the actin-binding domain of dystrophin with intermediate filaments containing keratin 19. Mol Biol Cell 16, 4280-4293.

Sun, N., Critchley, D.R., Paulin, D., Li, Z., and Robson, R.M. (2008). Human alpha-synemin interacts directly with vinculin and metavinculin. Biochem J 409, 657-667.

Taylor, G.S., Maehama, T., and Dixon, J.E. (2000). Myotubularin, a protein tyrosine phosphatase mutated in myotubular myopathy, dephosphorylates the lipid second messenger, phosphatidylinositol 3-phosphate. Proc Natl Acad Sci U S A 97, 8910-8915.

Taylor, M.R., Slavov, D., Ku, L., Di Lenarda, A., Sinagra, G., Carniel, E., Haubold, K., Boucek, M.M., Ferguson, D., Graw, S.L., et al. (2007). Prevalence of desmin mutations in dilated cardiomyopathy. Circulation 115, 1244-1251.

Thornell, L., Carlsson, L., Li, Z., Mericskay, M., and Paulin, D. (1997). Null mutation in the desmin gene gives rise to a cardiomyopathy. J Mol Cell Cardiol 29, 2107-2124.

Tolstonog, G.V., Sabasch, M., and Traub, P. (2002). Cytoplasmic intermediate filaments are stably associated with nuclear matrices and potentially modulate their DNA-binding function. DNA Cell Biol 21, 213-239.

Tsoupri, E., and Capetanaki, Y. (2013). Myospryn: a multifunctional desmin-associated protein. Histochem Cell Biol 140, 55-63.

Tsyba, L., Nikolaienko, O., Dergai, O., Dergai, M., Novokhatska, O., Skrypkina, I., and Rynditch, A. (2011) Intersectin multidomain adaptor proteins: regulation of functional diversity. Gene 473, 67-75.

Ursitti, J.A., Lee, P.C., Resneck, W.G., McNally, M.M., Bowman, A.L., O'Neill, A., Stone, M.R., and Bloch, R.J. (2004). Cloning and characterization of cytokeratins 8 and 19 in adult rat striated muscle. Interaction with the dystrophin glycoprotein complex. J Biol Chem 279, 41830-41838.

van Spaendonck-Zwarts, K.Y., van Hessem, L., Jongbloed, J.D., de Walle, H.E., Capetanaki, Y., van der Kooi, A.J., van Langen, I.M., van den Berg, M.P., and van Tintelen, J.P. (2011). Desmin-related myopathy. Clin Genet 80, 354-366.

Vogel, B., Meder, B., Just, S., Laufer, C., Berger, I., Weber, S., Katus, H.A., and Rottbauer, W. (2009). In-vivo characterization of human dilated cardiomyopathy genes in zebrafish. Biochem Biophys Res Commun 390, 516-522.

Volkers, M., Rohde, D., Goodman, C., and Most, P. (2010). S100A1: a regulator of striated muscle sarcoplasmic reticulum Ca2+ handling, sarcomeric, and mitochondrial function. J Biomed Biotechnol 2010, 178614.

Walsh, M.P., Busaan, J.L., Fraser, E.D., Fu, S.Y., Pato, M.D., and Michalak, M. (1995). Characterization of the recombinant C-terminal domain of dystrophin: phosphorylation by calmodulin-dependent protein kinase II and dephosphorylation by type 2B protein phosphatase. Biochemistry 34, 5561-5568.

Walter, M.C., Reilich, P., Huebner, A., Fischer, D., Schroder, R., Vorgerd, M., Kress, W., Born, C., Schoser, B.G., Krause, K.H., et al. (2007). Scapuloperoneal syndrome type Kaeser and a wide phenotypic spectrum of adult-onset, dominant myopathies are associated with the desmin mutation R350P. Brain 130, 1485-1496.

Wang, X., Osinska, H., Dorn, G.W., 2nd, Nieman, M., Lorenz, J.N., Gerdes, A.M., Witt, S., Kimball, T., Gulick, J., and Robbins, J. (2001). Mouse model of desmin-related cardiomyopathy. Circulation 103, 2402-2407.

Weisleder, N., Soumaka, E., Abbasi, S., Taegtmeyer, H., and Capetanaki, Y. (2004a). Cardiomyocyte-specific desmin rescue of desmin null cardiomyopathy excludes vascular involvement. J Mol Cell Cardiol 36, 121-128.

Weisleder, N., Taffet, G.E., and Capetanaki, Y. (2004b). Bcl-2 overexpression corrects mitochondrial defects and ameliorates inherited desmin null cardiomyopathy. Proc Natl Acad Sci U S A 101, 769-774.

Weitzer, G., Milner, D.J., Kim, J.U., Bradley, A., and Capetanaki, Y. (1995). Cytoskeletal control of myogenesis: a desmin null mutation blocks the myogenic pathway during embryonic stem cell differentiation. Dev Biol 172, 422-439.

Windoffer, R., Beil, M., Magin, T.M., and Leube, R.E. (2011) Cytoskeleton in motion: the dynamics of keratin intermediate filaments in epithelia. J Cell Biol 194, 669-678.

Winter, D.L., Paulin, D., Mericskay, M., and Li, Z. (2014). Posttranslational modifications of desmin and their implication in biological processes and pathologies. Histochem Cell Biol 141, 1-16.

Winter, L., and Wiche, G. (2013). The many faces of plectin and plectinopathies: pathology and mechanisms. Acta Neuropathol 125, 77-93.

Wong, K.A., Wilson, J., Russo, A., Wang, L., Okur, M.N., Wang, X., Martin, N.P., Scappini, E., Carnegie, G.K., and O'Bryan, J.P. (2012). Intersectin (ITSN) family of scaffolds function as molecular hubs in protein interaction networks. PLoS One 7, e36023.

Yamada, K., Nomura, N., Yamano, A., Yamada, Y., and Wakamatsu, N. (2012). Identification and characterization of splicing variants of PLEKHA5 (Plekha5) during brain development. Gene 492, 270-275.

Zheng, Q., Su, H., Ranek, M.J., and Wang, X. (2011). Autophagy and p62 in cardiac proteinopathy. Circ Res 109, 296-308.

Zou, Y., and Zhong, W. (2012). A likely role for a novel PH-domain containing protein, PEPP2, in connecting membrane and cytoskeleton. Biocell 36, 127-132.

Malformation	Locus	Mutated gene	Studied in zebrafish
Hemangioma	5q31–33	?	
Arterial malformations			
Ehlers-Danlos syndrom	2q31	COL31A	
Venous malformations			
Cutaneomucosal venous malformation	9p21	TIE2 (TEK)	**
Glomuvenous malformation	1p21–22	GLOMULIN	
Blue rubber bleb nevus syndrome	?	?	
Maffucci syndrome	?	?	
Klippel-Trenaunay syndrome	?	?	
Capillary and small vessels malformations			
Capillary malformation-arteriovenous malformation	5q13–22	RASA1	
Hereditary capillary malformation	?	?	
Hyperkeratotic cutaneous capillary-venous malformation	7q11–22	CCM1 (KR1T1)	**
Arteriovenous malformation	?	?	
PTEN hamartoma syndrome	10q23	PTEN	**
Hereditary hemorrhagic telangiectasia (HHT or Rendu-Osler-Weber syndrome)	9q33–34	Endoglin (ENG)	**
Hereditary hemorrhagic telangiectasia	12q11–14	ALK1 (acvrl1)	**
Hereditary hemorrhagic telangiectasia	5q	?	
Hereditary hemorrhagic telangiectasia	7p14	?	
Hereditary hemorrhagic telangiectasia	3p22	?	
Juvenile polyposis/HHT syndrome	18q21.1	SMAD4	*
Progressive patchy capillary malformation (angioma serpinosum)	Xp11.3–q12	?	
Ataxia-telangiectasia	11q23	ATM	*
Cerebrovascular diseases			
Cutis Marmorata Telangiectatica Congenita	?	?	
Macrocephaly Cutis Marmorata	?	?	
Cerebral cavernous (or capillary) malformation	7q11–22	CCM1 (KR1T1)	**
Cerebral cavernous (or capillary) malformation	7p13	CCM2 (Malcavernin)	**
Cerebral cavernous (or capillary) malformation	3q26.1	CCM3 (PDCD10)	**
Cerebral cavernous (or capillary) malformation	3q26.3–27.2	?	
Cerebral autosomal-dominant arteriopathy with subcortical infarcts and leukoencephalopathy (CADASIL)	19p13.2–13.1	Notch3	**
Moyamoya disease	Xq28	BRCC3	**

Table 3: Inherited human vascular diseases and associated genes.

Adapted from Brouillard et al., 2007 and Tille et al., 2004. * studied in zebrafish in another context, ** studied in zebrafish in the context of vascular disease.

III/ Zebrafish as a model of vasculopathy: example of arterial hypertension and pulmonary veno-occlusive disease (PVOD)

A. Human vasculopathies and genetic involvement

Vascular diseases include any condition that affects the circulatory system. It ranges from diseases of arteries, veins and lymph vessels to blood disorders that affect circulation. In the current study, we will focus only on the diseases of the blood vessels and exclude lymphatic vessel diseases and lymphatic system description.

The most current pathology corresponding to blood vessel related vascular diseases include:

- Peripheral Artery Disease, which is a common circulatory problem in which narrowed arteries reduce blood flow to the limbs. It is mostly linked with arteriosclerosis corresponding to the build-up of fat and cholesterol deposits, called plaque, on the inside wall of vessels. This condition results in ischemia, defined as a restriction in blood income in the tissues and leading to a deprivation in oxygen and nutriments. When this happens in the coronary arteries, it leads to the symptoms of chest pain (angina) or to a heart attack. Blockage in the carotid arteries can lead to a transient ischemic attack or stroke and blockage in the renal arteries causes a renal artery disease or stenosis.
- Aneurysm, which is an abnormal blood-filled bulge structure in the wall of a blood vessel. Aneurysms can form in any blood vessel, but they occur most commonly in the aorta (aortic aneurysm). The rupture of an aneurysm can lead to bleeding and subsequent hypovolemic shock.
- Peripheral venous disease, corresponding to the pooling of blood and swelling in the vein in response to damaged valves within a vein (e.g. varicose veins) or to venous blood clot formation. Venous blood clots can lead to deep vein thrombosis, chronic venous insufficiency and pulmonary embolism.
- Arterial hyper- and hypo-tension (see detailed description in paragraph III.B.1).

Most vascular diseases are the consequence of environmental factors like pathogens, oxidized LDL particles, cigarette smoking and other inflammatory stimuli. Nevertheless, a small number of pathologies are reminiscent of congenital defects and develop progressively in the patient. Even if sporadic cases are the most common, genetic studies in human have revealed a number of heretofore unsuspected gene candidates involved in the development of familial vascular anomalies. Hereditary genetic diseases were reviewed in Tille et al., 2004 and Brouillard et al., 2007 and were summarized in Table 3. They are divided into two functional groups: vascular tumors (mainly the hemangiomas, of unknown etiology) and vascular malformations classified according to the type of vessel or organs they affect.

B. Arterial hypertension

1) General description of arterial hypertension

Arterial blood pressure is highly controlled to maintain adequate tissue perfusion. Blood pressure can be modeled with the Ohm's law: blood pressure depends on both blood flow, determined by cardiac output and total blood volume and resistance and on the vessel's diameter and therefore on the contractile state of smooth muscle cells surrounding the arteries and arterioles. Blood flow regulation mechanisms are acting on these different parameters and include interactions, compensation mechanisms and feedback regulation loops between each other. Baroreflexes and vasoactive hormones permit short-term regulation of blood pressure. In particular, β-adrenergic neurotransmitters contribute to the short term overall balance between vasoconstriction and vasodilation of arterioles. Long-term regulation is principally achieved through the renal fluid volume regulation mechanism, as the total blood volume depends on the extracellular fluid volume, which is controlled by kidney activity and tightly linked with the total body sodium level (Bolivar, 2013). In parallel, the renin-angiotensin-aldosterine system is an endocrine system which directly controls vasodilation of arterioles in response to water/sodium homeostasis in the kidney (Moon et al., 2013). Defects in this regulation lead to hyper- or hypotension.

Arterial hypertension is the most important risk factor for premature death worldwide (Lim et al., 2010). It is a chronic medical condition in which the blood pressure in the arteries is elevated. For adult patients, hypertension is defined by pressure measurements above 140/90 mmHg, with normal measurements being 100–140mmHg for the systolic pressure and 60–90mmHg for the diastolic pressure. 90–95% of hypertension cases are categorized as primary hypertension which consists of high blood pressure with no obvious underlying medical cause. The remaining 5–10% of cases are referred to as secondary hypertension and are caused by other conditions that affect the kidneys, arteries, heart or endocrine system.

Carotid arteries (irrigating the brain), coronary arteries of the myocardium, renal and lower limb arteries are the most frequently affected by hypertension. Hypertension increases the risk of a large range of cardiovascular diseases, including ischemic heart disease and strokes, peripheral vascular disease, heart failure, aortic aneurysms, diffuse atherosclerosis and pulmonary embolism. Hypertension is also a risk factor for cognitive impairment, dementia and chronic kidney disease. Other complications include hypertensive retinopathy and hypertensive nephropathy. Moreover, the arterial pressure induces compensation mechanisms indirectly increasing heart activity in order to maintain a constant blood flow, leading to left ventricular hypertrophy and progressive contraction impairment often linked with heart failure. These numerous complications are mostly due to long term consequences of hypertension on different organs. Only rare cases of rapid increase in arterial pressure are reported. They lead to sudden weakness, violent headache or respiratory insufficiency and require a rapid care.

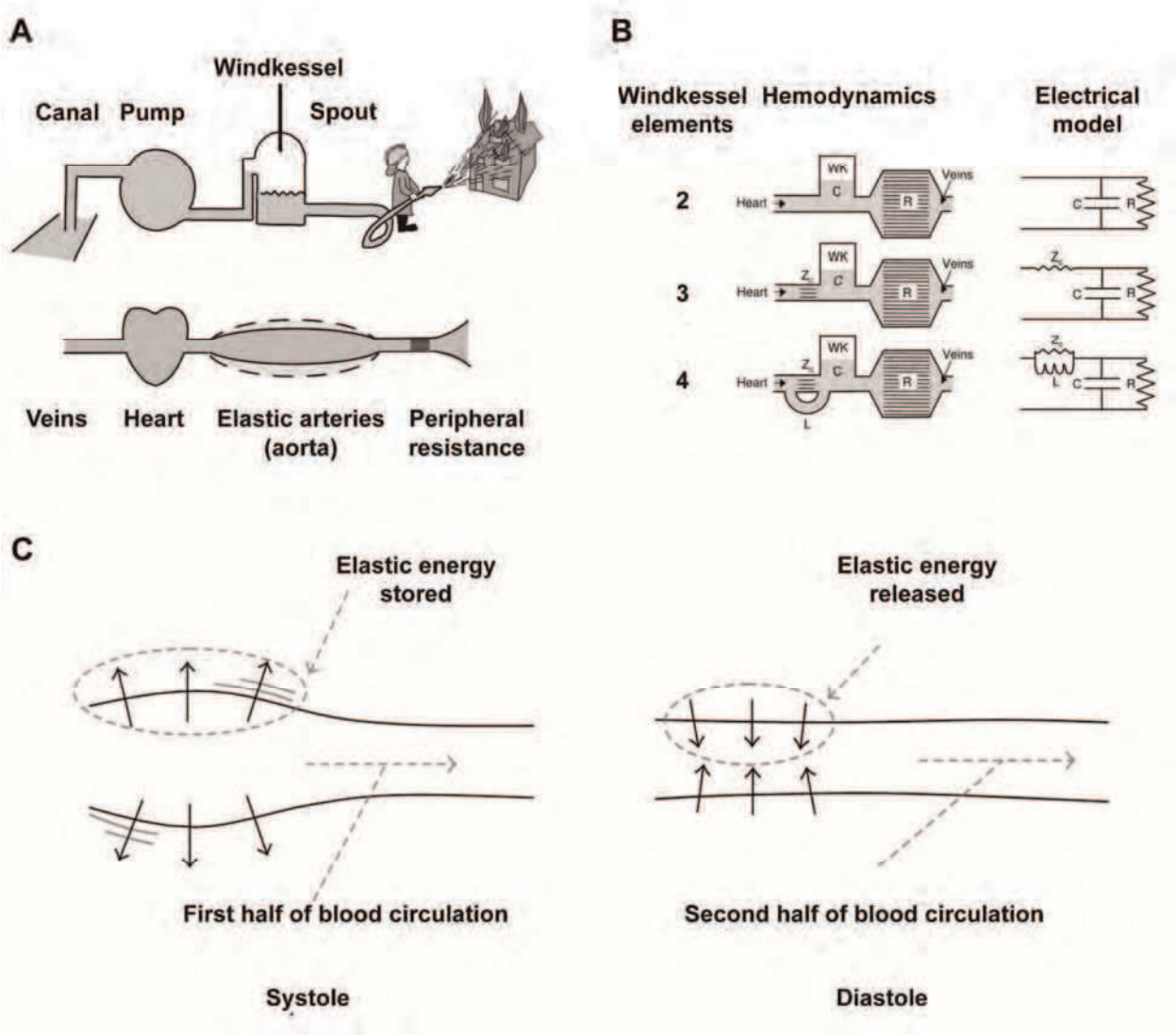

Figure 12: The Windkessel effect modelling the effect of arterial stiffness in hypertension

(A) Adapted from Westerhof et al., 2009. The "Windkessel" corresponds to an air reservoir of mechanical engines, which will enable the effect of a pump to be buffered. This is analogous to the situation in the circulatory system where the heart corresponds to the pump, the capillaries and their peripheral resistance to the final spout and the elastic arteries as the buffering Windkessel. Together, it results in a constant peripheral flow, while the pumped flow is pulsative. (B) Adapted from Westerhof et al., 2009. The two-, three- and four- elements Windkessel are represented by a hydrolic circuit and modeled by an electric circuit. R is the resistance, C the compliance (or capacitance) and Zc is the aortic characteristic impedance, which connects the Windkessel model with wave transmission models. (C) Adapted from Roy et al., 2012. Result of the Windkessel effect on the aorta. During systole, the high energy accompanying high blood pressure will be absorbed and stored by the elastic aorta. Once this first phase of high blood pressure is over, the stored energy is released and pressurizes the low pressure diastolic blood flow to equilibrate the pressure levels. This is not possible in the presence of a stiff artery, which leads to further vascular remodeling and hypertension.

Many factors were shown to favor hypertension. They include age, diabetes, obesity, hypercholesterolemia, pregnancy, elevated dietary sodium intake, chronic mental stress, tobacco smoking, alcohol consumption, lack of physical exercise etc.

2) Arterial stiffening and calcification

Primary hypertension was linked predominantly with arterial stiffening, in particular in cases of appearance with age (Martins et al., 2011). Arterial stiffening (AS) is a natural phenomenon with aging, but it is exacerbated by the presence of cardiovascular risk factors and can be either a cause or a consequence of arterial hypertension. Using arterial tonometry, aortic ultrasound, carotid ultrasound or magnetic resonance imaging, AS is becoming more and more frequently used as a tissue biomarker of cardiovascular disease risk in patients. It can be explained by an increase of the collagen/elastin ratio due to elastin fragmentation. Elastin fragmentation is further intensified in the presence of arteriosclerosis.

Arterial calcification (AC) represents a major covariate of AS. AC is an active process, implying a variety of genes implicated in mineral and bone metabolism, leading to the differentiation of vascular smooth muscles cells (VSMC) and pericytes into “osteoblast-like” cells. This metabolic cascade is triggered by inflammation, which promotes calcification by activating Bmp, Msx2 and Wnt signaling associated with osteochondrogenic conversion, elastolysis and degradation of the extracellular matrix (London et al., 2013).

AS and AC lead particularly to an increase of the systolic pressure, leading to an increase of wall stress and cardiac workload, which triggers adaptive mechanisms, including left ventricle hypertrophy. The importance of arterial elasticity in the efficient transfer of blood flow from the heart to organs, and in particular for the transformation of the flow from a pulsatile to a steady pattern, is clearly established (Hales, 1735). The pressure buffering role of arteries was then modeled by the so-called Windkessel model (Westerhof et al., 2009).

3) The Windkessel model

The elasticity of arteries was described in 1735, when Hales first measured arterial blood pressure and realized it was not constant from the more cardiac extremity to the extremity close to capillaries. In 1899, Frank proposed the establishment of a model of arteries, in which they are characterized using two of their physical parameters: their resistance and their compliance. This gave birth to the so-called two-element Windkessel model (Frank, 1899). This Windkessel model, meaning “air chamber” in German, compares the heart to an engine pumping system, the peripheral resistance to a spout and the arteries to an elastic reservoir (Figure 12). It then reflects the property of arteries to use their elasticity to generate a steady flow from the pulsatile flow coming out of the cardiac pump.

It was shown that the resistance of a vessel is inversely proportional to its radius to the fourth power (Poiseuille law, 1838). The resistance of the global arterial system can be estimated as the sum of the resistances of the smaller vessels, in which low radius triggers the highest resistance. The compliance is defined as the ratio between a volume change and the resulting pressure change (Wersterhof et al., 2009). The two-element model, implemented with these parameters, presents the arteries as a capacitor and predicts the decay of the diastolic pressure as exponential.

Further adjustments of the model were proposed progressively in relation to new discoveries enabling a better understanding of hemodynamics. The three-element Windkessel model was first proposed in 1956 (Wetterer, 1956) and included impedance of the main proximal artery. Impedance corresponds to a measure of the resistance of a structure to motion, when subjected to a harmonic force, and depends on the speed and density of the fluid and the cross sectional area of the artery. Adding this parameter complements the model with a wave transmission characteristic and reflects the presence of a time delay between pressure and flow curves. The four-element Windkessel (Stergiopulos et al., 1999) proposes an additional pressure difference (inertance) as a fourth parameter in the model to help understand the high frequency range of the system. Inertance is a measure of the pressure difference in a fluid required to cause a change in flow-rate with time and depends on the density of the fluid, the length of the vessel and its cross section (Westerhof at al., 2009).
The Windkessel model was used in the context of arterial hypertension in order to estimate arterial stiffness, load on the heart, cardiac output and left-ventricle overload. It was also used in the modelling and testing of artificial hearts and valves (Westerhof at al., 2009).

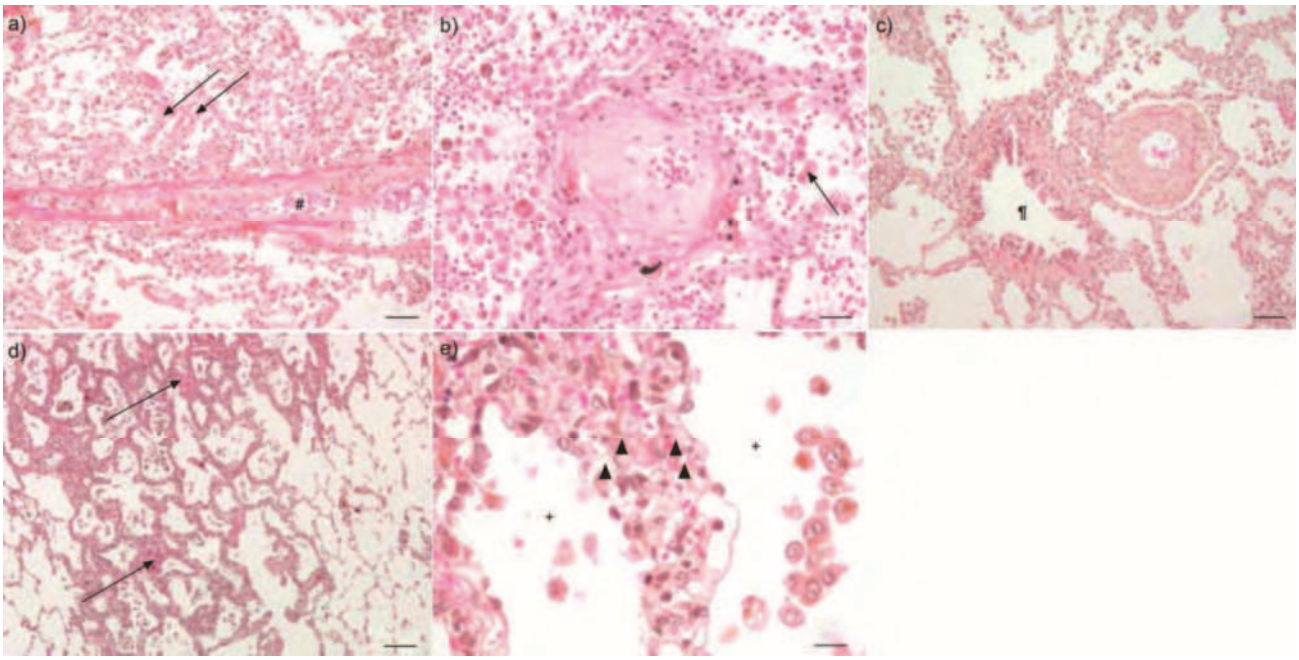

Figure 13: Pulmonary vascular lesions in a patient suffering from pulmonary veno-occlusive disease

From Montani et al., 2009. Lung histology from patient with PVOD showed by haematoxylin–eosin–saffron staining. a) Fibrous obstruction of a septal vein (#) and pre-septal venules (arrows). b) Pre-septal venule with occlusive remodelling. Note the intra-alveolar haemorrhage and siderin-laden macrophages (arrow). c) Muscular artery presenting with marked intimal fibrosis and adjacent bronchiole ("). d) Patchy thickening of alveolar septa in the presence of occlusive microvessels (arrows). e) Alveolar septum displaying capillary proliferation. Note the multi-layered lumen (arrowheads) separating two alveoli (+). a) and c) Scale bar=5100 mm; b) scale bar=550 mm; d) scale bar=5200 mm; e) scale bar=525 mm.

C. PVOD and association with GCN2 (EIF2AK4) mutation

1) PVOD is a rare case of pulmonary hypertension

Pulmonary hypertension is a rare, progressive disease which is defined as an increase in blood pressure in pulmonary arteries, veins or capillaries, leading to endothelial cell dysfunction and remodeling of lung vasculature. It is triggered by a large range of causes, including genetic and environmental causes, congenital malformations and apparition as a secondary manifestation of a pathology (HIV, cardiovascular disease etc.). Clinical signs include shortness of breath, dizziness, fainting, angina pectoris and leg swelling and can result in heart failure. Current classification splits pulmonary hypertension into six groups, namely pulmonary arterial hypertension (PAH), pulmonary veno-occlusive disease (PVOD) and/or pulmonary capillary hemangiomatosis (PCH), pulmonary hypertension owing to left heart disease, pulmonary hypertension owing to lung disease and/or hypoxia, chronic thromboembolic pulmonary hypertension and pulmonary hypertension with unclear multifactorial mechanisms (Simonneau et al., 2009).

PVOD and PCH form a sub-group (I') and are considered as rare and uncommon forms of PAH or group I pulmonary hypertension. PAH is a progressive and fatal disease characterized by an inappropriate elevation of pressure (considered pathologic when above 25mmHg) specifically in the small arteries and arterioles of the lung while the pressure in the lung capillaries is normal (lower than 15mmHg). This triggers progressive neointimal proliferation, smooth muscle cell hypertrophy and adventitial expansion leading to occlusions of the smallest vessels (Austin et al., 2014). PAH are divided in three groups containing respectively heritable PAH (linked with *BMPR2* or *ALK1* mutations for example), idiopathic PAH and PAH related to a variety of other systemic diseases or to toxin exposure. Clinically, the presence of PAH is assessed by invasive measurement of mean pulmonary pressure through right heart catherization.

2) PVOD characteristics

PVOD and PCH are difficult to distinguish from another. Some theories even postulate that they are two slightly different manifestations of the same disease (Austin et al., 2014). They are also difficult to distinguish from PAH, sharing many clinico-pathological characteristics (Palazzini et al., 2009), explaining why they were categorized as a subgroup of PAH in pulmonary hypertension classification.
PVOD is a rare and extremely severe cause of pulmonary hypertension. It presents either sporadically, or as familial cases with a recessive mode of transmission. Pathological hallmarks of PVOD consist in obliterative fibrotic vasculopathy of the smaller branches of the pulmonary venous vasculature. It is characterized histologically by a widespread collagen-rich fibrous intimal proliferation in septal veins and pre-septal venules and hypertrophy of VSMC causing a thickening of the lung venous vascular walls, frequently associated with pulmonary capillary dilatation and proliferation (Figure 13). Affected vessels therefore develop an arterialized appearance over time (explaining the difficulty of diagnostic), become progressively fully occluded and may present thrombosis. A significant

remodeling of capillaries and small arteries is often observed as well. Typical PVOD symptoms include progressive dysnoea, fatigue, dizziness, palpitations and chest discomfort worsened by exercise. Pulmonary haemodynamics are equivalent to those observed in PAH, with arterial pressure higher than 25mmHg and capillary pressure around 15mmHg or less. The chronically elevated pressure in a patient's lung inevitably triggers right ventricular dysfunction, which is generally the cause of the patient's death. PVOD remains poorly understood, both in term of its clinical manifestation and its mechanism and is often diagnosed late. The life expectancy therefore does not exceed 2 years after diagnosis (Montani et al., 2010).

Sporadic PVOD develops in particular as a complication in patients with connective tissue disease (CTD). They include, in particular, systemic sclerosis (an autoimmune disease causing a progressive fibrosis of skin and internal organs), systemic lupus erythematosus (a systemic autoimmune disease involving skin, pericardium, kidney and nervous system) and mixed CTD (a multisystem disorder, regrouping clinical features of both previously mentioned diseases and polymyositis). In all these cases, lung parenchymal involvement with severe pulmonary hypertension including PVOD can develop as a consequence of interstitial pulmonary fibrosis. A number of PVOD cases have also been reported in patients with several other inflammatory diseases like sarcoidosis and chronic active hepatitis. Other potential risk factors include exposure to various cytotoxic agents, peripheral blood cell transplantation, bone marrow transplantation, solid organ transplantation and radiotherapy (O'Callaghan et al., 2011). Genetic causes include several mutations of the *BMPR2* gene (Runo et al., 2003), implicated in genetic PAH as well and mutations in *General control nonderepressible 2* (*GCN2)* (Eyries et al., 2014).

Aetiology of PVOD is unknown and its study is challenging because its causes and disease associations are difficult to distinguish. It is likely that the disease pathogenesis is multifactorial and includes the presence of an early endothelial injury and the intervention of aberrant repair mechanism, leading to widespread fibrosis of the microvasculature (Montani et al., 2010).

In the past decades, advances in PAH therapeutics have led to the development of drugs acting on several targets and ameliorating patient's pathological conditions. Nevertheless, most of them cannot be applied for the treatment of PVOD and even often worsen this pathology. Therefore, there is an urgent need for understanding of PVOD and for development of novel specific treatments (O'Callaghan et al., 2011). Currently, the only potential life-saving intervention proposed to patients is orthopic lung transplantation.

3) GCN2 mutation as a cause of PVOD

Eukaryotic Translation Initiation Factor 2 Alpha Kinase 4 (EIF2AK4) is a serine-threonine kinase also called GCN2 and was recently identified in two separate WES studies as a genetic cause of PVOD (Eyries et al., 2014) and PCH (Best et al., 2014). Both studies contained several un-related families presenting either PVOD or PCH and found mutations in the *EIF2AK4* gene segregating with the

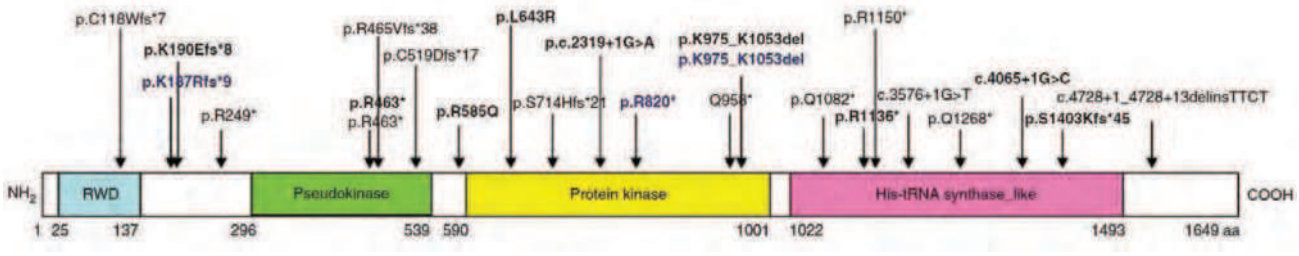

Figure 14: EIF2AK4 mutation leading to PVOD in patients

From Eyries et al., 2014. The locations and consequences of the recessive mutations in patients with familial PVOD (black) or sporadic PVOD (blue) are shown on a schematic of the EIF2AK4 protein. Mutations found in a homozygous state are shown in bold; the other mutations were found in a heterozygous state. For non-synonymous and frameshift mutations, the protein effects are shown, and for splicing variants, the nucleotide changes are indicated. In the figure, amino acids are indicated by their one-letter abbreviations.

disease with an autosomal recessive inheritance. Moreover, *EIF2AK4* biallelic mutations were identified in PVOD and PCH patients without familial history.

In particular, our collaborators (Prof. Florent Soubrier, La Pitié Salpetrière, Paris) focused their study on PVOD patients, studying 13 families and 20 sporadic cases of PVOD (Eyries et al., 2014). Biallelic mutation in the *EIF2AK4* gene was found in all the studied families and in 25% of the sporadic cases either at homozygous or compound heterozygous state. They identified a total of 22 pathological mutations in the *EIF2AK4* gene (Figure 14).

Despite the difficulty in assessing the penetrance of the gene mutation due to the low number of patients studied and the difficulty of diagnostic between PVOD, PCH and even PAH, *EIF2AK4* seems to be the major gene responsible for PVOD development, and its mutation significantly contributes towards understanding the complex genetic architecture of pulmonary hypertension.

4) GCN2

EIF2AK4 (GCN2) is present in all eukaryotes and encodes a serine-threonine kinase. It consists in the main sensor of amino acid (aa) availability and can induce the activation of the aa response (AAR) signal transduction pathway in the cell, in response to aa deprivation. EIF2AK4 belongs to a family of four kinases which phosphorylate the α-subunit (eIF2α) of the eukaryotic translation initiation factor 2 (eIF2) (Donnelly et al., 2013) (Figure 15). eIF2 functions by directing the binding of initiator methionyl-tRNA to 40S ribosomal subunits in the specific context of the translation of a small number of mRNAs. This results in increased translation of the transcription factors ATF4 (CREB-2) and CHOP detrimentally to decreased global translation in the cell.

Interestingly, it was recently shown that GCN2 induction in dendritic cells was responsible for a better immunization by vaccination. Activated macrophages express indoleamine 2,3-dioxygenase (IDO) which decreases tryptophan levels in dendritic cells and consequently activates GCN2. GCN2 triggers activation of the aa deprivation pathway, induction of autophagy in dendritic cells and increased antigen presentation to both CD4+ and CD8+ T cells (Ravindran et al., 2014).

A *GCN2*-null mouse model was already described, is viable and has apparent normal longevity, although they display several abnormalities. They showed no decrease in protein translation in the liver and died in a high proportion (8/20) within 6 days of a leucine-deficient diet, showing the importance of GCN2 in the aa deprivation response (Anthony et al., 2004). The expression of ATF4 was shown to be reduced as expected in the hippocampus of *GCN2*$^{-/-}$ mice (Costa-Mattioli et al., 2005). *GCN2*$^{-/-}$ mice show an increase in protein carbonylation, a marker of oxidative stress which is an important factor for pulmonary hypertension development when fed with a leucine-imbalanced diet during 3 weeks (Chaveroux et al., 2011). They also display a deficient immune system when treated with asparaginase which mimics aa starvation (Bunpo et al., 2010).

More recently, GCN2$^{-/-}$ mice were studied in the context of transverse aortic constriction (TAC) (Lu et al., 2014). In basal conditions, *GCN2*$^{-/-}$ mice did not exhibit abnormal cardiovascular functions and lungs were apparently normal. After TAC surgery, *GCN2*$^{-/-}$ mice showed less heart contractile dysfunction, less increase in lung weight, less increase in lung inflammation and vascular remodeling,

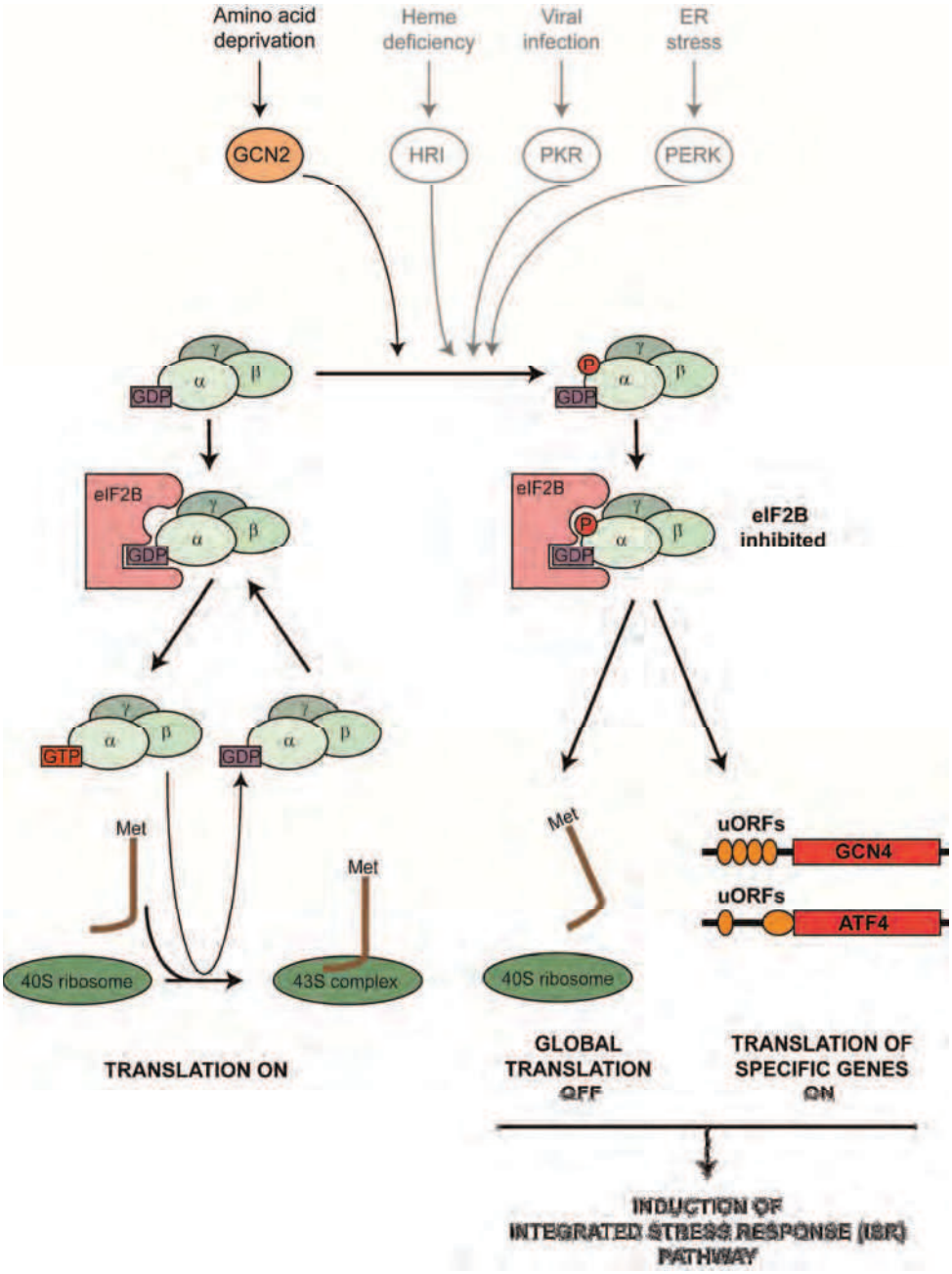

Figure 15: Implication of GCN2 (EIF2AKA) in the induction of the integrated stress response pathway (ISR)

Like all eIF2α kinases, GCN2 acts by phosphorylating specific amino acids on the α-subunit of eIF2 (eIF2α). Other parallel phosphorylation of eIF2α occurs in the context endoplasmic reticulum (ER) stress (by protein kinase-like ER kinase (PERK)), viral injection (by the double-stranded RNA-activated protein kinase (PKR)) and heme deficiency (by the heme-regulated inhibitor kinase (HRI) upstream of eIF2α). eIF2, in a GTP bound form, is essential for the delivery of the Met-tRNA to the 40S subunit of the ribosome for translation initiation. After the binding of the 4SS ribosomal complex (40S unit + Met-tRNA), eIF2 is released in a GDP bound form and requires recycling by the guanine nucleotide exchange factor eIF2B. Phosphorylation of eIF2α by GCN2 converts eIF2 to a competitive inhibitor of eIF2B, leading to the absence of functional eIF2, reduction of the global translation machinery and specific translation of mRNAs containing a upstream open reading frame in their 5'UTR region. This is the case for the mRNA of ATF4.

and less myocardial apoptosis and fibrosis compared to wild-type mice, despite an equivalent degree of left ventricular hypertrophy. Marked effects on the apoptosis pathway were also observed since the expression of the anti-apoptotic Bcl2 was significantly increased in *GCN2* deficient hearts, an effect which was reproduced in cultured neonatal cardiomyocytes with a *GCN2* KD.

It was proposed that GCN2 involvement in PVOD could either be directly related to its aa starvation sensor function and subsequent translational and transcriptional changes downstream of its activation of eIF2α or related to its kinase activity which might have substrates other than eIF2α, as also suggested (Eyries et al., 2014). Since the role of immunity in the pathological process of pulmonary hypertension is considered of major importance (El Chami et al., 2012), GCN2-mediated increased antigen presentation could be another potential candidate for PVOD mechanism although these results would favor a beneficial effect of GCN2 deficiency.

5) Hypothetical implication of eIF2α phosphorylation and ATF4 downstream of GCN2 in the establishment of PVOD

Phosphorylation of eIF2α constitutes a signalization “hub” since different pathways converge towards this step. Indeed, the unfolded response pathway to the endoplasmic reticulum (ER) stress involves eIF2 phosphorylation by protein kinase-like ER kinase (PERK), viral injection triggers phosphorylation by the double-stranded RNA-activated protein kinase (PKR) and heme deficiency implicates the heme-regulated inhibitor kinase (HRI) upstream of eIF2α. eIF2α phosphorylation inactivates eIF2 and leads to decreased global translation in the cell and induction of ATF4 (CREB-2) and CHOP translation, which in turn induces transcription of ATF5 and the phosphatase DNA damage-inducible 34 (GADD34) among other target genes (Donnelly et al., 2013).

ATF4 represents the major signal transmitter of the so-called Integrate Stress Response (ISR), occurring in response of aa or heme deficiency, ER stress and viral infection. eIF2-mediated ATF4 translational activation induces or inhibits the transcription of several target genes, through ATF4 binding to specific response elements in their promoters. These response elements are called CCAAT-enhancer binding protein (C/EBP) activating transcription factor response elements (or CARE) or AAR Element in the context of aa deprivation. They have a 9 bp core element, variable by one or two nucleotides between genes and composed of two half-sites: an ATF4 binding site and a C/EBP binding site (Chen et al., 2004).

Thus, ATF4 can form heterodimers with different partners that will bind the C/EBP half-site enabling the specificity of binding. Activation of ATF4 target genes triggers ISR remodeling, including major phenotypical changes in the cell like angiogenesis properties and resistance to oxidative stress (Harding et al., 2003). In particular, several target genes of ATF4 have been identified such as C/EBP homology protein (CHOP) (Kilberg et al., 2009) or VEGF (Chen et al., 2004). ATF4 and CHOP cooperate to induce the transcription of genes such as TRB3 which modulates BMP signaling, an important pathway for PAH development (Kilberg et al., 2009, Carraro et al., 2010).

Moreover eIF2α phosphorylation causes induction of DNA-damage-inducible transcript 4 protein (DDIT4) (or REDD1) expression in an ATF4 dependent manner (Whitney et al., 2009), which in turn suppresses mTOR activity and triggers stress-induced expression of autophagy genes (B'Chir et al., 2013).

Under oxidative stress, ATF4 has been shown to induce VEGF transcription (Roybal et al., 2005). Through ATF4-induced expression of CHOP, the pro-apoptotic Bcl-2 homology 3-only member PUMA is increased and the anti-apoptotic BCL2 expression is inhibited. Bone angiogenesis has been studied in *ATF4*$^{-/-}$ mice, where reduced bone microvascular density was associated with decreased expression of HIF1α and VEGF, showing that ATF4 is a key regulator of VEGF in a local bone environment. This contributes to increased bone angiogenesis. Reduced endothelial sprouting was rescued by VEGF but not by FGF (Zhu et al., 2013). *ATF4*$^{+/-}$ mice display reduced neovascularization of the retina in an oxygen-induced retinopathy model (Wang et al., 2013). Several changes in angiogenesis gene expression, such as HIF1α and *VEGF-A/FLT1*, were observed but the heterozygous ablation of the *ATF4* gene makes it difficult to interpret these results, since counter-regulatory mechanisms may lead to misinterpretation of the actual gene interactions.

Therefore, from available results, it can be deduced that the eIF2/ATF4 pathway regulates key angiogenic factors and mediators of apoptosis, but integrating these results in a working hypothesis on the development of PVOD is not feasible at this stage.

Objectives

As suggested in my introduction, the studies of the described diseases: desminopathy, arterial hypertension and PVOD, leave a certain number of open questions. In particular, their study reaches a point where there is a need of a new model:

- to bridge studies from the filament to the organism level, in the case of desminopathy,
- for direct live imaging of the blood flow and its impact on the artery deformation, in the context of arterial hypertension,
- for a quick validation of the implication of GCN2 in venous specific phenotypes observed in PVOD.

Zebrafish advantages were reviewed in the present introduction. It is a powerful model, which fits nicely these needs. The main goal of my PhD thesis was then to validate the use of zebrafish for arterial hypertension modelling and to generate and characterize novel disease models of desminopathy and PVOD.

While doing so, we aimed to optimize the use of cutting edge techniques (correlative light and electron microscopy (CLEM), second harmonic generation (SHG), 4D reconstruction of beating heart, live Ca^{2+} imaging, etc.), which were previously used almost exclusively in the context of developmental biology studies, for disease modeling in the zebrafish embryo.

Furthermore, these studies were included into large collaborative projects. The desminopathy project was designed as a test project and optimization step for the construction of a pipeline from the validation of myopathy patients WGS/WES candidate genes to the realization of high-throughput drug screens in zebrafish models. The PVOD project is part of a collaborative project for the validation and the characterization of the implication of GCN2 in venous-specific lung phenotypes, based on a multi-model (mice, zebrafish and cultured cells) comparison.

Specific aims of each project will be detailed as a forword to the corresponding results presentation.

Results

Chapter I

Characterizing novel zebrafish models for new insights into desmin function and aggregation in desminopathies

Foreword

To study desmin function in normal and pathological desminopathy conditions, several types of model were developed. First, the biomechanical properties of desmin filaments were analyzed using atomic force microscopy and scanning force microscopy *in vitro* on isolated filaments (Kiss, et al.,2006, Kiss, et al.,2011). Aggregation properties of human desmin mutants were extensively studied *in vitro* (Bar et al., 2005) and in cell models (often transfected in muscular cells) (Brodehl et al., 2011). Most of the characterized patient mutations were subjected to these tests and this helped to characterize several patients aggregates (Bar et al., 2010). Finally, several mouse models have been generated, including mouse KO to assess desmin function and some DRM and DRCM aggregate presenting models for a better understanding of the physiopathology of desminopathies (see Manuscript 1 above, for a review of desmin loss and desminopathy animal models) (Figure 16).
Nevertheless, there is an obvious need to study these different aspects *in vivo* and to confront the knowledge gathered *in vitro,* in an animal model. Implication of desmin biomechanics in muscle contraction patterns and resistance to stretch are still poorly explored *in vivo*. Moreover, the contractile muscular system is mechanically active, thereby generating a dynamic environment. Thus there is a need for studies in live conditions, in a comparable dynamic environment. Indeed, many of desmin functions (as well as other IF proteins) remain to be tested in a mechanically active environment in order to conclude about the origins of the defects observed in the described desmin-related myopathies. Importantly, previous models were not helpful to address desmin aggregation impact on different cellular processes due to the lack of approaches permitting direct visualization of contraction, in particular in the heart over time, *in vivo* and at high temporal and spatial resolution. Therefore, we analysed a model of desminopathy in zebrafish, which is a suitable model for studies from the filament to the organism level in live dynamic conditions.

Moreover, an open question in the field concerns the implication of desmin aggregates in desminopathy phenotypes. Indeed, the lack of functional desmin leads to some clinical signs comparable to what was observed in patients and could be implicated, to a large extent, to the establishment of desminopathy phenotypes (Li et al., 1996; Milner et al., 1996). On the other hand, aggregates can have a toxic effect on muscle cells and trigger specific cell responses that could be detrimental to the cell integrity. In particular, protein quality control pathways were shown to be perturbed in presence of desmin aggregates including increased autophagy (Zheng et al., 2011) and impaired proteasome response (Liu et al., 2005).

To date, patient suffering from desminopathies are treated by lowering secondary effects and related pain but no drug is available to treat the causes of the disease (Clemen et al., 2013). Our assumption is that a novel animal model that can be easily subjected to new drugs testing through high-throughput drug screening could be useful to develop new drugs. Moreover, approaches for screening potential drugs affecting or correcting desmin malfunction have not yet been performed *in vivo* and in a

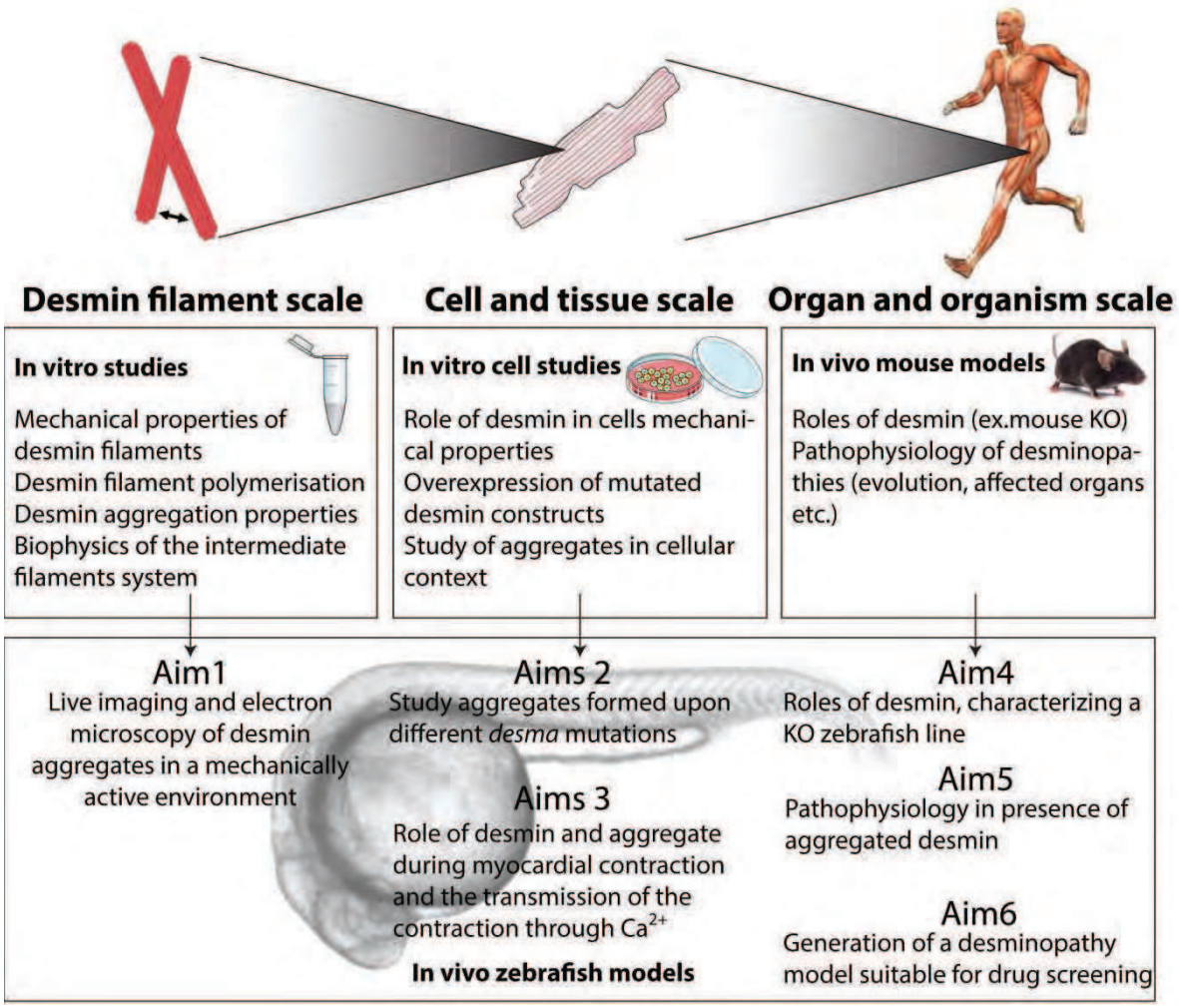

Figure 16: Aims of the « Desminopathy in zebrafish » project

The whole scale, from the filament properties to the patient physiopathology, has been previously studied in different systems, including *in vitro* studies, cell and mouse models. We proposed to study these different aspects in a single model, zebrafish, to allow a multiscale analysis of desminopathies and a better understanding of crucial aspects that still remain poorly understood in the field. Our specific aims are shown in this figure.

mechanically active context. A requirement for such a model is a clear label of aggregation. Moreover, the demonstration that desmin aggregation reduction is feasible is necessary.

In consequence, our major aims for this project have consisted of:

- Generating a desminopathy model in zebrafish amenable for live imaging of the aggregates formation and development in live animals,
- Addressing the mutations specificities in terms of shape, structure, localization and evolution of aggregates formed from different desmin mutations, in particular by using a combination between live confocal and electron microcopy,
- Assessing the influence of desmin aggregates and loss of function at the cellular level and their influence on myocardial muscle contraction and Ca^{2+} propagation,
- Understanding the roles of normal and mutated desmin in zebrafish,
- Addressing the role of desmin aggregates in the establishment of desminopathy skeletal muscle and cardiac phenotype,
- Demonstrating that our model is amenable for high-throughput drug screen.

The main results obtained are presented in the following manuscript. Additional results concerning the implementation of a drug screening and a molecular analysis of the desmin mutants are presented in the following section.

Manuscript 2: Developmental alterations in heart biomechanics and skeletal muscle function in desmin mutants suggest an early pathological root for desminopathies

Caroline Ramspacher, Coralie Spiegelhalter, Nadia Messaddeq, Le Trinh, Federico Tessadori, Jeroen Bakkers, Jocelyn Laporte, Karim Hnia, Julien Vermot

(submitted)

Developmental alterations in heart biomechanics and skeletal muscle function in desmin mutants suggest an early pathological root for desminopathies

Caroline Ramspacher[1,2,3,4], Coralie Spiegelhalter[1,2,3,4], Nadia Messaddeq[1,2,3,4], Le Trinh[5], Federico Tessadori[6], Jeroen Bakkers[6], Jocelyn Laporte[1,2,3,4], Karim Hnia[1,2,3,4], Julien Vermot[1,2,3,4,*]

[1]Institut de Génétique et de Biologie Moléculaire et Cellulaire, Illkirch, France
[2]Centre National de la Recherche Scientifique, UMR7104, Illkirch, France
[3]Institut National de la Santé et de la Recherche Médicale, U964, Illkirch, France
[4]Université de Strasbourg, Illkirch, France
[5]Molecular and Computational Biology, University of Southern California, Los Angeles, CA, USA
[6] Hubrecht Institute-KNAW and University Medical Center Utrecht, Utrecht 3584 CT, The Netherlands
* To whom correspondence should be addressed: julien@igbmc.fr

Abstract

Desminopathies are congenital myopathies due to desmin mutations and usually lead to a distinct form of protein aggregate myopathy. To date, the initial pathological steps of desminopathies as well as the impact of desmin aggregates in the genesis of the disease are still unclear. Here we analysed two genetically engineered zebrafish models of desminopathies in order to directly address the effect of desmin aggregate formation in comparison to a desmin loss of function allele during embryonic development. Using live, high-resolution microscopy we show that desmin is essential for embryonic skeletal muscle and cardiovascular functions. We found desmin aggregates promote skeletal muscles defects and contribute to altered heart biomechanics. In addition, we show that calcium dynamics associated with heart contraction are impaired and lead to aberrant blood flow in the vascular network. This defect is associated with the dilatation of the sarcoplasmic reticulum suggesting the involvement of desmin in excitation contraction coupling machinery both in skeletal and cardiac muscle. Finally, we demonstrate that pharmacological inhibition of aggregate formation and decreased desmin expression is beneficial for embryonic skeletal muscle development in this desmin mutant. Together, the combination of genetics with *in vivo* optical mapping techniques identifies an early function for desmin, and shows that desmin aggregation and loss of function can both impact on skeletal and cardiac muscle function. However, our data show that the presence of aggregates and not desmin loss is the main cause of pathological feature in zebrafish models of desminopathies and that decreased desmin level can reduce aggregates formation and concomitantly the pathology. This raises the possibility of novel therapeutic approaches and will help to further understand the molecular determinants modulating desmin aggregates formation.

Author's summary

Proteinopathies comprise diseases involving protein aggregation, such as desminopathies. Pathological desmin aggregation leads to a broad spectrum of defects, such as skeletal muscle and cardiovascular defects. Despite its pivotal role in muscle cell maintenance, the developmental role of desmin is poorly understood and our understanding of the developmental origins of the desminopathy that can trigger these detrimental defects remains incomplete. The zebrafish model presents an excellent system in which to define the developmental function of desmin and the origin of the cellular defects associated with the disease. Thus, we used zebrafish mutants to analyze the role of desmin and the effect of desmin aggregates in skeletal and cardiovascular system development. We found that zebrafish desmin mutant embryos, which survive to adulthood, display defects in heart pumping and early vascular function. At the molecular level, desmin impact the electrical cardiac conduction and regulates the development of the heart contractility. Therefore, our work reveals a broad and early role for desmin in cardiovascular system morphogenesis. Future implications include the use of these zebrafish lines for drug screening targeting desminopathies *in vivo*.

Introduction

Proteinopathies form a group of diseases with well-recognized features mainly hallmarked by protein aggregation. The proteinopathies include neurodegenerative diseases like Parkinson's disease, various forms of dementia and amyotrophic lateral sclerosis. Pathological protein aggregation has also been established in a broad spectrum of muscle diseases comprising congenital myopathies, the group of inclusion body myositis, distal myopathies and certain limb girdle muscular dystrophies. Desminopathies belong to the myofibrillar myopathies and comprise primary Desmin Related Myopathy and Cardiomyopathy (DRM and DRCM). Both DRM and DRCM are characterized by intracellular accumulation of misfolded proteins and the presence of desmin-positive insoluble granulofilamentous aggregates. Desmin-related diseases lead to progressive skeletal muscle weakness, cardiomyopathy and conduction defects [1]. Genetic inheritance is mostly autosomal dominant [2] though sporadic cases of *de novo* mutations [3,4] and recessive transmission [5] have also been reported. The first symptoms of desminopathies in humans generally occur in the third decade, but the disease onset and the rate of progression of desminopathies are highly variable. Interestingly, numerous muscular disorders have been characterized as secondary DRM by the presence of desmin aggregates. They include pathologies linked with mutations in myotubularin (MTM1), Z-band alternatively spliced PDZ-containing protein (ZASP), filamin C (FLNC), Bcl2 associated athanogene-3 (BAG3) and the small heat shock protein αB-crystallin (CRYAB) which specifically leads to DRCM. Most of these proteins directly bind desmin *in vivo*, and altered interaction or absence of these partners in pathological conditions can promote aggregation and accumulation of misfolded desmin [6,7,8,9]. Desmin aggregates form within minutes when overexpressed in cell culture [7]. However, the kinetics of aggregate formation *in vivo* remains unclear and the contribution of these aggregates to developmental defects is still unknown. Thus, understanding the dynamics of desmin aggregation and its impact on muscle function during embryogenesis will help elucidate the developmental defects underlying desminopathies.

Desmin is a muscle-specific type III intermediate filament protein essential for proper muscular function [10,11]. Mutations affecting desmin function or promoting desmin aggregation can promote skeletal or cardiac muscle phenotypes or both. Desmin knockout (KO) mice [10,11] exhibit a loss of lateral alignment of myofibrils from the second week after birth. This phenotype is more severe in the heart and leads to progressive degeneration, calcification and necrosis of the myocardium. Desmin was proposed to act as a scaffolding protein providing viscoelastic properties in the vascular wall [12], stiffness to myocytes [13], the lung airways [14] as well as the cardiomyocytes [15,16,17]. It is clear that embryonic heart pumping is dependent on the biomechanical properties of cardiomyocytes [18], yet, the role of desmin on heart biomechanics *in vivo* remains largely unexplored. Therefore, addressing whether there are mechanical mechanisms associated with desmin function that influence heart pumping and whether desmin aggregates affect these biomechanical mechanisms during embryonic development would help to solve this issue.

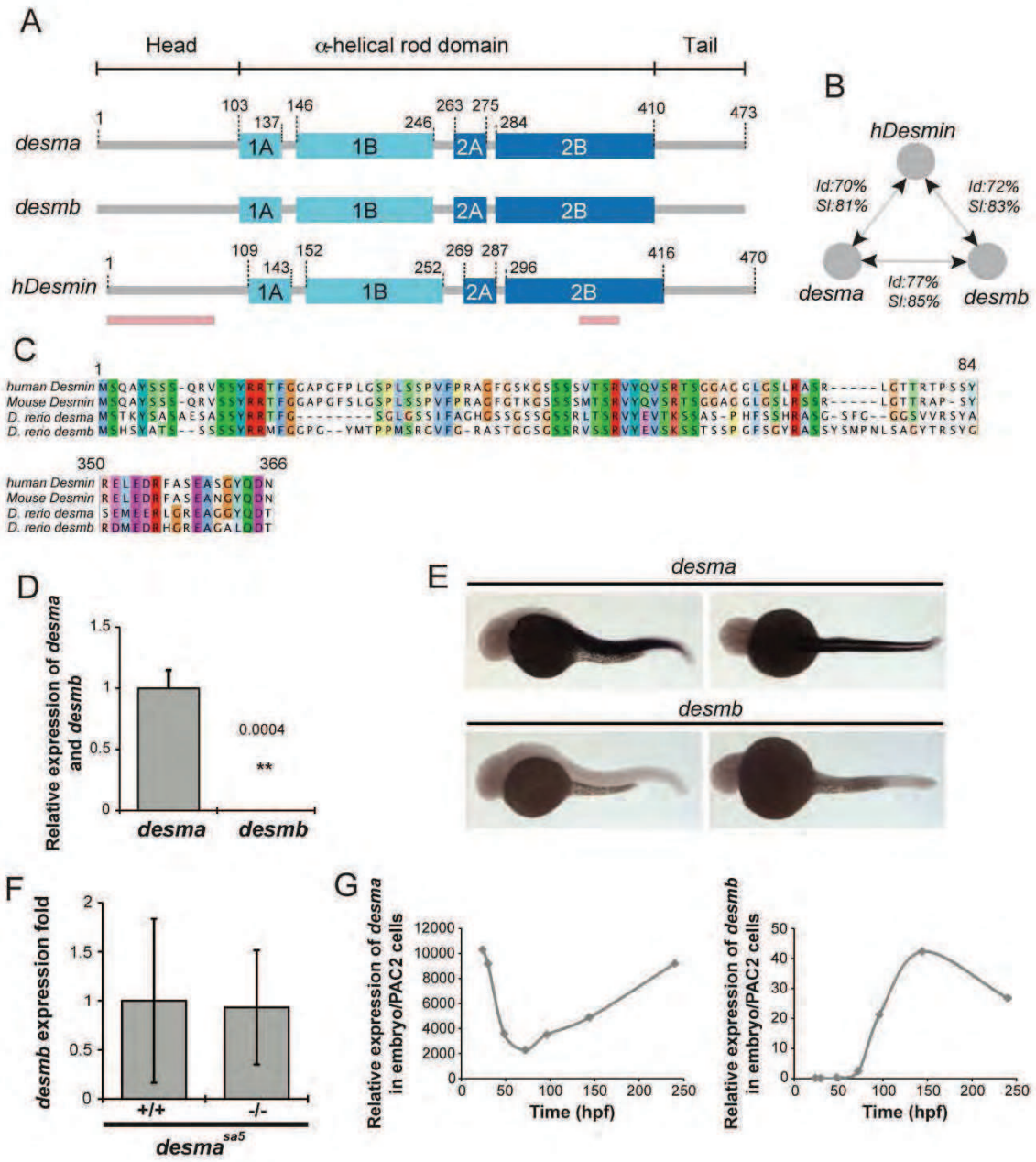

Manuscript 2/ Supplementary Figure 1: *desma* is the main ortholog of desmin in zebrafish.

(A) Scheme showing the structural homology between zebrafish *desma*, *desmb* and human desmin. Pink lines show the position, where the alignments were not complete and are presented in C. (B) Scheme showing results of identity (Id) and similarity (SI) calculated by alignment of *desma*, *desmb* and human desmin (hdesmin). Alignment and calculations were performed on ClustalW2. (C) Protein sequence alignments of regions of lower similarity between mouse, human desmin and zebrafish *desmin a* (zdesma) and *desmin b* (zdesmb). (D) qPCR of *desma* and *desmb* on RNA extracted from pools of WT 48hpf embryos shows a 2500 fold enrichment in *desma* compared to *desmb.* (E) In situ hybridization confirms the low expression of *desmb* compared to the clear *desma* signal observed in all muscle cell types of 30hpf zebrafish embryos (skeletal muscle and myocardium, no smooth muscle present at this stage). (F) qPCR on RNA extracted from pools of WT and *desma*$^{Sa5-/-}$ shows that *desmb* expression is not altered in *desma*$^{Sa5-/-}$. (G) qPCR on RNA made from pools of WT zebrafish larvae from 30hpf to 14dpf show the evolution of *desma* and *desmb* expression over time. Expression levels are given relative to the expression in PAC2 zebrafish cells. *Desma* expression is high at early stages and decreases around 50 hours to increase again linearly from 50 to 250 hpf. *Desmb* expression is very low until 96 hpf and then peaks at 150 hpf but without reaching levels comparable to *desma* enrichment.

To date, several mouse models of desmin-related myopathy, consisting of knock-in mice carrying specific patient's point mutations, were generated, yet most of them did not present clear aggregate structures and subsequent phenotypes were often associated to dominant–negative effects on the desmin network rather than to aggregate formation [19,20,21]. So far, desmin aggregation was observed in mouse cardiomyocytes carrying a specific desmin mutation [22] or *CRYAB* mutation [23]. Cardiac muscle from these mice displayed mitochondrial dysfunction, abnormal metabolism, and general alterations in muscle structure. Heterozygous DesD7 (in which 7 amino acids R173-E179 have been deleted) transgenic mice displayed characteristic desmin aggregates in the perinuclear region of cardiomyocytes, accompanied by myofibrillar disarray, hypertrophy, loss of mitochondrial organization, fibrosis and progression to heart failure by 9 months of age. Nevertheless, the sequence of events leading to these cellular alterations and their temporal relationship with protein aggregation have not yet been investigated. Thus a comparison between desmin loss of function and pathological desmin aggregation would help to identify the cellular defects associated with either desmin depletion or aggregate formation alone.

Here, we used genetically engineered zebrafish models allowing the comparative study of the effect of desmin aggregate formation and desmin loss of function to answer these questions. We found that desmin loss of function and the formation of desmin aggregates participate in multiple defects affecting skeletal and cardiac muscles, as well as vascular development and function in the zebrafish larvae. Our data show that both mitochondrial degeneration and sarcoplasmic reticulum alterations are accompanied by perturbations in calcium homeostasis and constitute the primary signs of the disease in the presence of aggregates. Finally, doxycycline and morpholino treatments reduce the size of aggregates and the pathology, and correspond to potential candidates for treatment of desminopathies. Altogether, our results identify Desmin as an essential element in controlling embryonic cardiovascular and skeletal muscle function, due to its role in controlling myocardial cell contractile properties and calcium signalling. Furthermore, despite desmin being essential for heart function, its reduction is beneficial when aggregates are present and represents a potential therapeutic approach for patients.

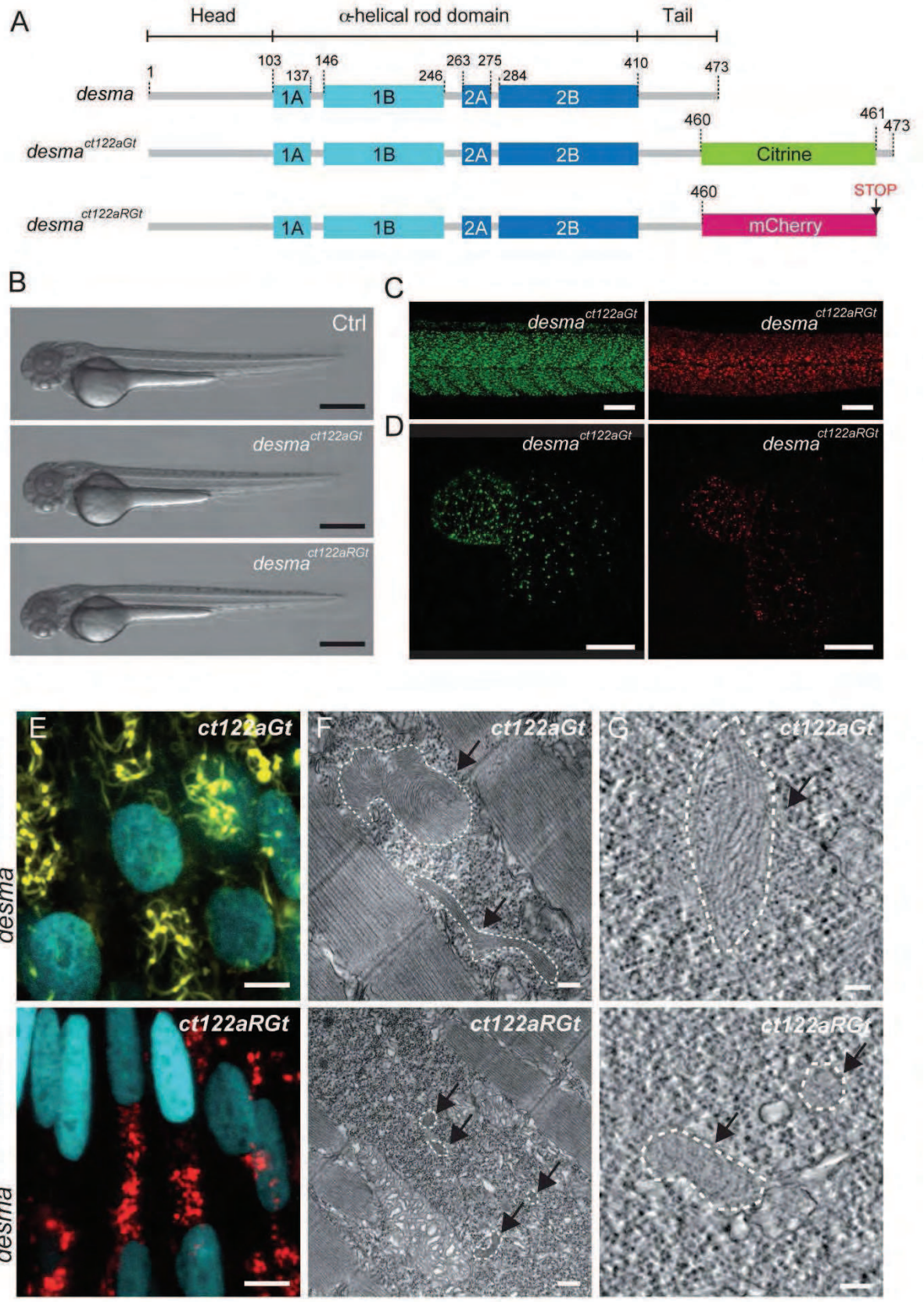
A
Head
α-helical rod domain
Tail
desma
desma^ct122aGt
desma^ct122aRGt
1A
1B
2A
2B
Citrine
mCherry
STOP
B
Ctrl
C
D
E
F
G
ct122aGt
ct122aRGt
desma^ct122aGt/ct122aGt
desma^ct122aRGt/ct122aRGt

Results

Zebrafish *desmin a* is the main embryonic desmin

The zebrafish *desmin a* (*desma*) gene is homologous to human desmin with 81% similarity in the protein sequences. *desmin b (desmb),* a second homolog of human Desmin sharing 83% similarity, also exists in zebrafish (Supplementary Figure 1A, B, C). qPCR experiments (Supplementary Figure 1D) and *in situ* hybridization (Supplementary Figure 1E) showed that the expression level of *desmb* is low at early times of development (around 2500 fold lower than the level of *desma* in 48hpf wild-type embryos) and no overexpression of *desmb* was observed upon *desma* depletion (Supplementary Figure 1F). Despite increases in *desmb* expression occuring at later stages, levels of expression remain significantly lower than those of *desma* (Supplementary Figure 1G). Accordingly, we conclude that the uncovered desmin protein distribution is reminiscent of Desma and that the expression of *desmb* can be neglected before 96hpf.

Generation and characterization of the *desma* Citrine (*desma*^{Ct122aGt}) and *desma* mCherry (*desma*^{Ct122aRGt}) zebrafish lines

Desmin intermediate filaments polymerize to form polymers following gradual steps of the classical assembly of intermediate filaments [24]. Several desmin mutations have been shown to interfere with proper filament assembly when tested *in vitro* [25,26]. Such mutations could also promote aggregate formation when transfected into cultured cells [27]. However these observations are at the steady-state level and do not provide information on aggregate formation and dynamics. In order to address the role of desmin aggregates *in vivo*, we used a knock-in line where citrine has been inserted between amino acids 460 and 461 in the C-terminus of *desmin a.* This line, named *desma*^{Ct122aGt} (or *ct122aGt* when referring to the homozygous), was obtained from a gene trap screen. In this genetic context, the *desma* gene contains an artificial exon intercalating the citrine fluorescent protein coding sequence within the gene. This method enables *in vivo* expression of labeled Desmin at endogenous levels [28]. For the second line, we made use of the FlipTrap capability in the *desma*^{ct122aGt} line to undergo Cre-lox recombination. Upon Cre-lox recombination, the *desma*^{ct122aGt} is converted to a mCherry fusion that truncates the Desma protein, leading to a mCherry tag followed by a stop codon in the case of the reverted *desma*^{Ct122aRGt} (or *ct122aRGt* when referring to the homozygous) version, leading to the deletion of 13 C-terminal amino acids in the tail domain (Figure 1A). The insertion of the fluorescent tag leads to Desmin aggregation in both lines in myocardial and skeletal muscles at 48hpf (Figure 1C,D). We analysed the global shape of the embryo and larvae as well as the viability of the *ct122aGt* and found they display no overall defects and develop normally with no increased lethality (Figure 1B,C). Correlative light and electron tomography (CLEM) showed that *ct122aGt* aggregates are positioned throughout the cytoplasm and have a fibrous structure and an average size of 9.7±0.4 µm at 48hpf (Figure 1E,F; Supplementary Video 1). We next resolved parts of the 3D structure of the aggregates, by performing electron tomography, allowing details of the filamentous organization of the aggregates to be extracted. We segmented the aggregates in 3D and analysis of the reconstruction

(see figure on the previous page)

Manuscript 2/ Figure 1: Desmin Flip trap fish lines, *desma*^{ct122aGt} and *desma*^{ct122aRGt}, enable formation and visualization of desmin aggregates.

A. Schematic drawing of the *desma* gene in WT, *desma*^{ct122aGt} or *ct122aGt* (with citrine fusion) and *desma*^{ct122aRGt} or *Ct122aRGt* (with mcherry fusion) fish lines. The *ct122aRGt* line presents a 13 amino acids deletion at the end of the tail domain and the *ct122aGt* line presents a full *desma* sequence containing the citrine fluorescent protein. B. Side views of *ct122aGt* and *ct122aRGt* zebrafish embryos at 55hpf. Scale bar=500µm. C, D. Desmin aggregates are observed in skeletal muscles (scale bar=100µm) (C) and in the myocardium (scale bar=50µm) (D) in *ct122aGt* and *ct122aRGt* 48hpf embryos. E-G: Semi-correlative light and electron microscopy of skeletal muscles of *ct122aGt* and *ct122aRGt* 48hpf embryos. (E) Confocal micrograph at high magnification of ct122aGt and *ct122aRGt* embryos. Nuclei are labelled with H2B-Cerulean. Scale bar=5µm. (F) Electron micrograph analyses of the same region showed cytosolic aggregates (the black arrows are pointing to the aggregates circled by the dotted lines) in *ct122aGt* and *ct122aRGt* embryos. Scale bar=200nm. (G) Electron tomography at high magnification showing filamentous aggregate structures in ct122aGt and compact aggregates with regular condensed structure in the *ct122aRGt* (the black arrows are pointing to the aggregates circled by the dotted lines). Scale bar=100nm. *ct122aGt* and *ct122aRGt* refers to homozygous embryos

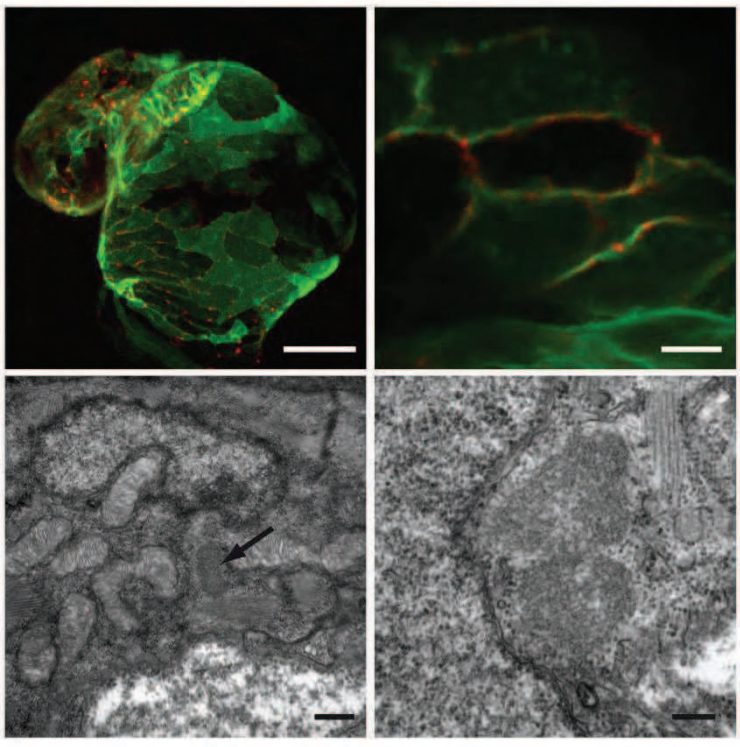

Manuscript 2/ Supplementary Figure 2: Myocardial Desma aggregates present a membrane localization.

Z-stack maximal projection of confocal images of *ct122aRGt*; *Tg(myl7:ras-eGFP)*^{s883} and electron micrograph in *ct122aRGt* myocardium in 48hpf embryos. *Tg(myl7:ras-eGFP)*^{s883} marks the cardiomyocyte membrane and colocalizes with the mCherry-positive aggregates. Upper left panel: Scale bar=50µm. Upper right panel: Scale bar = 5µm. Lower left panel: Scale bar = 0.5µm. Lower right panel: Scale bar = 200nm. Black arrow shows the position of an aggregate observed in a cardiomyocyte. . *ct122aRGt* indicates *desma*^{ct122aRGt} homozygous embryos.

shows that the core structure of the aggregates is a cluster of Desmin filaments packed into a disorganized network (Figure 1G).

Similar to *ct122aGt*, aggregates were observed both in the heart and skeletal muscles in the *ct122aRGt* line. Subsequent analysis of the Desma aggregate size and structure by electron tomography revealed that *ct122aRGt* aggregates are positioned throughout the cytoplasm similarly to what is observed in *ct122aGt* but they are more electron dense and have a more granular structure than the *ct122aGt* aggregates. Their average size was also smaller (1.4±0.05µm). In the myocardium, these aggregates were found preferentially close to cardiomyocyte membranes (Supplementary Figure 2). The differences observed between these two model lines suggest that Desma aggregation properties depend on its sequence integrity and highlight the heterogeneity of aggregate size and shape reminiscent of *desmin* mutations, which is also observed in different human mutations [27,29].

Desmin loss or aggregation leads to muscle disorganization and altered organelles

Desminopathies are characterized by accumulation of granulo-filamentous material leading to progressive muscle weakness with specific histological hallmarks, such as perturbed mitochondria localisation and structure, z-band streaming and myofibrillar degeneration [30]. In mouse, desmin knockout (KO) leads to several histological hallmarks commonly observed in desminopathy patients despite the absence of desmin aggregates. A desmin KO line *desma*$^{sa5-/-}$ was obtained from the Sanger Institute ENU-mutagenesis screen. The *desma*^{sa5} allele is a point mutation leading to a premature stop codon at the beginning of the 2B alpha helix (Figure 2A,B). This leads to a complete depletion of *desmin* expression as verified by western blot and *desma* mRNA quantification. This suggests the mutation leads to mRNA decay and that *desma*^{sa5} is a null allele (Figure 2C). When analysing the viability of the *desma*$^{sa5-/-}$, we found that *desma* depletion does not affect early embryonic overall morphology or survival (Figure 2D) and that mutants do not display increased lethality at adult stages.

To assess the organization of muscle fibres in the tail of embryos from both *desma*$^{sa5-/-}$ and *ct122aGt*, we used Second Harmonic Generation (SHG) microscopy. Second harmonic light can be generated when 2 photons with the same frequency interact with non-centrosymmetric structures and are effectively combined to generate new photon with twice the energy. This approach allows muscle fibres to be imaged without any exogenous labeling [31]. From 48hpf onwards, *desma*-null embryos present perturbed organization of myofibrils with a misalignment of fibres (Figure 3A). Further investigation of *desma* loss of function was performed using two morpholinos, one translation blocking and one splice blocking, with a mismatch MO used as a control. Our results show that both *desma* morphants lead to similar skeletal muscle phenotypes observed for *desma*$^{sa5-/-}$ (data not shown). The same phenotype is observed in *ct122aGt* embryos from 48hpf and is accompanied by breaks in myofibril organization in 43 % of embryos at 96hpf (n=35). In some cases, characterized as “extreme phenotypes”, the sarcomere organization was completely lost as no SHG signal was observed (17%). In line with these SHG observations, a touch evoke assay was performed to obtain functional insight into the observed phenotypes. *ct122aGt* embryos showed a decreased swimming capacity compared to their corresponding controls with lower swimming distance and velocity while *desma*$^{sa5-/-}$ behaved in

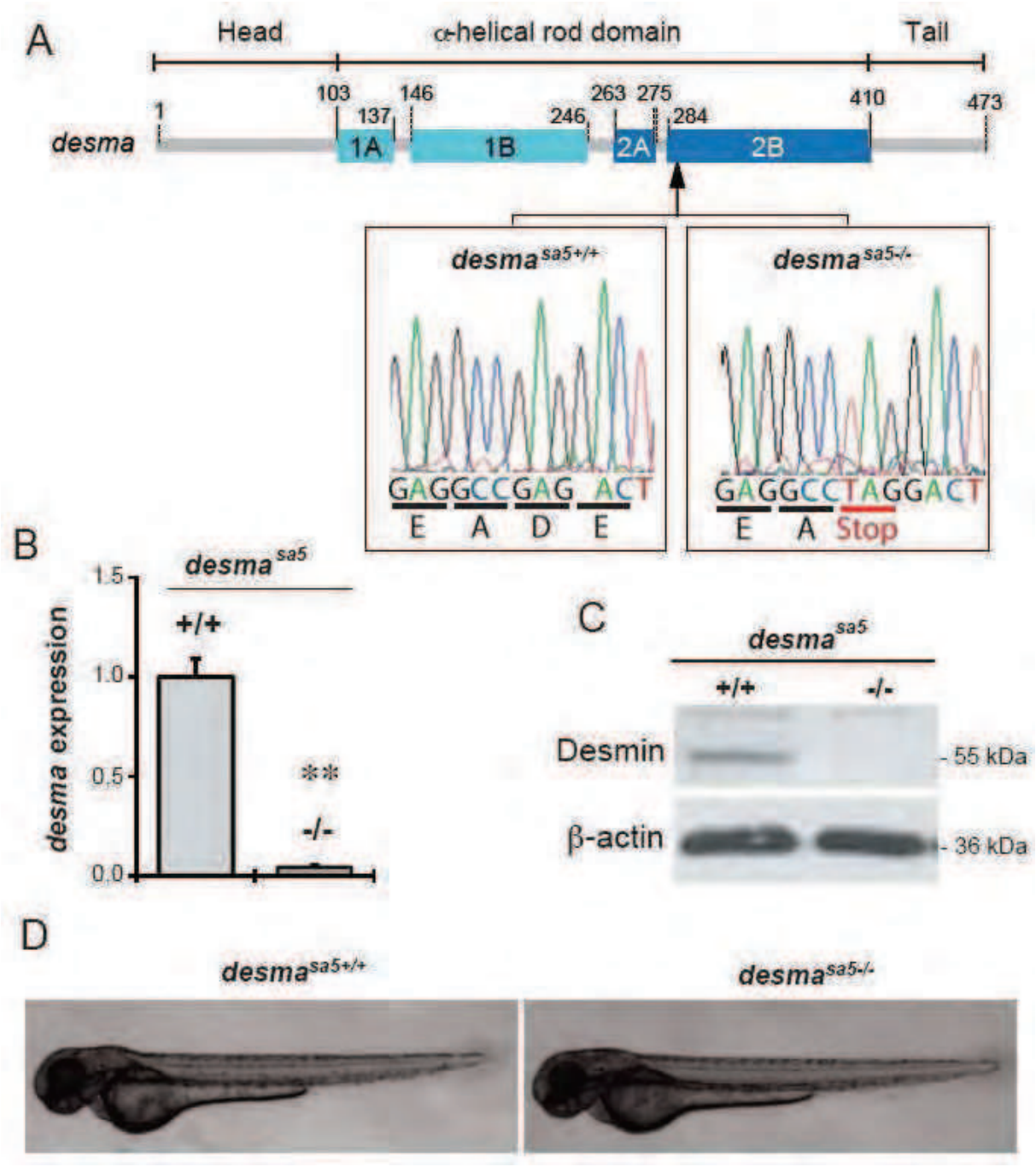

Manuscript 2/ Figure 2: Loss of *desma* transcripts in the *desma*$^{sa5-/-}$

(A) Scheme of the WT *desma* gene in zebrafish. Arrow indicates the position of the mutation in the *desma* gene sequence. Sequencing of genomic DNA from *desma*$^{sa5+/+}$ and *desma*$^{sa5-/-}$ larvae reveals a G to T mutation resulting in a stop codon that leads to truncated Desma in *desma*$^{sa5-/-}$ mutants. (B) Reverse transcriptase quantitative PCR (qPCR) on RNA extracted from pools of WT and *desma*$^{sa5-/-}$ mutants demonstrates defective amplification of the mutant transcripts of exons 3-4 demonstrating that the corresponding mRNA is degraded. (C) Immunoblot of 2dpf WT and *desma*$^{sa5-/-}$ mutants demonstrating full knockdown of Desma protein. (D) Side views of zebrafish *desma*$^{sa5+/+}$ and *desma*$^{sa5-/-}$ embryos at 55hpf. Scale bar=500μm.

a similar manner to *desma*$^{sa5+/+}$ (Figure 3B). For a better understanding of the differences observed between *ct122a* and *desma*$^{sa5-/-}$ phenotypes, both at the morphological and the functional level, the ultrastructure of their skeletal muscles was explored. Transmission Electron microscopy (TEM) analysis at 52hpf in *desma*$^{sa5-/-}$ and *ct122aGt* embryos (Figure 3C) showed misalignment of muscle fibres, a concomitant misalignment of T-tubules and dilatation/disorganization of the sarcoplasmic reticulum (SR) while the endoplasmic reticulum (ER) seems unaffected in both lines. Moreover, abnormal mitochondria and mitophagy were only observed in *ct122aGt* embryos at 52hpf. Additionally, these embryos displayed degenerating cells with loss of material and the presence of autophagosomes. Taken together, these data validate previously reported observations made in other models of desminopathies and suggest that our lines are novel and appropriate models to study desmin function *in vivo*. Furthermore, our data indicate that desmin aggregates lead to a more severe muscle phenotype than desmin loss at the ultrastructural, cellular and functional level.

desma knockdown in ct122aGt restores muscle morphology

Formation of desmin granulo-filamentous material within muscle fibres is a hallmark of desminopathy. We hypothesised that the muscular phenotypes observed in the *ct122aGt* line is due to the presence of desmin aggregates and predicted that decreased Desmin expression would limit the extent of the observed phenotypes. To test this hypothesis, we analysed the impact of decreasing desmin expression on the formation of aggregates in the *ct122aGt* line using a morpholino-based approach. Injection of two different concentrations, 33 and 100 µM, lead to a drastic decrease in size or both size and number of aggregates, respectively (Figure 4A, B). The corresponding skeletal muscles phenotypes were assessed at 48, 72 and 96hpf using SHG and categorized into normal (N), weak (W), strong (S) and extreme (E). We defined a scale of SHG phenotypes in which weak phenotype corresponds to the situation where muscle fibres are misaligned or present abnormal curvatures (Figure 4C). A strong phenotype is attributed when muscles display degenerated and/or broken fibres, a global decrease in the size of the musculature or a global decrease in the intensity of the SHG signal. A phenotype is called extreme when the muscle disorganization is such that no SHG signal is observed anymore (Figure 4C). Finally, a normal phenotype is attributed to embryos with a similar muscle organisation as the controls. Only weak phenotypes were observed in embryos injected with the morpholinos regardless of the concentration used corresponding to the phenotype observed previously in the absence of *desma* (Figure 4D). Our data show that the presence of aggregates is the main cause of pathological feature in zebrafish models of desminopathies and that decreased desmin level can reduce aggregates formation and, concomitantly, the pathology.

Doxycycline treatment decreases aggregates and ameliorates the skeletal muscle phenotype in the _ct122aGt_ line

To further validate that reducing the aggregates is leading to a rescue of the pathology, we next tested the predictability of the drug response in the *ct122aGt* line. Compounds or drugs with the potential to act negatively on protein aggregates have raised lots of interest in the last few years and are likely the most appropriate therapeutic approach for ameliorating desminopathies. Recently proposed

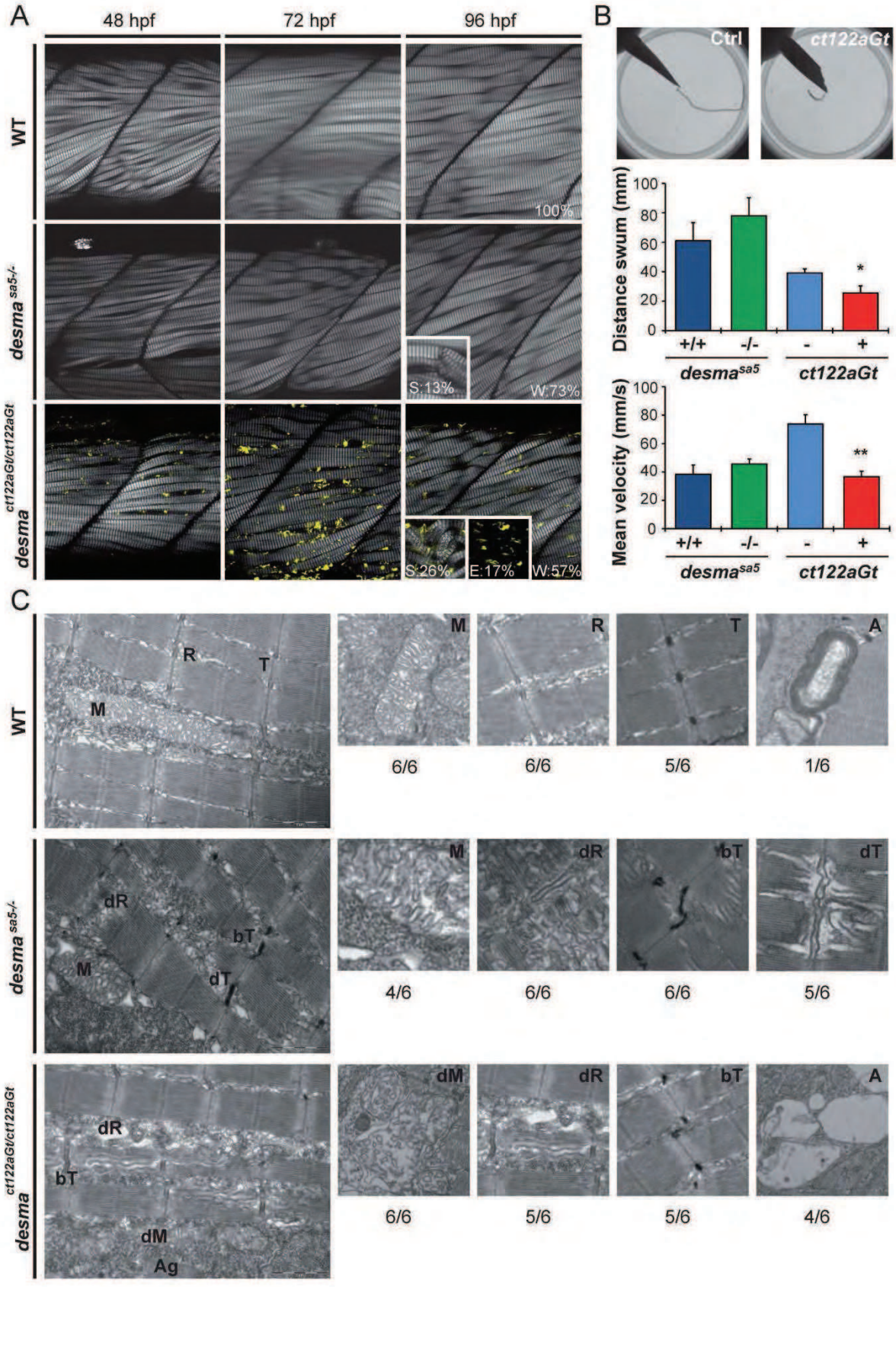
A
48 hpf
72 hpf
96 hpf
WT
desma sa5-/-
desma ct122aGt/ct122aGt
100%
S:13%
W:73%
S:26%
E:17%
W:57%
B
Ctrl
ct122aGt
Distance swum (mm)
Mean velocity (mm/s)
+/+
-/-
-
+
desmasa5
ct122aGt
C
R
T
M
dR
bT
dT
dM
Ag
A
6/6
6/6
5/6
1/6
4/6
6/6
6/6
5/6
6/6
5/6
5/6
4/6

compounds include doxycycline (Doxy) (Zheng et al., 2010) and the chemical chaperone 4-phenylbutyrate (Winter et al., 2014). Doxy treatment lowers the aggregate content in many proteinopathies (e.g. Huntington disease) and can partially rescue the desmin-related cardiomyopathy phenotype in the αB-crystallin mouse model (Wang et al., 2001, Zheng et al., 2010). The function of Doxy to reduce aggregate formation remains unclear, but it has been proposed that Doxy acts as a chemical chaperone or by intervening at another level in the maintenance of protein quality control [32] without activating autophagy (Zheng et al., 2010). We treated *ct122aGt* embryos with this drug from 12hpf and measured aggregate size and number using confocal microscopy after 36 hours of treatment (Figure 4E-G). We performed CLEM on Doxy treated embryos to address the structure of the aggregates and clearance activity. The analysis revealed a more condensed and spherical structure of aggregates lacking filamentous extensions compared to vehicle-treated embryos (Figure 4E). Moreover, the size of the aggregates was found to be dramatically smaller in Doxy treated embryos (3.2±0.5µm vs 9.7±0.4µm in untreated *ct122aGt*) (Figure 4G). We next addressed the impact of Doxy treatment on muscle phenotype using SHG and found that Doxy-*ct122aGt* embryos displayed a weak phenotype (100% *vs.* 50% in corresponding controls at 72hpf) suggesting that the presence of aggregates but also their cellular distribution as well as their size may have a direct impact on the severity of the phenotypes (Figure 4H). We conclude that Doxy treatment changes the morphology of the aggregates and partially rescues the muscular defects observed without treatment. Together, these experiments validate the predictability of the line and demonstrate our model is a good tool to study drugs affecting aggregate formation *in vivo*. It also unambiguously confirms that desmin aggregates are linked to the pathology.

Desma is required for early heart function

Desmin aggregates lead to a large spectrum of phenotypes in both skeletal and cardiac muscle. The variability of phenotypes is often observed in cardiomyopathies and includes dilated, hypertrophic and restrictive cardiomyopathy. Also in certain cases additional conduction defects are be observed in adult patients [33]. Nevertheless the impact of desmin on early heart function remains unclear. Therefore, we took advantage of the embryonic transparency to directly investigate heart function in the embryo by assessing cardiac contractility using high temporal imaging of the beating heart. We found that *ct122aGt*, *ct122aRGt* and *desma*$^{sa5-/-}$ all display an increased heart rate at 30 and 48hpf compared to corresponding controls (Supplementary Figure S3A). We next characterized heart function by measuring the difference between diastolic and systolic chamber diameter over the corresponding diastolic diameter (also known as atrial and ventricular fractional shortening (FS%). *desma*$^{sa5-/-}$ embryos show a significantly lower atrial but a significantly higher ventricular fractional shortening at 48hpf compared to *desma*$^{sa5+/+}$. Importantly, rescue of the heart function was observed at 48hpf in *desma*$^{sa5-/-}$ by overexpressing the zebrafish *desma* full length mRNA, demonstrating that the abnormal heart function is specifically due to the loss of Desma in the *desma*$^{sa5-/-}$ (Supplementary Figure S3A). Furthermore, *ct122aGt* and *ct122aRGt* embryos present higher atrial and lower ventricular fractional shortening at 48hpf than the controls and the *desma* mutants. This suggests that

(see figure on the previous page)

Manuscript 2/ Figure 3: Aggravation of the skeletal muscle phenotype is observed in *desma*^{ct122aGt} embryos compared to *desma*$^{sa5-/-}$

(A) Optical sections of the mid trunk region using SHG imaging show misalignment of muscle fibers in *desma*$^{sa5-/-}$ and *desma*^{ct122aGt} homozygous embryos compared to WT siblings at 48, 72 and 96 hpf. In *ct122aGt* mutants, muscle fiber misalignment is often accompanied by fiber breaks and degeneration from 48hpf. At 96hpf, phenotypes are separated in to three categories, weak *(W)* with misalignment only, strong *(S)* (see inset at 96 hpf for the *desma*^{ct122aGt} and *desma*$^{sa5-/-}$) with misalignment accompanied with breaks, degenerations and/or general decrease of the SHG intensity and extreme *(E)* (see inset at 96 hpf for the *desma*^{ct122aGt}) were the SHG signal is absent because of the complete disorganization of sarcomeric structures. (B) Touch-evoke response assays show reduced swimming distance and velocity in *ct122aGt* embryos compared to controls while the locomotion capacity of *desma*$^{sa5-/-}$ is similar to *desma*$^{sa5+/+}$. (C) Electron micrograph of mitochondria (M), sarcoplasmic reticulum (R), T-Tubules (T) and autophagy structures (A) in controls, *desma*$^{sa5-/-}$ and *ct122aGt* mutants. Note the sarcomeric reticulum dilatation (dR) T-tubule dilation (dT) and T-tubule bending (bT) in *desma*$^{sa5-/-}$ and the dilated mitochondria in the *ct122aGt* (dM) while these structures are normal in wild-type animals. The ratio indicates the respective frequencies (n=6). *ct122aGt* indicates *desma*^{ct122aGt} homozygous embryos.

(see figure on the next page)

Manuscript 2/ Figure 4: Reduction of Desma aggregation ameliorates skeletal muscle phenotypes observed in *desma*^{ct122aGt} homozygous embryos.

(A-B) Size (A) and number (B) of aggregates in *ct122aGt* injected with two different concentrations of morpholino (C1 (33 nM) <C2 (100 nM)). Embryos injected with C2 present a high reduction in aggregate numbers while C1 do not reduce the aggregate number. (C) Classification of the skeletal muscle phenotypes obtained with SHG. Normal phenotype is attributed to embryos with similar muscle shape as the controls. Weak phenotype corresponds to the situation where muscle fibres are misaligned or present abnormal curvatures. A strong phenotype is attributed when embryonic muscle display degenerated and/or broken fibers, a global decrease in the size of the musculature or a global decrease in the intensity of the SHG signal. A phenotype is called extreme when the muscle disorganization is such that no SHG signal is observed anymore. (D) Evaluation of phenotypes in *ct122aGt* injected with the two different concentrations of morpholino, uninjected and WT embryos from 48 to 96 hpf. The assessment of a phenotype is based on the scale presented in C after SHG imaging. (E) Confocal images and electron micrograph of aggregates in *ct122aGt* embryos treated with Doxycycline (Doxy) or the corresponding vehicle (EtOH). Doxy treated embryos show more condensed and smaller aggregates compared to the controls. (F-G) Quantification of aggregate size and number in Doxy treated embryos compared to the corresponding vehicle treated embryos. (H) Evaluation of the phenotypes of Doxy and vehicle treated embryos using SHG and the scale defined in C shows that only weak and normal phenotypes were observed after Doxy treatment while strong phenotypes are present in the controls. *ct122aGt* indicates *desma*^{ct122aGt} homozygous embryos.

desmin aggregates and desmin expression impact on wall motion in early embryonic heart and that desminopathies can lead to early cardiac defects.

Alteration of blood vessel formation and blood flow in *desma*$^{sa5-/-}$ and ct122aGt/ ct122aRGt lines

At early embryonic stages, zebrafish blood vessels lack muscle cells, the heart is valve-less and the pulse propagation in the developing vascular network is a direct readout of the heart pumping efficiency [34]. We thus hypothesised that blood flow forces along the vascular network may be abnormal when desmin function is altered. To address the impact of the abnormal heart function on the embryonic vascular function, we determined the pulse propagation properties of blood in the dorsal aorta (Supplementary Figure S3B). We measured flow velocity in the dorsal aorta of *desma*$^{sa5-/-}$, *ct122aGt* and *ct122aRGt* embryos. *desma*$^{sa5-/-}$ displayed an increased arterial blood flow while *ct122aGt* and *ct122aRGt* embryos showed lower blood flow velocities compared to controls. We hypothesized that the variations in flow propagation profiles could be linked to an abnormal vascular network function. We thus quantified the number of inter-segmental vessels (ISVs) with circulating blood cells at 50hpf. We found that 33%, 22% and 13% of the vessels were not circulating in *desma*$^{sa5-/-}$ (n=35 ISV in 6 embryos), *ct122aGt* (n=129 ISV in 15 embryos) and *ct122aRGt* (n=64 ISV in 10 embryos) embryos, respectively, compared to only 9% in control embryos (n=40 ISV in 6 embryos) (Figure Supplementary S3C), leading to an increased resistivity of the network in the mutants. Moreover the diameter of the ISVs is highly variable in *desma*$^{sa5-/-}$ and *ct122aGt* compared to the corresponding controls (Supplementary Figure S3D). Considering that desmin is not expressed in endothelial cells and that blood flow is essential for blood vessel development [35], these defects might be due to an indirect effect of the abnormal flow force propagation in the vascular network of the desmin mutants, as shown in angiogenesis mutants [34].

Heart biomechanics are perturbed upon *desma* depletion or desmin IF aggregation

To further characterise the requirement of desmin on cardiomyocyte function *in vivo*, we addressed the contribution of desmin to the biomechanics of the heart by monitoring key parameters defining heart wall motion *in vivo*. We investigated the heart contraction pattern in 4D in order to precisely quantify heart wall motion during a typical heartbeat [18]. To do so, we used the myocardial specific *Tg(myl7:EGFP)* transgenic line. 4D reconstructions were obtained for 48hpf *Tg(myl7:EGFP) desma*$^{sa5+/+}$ (n=5) and *desma*$^{sa5-/-}$ (n=5) and for 48hpf *ct122aGt* (n=6) embryos (Figure 5A, Supplementary Videos 2,3,4). Then, we performed a quantification of the heart wall motion in both heart chambers and found that *ct122aGt*, *ct122aRGt* and *desma*$^{sa5-/-}$ embryos all present an abnormal ventricular contraction profile (Figure 5B). As the heart pumping depends on a contraction wave going from the atrium to the ventricle, the AVC displacement was used as readout of the global pattern of the contraction. Live imaging shows that the AVC serves as a hinge, which is passively subjected to constraint due to the contraction of the atrium and ventricle. Thus, the AVC lateral motion is a mark of the synchronization between both chamber contractions (Figure 5C). To quantify the chamber synchronisation, we specifically tracked the motion of the AVC cells in relation to myocardial contraction and extracted the velocity profiles of the AVC cells in the different conditions. In the

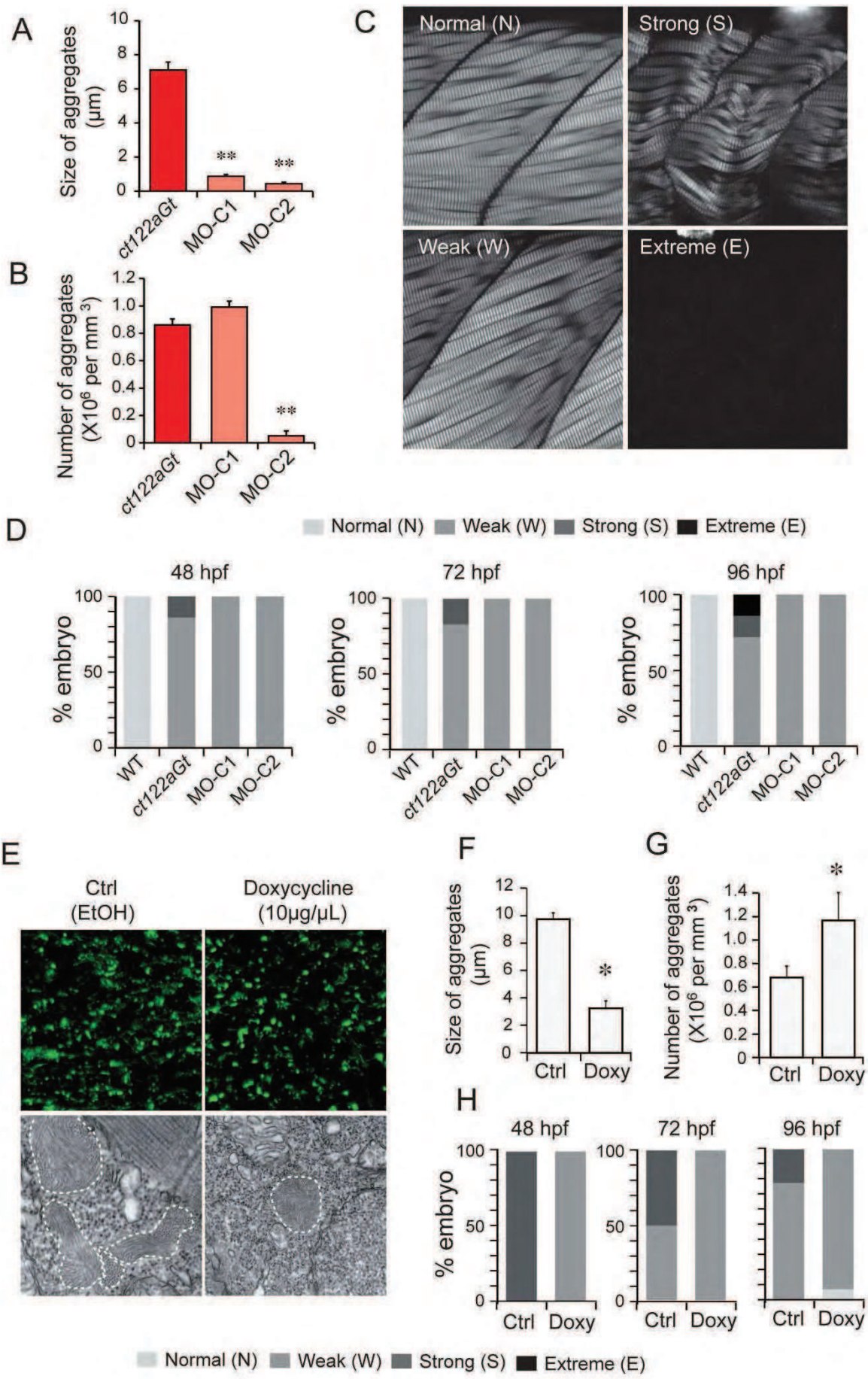
A
Size of aggregates (μm)
10
8
6
4
2
0
**
**
ct122aGt
MO-C1
MO-C2
B
Number of aggregates (X10^6 per mm^3)
1.2
1.0
0.8
0.6
0.4
0.2
0
**
ct122aGt
MO-C1
MO-C2
C
Normal (N)
Strong (S)
Weak (W)
Extreme (E)
D
Normal (N)
Weak (W)
Strong (S)
Extreme (E)
48 hpf
72 hpf
96 hpf
% embryo
100
50
0
WT
ct122aGt
MO-C1
MO-C2
E
Ctrl (EtOH)
Doxycycline (10μg/μL)
F
Size of aggregates (μm)
12
10
8
6
4
2
0
*
Ctrl
Doxy
G
Number of aggregates (X10^6 per mm^3)
1.4
1.2
1.0
0.8
0.6
0.4
0.2
0
*
Ctrl
Doxy
H
48 hpf
72 hpf
96 hpf
% embryo
100
50
0
Ctrl
Doxy
Normal (N)
Weak (W)
Strong (S)
Extreme (E)

control, a single velocity peak was observed when the contraction wave traverses the AVC, as expected from regular wave propagation. In the absence of desmin, two velocity peaks were typically observed, demonstrating that the contraction wave does not spread uniformly along the length of the heart (Figure 5D). Together, these data show that *desma* is required to maintain proper synchronization of heart wall motion and has an important role in coordinating the contraction wave of the heart.

D*esma*$^{sa5-/-}$ and *Ct122aRGt* display alterations in the embryonic heart conduction system

Since no role for Desmin in heart function has been reported in the embryo thus far, we further investigated how Desmin regulates heart contraction. Desmin pathological changes are associated with arrhythmias and several examples have shown defects in the cardiac conduction system including calcifications (Yuri et al., 2007). As heart contraction waves are directly controlled by calcium propagation in the myocardium, we tested the dynamics of calcium propagation in our models. We used Gcamp3.0, a genetically encoded calcium indicator [36], which reveals calcium dynamics in the heart and the activity of the conduction system *in vivo* [37]. We characterized the calcium transient generation in the myocardium by analysing the *desma*$^{sa5-/-}$ and *ct122aRGt* embryos being double transgenic for *Tg(myl7:galFF)* and *Tg(UAS:GCaMP3.0)*. This permits to image calcium using fast confocal microscopy and subsequent 4D reconstruction of the heartbeat, and enables the intra-cardiac calcium fluxes to be recorded concomitantly with the native heart wall motion. (Figure 6A, Supplementary Videos 5, 6, 7). To quantify the calcium wave, the relative fluorescence intensity was measured locally over time at the base of the atrium (1), the top of the atrium (2), the tip of the ventricle (3) and the middle of the ventricle outer curvature (4). In controls, the peaks of intensity followed the contraction wave exactly and clear oscillations of fluorescence matching the contraction wave were recorded in all of the analysed regions. By contrast, a constant elevated calcium concentration was observed at the tip of the ventricle (region 3) of *desma*$^{sa5-/-}$ and *ct122aRGt* embryos. Similar observations were made in the region corresponding to the outer curvature of the ventricle, where Ca^{2+} oscillations were lost and constantly high in *ct122aRGt* embryos (Figure 6B). These data suggest that the absence of functional Desmin filaments (*desma*$^{Sa5-/-}$ and *ct122aRGt*) leads to locally increased calcium levels as well as possible constant contraction of the ventricular tip cells. These observations provide the physiological basis for the aberrant contraction wave observed in the absence of functional desmin filaments as well as the abnormal synchronization between atrium and ventricle during the contraction cycles.

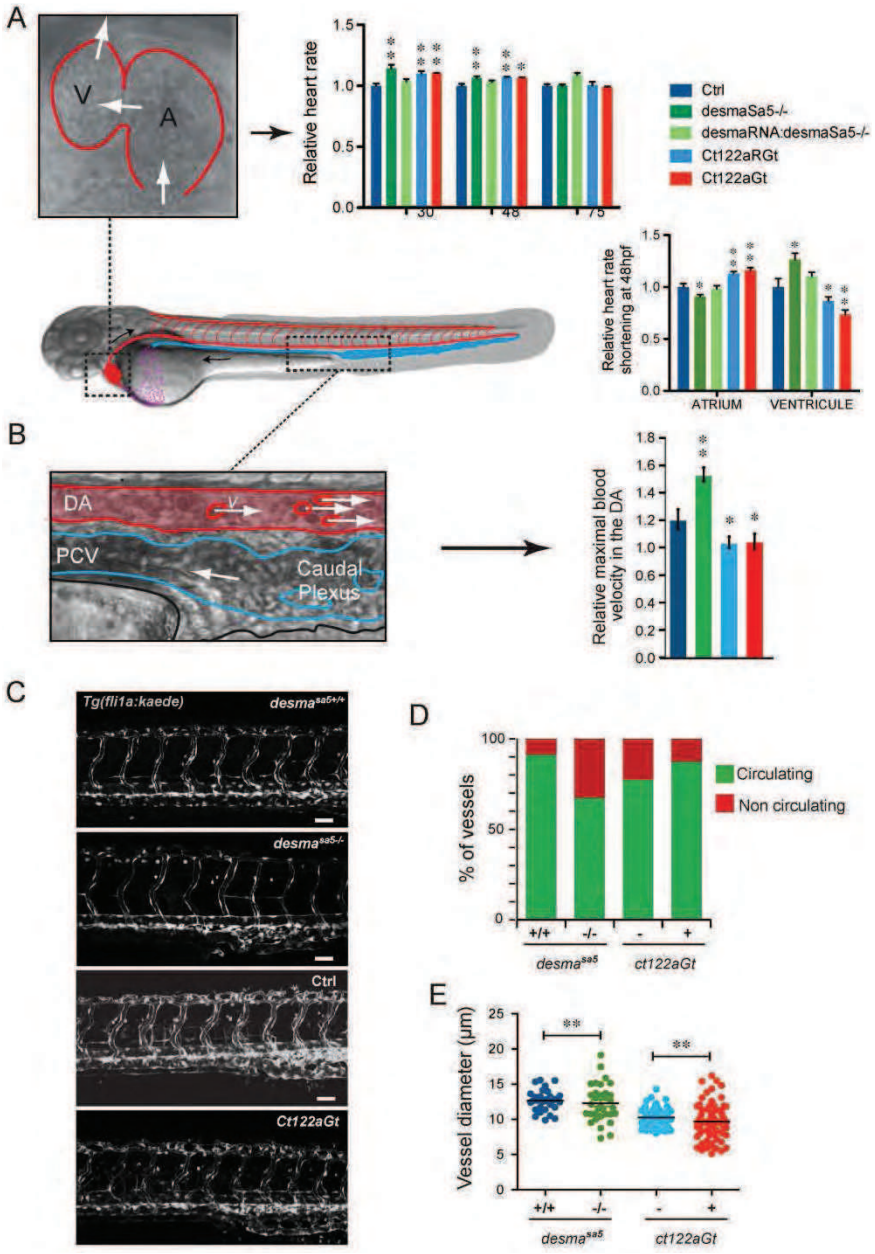

Manuscript 2/ Supplementary Figure 3: Cardiac parameters and vasculature defects are observed in *desma*$^{Sa5-/-}$, *desma*^{ct122aGt} homozygous embryos and *desma*^{ct122aRGt} homozygous embryos.

ct122aRGt indicates *desma*^{ct122aRGt} homozygous embryos. Side view of a zebrafish embryo highlighting the embryonic circulatory network, where the heart and the dorsal aorta (DA) are underlined in red and the venous vessels (posterior cardinal vein, PCV) in blue. (A) Measurements of cardiac parameters in *desma*$^{sa5-/-}$, *ct122aGt*, *ct122aRGt* and control embryos including heart rate and fractional shortening analysis. The fractional shortening (FS%) is calculated as the ratio of the difference between diastolic and systolic chamber diameter over the diastolic diameter. (B) Zoom on the DA and PCV showing the flowing red blood cells which were tracked to measure the blood flow velocity. The graph shows the relative maximal blood flow velocity measured in the DA of the trunk as readout of the pumping efficiency in *desma*$^{sa5-/-}$ and in *ct122aGt* embryos compared to their relative controls. (C) Z-stack maximal projections showing the organization of the intersegmental vessels (ISVs) in *desma*$^{sa5+/+}$, *desma*$^{sa5-/-}$; *ct122aGt* positive and control *Tg(fli:gal4FF*^{ubs}*; UAS:kaede)* embryos at 50hpf. (D) Percentage of circulating versus non-circulating vessels *desma*$^{Sa5-/-}$, *ct122aGt* and *ct122aRGt* embryos compared to control embryos. (E) Measurements of ISV diameters show a higher variability in *desma*$^{sa5-/-}$ and *ct122aGt* compared to their corresponding controls. *ct122aGt* and *ct122aRGt* indicate *desma*^{ct122aGt} and *desma*^{ct122aRGt} homozygous embryos.

Discussion

We describe here the characterization of two novel zebrafish *desma* mutants; a *desma* KI mutant allele from a gene trap screen and a mutant KO allele from a mutagenized library. By analysing these mutant embryos, we observed the presence of aggregates when the protein is truncated or fused with citrine. This allowed us to confirm the strong homologies between the phenotypes observed in zebrafish with human desminopathies, to predict the effects of drugs as well as to modulate the severity of the desminopathy-related defects observed by decreasing the amount of endogenous desmin and demonstrate a role for desmin in controlling heart pumping. Our analysis reveals that desmin aggregation and loss of function can both impact skeletal and cardiac muscle function, but that the presence of aggregates leads to stronger defects than the absence of desmin. While biochemical and cellular characterisation of desmin aggregates was extremely helpful to understand properties and dynamics of this aggregates *in vitro* [24], this work should help to clarify the details of the cellular basis of desminopathies *in vivo*.

The requirement of intermediate filaments in controlling heart pumping and biomechanics is expected but the role of desmin remains poorly characterized *in vivo*. Here we took advantage of the zebrafish to analyse desmin function and desmin aggregation to study heart function *in vivo*. We found that heart defects are visible in zebrafish at embryonic stages and as the myocardium matures. The first signs of desminopathies are most frequently observed in adulthood in both mouse models and patients [2]. We found that embryonic heart contractility is abnormal in the absence of desmin and in the presence of desmin aggregates in zebrafish. Furthermore, we show that the cardiac defects associated with desmin loss of function and aggregates affects cardiac physiology, in particular myocardial calcium fluxes and heart contractile biomechanics, which in turn can impact on vascular function and development. Desmin-null mice present arterial defects attributed to altered smooth muscle cells function where desmin is well expressed [10]. In the zebrafish embryo, smooth muscle cells appear at larvae stage. Considering that *desma* is not detectable in endothelial cells, our results suggest that the reported vascular phenotypes could result from indirect impact of blood flow alteration. Although not frequent or poorly diagnosed in human desminopathies, subtle vascular abnormalities should be further investigated in relation to heart and muscle function.

The altered cardiovascular physiology observed in desmin mutants is accompanied with conduction defects leading to abnormal ventricular contraction. Remodelling of gap junctions and mislocalisation of Cx43 and other mechanical junction proteins like desmoplakin, plakoglobin and N-Cadherin were shown previously in a mouse model of desmin-related cardiomyopathy [38]. Mislocalisation of intercellular junction components is commonly observed in arrhythmogenic cardiomyopathies and triggers a loss of mechanical and electrical coupling of cardiomyocytes [39,40]. We speculate that this could explain conduction phenotypes observed in 62% of desminopathy patients [1] and in our model. As morphogenesis of cardiomyocytes can be influenced by endogenous electrical currents in the embryonic heart [37], it is possible that desmin indirectly controls the final steps of heart development

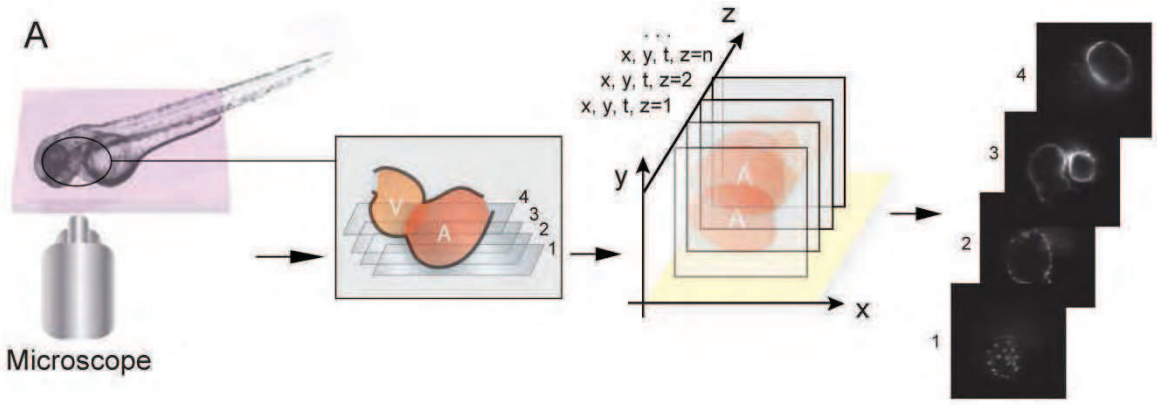
A
Microscope
V
A
4
3
2
1
z
x, y, t, z=n
x, y, t, z=2
x, y, t, z=1
y
x

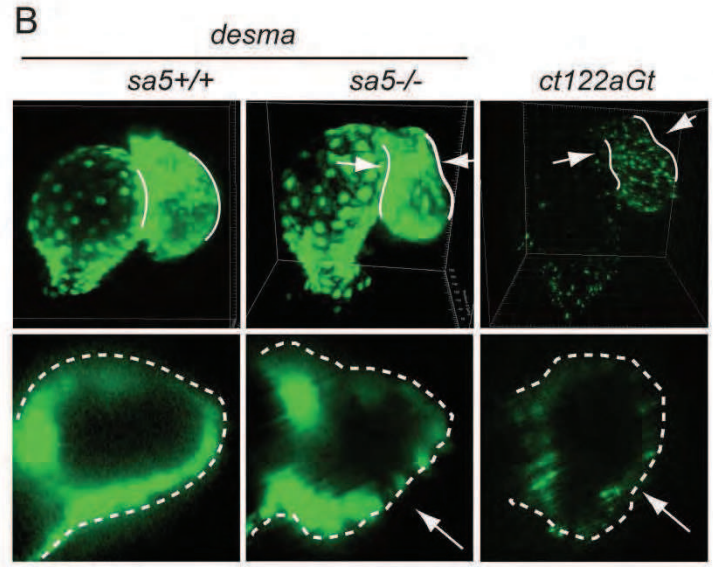
B
desma
sa5+/+
sa5-/-
ct122aGt

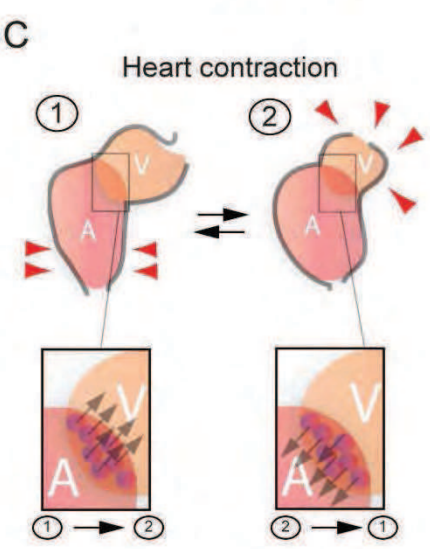
C
Heart contraction
1
2
V
A

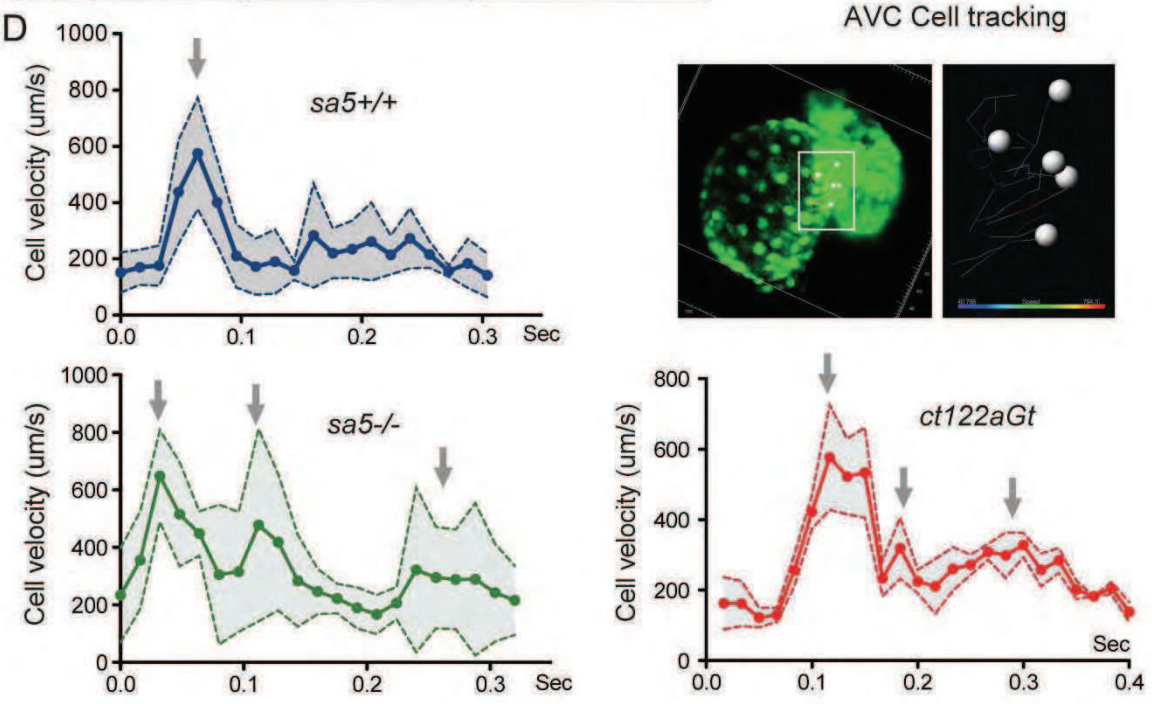
D
AVC Cell tracking
Cell velocity (um/s)
sa5+/+
sa5-/-
ct122aGt
Sec

and morphogenesis through the regulation of Ca^{2+} conduction in cardiomyocytes. As this study corresponds to the first demonstration that the physiological mechanism of cardiac defects in desminopathies is associated to an abnormal calcium dynamics in the cardiomyocytes, further analysis in mouse embryos or juveniles could highlight similar features in higher vertebrates.

Although the zebrafish has been used extensively to identify new regulators of cardiac and skeletal muscle function by conducting forward genetic screens, there has been very limited success identifying novel mutants displaying aggregation phenotypes and proteinopathies using endogenously tagged proteins. In our study, we demonstrate that protein trap screens are useful to investigate desmin aggregation properties and their effects *in vivo*. This allowed us to show that the presence of desmin aggregates leads to more severe phenotypes in both skeletal and heart muscles compared to the loss of *desma* function. Using morpholino knock down, we found decreasing desmin level at early embryonic stages was sufficient to restore parts of the muscular defects observed in presence of desmin aggregates. The future use of the *ct122aGt* and *ct122aRGt* might help to apply screening strategies for the identification of chemical compounds inhibiting desmin aggregation, as new strategies are now emerging for drug screening using whole zebrafish embryos. In conclusion, we have identified desmin itself as a potential therapeutic target for desminopathies and several usefull zebrafish lines modeling desminopathies.

(see figure on the previous page)

Manuscript 2/ Figure 5: Heart biomechanics are altered in the absence of *desma* and in the presence of desmin aggregates

(A) 4D reconstructions of the heart wall dynamics were obtained from 2D series recorded at a rate of 120 frames/s (fps) in successive planes. Periodic contractions were reconstructed in three dimensions using postacquisition synchronization of 48hpf embryonic hearts. (B) Comparison of myocardial wall shape in *desma*$^{sa5+/+}$, *desma*$^{sa5-/-}$ and *ct122aGt* 4D reconstructed hearts shows a squeezing of the ventricle in both mutants (Supplementary Videos 2,3,4). The lower panels show a zoom of an optical transverse section through the middle of the ventricle of *desma*$^{sa5+/+}$, *desma*$^{sa5-/-}$ and *ct122aGt* revealing the squeezing in absence of functional Desma (red arrows). (C) Schematic drawing recapitulating the myocardial movements associated with heart contraction and the subsequent movement of the atrio-ventricular canal (AVC). Examples of AVC cells tracks are shown in the lower panel. Their velocity was used as a readout of the global contraction pattern of the heart. (D) Graph representing the velocity of myocardial cell motion in the AVC region following 3D cell tracking in *desma*$^{sa5+/+}$, *desma*$^{sa5-/-}$ and *ct122aGt* (E). Individual nuclei were tracked automatically and their speed was extracted. *ct122aGt* indicates *desma*^{ct122aGt} homozygous embryos.

(see figure on the next page)

Manuscript 2/ Figure 6: Ca^{2+} propagation in the beating heart is deficient in the absence of functional desmin.

(A) Snapshots from videos corresponding to the 4D reconstructions of a single heart beat in Tg(myl7:GalFF; UAS:Gcamp3.0) WT, desmasa5-/- and ct122aRGt 48hpf embryos (Supplementary Videos 5,6,7) show perturbations in the Ca^{2+} signal at the ventricle tip in the absence of functional Desma. (B) Ca2+ intensity plots and quantification of the amplitude of the Ca2+ peak upon contraction in four different regions of the heart (1, inflow tract; 2, atrium outer curvature; 3, ventricle proximal outer curvature; 4, ventricle distal outer curvature). The amplitude is significantly reduced in region 3 of the desmasa5-/- and in regions 3 and 4 of the ct122aRGt (n=5 embryos, n≥10 cells for each condition). Plots correspond to a representative exemple of each conditions. Note that the heart contraction sequences for each conditions are not starting at the same moment of the contraction cycle. Grey arrows indicate the direction of blood flow through the heart. ct122aRGt indicates desmact122aRGt homozygous embryos.

Material and Methods

Zebrafish Husbandry and Embryo Treatments

The following zebrafish lines were used in this study: wild-type AB, *desma*^{ct122Gta} and *desma*^{ct122aRGt} lines [28], *desma*^{sa5}[41], *Tg(myl7:egfp)* [42], *Tg(myl7:ras-eGFP)*^{s883} [43], *Tg(fli1a:neGFP)*^{y7} (Roman et al., 2002), *Tg(fli:gal4FF*^{ubs}*; UAS:kaede)* [44], *Tg(myl7:GalFF; UAS:RFP)*^{hu6228} [45], *Tg(UAS:gcamp3.0; Gal4s1020t)*[36] and were described previously. Embryos were staged according to hours (hpf) and days postfertilization (dpf). They were incubated at 28.5°C in 0.3% Danieau medium supplemented with 0.003% (wt/vol) 2-phenylthiourea to inhibit pigment formation. All zebrafish strains were maintained at the IGBMC under standard husbandry conditions. Animal experiments were approved by the Animal Experimentation Committee of the Institutional Review Board of the IGBMC.

desma^{Sa5} fish were genotyped using the following primers: FP: ACACACACTCGCCAAACAAA and RP: GTCTCAGCAACTTCCGGTTC.

For imaging, embryos were anesthetized with 0.02% Tricaïne (Sigma Aldrich, Saint-Louis, USA) solution and were mounted on glass bottom Petri dishes embedded in 0.8% low melting point (LMP) agarose (Sigma Aldrich). Before fixation for electron microscopy and still heart imaging, embryos were treated for 10 min with 40 mM 2,3-Butanedione monoxime (BDM) as a myosin inhibitor to have their muscle in a constant relaxed state. Doxycycline (Sigma Aldrich) was supplemented in the fish medium from 12hpf at 10µg/mL.

Morpholino knockdown and mRNA rescue

One translation start site blocking and one splice site blocking morpholino were designed to knockdown zebrafish *desma* (Gene Tools, Philomath, USA). Their sequences are respectively: *desma* ATG MO: (translational) GGCTGAATATTTCGTGCTCATGACT, *desma* splice MO (exon 2-intron 2): ATGACATAAAGTACATACAGCTCTG. *desma* ATG mismatched morpholino (GGCTCAAAATTTGGTCCTCATCACT) was used as control.

Morpholinos were dissolved in water to a concentration of 100µM and 2,3nL were injected into embryos at 1 cell stage. For rescue experiments in *desma*$^{sa5-/-}$, full-length zebrafish *desma* cDNA was obtained in pME18SFL3 (Source Bioscience, Nottingham, UK) and amplified using TAATACGACTCACTATAGGGACCATGAGCACGAAATATTCAGC and GGATCCAGACATGATAAGATAC primers. The resulting fragments were transcribed *in vitro* using mMessage mMachine T7 Kit (Ambion, Austin, USA). 0,25ng of the mRNA was injected into embryos at the one-cell stage.

Bright field Imaging

Imaging of whole embryos was performed using a Leica (Wetzlar, Germany) M420 bright field macroscope. The touch evoke response assay was performed using a Photron SA3 high speed CMOS camera (Photron, San Diego, CA) mounted on a Leica Z6 APO optical system. Fish trajectories were measured on minimal projections using ImageJ (NIH, USA).

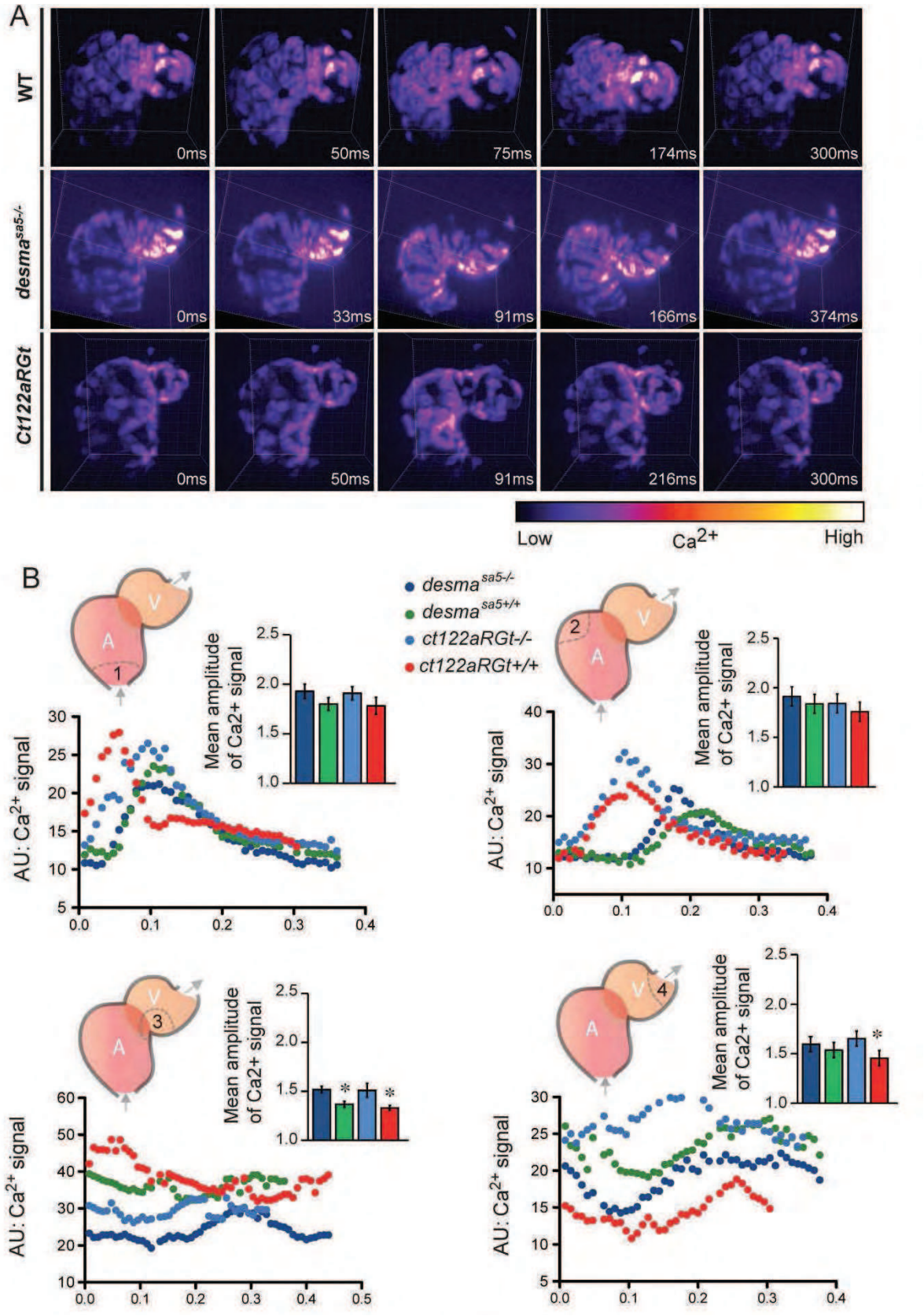
A
WT
0ms
50ms
75ms
174ms
300ms
desma sa5-/-
0ms
33ms
91ms
166ms
374ms
Ct122aRGt
0ms
50ms
91ms
216ms
300ms
Low
Ca2+
High
B
desma sa5-/-
desma sa5+/+
ct122aRGt-/-
ct122aRGt+/+
V
A
1
2
3
4
AU: Ca2+ signal
Mean amplitude of Ca2+ signal
*

Fractional shortening and arterial blood velocity measurements were obtained from bright field imaging in transmission configuration using white light illumination. These experiments were performed on a Leica DMIRBE inverted microscope using Photron SA3 high speed CMOS camera. For the fractional shortening measurements, time-lapse sequences were acquired at 500 frames per second (fps) using a Leica (20x, N.A=0.7) water immersion objective. For the blood cell tracking experiments, the time-lapse sequences were acquired at 250fps with a Leica (63x, N.A=1.2) water immersion objective. The velocity of red blood cells was determined by manual tracking using ImageJ. All microscopy setups used were equipped with a heating device that ensured the embryos were kept at 28°C during imaging.

Confocal imaging

Confocal images were acquired using a Leica SP2 microscope equipped with Leica (20x, N.A=0.7) water or (63x, N.A=1.2) oil immersion objectives except when mentioned differently in this section. Second harmonic generation for label-free visualization of sarcomere structures was generated using a Coherent (Santa-Clara, USA) multi-photon laser at 940nm on a Leica TCP SP5 direct microscope using a low magnification water immersion objective (Leica, 25x, N.A=0.95). A lambda/4 quarter-wave plate was inserted into the excitation light path to provide circular polarization and ensure homogeneous (orientation independent) SHG signal.

Semi-correlative light and electron microscopy and tomography

The general method of correlative light and electron microscopy was mostly performed as in [46]. Individual embryos, previously injected with 2.3nL of 200ng/µL H_2B-Cerulean mRNA to label nuclei as landmarks, were mounted in 0.8% LMP agarose and imaged using a Leica SP5 inverted microscope using a low magnification water immersion objective (Leica, 20x/0.7NA). The region of interest was defined using the excretory canal as a landmark and keeping track of the depth into the sample. Then samples were fixed with 2.5% glutaraldehyde and 2.5% formaldehyde solution in 0.1M cacodylate buffer (pH 7,2) overnight at 4°C. Samples were rinsed two times in cacodylate buffer followed by a 1 hour post-fixation incubation in 1% osmium tetroxide [OsO4] reduced by 1% potassium ferricyanure [K3Fe(CN)6] in the dark on ice. Samples were washed once in cacodylate buffer and after extensive rinses in distilled water, an *en bloc* staining was carried out by incubating in 1% uranyl acetate, for 2 hours on ice, then rinsed in water. Dehydration was performed in graded series of ethanol solutions (50%, 70%, 90% and 100%; quickly rinsed and incubated for 20min each), to be then infiltrated with epoxy resin again through a graded series of dilutions (25%, 50%, 75% for 45 min each and 100% 2 times for 1,5 hours). The blocs were finally polymerized at 60°C for 48 hours. For electron tomography, semi-thin sections (250 nm) were generated using an ultracut UCT ultramicrotome (Leica Microsystems, Vienna, Austria) and histological diamond knife. Sections were picked up on 1% pioloform coated copper slot grids (Electron Microscopy Sciences) and contrasted with uranyl acetate (30 min) and lead citrate (15 min). Automated data acquisition of the single tilt series through an angular range of -68° to +68° (*ct122aGt*) and -63° to 68° (*ct122aRGt*) with 1° increments was performed using a field emission gun electron microscope operating at 200kV (Tecnai F20; FEI

Company, Eindhoven, The Netherlands). Images were acquired on a Gatan 2K CCD camera controlled by the Xplore3D software (FEI). Tomograms and 3D models were computed using Etomo and Imod (Kremer et al., 1996; Mastronarde et al., 1997). For serial sections and morphological studies, ultrathin sections (60 nm) were cut with an ultracut UCT and ultrathin diamond knife and were collected on 1% pioloform coated copper slot grids in an ordered manner. They were then stained with uranyl acetate (20 min) and lead citrate (10 min) and observed with a transmitted electron microscope (CM12, Philips; FEI Electron Optics, Eindhoven, the Netherlands) operated at 80kV. Images were acquired using an Orius 1000 ccd camera (Gatan, Pleasanton, USA).

4D reconstruction of heart contraction and Ca^{2+} transient analysis

4D imaging of the myocardium (*desma*^{sa5}; *Tg(myl7:egfp)* and *desma*^{ct122aGt} and of myocardial Ca^{2+} transient (*desma*^{Sa5}; *Tg(myl7:GalFF; UAS:Gcamp*) and *desma*^{ct122aRGt}, *Tg(myl7:GalFF; UAS:Gcamp)*) were performed using a Zeiss LSM 780 live microscope and the Multiple Time Series Macro (MTS) macro. Consecutive xy(c)tz time-lapse acquisitions every 2µm through the complete heart were recorded with a frame rate of 60fps (80 frames acquired per position) for myocardium and *ct122aGt* imaging and 120fps (120 frames acquired per position) for Ca^{2+} imaging. Time series were acquired at a random time during the cardiac contraction cycle. Realignment of stacks was obtained using the custom-made software [47].

To quantify the overall contraction profile of the heart, bulges corresponding to nucleus position in *Tg(myl7:egfp)* embryos and groups of aggregates in *ct122aGt* were tracked automatically using Imaris (Bitplane, Zurich, Switzerland) and velocity profiles were extracted. Landmarks in the atrio-ventricular canal (AVC) region were selected as a readout of the overall heart contraction profile. For Ca^{2+} intensity measurements, the background of reconstructed stacks was subtracted and the signal was segmented automatically using a custom made macro on Image J (Java). The volume segmentation, cell tracking and intensity measurements were done using Imaris (Bitplane). Cells in 4 regions of interest of the heart, namely the base of the atrium, top of the atrium, tip of the ventricle and middle of the ventricle outer curvature, were selected. The Gcamp3.0 fluorescent intensity profile was extracted in Excel (Microsoft Office) and the amplitude of the peak was measured by taking the ratio between the minimal and maximal intensity reached.

RT-qPCR

RNA was extracted from a pool of 30 whole embryos from 48 to 96hpf using Trizol reagent (Invitrogen, Carlsbad, USA) according to the manufacturer's instructions. A DNAse step followed by column purification was performed using material and instructions from the NucleoSpin RNA XS Kit (Macherey-Nagel, Düren, Germany). cDNAs were synthetized from 1µg of total RNA using SuperScript VILO^{TM} reverse transcriptase (Invitrogen). Quantitative PCR amplification of cDNAs was performed using the Universal Probe Library system (UPL) (Roche Applied Sciences, Basel, Switzerland) on Light Cycler 480 (Roche Applied Sciences). *tbp* was used as a control as expression of this gene varies little during zebrafish development. The sequences of primers used were: *desma* (F: GGTCTTCACGAAGAGATTGCAT, R: CATCTGGTTCTGCAGCTCAC), *desmb* (F:

CATCGCTGCCAAGAACATC, R: GCCTGGTTAAGATCCGACAC), *tbp* (F: TCTTCAGCTCGGGGAAGAT, R: TGCCAATCGAGACTGTTCCT).

Western blotting

Zebrafish embryos were deyolked using deyolking buffer (55mM NaCl, 1.8mM KCl, 1.25mM $NaHCO_3$) and washed with 110mM NaCl, 3.5mM KCl, 2.7mM $CaCl_2$, 10mM Tris HCl, pH8.5. They were lysed in buffer containing 10mM Tris HCl, pH 8, 20% Glycérol, 0,4M KCl, 1X protease inhibitor mixture (Complete Mini, Roche Diagnostics), 10 µL/ml VanNa and 20 µL/ml NaF. Full protein extracts were loaded on SDS-PAGE gel (10%), transferred to nitrocellulose membrane and stained with Ponceau (Biorad, Hercules, USA) to verify equal loading. The blots were probed overnight with antibodies specific for Desmin (polyclonal rabbit anti-desmin D3231, Sigma-Aldrich) and beta-actin (monoclonal mouse anti-beta-actin 2D8, IGBMC, Illkirch, France). Detection was carried out using enhanced chemiluminescence (GE Healthcare, Cleveland, USA).

Quantifications and statistical analysis

Size and numbers of aggregates in *ct122aGt* skeletal muscles upon treatments were measured manually using ImageJ (NIH). Circulating vessels were counted manually under a Leica DMIRBE inverted microscope with Leica (20X, N.A.=0.7) objective. Vessel diameters were measured manually using ImageJ (NIH).

Data were statistically analysed in Excel (Microsoft Office) by parametric Student t-test and were considered significant when $p<0.05$ (*) ; ** means $p<0.01$. Error bars depict SEM. Values in the text are presented as mean ± SEM.

ACKNOWLEDGEMENTS

We thank Emily Steed and Denise Paulin for thoughtful comments on the manuscript. We thank Salim Abdelilah-Seyfried, Markus Affolter and Claire Wyart for providing fish stocks. We thank Stephane Roth for technical help. We thank the IGBMC fish facility (Sandrine Geschier and Sylvie Gredler) and the IGBMC imaging center, in particular Pascal Kessler, Marc Koch and Didier Hentsch. This work was supported by HFSP, INSERM, AFM, FRM and the seventh framework program (MC-IRG256549 (JV)). CR was supported by the AFM.

References

1. van Spaendonck-Zwarts KY, van Hessem L, Jongbloed JD, de Walle HE, Capetanaki Y, et al. (2011) Desmin-related myopathy. Clinical genetics 80: 354-366.

2. Goldfarb LG, Dalakas MC (2009) Tragedy in a heartbeat: malfunctioning desmin causes skeletal and cardiac muscle disease. J Clin Invest 119: 1806-1813.

3. Sugawara M, Kato K, Komatsu M, Wada C, Kawamura K, et al. (2000) A novel de novo mutation in the desmin gene causes desmin myopathy with toxic aggregates. Neurology 55: 986-990.

4. Pinol-Ripoll G, Shatunov A, Cabello A, Larrode P, de la Puerta I, et al. (2009) Severe infantile-onset cardiomyopathy associated with a homozygous deletion in desmin. Neuromuscul Disord 19: 418-422.

5. Henderson M, De Waele L, Hudson J, Eagle M, Sewry C, et al. (2013) Recessive desmin-null muscular dystrophy with central nuclei and mitochondrial abnormalities. Acta neuropathologica 125: 917-919.

6. Griggs R, Vihola A, Hackman P, Talvinen K, Haravuori H, et al. (2007) Zaspopathy in a large classic late-onset distal myopathy family. Brain : a journal of neurology 130: 1477-1484.

7. Hnia K, Tronchere H, Tomczak KK, Amoasii L, Schultz P, et al. (2011) Myotubularin controls desmin intermediate filament architecture and mitochondrial dynamics in human and mouse skeletal muscle. The Journal of clinical investigation 121: 70-85.

8. Selcen D, Muntoni F, Burton BK, Pegoraro E, Sewry C, et al. (2009) Mutation in BAG3 causes severe dominant childhood muscular dystrophy. Annals of neurology 65: 83-89.

9. Vorgerd M, van der Ven PF, Bruchertseifer V, Lowe T, Kley RA, et al. (2005) A mutation in the dimerization domain of filamin c causes a novel type of autosomal dominant myofibrillar myopathy. American journal of human genetics 77: 297-304.

10. Li Z, Colucci-Guyon E, Pincon-Raymond M, Mericskay M, Pournin S, et al. (1996) Cardiovascular lesions and skeletal myopathy in mice lacking desmin. Developmental biology 175: 362-366.

11. Milner DJ, Weitzer G, Tran D, Bradley A, Capetanaki Y (1996) Disruption of muscle architecture and myocardial degeneration in mice lacking desmin. J Cell Biol 134: 1255-1270.

12. Lacolley P, Challande P, Boumaza S, Cohuet G, Laurent S, et al. (2001) Mechanical properties and structure of carotid arteries in mice lacking desmin. Cardiovascular research 51: 178-187.

13. Anderson J, Li Z, Goubel F (2001) Passive stiffness is increased in soleus muscle of desmin knockout mouse. Muscle Nerve 24: 1090-1092.

14. Shardonofsky FR, Capetanaki Y, Boriek AM (2006) Desmin modulates lung elastic recoil and airway responsiveness. Am J Physiol Lung Cell Mol Physiol 290: L890-896.

15. Balogh J, Merisckay M, Li Z, Paulin D, Arner A (2002) Hearts from mice lacking desmin have a myopathy with impaired active force generation and unaltered wall compliance. Cardiovasc Res 53: 439-450.

16. Costa ML, Escaleira R, Cataldo A, Oliveira F, Mermelstein CS (2004) Desmin: molecular interactions and putative functions of the muscle intermediate filament protein. Braz J Med Biol Res 37: 1819-1830.

17. Rezniczek GA, Konieczny P, Nikolic B, Reipert S, Schneller D, et al. (2007) Plectin 1f scaffolding at the sarcolemma of dystrophic (mdx) muscle fibers through multiple interactions with beta-dystroglycan. The Journal of cell biology 176: 965-977.

18. Forouhar AS, Liebling M, Hickerson A, Nasiraei-Moghaddam A, Tsai HJ, et al. (2006) The embryonic vertebrate heart tube is a dynamic suction pump. Science 312: 751-753.

19. Raats JM, Schaart G, Henderik JB, van der Kemp A, Dunia I, et al. (1996) Muscle-specific expression of a dominant negative desmin mutant in transgenic mice. European journal of cell biology 71: 221-236.

20. Kostareva A, Sjoberg G, Bruton J, Zhang SJ, Balogh J, et al. (2008) Mice expressing L345P mutant desmin exhibit morphological and functional changes of skeletal and cardiac mitochondria. J Muscle Res Cell Motil 29: 25-36.

21. Joanne P, Chourbagi O, Hourde C, Ferry A, Butler-Browne G, et al. (2013) Viral-mediated expression of desmin mutants to create mouse models of myofibrillar myopathy. Skeletal muscle 3: 4.

22. Wang X, Osinska H, Dorn GW, 2nd, Nieman M, Lorenz JN, et al. (2001) Mouse model of desmin-related cardiomyopathy. Circulation 103: 2402-2407.

23. Wang X, Osinska H, Klevitsky R, Gerdes AM, Nieman M, et al. (2001) Expression of R120G-alphaB-crystallin causes aberrant desmin and alphaB-crystallin aggregation and cardiomyopathy in mice. Circ Res 89: 84-91.

24. Herrmann H, Strelkov SV, Burkhard P, Aebi U (2009) Intermediate filaments: primary determinants of cell architecture and plasticity. The Journal of clinical investigation 119: 1772-1783.

25. Bar H, Fischer D, Goudeau B, Kley RA, Clemen CS, et al. (2005) Pathogenic effects of a novel heterozygous R350P desmin mutation on the assembly of desmin intermediate filaments in vivo and in vitro. Human molecular genetics 14: 1251-1260.

26. Bar H, Schopferer M, Sharma S, Hochstein B, Mucke N, et al. (2010) Mutations in desmin's carboxy-terminal "tail" domain severely modify filament and network mechanics. Journal of molecular biology 397: 1188-1198.

27. Bar H, Mucke N, Kostareva A, Sjoberg G, Aebi U, et al. (2005) Severe muscle disease-causing desmin mutations interfere with in vitro filament assembly at distinct stages. Proc Natl Acad Sci U S A 102: 15099-15104.

28. Trinh le A, Hochgreb T, Graham M, Wu D, Ruf-Zamojski F, et al. (2011) A versatile gene trap to visualize and interrogate the function of the vertebrate proteome. Genes Dev 25: 2306-2320.

29. Brodehl A, Hedde PN, Dieding M, Fatima A, Walhorn V, et al. (2012) Dual color photoactivation localization microscopy of cardiomyopathy-associated desmin mutants. The Journal of biological chemistry 287: 16047-16057.

30. Schroder R, Schoser B (2009) Myofibrillar myopathies: a clinical and myopathological guide. Brain pathology 19: 483-492.

31. Mojzisova H, Vermot J (2011) When multiphoton microscopy sees near infrared. Curr Opin Genet Dev 21: 549-557.

32. Villarreal F, Lew WY (2010) Protein quality control in heart disease: using established drugs to target novel mechanisms. Journal of the American College of Cardiology 56: 1427-1429.

33. Clemen CS, Herrmann H, Strelkov SV, Schroder R (2013) Desminopathies: pathology and mechanisms. Acta neuropathologica 125: 47-75.

34. Anton H, Harlepp S, Ramspacher C, Wu D, Monduc F, et al. (2013) Pulse propagation by a capacitive mechanism drives embryonic blood flow. Development 140: 4426-4434.

35. Freund JB, Goetz JG, Hill KL, Vermot J (2012) Fluid flows and forces in development: functions, features and biophysical principles. Development 139: 1229-1245.

36. Warp E, Agarwal G, Wyart C, Friedmann D, Oldfield CS, et al. (2012) Emergence of patterned activity in the developing zebrafish spinal cord. Current biology : CB 22: 93-102.

37. Chi NC, Bussen M, Brand-Arzamendi K, Ding C, Olgin JE, et al. (2010) Cardiac conduction is required to preserve cardiac chamber morphology. Proceedings of the National Academy of Sciences of the United States of America 107: 14662-14667.

38. Gard JJ, Yamada K, Green KG, Eloff BC, Rosenbaum DS, et al. (2005) Remodeling of gap junctions and slow conduction in a mouse model of desmin-related cardiomyopathy. Cardiovascular research 67: 539-547.

39. Agullo-Pascual E, Cerrone M, Delmar M (2014) Arrhythmogenic cardiomyopathy and Brugada syndrome: diseases of the connexome. FEBS letters 588: 1322-1330.

40. Asimaki A, Kapoor S, Plovie E, Karin Arndt A, Adams E, et al. (2014) Identification of a new modulator of the intercalated disc in a zebrafish model of arrhythmogenic cardiomyopathy. Science translational medicine 6: 240ra274.

41. Kettleborough RN, Busch-Nentwich EM, Harvey SA, Dooley CM, de Bruijn E, et al. (2013) A systematic genome-wide analysis of zebrafish protein-coding gene function. Nature 496: 494-497.

42. Huang CJ, Tu CT, Hsiao CD, Hsieh FJ, Tsai HJ (2003) Germ-line transmission of a myocardium-specific GFP transgene reveals critical regulatory elements in the cardiac myosin light chain 2 promoter of zebrafish. Developmental dynamics : an official publication of the American Association of Anatomists 228: 30-40.

43. D'Amico L, Scott IC, Jungblut B, Stainier DY (2007) A mutation in zebrafish hmgcr1b reveals a role for isoprenoids in vertebrate heart-tube formation. Current biology : CB 17: 252-259.

44. Herwig L, Blum Y, Krudewig A, Ellertsdottir E, Lenard A, et al. (2011) Distinct cellular mechanisms of blood vessel fusion in the zebrafish embryo. Current biology : CB 21: 1942-1948.

45. Thessadori F, Bakkers J (submitted).

46. Goetz JG, Monduc F, schwab Y, Vermot J (in press) Using Correlative Light and Electron Microscopy to Study Zebrafish Vascular Morphogenesis. Methods in Cell Biology.

47. Liebling M, Forouhar AS, Gharib M, Fraser SE, Dickinson ME (2005) Four-dimensional cardiac imaging in living embryos via postacquisition synchronization of nongated slice sequences. Journal of biomedical optics 10: 054001.

Supporting information

Supplementary figures (intercalated previously)

Supplementary videos:

Supplementary Video 1: Serial electron micrograph sections were reconstructed to show a citrine tagged aggregate in its cellular context in 52hpf *ct122aGt* skeletal muscle. Segmentation shows the aggregate in green, the borders of the sarcomeres in red, the nuclear envelope in blue and the mitochondria are punctuated in yellow.

Supplementary Video 2: 4D reconstruction of heart wall dynamics of a *desma$^{sa5+/+}$; Tg(myl7:egfp)* embryo at 48 hpf, obtained by serial time-lapse imaging with a line-scanning microscope and post-acquisition synchronization and reconstruction.

Supplementary Video 3: 4D reconstruction of heart wall dynamics of a *desma$^{sa5-/-}$; Tg(myl7:egfp)* embryo at 48 hpf, obtained by serial time-lapse imaging with a line-scanning microscope and post-acquisition synchronization and reconstruction.

Supplementary Video 4: 4D reconstruction of heart wall dynamics of a *ct122aGt* embryo at 48 hpf, obtained by serial time-lapse imaging with a line-scanning microscope and post-acquisition synchronization and reconstruction.

Supplementary Video 5: 4D reconstruction of heart wall dynamics in the presence of the GCamp3.0 calcium indicator in a *desma$^{sa5+/+}$; Tg(myl7:GalFF; UAS:GCamp3.0)* embryo at 48 hpf, obtained by serial time-lapse imaging with a line-scanning microscope and post-acquisition synchronization and reconstruction. A regular propagation of the calcium wave is seen, with a peak of intensity observed in each myocardial zone.

Supplementary Video 6: 4D reconstruction of heart wall dynamics in the presence of the GCamp3.0 calcium indicator in a *desma$^{sa5-/-}$; Tg(myl7:GalFF; UAS:GCamp3.0)* embryo at 48 hpf, obtained by serial time-lapse imaging with a line-scanning microscope and post-acquisition synchronization and reconstruction. The regular propagation of the calcium wave at the tip of the ventricle can be seen to be perturbed.

Supplementary Video 7: 4D reconstruction of heart wall dynamics in the presence of the GCamp3.0 calcium indicator in a *ct122aRGt; Tg(myl7:GalFF; UAS:GCamp3.0)* embryo at 48 hpf, obtained by serial time-lapse imaging with a line-scanning microscope and post-acquisition synchronization and reconstruction. A perturbation of the regular propagation of the calcium wave at the tip and outer curvature of the ventricle can be seen.

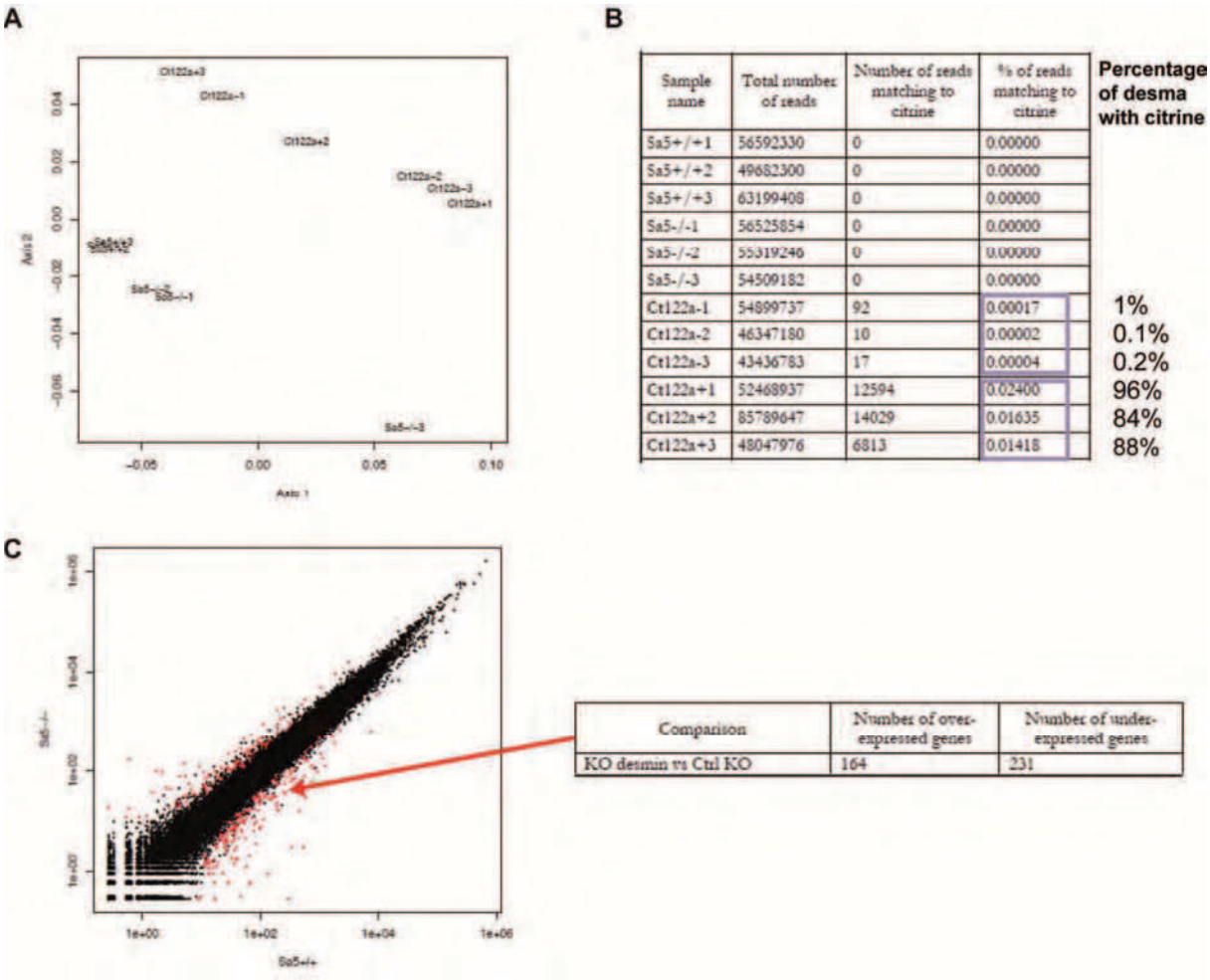

Sample name	Total number of reads	Number of reads matching to citrine	% of reads matching to citrine	Percentage of desma with citrine
Sa5+/+1	56592330	0	0.00000	
Sa5+/+2	49682300	0	0.00000	
Sa5+/+3	63199408	0	0.00000	
Sa5-/-1	56525854	0	0.00000	
Sa5-/-2	55319246	0	0.00000	
Sa5-/-3	54509182	0	0.00000	
Ct122a-1	54899737	92	0.00017	1%
Ct122a-2	46347180	10	0.00002	0.1%
Ct122a-3	43436783	17	0.00004	0.2%
Ct122a+1	52468937	12594	0.02400	96%
Ct122a+2	85789647	14029	0.01635	84%
Ct122a+3	48047976	6813	0.01418	88%

Comparison	Number of over-expressed genes	Number of under-expressed genes
KO desmin vs Ctrl KO	164	231

Figure 17: Graphical results of mRNA sequencing of *desma*$^{sa5-/-}$ and *ct122aGt* 48hpf embryos and their corresponding controls

(A) Graph showing the first factorial plane of a correspondence analysis. Correspondence analysis was calculated on variance stabilized data calculated by the method proposed by Anders and Huber (2010). The first factorial plan is represented on this figure. The first axis explains 48% of the variability and the second axis 15%. (B) Table recapitulating the total number of reads and their content in citrine for the different samples. (C) Gene expression comparison between *desma*$^{sa5-/-}$ and control samples by plotting the number of reads for each gene in one condition *vs.* the other. The plotted red dots correspond to genes with adjusted p-value < 0.05 and |log2Fold Change| > 1. Corresponding significantly differentially expressed genes numbers are summarized in the table on the right.

Supplementary unpublished and preliminary results

1) mRNA sequencing

To better understand the molecular aspects implicated in the establishment of desminopathy phenotype, we performed in parallel the whole mRNA sequencing of *desma*$^{sa5-/-}$ and their *desma*$^{sa5+/+}$ controls as well as of *ct122aGt* samples and their corresponding non-fluorescent siblings. Comparing these conditions enables to assess precisely the implication of the mutated desmin aggregates compared to the implication of desmin loss of function in the disease.

a) Experimental procedure

Step1: RNA extraction (Caroline Ramspacher)
RNA was extracted and purified from three pools of 30 whole 48hpf embryos per condition according to the protocol presented in Manuscript 2 above.
Step2: Samples preparation and sequencing (Claire Feger, Sequencing platform, IGBMC)
After isolation of total cellular RNA, a library of template molecules suitable for high throughput DNA sequencing was created following the Illumina “mRNA sequencing sample preparation guide” (part #1004898 Rev.D) with some modifications. Briefly, mRNA was purified from 2 µg total RNA using oligo-dT magnetic beads and fragmented using divalent cations at 94°C for 5 minutes. The cleaved mRNA fragments were reverse transcribed to cDNA using random primers, then the second strand of the cDNA was synthesized using DNA Polymerase I and RNase H. The next steps of RNA-Seq Library preparation were performed in a fully automated system using SPRIworks Fragment Library System I kit (ref A84801, Beckman Coulter, Inc) with the SPRI-TE instrument (Beckman Coulter, Inc). Briefly, in this system, double stranded cDNA fragments were blunted, phosphorylated and ligated to indexed adapter dimers, and fragments in the range of ~200-400 bp were size selected. The automated steps were followed by PCR amplification (30 sec at 98°C; [10 sec at 98°C, 30 sec at 60°C, 30 sec at 72°C] x 13 cycles; 5 min at 72°C), then surplus PCR primers were removed by purification using AMPure XP beads (Agencourt Biosciences Corporation). DNA libraries were checked for quality and quantified using a 2100 Bioanalyzer (Agilent). The libraries were loaded in the flow cell at 6pM concentration and clusters generated and sequenced in the Illumina Genome Analyzer IIX as single-end 54 base reads.
Step3: Bioinformatics (Céline Keime, Sequencing platform, IGBMC)
The reads’ quality were assessed with FastQC (S. Andrews, http://www.bioinformatics.babraham.ac.uk/projects/fastqc/). Then the reads were mapped onto the zv9 assembly of the zebrafish genome using Tophat v1.4.1 (Trapnell et al., 2009) and the bowtie v0.12.7 aligner (Langmead et al., 2009). Only uniquely aligned reads were retained for further analyses. Gene expression was quantified using HTSeq v0.5.3p5 (http://www-huber.embl.de/users/anders/HTSeq) and gene annotations from Ensembl release 69. Read counts were normalized across libraries with the method proposed by Anders et al. (Anders and Huber, 2010). To identify significantly differentially

Gene name	Description	log2 (KO/Ctrl)	Adjusted p-value
Down-regulated genes			
Immunoglobulin subtypes E=1,57			
zgc:198329	zgc:198329	-2,59	3,08E-08
sc:d217	sc:d217	-1,63	6,46E-03
si:dkey-222f2.7	si:dkey-222f2.7	-1,37	4,58E-02
si:dkey-253d23.4	si:dkey-253d23.4	-3,41	1,66E-14
si:rp71-1i20.2	si:rp71-1i20.2	-1,09	4,85E-02
Up-regulated genes			
Neurotransmitter E=1.30			
gabrr1	gamma-aminobutyric acid (GABA) receptor, rho 1	1,61	4,41E-03
glra4b	glycine receptor, alpha 4b	1,51	1,33E-02
npy8br	neuropeptide Y receptor Y8b	1,54	4,51E-04
Receptors E=1.30			
ddr2b	discoidin domain receptor tyrosine kinase 2b	1,26	1,53E-02
gabrr1	gamma-aminobutyric acid (GABA) receptor, rho 1	1,61	4,41E-03
grin2ab	glutamate receptor, ionotropic, N-methyl D-aspartate 2A, b	1,08	2,59E-02
glra4b	glycine receptor, alpha 4b	1,51	1,33E-02
npy8br	neuropeptide Y receptor Y8b	1,54	4,51E-04
nr1h5	nuclear receptor subfamily 1, group H, member 5	1,48	2,94E-06
Rho	rhodopsin	1,50	1,88E-02
Total list			
Lipid binding proteins			
fabp10a	fatty acid binding protein 10a, liver basic	1,88	4,15E-05
fabp11a	fatty acid binding protein 11a	-3,92	1,56E-19
PTGDS	prostaglandin D2 synthase 21kDa	1,02	4,29E-02
Rho	rhodopsin	1,50	1,88E-02

Table 4 : Gene clusters evidenced by the gene functional classification on David.

expressed genes, adjustment for multiple testing was performed with the Benjamini and Hochberg (Benjamini and Hochberg,1995) method.

Step 4: Interpretation (Caroline Ramspacher)

Enrichment analyses were performed using the gene functional classification tool on DAVID Bioinformatics Resources 6.7 (Huang et al., 2009, Nature Protocols) both from separated lists of up and down-regulated genes and the entire list. The critical value for significant enrichment was set to 1,30.

b) Results

So far, the molecular aspects of desminopathy were only poorly studied. Moreover, it was not possible with previous models to directly compare the impact of desmin loss of function with the defects associated with the presence of desmin aggregates due to differences in genetic background in mouse models. We used two desminopathy models in zebrafish, one KO and one KI model which enable a direct comparison of the “no desmin” and “aggregated desmin” situations. To take further advantage of our models and get molecular insights in desminopathy with an unbiased approach, we performed whole mRNA sequencing in collaboration with the sequencing platform of the IGBMC. The total RNA content of three pools of 30 embryos of *desma*$^{sa5-/-}$, *desma*$^{sa5+/+}$, *Ct122aGt* positive and *Ct122aGt* negative fish were analyzed and compared (Figure 17A). In the case of *desma*$^{sa5-/-}$ and *desma*$^{sa5+/+}$, the different pools of embryos tested had a similar profile on first factorial plane of correspondence analysis. Nevertheless, for the pools corresponding to *ct122aGt* embryos, the profiles were not forming the expected groups as one of the positive embryos sample clustered with the negative embryos and *vice versa*. To verify that the samples were correctly annotated, we compared the number of reads for the citrine mRNA in each condition and confirmed that all the groups annotated positive indeed were (Figure 17B). We therefore decided to consider only the results corresponding to the KO animals, as the variability between *ct122aGt* was too high to get significant results and the number of sample too low to decide to exclude one of them. Comparing the number of reads obtained for each gene in the *desma*$^{sa5-/-}$ and *desma*$^{sa5+/+}$ conditions, 164 genes were found to be significantly up-regulated while 231 down-regulated (Figure 17C). The complete lists of up- and down-regulated genes are presented in Appendix.

After gene functional classification on David, the lists of differentially expressed genes could be sorted into functionally related groups and the enrichment of these groups in our list was calculated. Groups were considered significantly perturbed for enrichment values of 1,30 and above (Table 4). The clusters analyzed included immunoglobulin subtypes, neurotransmitter, receptors and lipid binding proteins, which were not particularly expected. Further analysis and validations would be necessary to confirm the implication of desmin in mechanism related to these gene clusters. In particular, it would be interesting to assess further the role of desmin in lipid metabolism and for organization of the neuromuscular junction (NMJ).

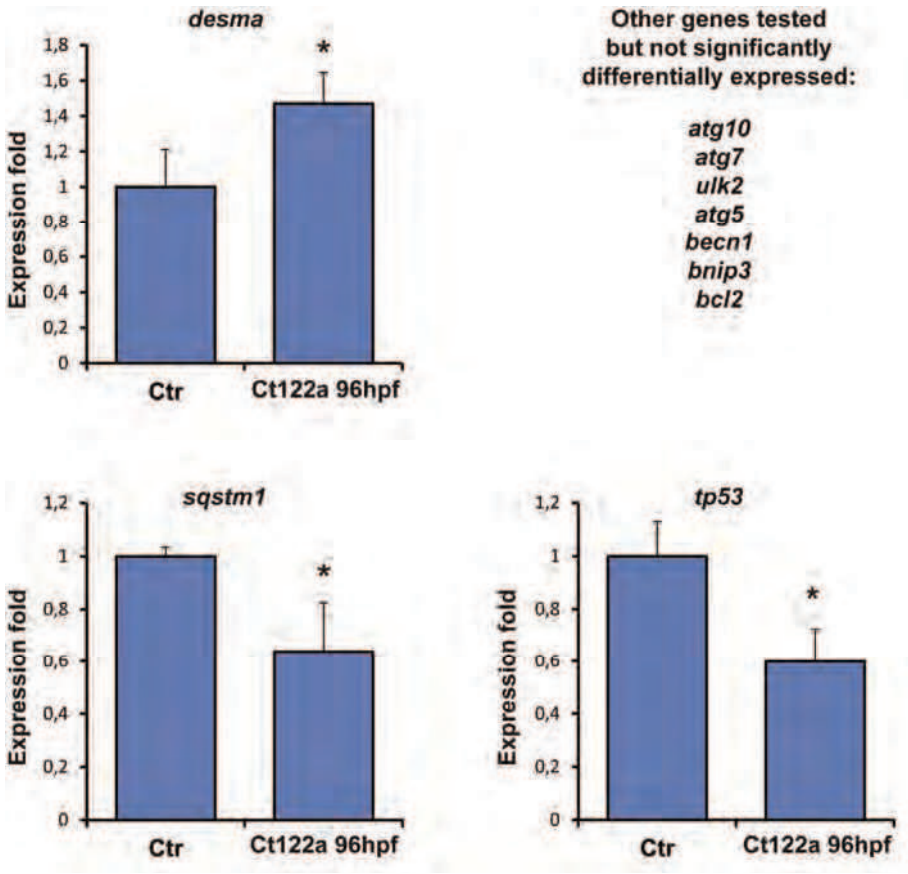

Figure 18: Expression of autophagy genes in 96hpf *ct122aGt* embryos *vs.* control

Quantitative RT PCR on mRNA of ct122aGt 96hpf embryos and their control non-fluorescent siblings. Expressions of *desma*, *sqstm1* and *tp53* were significantly altered and are presented on graphs. Expression of other autophagy related genes presented in the list on the upper right were not found significantly altered.

2) Implication and influence of autophagy in the desminopathy phenotype

a) Status of autophagy in our zebrafish desminopathy model

Autophagy was shown to be up-regulated in mouse models of desmin-related cardiomyopathy (Zheng et al., 2011). However, studies on a mouse model carrying the αB-crystallin mutation ($CRYAB^{R120G}$), promoting desmin aggregation in myocardial cells (Wang et al., 2001b), showed decreased autophagy fluxes (Pattison and Robbins, 2011) and an improvement of mice phenotype and cardiac function upon activation of autophagy (Bhuiyan et al., 2013). Therefore, the effect of desmin aggregation on autophagy seems to be context-dependent and its influence in desminopathy phenotypes remains an open question. Indeed, it is not clear whether autophagy is a direct consequence of desmin aggregates or a secondary reaction to clear-out damaged organelles, nor whether it is an enhancing or ameliorating mechanism in the context of the disease.

To confirm the observation made by electron microscopy suggesting that autophagy is activated in the presence of desmin aggregates in the *ct122aGt* embryos, we decided to perform qPCR for several autophagy genes listed in Figure 18. mRNA was prepared from pools of embryos of 48 (n=6), 72 (n=6) and 96hpf (n=3) but no significant difference was obtained at the two earliest embryonic stages tested (48 and 72hpf). We suspect that it is due to a large variability between samples in both the control and mutant groups, in agreement with the results obtained with the mRNA sequencing.
As an internal control, we tested the expression of *desma* in our desminopathy model line and confirmed that *desma* was upregulated in the context of its mutation and aggregation, as observed in patients (Goldfarb and Dalakas, 2010; Bar et al., 2005). Most of the autophagy genes tested including *atg7*, *atg10*, *ulk2*, *atg5*, *bnip3*, *becn1* and *bcl2* were not significantly differentially expressed. Nevertheless *sqstm1* (p62) and *tp53* were found to be down-regulated. p62 down-regulation was surprising in comparison with desmin-related cardiomyopathy mouse models, where p62 was found to be up-regulated at both the mRNA and protein level (Zheng et al., 2011). p62/SQSMT1 is a non-covalent ubiquitin receptors and mediates recognition of ubiquitinylated proteins during autophagy via their ubiquitin-binding domains (Lippai et al., 2014). Its down-regulation in the zebrafish model therefore suggests a context-dependent repression of selective autophagy pathways in desminopathies. Tp53 functions as a nuclear transcription factor and can induce autophagy through transcriptional effects (in response to DNA damage in tumor cells for example). On the other hand, cytoplasmic Tp53 can act as a repressor of autophagy via poorly characterized mechanisms (Maiuri et al., 2010). Therefore, it is difficult to conclude on the role of *tp53* decrease in our zebrafish desminopathy model and further investigation on the Tp53 protein level and localization should be considered.

b) Effect of activation of autophagy in *ct122aGt* embryos

Induction of autophagy by rapamycin was shown to have a protective role in many proteinopathies, including Huntington disease, tauopathies and certain spinocerebellar ataxias (Berger et al., 2006) by both eliminating toxic forms of the mutated proteins and protecting cells again apoptosis (Ravikumar et al., 2006). Recently activation of autophagy was shown as well to ameliorate survival and cardiac phenotype in CRYAB mutant models of desmin-related cardiomyopathy (Bhuiyan et al., 2013).

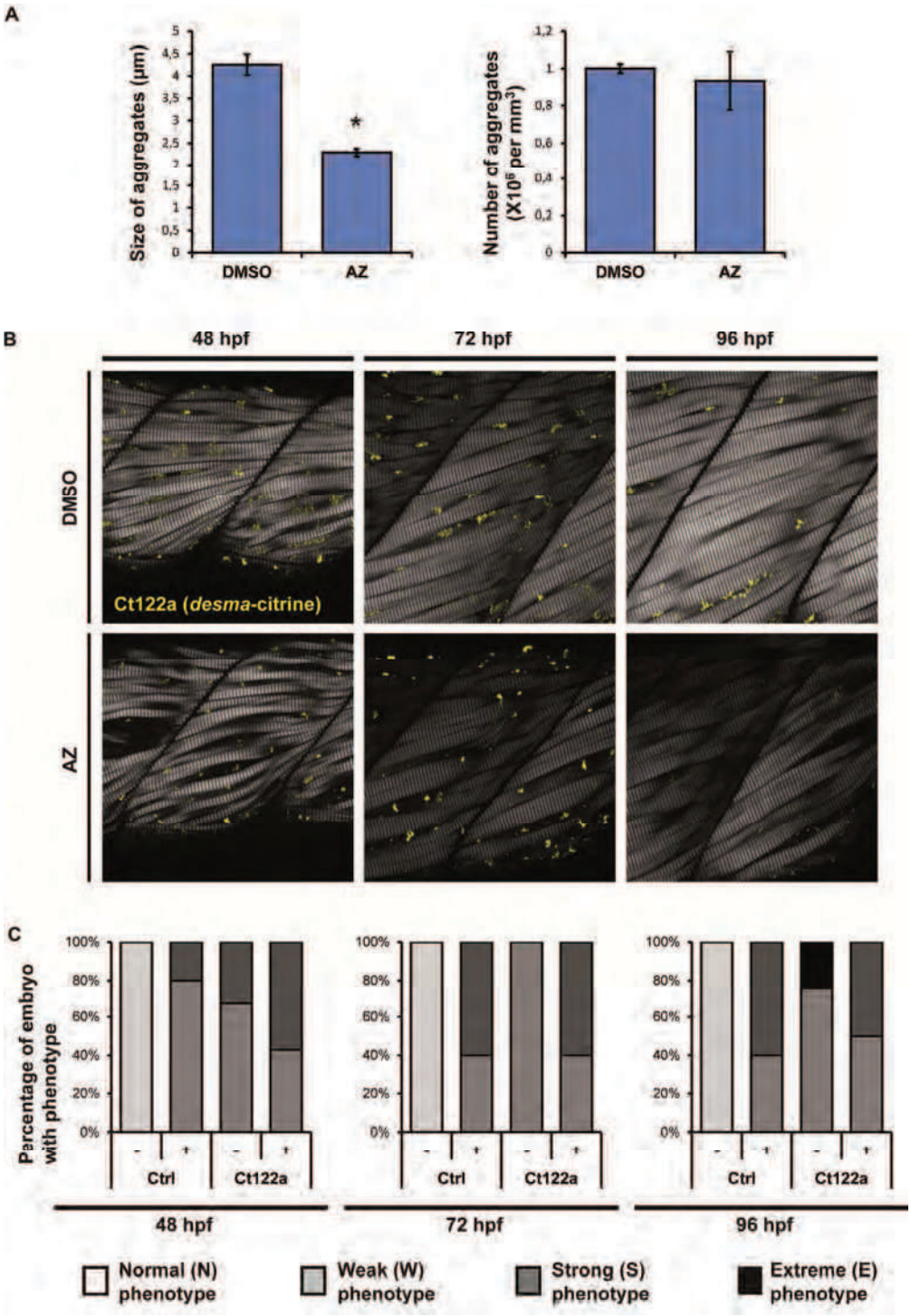

Figure 19: Activating autophagy decreases the size of desmin aggregates but doesn't ameliorate the skeletal muscle phenotype in zebrafish embryos

(A) Graph presenting the diameter and number of aggregates in vehicle (DMSO) and AZ-treated *ct122aGt* 48hpf embryos. (B) Optical sections of the mid trunk region using SHG imaging show misalignment of muscle fibers often accompanied by fiber breaks and degeneration at 48, 72 and 96hpf in both vehicle treated (DMSO) and AZ-treated embryos. The observed phenotypes are even stronger in the case of AZ treatment despite the reduction in desmin aggregates content. (C) Evaluation of the phenotypes of AZ and vehicle treated embryos using SHG and the scale defined in Figure 4C of Manuscript 2 shows that strong phenotypes were observed after AZ treatment in comparison to the controls. *ct122aGt* indicates *desma*^{ct122aGt} homozygous embryos.

We then addressed whether *desma* aggregates would be prone to be uptaken by the autophagy machinery and cleaned out, and whether activation of autophagy would rescue the phenotype in *ct122aGt*. *ct122aGt* embryos were treated from 24hpf with 3µg/mL of the rapamycin homolog S1555 (AZD8055) (AZ) (Selleckchem by Euromedex, Souffelweyersheim, France), which was shown to activate autophagy by inhibiting the mTOR pathway and therefore clear aggregates in proteinopathy (Proenca et al., 2013). Preliminary qPCR results showed up-regulation of *atg10*, *bcl2*, *bnip3*, *park2*, *sqstm1* and *ulk2* upon AZ treatment (results to be confirmed, data not shown) and confirmed the activation of autophagy. We performed SHG imaging at 48, 72 and 96hpf and classified the observed phenotypes as in Manuscript 2. Our results suggest that the skeletal muscle phenotype was not rescued compared to the corresponding controls despite a clear reduction in the aggregates size (Figure 19). Additionally, activation of autophagy led to strong skeletal muscle phenotypes in aggregate-free controls, comparable to those observed in *ct122aGt* individuals. This result suggests that activating autophagy is detrimental to muscle development and could participate in the establishment of desminopathy phenotype, instead of ameliorating it. Another hypothesis is that AZ is toxic at the concentrations that lead to aggregates clearance in the embryo.

3) Optimizing conditions for high-throughput drug screens to discover new aggregate content reducing drugs using the *ct122aGt* embryos.

High throughput drug screening is a method of choice for drug discovery but is difficult to perform with mammalian models due to cost, time and the number of animals required. Assays are often performed on invertebrate or cultured cell models, but they are sometimes too far from the human disease and lack functional outcome measures. Zebrafish model is advantageous as it combines some features of invertebrate models and the vertebrate biological relevance and constitutes a good model organism for novel drug discovery (Gibbs et al., 2013). Nevertheless, these advantages were not used so far in the context of discovery of new drugs decreasing aggregate content in the context of proteinopathies. Having validated our model of desminopathy with a clear readout of the aggregates content thanks to the fluorescent tagging of aggregates, we proposed to use it in a high-throughput drug screen. To do so, the first step was to find a positive control drug which would enable us to set the automated imaging conditions to detect the related difference in aggregate content. For that, we tested *desma* morpholinos and doxycycline (Doxy) and the results are presented in Manuscript 2 above. Doxy was selected for the convenience of its use and its chemical nature, comparable to the compounds we plan to screen, to serve as a positive control in a potential drug screen. After initiating a collaboration with the screening platform of IGBMC (Benoit Fischer, Anne Maglott-Roth, Laurent Brino), we went through the first steps of technical optimization of high-throughput screen on living *ct122aGt* zebrafish together.

a) <u>Problematic and optimization steps</u>

The principal conditions we needed to optimize were the following:

- the volume of medium and concentration of compound (taking into account the limitation of solvent percentage to avoid toxicity),

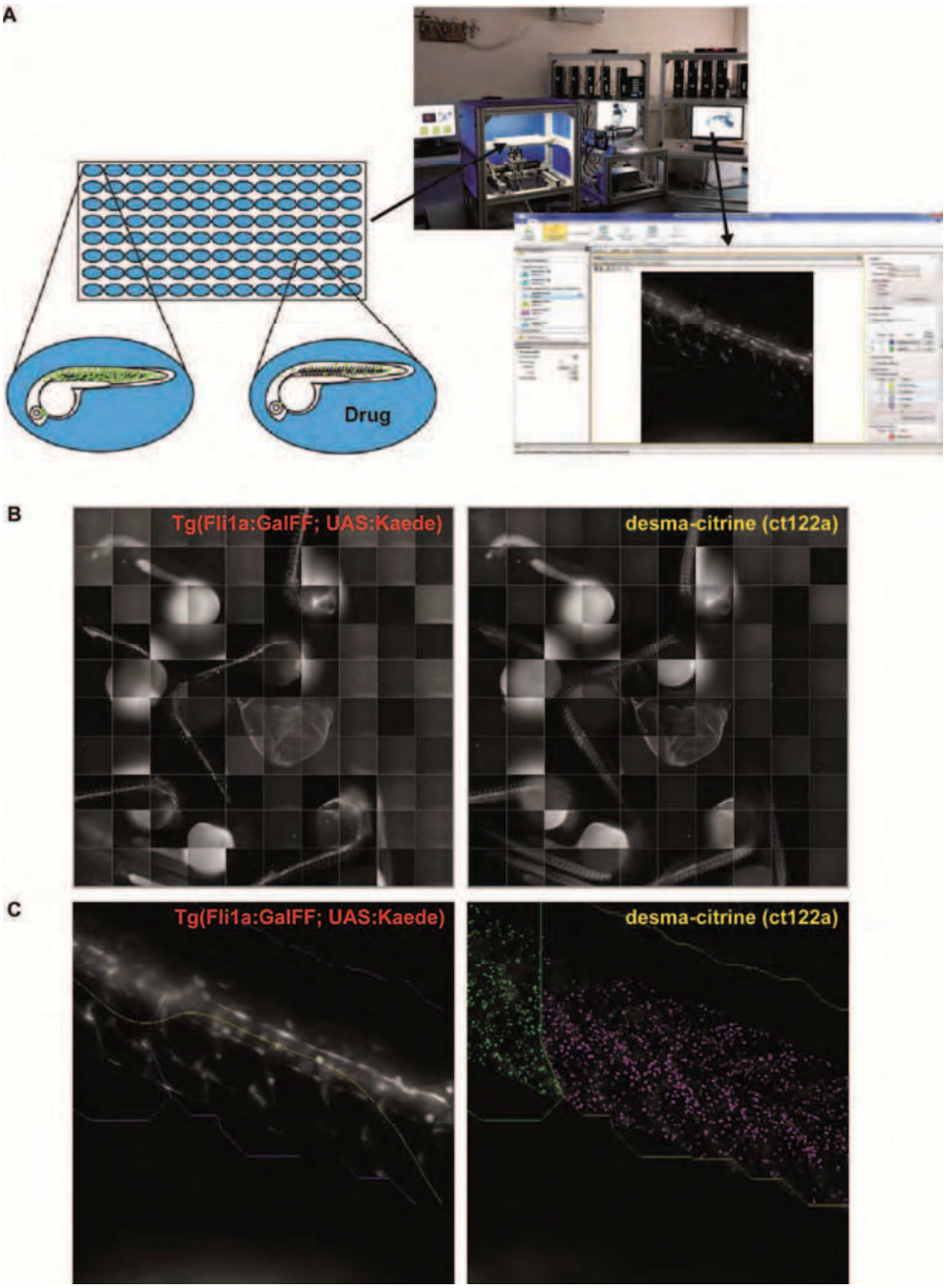

Figure 20: Set-up and obtained images from high-throughput screen tests for identification of chemical compounds able to decrease the aggregate content in *ct122aGt* embryos.

(A) Scheme presenting the principle and the used set-up of the high-throughput drug screen that we began to optimize with the IGBMC screening plateform. *Tg(Fli:GalFF; UAS:Kaede); ct122aGt* embryos were placed in a 96-well plate and treated with vehicle or drugs from 12hpf. At 30hpf, they were imaged using an automated epifluorescence microscope. After photoconversion of the Kaede fluorophore, both RFP (showing the vessels as landmarks) and GFP (showing the citrine aggregates) channels were acquired and the obtained images were automatically analysed using the automated microscope software (Thermofischer). (B) Images showing the reconstructing of a well with the RFP (left) and GFP (right) filters showing the vessels and aggregates in the fish, respectively. (C) Individual images were acquired by the automated epifluorescent microscope and analysed with the “Zebrafish” macro of the microscope software to determine the zone of interest from the vessel landmarks and apply it to the aggregates for measurements and calculations.

- the number of fish to use per well for sufficient statistical analysis without using multiple well for the same drug while avoiding toxicity of overpopulation,
- the necessity of landmarks in the fish to determine zones to be analyzed,
- the combination of colors to use according to the epifluorescence imaging system and the fish lines available for landmarks,
- the dechorionation procedure and timing,
- the treatment and imaging timing,
- the need of agarose coating in the 96well-plate to protect the chorion-free early embryos against exploding,
- the best imaging procedure, determining parameters like exposure mode and time, focus mode etc.,
- the z-sampling to access the total width of embryos,
- the total number of images taken to keep a reasonable (2h) interval between the first and the last imaged well,
- the best software for easy analysis and the most stringent parameters to compare treated and untreated conditions,
- the ability of the system to detect differences in aggregate content using Doxy as a positive control.

b) Selected experimental procedure

At least 1200 *Ct122aGt, Tg(Fli1a; UAS:Kaede)* embryos were collected. At 10hpf, they were dechorionated using 3mg/mL pronase in 0.3%Danieau medium for 1min40, rinsed in 0.3%Danieau and incubated 2h at 28°C in 0.3%Danieau on a 2% agarose coated plate (classical Petri dish). At 12hpf, ten embryos per well were transferred manually into a 96 well plate without agarose coating. For the preliminary optimization test, control EtOH and 10µg/mL Dox were used, diluted in 100µL of 0.3%Danieau, 0.003% PTU medium and pipetted manually. For future large scale screen, we plan to load 100µL of 0.3%Danieau, 0.003% PTU medium containing 0.1µM of the compound to be tested (1%DMSO), pipetted automatically in the wells using a Tecan Freedom EVO 150 liquid handler robot integrated with a microplate POWERWASHER 384. The plate was then incubated at 28°C for 18 hours. At 30hpf, the plate was loaded in a Thermofisher Scientific Cellomics Cell Insight NXT benchtop high-throughput imaging system, coupled with an Orbitor robotic arm with plate stacks to perform high-content analysis. This instrument, equipped with an X1 CCD camera, was used with a 20X Leica objective. Proper exposure time was determined on one well before the screen and was fixed for the whole experiment. The automated microscope was set to image entire wells. The first step consisted of the photo-conversion of Kaede in the endothelium (under the Fli1a promoter), in order to be able to image separately the vessels, as landmarks (red), and the aggregates (yellow-green). Photo-conversion was performed on each entire well just before it was imaged by 15s exposure with DAPI filter at 100% intensity. Then, for image acquisition, an autofocus mode was used and 5 z-stacks 15µm apart and centered on the z of autofocus were imaged with GFP and RFP filters. A maximal projection of these stacks was presented as an output. The “Zebrafish” macro on the Thermofisher

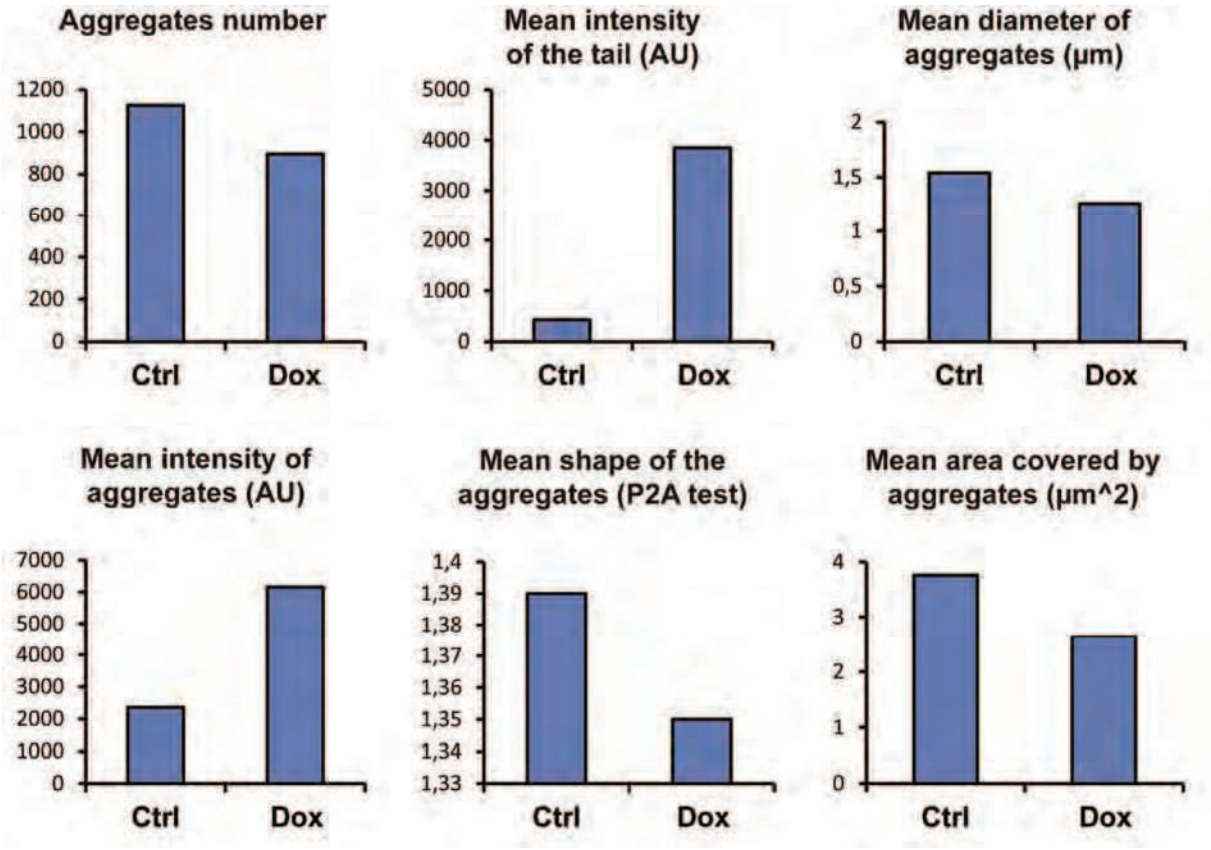

Figure 21: Preliminary results obtained with the positive control Doxycycline (Dox) while testing conditions for high-throughput drug screens for desmin aggregation decrease in *ct122aGt*

Graph showing the number of aggregates detected by the "Morphology" macro and studied for each condition, the mean intensity of the whole fish tail, the mean diameter of the detected aggregates, the mean intensity of individual aggregates, the mean shape of the aggregates using the P2A test (P2A value close to 1 indicate a sphere while higher values represent more elongated structures) and the mean total area covered by aggregates per tail (n=3).

Scientific Cellomics Cell Insight software was used to determine the position of the embryos' tails using the vascular landmarks. The "Morphology" macro was then use to measure the number, diameter, sphericity, surface area on maximal projections and intensity of the aggregates (Figure 20).

c) Preliminary results

Preliminary experiments performed compared only vehicle-treated (EtOH) and Doxy-treated embryos, and analysis was performed on a small number of embryos only (n=3). Further testing should be considered before going large-scale with compounds to test. The number of detected and studied aggregates was lower in the context of Doxy-treated embryos but was not normalized to a studied surface (Figure 21). They are therefore not comparable with the manually counted values presented in Manuscript 2. The intensities of the whole tail and individual aggregates, as well as the sphericity of aggregates were higher in the case of Doxy, corresponding to previous results using confocal microscopy and reflecting the higher condensation observed for Doxy aggregates (Ramspacher et al., manuscript 2). The mean diameter of aggregates was lower in Doxy treated *ct122aGt* embryos as observed previously. Nevertheless the difference between treated and un-treated aggregates size was not as important as previously measured, with the un-treated aggregates appearing smaller. This is possibly due to a bias in the automated detection system detecting big aggregates as many separate aggregates of a smaller size. Finally, the total coverage of aggregates was found to be lower as expected. Further tests should be performed on a higher number of fish and in real high-throughput conditions to finalize the optimization steps of this high-throughput drug screen. One or two of these parameters should then be selected as readout of the aggregates diminution. Preliminary results encourage choosing the mean area covered by aggregates.

Chapter II:

Validating zebrafish use and generating models for vascular pathologies including hypertension and PVOD

I/ Verifying the Windkessel model in zebrafish embryo for a better understanding of arterial stiffness implication in hypertension.

Foreword

Cardiovascular performance was shown to depend not only on the heart's pumping efficiency but also on the pressure-buffering properties and elasticity of the arteries (Coutinho et al., 2014; Westerhof et al., 2009). In particular, the lack of elasticity of arteries leads to hypertension and to a range of cardiac clinical manifestations in response to the system's adaptation to high pressure. For efficient blood flow transmission to the organs, the compliance of arteries is needed as it permits to transform the pulsatile flow ejected by the heart into a constant flow. This was described previously and modelled in the adult human system by the so-called Windkessel model (Westerhof et al., 2009). In this system, the Reynolds number, which depends on the vessel diameter, the flow velocity and viscosity, and which predicts the flow pattern of blood, was estimated typically around 1000 to 2000. The higher the Reynolds number is, the more prone to turbulence the flow is. Moreover, the peak Reynolds number in the human aorta has been measured to be approximately 4000 and pathological hypertension conditions lead to an average number of around 3000, showing a transition to a turbulent vascular flow in some specific location or situations (Fischer et al., 2007).

By comparison, the zebrafish embryo circulation shows a Reynolds number which is close to zero. In this low Reynolds number range, the blood flow characteristics are opposite to human adults because blood is highly viscous and velocities are usually low. These features make the fish susceptible to bradycardia and reversing flow. We therefore wanted to verify the validity of the Windkessel model and the implication of arterial elasticity for proper blood flow propagation in the zebrafish embryo. This would enable us to prove the validity of the zebrafish model in the context of arterial hypertension studies.

This project was carried out in the lab of Julien Vermot and was undertaken principally by Halina Anton, a former post-doc in the lab. Using live imaging and optical tweezing in parallel to a computational model, this work aimed to:

- verify that the blood flow is rectified along the zebrafish vasculature thanks to a capacitor effect of the elastic dorsal aorta,
- understand the behavior of blood cells in the vicinity of ISVs,
- verify that the resistivity of the system is adjustable through the presence and opening of the ISVs,
- model the effect of a stiffened artery on the heart work load.

I participated in this project, trying to understand the effect of increasing the system resistivity on the flow decay. This corresponds to a pathological situation, in which an obstruction or a reduction in

diameter of smaller arteries or capillaries occurs. To this end, I participated in the optimization and the realization of the *kdrl* MO experiments shown in Figure 4. This included the morpholino injection conditions' optimization, live confocal imaging and optogenetic manipulations to stop the heartbeat *in vivo* in *Tg(E1b:NpHR-mcherry)*^{s1003t} embryos. Moreover, I participated in the live imaging of the DA deformation, optimizing the conditions and imaging the DA using a Zeiss 780 Live microscope. Finally, I participated in verifying the computational model by testing the difference in flow velocity in two successive arterial ISVs, using a combination of live confocal microscopy to determine the identity of vessels with the arterial specific *Tg(Flt1enh:td-tomato)* line and bright field ultra-fast imaging to correlatively record the blood flow in the selected vessel pairs.

The results of this study were published in Development in 2013.

Manuscript 3: Pulse propagation by a capacitive mechanism drives embryonic blood flow

Halina Anton, Sebastien Harlepp, Caroline Ramspacher, Dave Wu, Fabien Monduc, Sandeep Bhat, Michael Liebling, Camille Paoletti, Gilles Charvin, Jonathan B. Freund and Julien Vermot

Development 140, 4426-4434 (2013) doi:10.1242/dev.096768

4426 RESEARCH ARTICLE

Development 140, 4426-4434 (2013) doi:10.1242/dev.096768

Pulse propagation by a capacitive mechanism drives embryonic blood flow

Halina Anton[1,*], Sebastien Harlepp[2], Caroline Ramspacher[1], Dave Wu[1], Fabien Monduc[1], Sandeep Bhat[3], Michael Liebling[3], Camille Paoletti[1], Gilles Charvin[1], Jonathan B. Freund[4] and Julien Vermot[1,‡]

SUMMARY

Pulsatile flow is a universal feature of the blood circulatory system in vertebrates and can lead to diseases when abnormal. In the embryo, blood flow forces stimulate vessel remodeling and stem cell proliferation. At these early stages, when vessels lack muscle cells, the heart is valveless and the Reynolds number (Re) is low, few details are available regarding the mechanisms controlling pulses propagation in the developing vascular network. Making use of the recent advances in optical-tweezing flow probing approaches, fast imaging and elastic-network viscous flow modeling, we investigated the blood-flow mechanics in the zebrafish main artery and show how it modifies the heart pumping input to the network. The movement of blood cells in the embryonic artery suggests that elasticity of the network is an essential factor mediating the flow. Based on these observations, we propose a model for embryonic blood flow where arteries act like a capacitor in a way that reduces heart effort. These results demonstrate that biomechanics is key in controlling early flow propagation and argue that intravascular elasticity has a role in determining embryonic vascular function.

KEY WORDS: Biomechanics, Blood vessels, Hemodynamics, Low Reynolds number, Zebrafish

INTRODUCTION

Embryonic blood flow is essential for proper organogenesis and angiogenesis. Whether it is through the transport of oxygen and nutrients or via exertion of physical forces, blood flow has been shown to be instrumental in controlling gene expression and endothelial cell behavior in the embryo (Jones, 2011; Freund et al., 2012). Genome-wide expression analysis in cell culture shows that endothelial cells discriminate between multiple flow profiles by expressing different sets of genes (Boon and Horrevoets, 2009) and regulating basic cell functions (Hahn and Schwartz, 2008). Furthermore, flow forces have been shown to control heart development, patterning of the vascular network and hematopoiesis in vertebrates (Hove et al., 2003; le Noble et al., 2004; Yashiro et al., 2007; Adamo et al., 2009; North et al., 2009; Vermot et al., 2009; Buschmann et al., 2010; Liu et al., 2010; Nicoli et al., 2010; Bussmann et al., 2011; Corti et al., 2011; Chen et al., 2012; Lin et al., 2012). Nevertheless, despite the crucial role of blood flow in cardiovascular development (Jones, 2011; Freund et al., 2012), very little is known about flow forces propagation at the embryonic scales, where viscous forces dominate. Because of the intricacies of the physical properties of blood flow *in vivo*, particularly the three-dimensional arrangements of blood vessels and the sophisticated dynamics of the heart, it is necessary to address the mechanics of blood motion *in vivo*. Importantly, oscillations in pulsatile flow and subsequent wave reflections in blood vessels are the prominent physical features that control the mechanical stimuli involved in vascular flow and function in adult tissues (Zamir, 2000). Because the relative importance of viscosity can lead to flow characteristics that will dictate the forces experienced by endothelial cells *in vivo*, we probed the vascular hydrodynamics and biomechanics at work in the embryonic vascular system.

[1]Institut de Génétique Moleculaire et Cellulaire, CNRS/INSERM/UdS, 1 rue Laurent Fries, BP10142, 67404 Illkirch, France. [2]Institut de Physique et de Chimie des Matériaux de Strasbourg, Université de Strasbourg, UMR 7504, 23 rue du Loess, 67034 Strasbourg, France. [3]Department of Electrical and Computer Engineering, University of California, Santa Barbara, CA 93106, USA. [4]University of Illinois at Urbana-Champaign, Urbana, IL 61801, USA.

*Present address: Laboratoire de Biophotonique et Pharmacologie, UMR 7213 CNRS, UdS, Faculté de Pharmacie, Illkirch, France
‡Author for correspondence (julien@igbmc.fr)

Accepted 12 August 2013

MATERIALS AND METHODS

Zebrafish

Zebrafish lines used in the study are wild-type AB, *Tg(flk1:eGFP)* (Jin et al., 2005), *Tg(flt1^{enh}:RFP)* (Bussmann et al., 2010) and *Tg(E1b:gal4-VP16)s1101t*, *Tg(UAS:NpHR-mCherry)s1003t* (Arrenberg et al., 2010). The embryos were raised at 28°C in the dark and treated with 1-phenyl-2-thiourea (PTU) (Sigma Aldrich) at 10 hpf to inhibit pigment formation. For the imaging, they were anesthetized with 0.02% tricaine solution and were mounted on a glass-bottom Petri dish embedded in 0.8% low melting point agarose (Sigma Aldrich). *gata1* and *kdrl* morpholino (MO) injections were performed as described previously (Vermot et al., 2009; Habeck et al., 2002).

Imaging

Confocal imaging was performed on a Leica TCP SP5 direct microscope using a low-magnification, water-immersion objective (Leica, 25×, N.A.=0.95). By using the resonant scanner, and depending on the number of lines per frame, the acquisition frame-rate varied between 50 and 200 fps.

Bright-field imaging experiments were performed on a Leica DMIRBE inverted microscope using a Photron SA3 high speed CMOS camera (Photron, San Diego, CA, USA). For the blood cell-tracking experiments, the time-lapse sequences were acquired at 250-500 Hz frame rate, in transmission configuration using white light illumination and a water immersion objective (Leica, 63×, N.A.=1.2).

The optomanipulating experiments were performed by adding a second halogen lamp and filter cube for activating the NpHR-mCherry light gated pump. A manual shutter was placed in the illumination path in order to control the illumination period. A low-magnification water-immersion objective (Leica, 20×, N.A.=0.7) was used for both imaging and delivering the green light activating the NpHR ion pump. The acquisition times were 10-20 seconds at 60-200 fps. The embryos did not show any sign of phototoxicity during or post acquisition.

All microscopy setups used were equipped with a heating device that ensured the embryos were kept at 28°C during the imaging.

The velocity of red blood cells was determined by manual tracking and kymograph analysis using ImageJ (NIH) and Matlab (MathWorks) software.

Optical tweezers

Optical tweezers experiments were performed using a home-built microscope described previously (Drobczynski et al., 2009). Briefly, the optical setup contains a laser (Spectra Physics YAG 1064 nm), focused through a high numerical aperture oil immersion objective (Zeiss, ×100, 1.25 N.A.). The light scattered by the trapped cell is collected through a second objective (Olympus, X40, 0.6 N.A.) before being imaged on a four-segment photodiode. The sum (ΣI) and the difference (ΔI) of the intensities collected by each segment are sampled at 4 kHz and digitized with a 16-bits resolution, using a National Instruments card NI PCIe-6259. The subsequent signal treatment was performed using LabView 7.2 (National Instruments) under Windows XP. The laser power used to trap the blood cells varied from 2 to 3 W (laser head output), depending on the location of the blood cell. The beam energy was dissipated by the flow, trapping blood cells without inducing any other side effect on the fish.

To visualize the sample we use a second path for the white light. The white light is brought to the setup with an optical fiber and collimated with the objective lens O3 (Leica, ×10, 0.3 N.A.). We imaged the sample using a Basler A602f CMOS camera for image acquisition at high frame acquisition (200 Hz). The camera was synchronized with the acquisition done on the photodiode in order to follow all motions (fish, blood cells and vessels). The setup allows following the blood cell displacement within the trap either with the quadrant photodiode or the Basler camera. Movies and photodiode traces were both used for subsequent analysis.

Video analysis and ϕ measurements

We used ImageJ and Wavemetrics IgorPro to analyze the motions of red blood cells within the trap. Stacks were realigned so that X or *y*-axis are aligned along the DA, X being in the axis and Y orthogonal to the DA. This allowed us to limit the cross contributions of the displacements in case the blood flow had an angle with respect to these axes. Once this angle was fixed, an orthogonal view on the center of the cell was performed to get the time trace. The traces were saved as a text file and IgorPro was then used to perform the quantitative analysis. Using the calibration curve, we transformed the orthogonal views in time and position graphs, taking into account the rotation applied during the first steps of analysis. The spatial resolution is 120 nm in both directions after treatments

We adjusted the time traces with a sine function to extract the frequency and phase. From these adjustments, we obtained the phase shift between both signals.

We confirmed the Y motion was not due to deformability of the DA by comparing the amplitude of motion of the blood cell with endothelial cells. On average, blood cell motion amplitude in Y is 10 times bigger than endothelial amplitude in the area of ISV attraction.

The anatomy and position of the ISV was extracted by analyzing the tracks and diameter of the blood cells flowing into it.

Photodiode data analysis

The photodiode directly converts the displacement of the blood cell from the trap center into a different voltage. We took a 4-second time trace with an acquisition frequency of 4 kHz. We then extracted the power spectrum from that time trace. This power spectrum directly showed the heart beat frequency and also the cut-off frequency f_c. This cut off frequency is directly correlated to the trap stiffness k_{Trap} by the following equation: $k_{Trap}=2\pi\zeta f_c$, where ζ is the friction of the blood cell.

This trap stiffness was then used to convert the displacement extracted from the movies into forces.

The theoretical hydrodynamic force applied to the blood cell can be given in first approximation by the formula $F_{hyd}= 6\pi\eta Rv$, where η represents the fluid viscosity (≈2.10^{-3} Pa.s), R the radius exposed to the fluid flow (≈1 μm) and v the fluid velocity (≈2000 μm/sec). The viscosity, η, was obtained using the method described below. This measure is overestimated due to the presence of the arterial walls. The calculated error is less than 15% and does not affect the general described behavior.

Given these values, the maximal hydrodynamic force exerted on the blood cell is around 75 pN. This value is taken in the center of the aorta and decreases when the blood cell approaches the membrane wall. The values found with the optical trap are thus in good agreement with the theoretical value calculated above.

Zebrafish mounting for tweezing experiments

The sample was mounted on a two-axes piezoelectric crystal (Physics Instruments GmbH, displacement range 0-100 μm, resolution 0.2 nm) perpendicular to the optical *z*-axis. Fish were incubated in a thermal bath regulated at 27°C until mounting on the sample holder consisting of a microscope slide with a hole, onto which a coverslip was fixed to both sides. The fish was adsorbed to one of the coverslips using 0.8% agarose in Danieau and then covered with 1% low melting point agarose (with 0.0001% lidocaine). Then, we placed this slide under the microscope for the observations. The room temperature was set to 24°C. The embryos were positioned in the microscopic framework in order to overlap the DA longitudinal axis with the *x*-axis and the ISV with the *y*-axis.

Plasma viscosity measurements

Viscosity was measured by particle tracking a cell nucleus in the dorsal aorta in a 2,3-butanedione monoxime (BDM)-treated fish injected with *gata1* MO. Fish were imaged at 20× magnification at 1000 Hz. Sub-pixel particle tracking was performed by fitting images of the nucleus to a two-dimensional Gaussian using custom Matlab software. We confirmed that the motion of the nucleus reflected the motion of the entire cell, and that the cell was not tethered to the vessel wall. The histogram of the motion was then fitted to the probability distribution function of a freely diffusing particle of equivalent size; the second moment then reflects diffusion coefficient:

$$\left\langle \Delta x^2 \right\rangle = 4D\Delta t \,.$$

As $D = k_B T(6\pi\eta a)^{-1}$ [where k_B is the Boltzmann constant, T (303 K) is the temperature and a (5 μm) is the radius of the tracked cell], the extracted viscosity is 0.0022±0.0007 Pa seconds.

Blood cell velocity measurements

Velocities were calculated by hand or by performing a kymograph along the direction of flow. The kymograph then shows space along one axis and time along the other axis, with time step Δt given by the frame-rate (between 250 and 500 fps). Cells that move along the direction of flow leave a trace in time as they move through the vessel in space. These traces were then segmented in Matlab using the Canny edge-finding algorithm. The segmented traces consisted of an image of pixels that trace out an approximate curve. The curves were then converted into coordinates by fitting a line through each nearest neighbor segment of the curve. The fit lines are median filtered through a 3-point filter to remove spurious noise. As many cells flow through the kymograph in a given Δt, the velocity in the vessel is constructed statistically by averaging the velocity of many cells at Δt of the kymograph. This procedure was performed for dorsal aorta, posterior cardinal vein and intersegmental vessels.

Circulation model and heart work calculation

The model is presented in the supplementary information. We used *Mathematica* to run our flow model (Wolfram Research). All the parameters used come from *in vivo* measurements. The model was validated against analytical solutions for small systems. All numerical results were confirmed to be independent of the resolution as set by the order of the polynomial basis functions. An adaptive time-stepping scheme assured time accuracy. In the analysis we neglected terms proportional to the radius change squared: δR^2. For changes in vessel radius of <10%, this is estimated to cause a 1% error and can therefore be considered small.

Heart work rate (Power) was calculated as follows. Heart work rate=Force × Velocity. We specified the inflow velocity based upon the data. The pressure was computed as part of solving the numerical model. The obtained pressure multiplied by the area of the aortic root gave the force.

RESULTS

Blood flow is rectified along the zebrafish embryonic vascular network

We performed high temporal resolution imaging in zebrafish to characterize the flow in the axial vascular network of the embryonic trunk (Fig. 1A,B). By 48 hours post-fertilization (hpf) blood circulates in most of the intersegmental vessels (ISVs) and by 72 hpf the network is fully functional (Ellertsdóttir et al., 2010). At these stages, the anatomy of the tubing network is relatively simple: blood cells move through one of the 15 or so loops closed by intersegmental artery-vein pairs between the dorsal aorta (DA) and the posterior cardinal vein (PCV) (Fig. 1B) (Weinstein and Fishman, 1996). We compared blood cell motion in the DA, the PCV and the intersegmental loops (Fig. 1C). In the DA, blood cell motion reflects the heartbeat rhythm with regular intermittent propagation of fluid and almost no flow in between the pulses (Fig. 1D). Interestingly, ISV flow is pulsatile but with a profile significantly different to that of the DA. Its peak flow is slower than in the DA (the velocity peak is 1200±300 μm/second compared with 2100±400 μm/second in the DA in the tail region at 48 hpf), and motion seldom ceases during an oscillatory cycle (Fig. 1D,E). By contrast, blood flow is relatively steady in the PCV (Fig. 1D). This corresponds to a 57% drop in the pulse amplitude, indicating a strong flow rectification between the two vessels. A particularly notable effect is observed near the ISV entry where cells were observed to move toward the heart in the opposite direction to the predominant DA flow (Fig. 1F-H). In some dramatic cases, blood flow in the ISV appears to be completely independent of DA flow (Fig. 1I-K; supplementary material Movie 1). Thus, the relationship between the flows of the ISV and DA is not simple and suggests that a strong flow rectification occurs between these two branches of the vascular network. This feature is key as it will affect perfusion and local hemodynamic stresses experienced by the vessels.

For pulsatile flow, it is important to recognize the pulse strength relative to viscous effects, which is quantified by the Womersley number [$Wm=R(\omega/\nu)^{1/2}$, where R is the vessel radius, ω the pulse frequency and ν the kinematic viscosity]. The low $Wm \approx 0.08$ of the zebrafish embryo at 72 hpf indicates that the cardiac frequency does

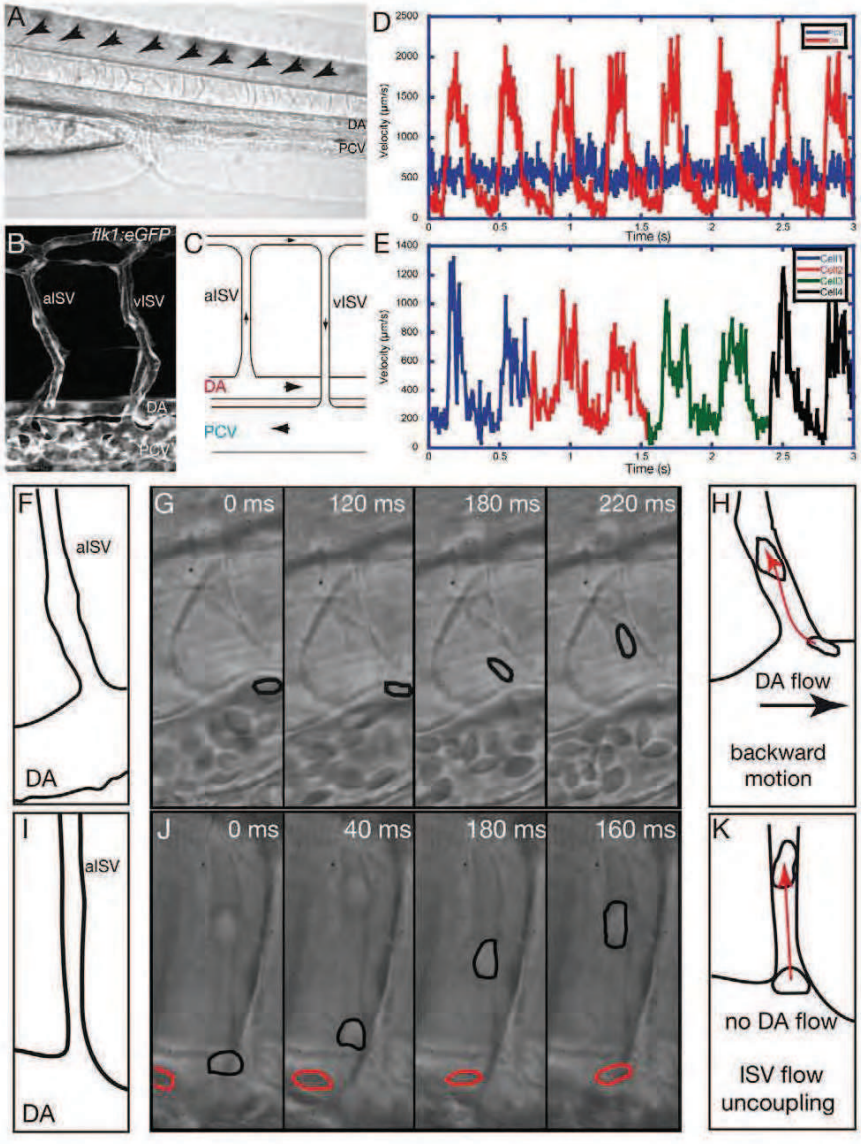

Fig. 1. Blood cell motions demonstrate flow rectification and an additional force at the ISV entry of the embryonic vascular network. (**A**) Lateral view of the zebrafish larvae at 72 hpf. Blood vessels of the tail are visible in the focal plane. Blood cells are present in the dorsal aorta (DA) and the posterior cardinal vein (PCV). Arrows indicate the intersegmental vessels (ISV). (**B**) View of a typical vascular loop between the DA and the PCV through *z* projection of a confocal stack obtained with the *Tg(flk1:eGFP)* transgenic line expressing the EGFP specifically in the endothelial cells. Arterial ISV (aISV) and venous ISV (vISV) are labeled. (**C**) A typical vascular loop observed in the trunk vasculature with the black arrows indicating the direction of blood flow. The blood cells in the DA enter into the aISV, pass in to vISV and move towards the PCV and the heart. (**D**) Typical velocity profile of the blood cells circulating in the DA (red) and PCV (blue). The DA displays a pulsatile flow, whereas the PCV flow is relatively steady. (**E**) Typical velocity pattern of blood cells observed in the ISV. Flow is pulsatile but not fully synchronized with the DA flow. (F-K) Fast imaging of blood cell motion at the ISV entry. (**F**) The observed topography at the ISV entry in G. (**G**) Fast time-lapse imaging showing a blood cell (outlined in black) moving against the DA flow towards the ISV. (**H**) Summary of the backward blood cell motion towards the ISV (red arrow) as opposed to DA flow (black arrow). (**I**) The observed topography at the ISV entry in J. (**J**) Fast time-lapse imaging showing blood cell displacement in the ISV (outlined in black) is much greater than in the DA (outlined in red). (**K**) Summary of the additional cell motion within the ISV (red arrow) when there is no visible DA flow.

not introduce significant inertia via the introduction of a fast time scale. In this context, the residual blood cell motion in the ISV in the absence of blood cell motion in the DA cannot be due to inertia, thus indicating an additional force generated in the network. At the same time, it is surprising in a low *Re* environment (where viscous forces dominate) that flow does not directly follow the pump in a closed network.

The dynamics of blood flow forces is complex at the ISV entry

To investigate the temporal and spatial relationships leading to the apparent attraction of blood cells towards the ISV entry, we developed a probing assay allowing the characterization of blood cell motion over time at a fixed location. Blood cells track the flow, but only at the locations of the cells, which move. It is thus nearly impossible to characterize blood cell motion at a point of the network over time using conventional cell tracking. To circumvent this limitation, we immobilized blood cells within an optical trap and followed their motion in response to flow as an indicator of flow direction. We trapped at 1064 nm, a non-phototoxic wavelength, so that embryonic and vascular development was not affected when compared with non-manipulated embryos from the same clutch (n=20). This approach allowed us to assess directly the *in vivo* pulsatile flow in the DA (Fig. 2A-C; supplementary material Movie 2) and to precisely investigate blood cell motion near the ISV entry. To suppress interference from other cells, we artificially decreased the number of circulating blood cells by inhibiting hematopoiesis through partial knockdown of *gata1*, a pro-hematopoietic transcription factor in zebrafish (Galloway et al., 2005). The obtained *Wm* in *gata1* morphants is 0.042 and is lower

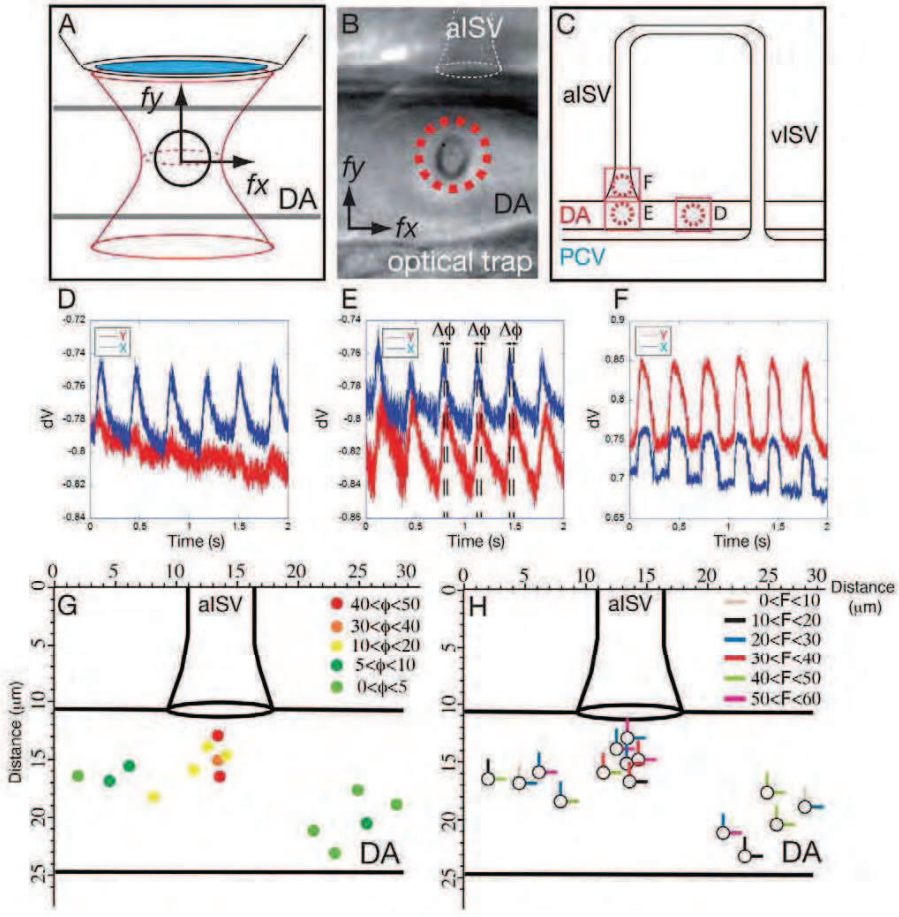

Fig. 2. Blood cell attraction towards the ISV follows two oscillatory phase-shifted forces. (**A**,**B**) Schematic representation (A) and *in vivo* live image (B) to detail the optical tweezing experiments undertaken to characterize blood cell motion near the ISV entry. Detection of the constrained blood cell motion within the optical tweezer reflects the effects of surrounding flow forces. The reconstruction of the displacement along the *x* and *y* axes allowed us to decipher the force applied to the cell (*fx* and *fy*). (**C**) *In vivo*, blood cells are trapped at different positions in the DA near and at the ISV entry, with dotted red circles representing the immobilizing focus of the optical tweezer in the same embryo (B,C). The corresponding motion patterns are shown in D-F. (**D-F**) Real-time blood cell displacement (represented by the signal from the quadrative detector, dV) is plotted as a function of time, illustrating the typical motion resulting from blood flow. When blood cells are positioned in the DA away from the ISV, the displacement along the *x*-axis is predominant, showing the effect of pulsatile flow in the DA (D). When positioned near the ISV entry, an additional motion in Y is observed that is always out of phase from the X direction (Δφ) (E). The attractive force is thus oscillating and is not fully coupled with DA flow. When positioned in the ISV, blood cell motion in X and Y directions are in phase again (F). (**G**) Phase-shift (Δφ) mapping at the ISV entry demonstrates the attractive force is correlated with the proximity to the ISV entry and shows the XY correlation decrease when closer to the ISV. (**H**) Force map in pN obtained after optical-tweezer measurement. The maps in G and H were obtained by analysing three different embryos.

than the controls due to the lower viscosity. Nevertheless, as the *Wm* is still near zero, the general flow features will be similar to the controls. Typically, trapped blood cells displayed an oscillatory movement (supplementary material Movie 2). The frequency associated with one cycle of blood cell motion was F=3.22±0.25 Hz, correlating with the frequency of the heartbeat and the motion profile of the non-trapped blood cells in the DA (3.21±0.88 Hz). Altogether, these data show that optical tweezers can be used to precisely probe flow in the vicinity of the ISV entrance.

In order to mark the transition between DA-dominated versus ISV-dominated flow, we investigated blood cell behavior at different distances from the ISV entrance. Typical time traces of the displacement of the trapped cells in different positions in the DA and ISV are shown in Fig. 2D-F. By comparing the time traces projected on the X and Y axes (Fig. 2C-F), we can define a phase shift ($\Delta\phi$) between the two motions. When trapped in the DA away from the ISVs (d >12 μm) (Fig. 2D), the displacement in X direction is dominant, which means that blood cells are advected along the DA and are entrained in the pulsatile, unidirectional flow. This leads to a highly correlated XY pattern ($\Delta\phi$=3.2±4.2°). By contrast, $\Delta\phi$ increases dramatically when blood cells are trapped near the ISV entry (Fig. 2E), showing that the attractive force in this area is out of phase with the DA flow ($\Delta\phi$=43±4° at 2.2 μm of the ISV entry). As shown in Fig. 2F, the X and Y movements are again synchronized in the ISV. These results indicate that a clear separation between a correlated and non-correlated XY movement can be seen close to the ISV entry, which is maximal when flow velocity is decreasing in the DA (Fig. 2D-G). To locate precisely the attractive area, we mapped $\Delta\phi$ at a higher spatial resolution in several embryos (n=4). Fig. 2G,H represent the obtained composite map of $\Delta\phi$ and measured forces, respectively. These maps confirm that near the ISV entry the $\Delta\phi$ is higher than in the DA. Using the optical tweezers as a picodynamometer, the displacements of the blood cells in the trap were converted into forces confirming that the orthogonal forces increase at the ISV entry (Fig. 2H). Altogether, these data confirm the presence of an attractive force and that the ISV influence can be detected several microns away from the ISV entry (6.5±2.5 μm) (Fig. 2G,H). Moreover, $\Delta\phi$ is maximal when the DA velocity is close to zero, indicating that flow is maintained near the ISV entry, after the heart-induced flow into the DA has ceased, at every cycle of contraction.

The embryonic dorsal aorta acts as a capacitor

To gain insight into the physical origins of the flow maintenance in the ISV, we developed a physical model of the vascular network that simulates the flow in a network representing the essential features of the zebrafish vascular anatomy. We hypothesized that vascular elasticity could provide a capacitance to the DA, which leads to the flow at the ISV entry and overall a rectification of the pulse. This mechanism is comparable in the current viscous limit to the so-called Windkessell effect occurring in the big arteries and vessels in the adult vascular network (Westerhof et al., 2009). We therefore developed a mathematical model of the zebrafish vascular network for Poiseuille flow in a distensible network (see supplementary material Appendix S1 for the complete description of the model).

We considered the vessels as straight, round tubes of radius R. They are distensible, with distensibility D defined as:

$$D \equiv \frac{1}{A}\frac{dA}{dp}, \qquad (1)$$

where $A=\pi R^2$ and p is the excess pressure in the tube above that of the local environment. We assume that the blood is a Newtonian fluid with viscosity μ. For the microvasculature, with tube diameters $2R$<100 μm and mean flow velocities $U\leqslant$1 mm/s, and assuming a blood kinematic viscosity $\nu=5\times10^{6}$m^2/s (about five times that of water), the Reynolds number is $Re=U(2R)/\nu\leqslant$0.02. Thus, inertia is anticipated to play at most a very small role. Similarly, for pulse rates <2/s the Womersley number is:

$$Wm \equiv R\left(\frac{\omega}{\nu}\right)^{\frac{1}{2}} \lesssim 0.04,$$

as observed *in vivo*.

In this low *Re*, low *Wm* limit, the Newtonian flow is Poiseuille, with the unidirectional streamwise velocity related to the streamwise pressure gradient as:

$$u(r) = -\frac{1}{4\mu}\frac{\partial p}{\partial x}\left(R^2 - r^2\right), \qquad (2)$$

where r is a radial coordinate in the tube measured from its axis. Integrating over the tube cross-section yields volumetric flow rate:

$$Q = \int_0^R u(r)2\pi r\,dr = -\frac{\pi R^4}{8\mu}\frac{\partial p}{\partial x}, \qquad (3)$$

which is a conserved quantity for a constant density fluid such as blood. The fourth-order dependence on the radius of this volume flux reflects a perhaps unintuitively strong dependence on vessel diameter that should be considered in interpreting results. The corresponding mean flow velocity is:

$$\bar{u} = \frac{Q}{A} = -\frac{R^2}{8\mu}\frac{\partial p}{\partial x}. \qquad (4)$$

Blood is well known to be modestly non-Newtonian in small vessels. A model with a more realistically blunted mean profile could be developed based upon the empirical data available. However, as these do not differ significantly from the Newtonian fluid model, for this study we consider a Poiseuille flow. Such a model is too crude to reproduce specific measurements exactly but usefully illustrates the key physical mechanisms (supplementary material Fig. S1). By fitting our *in vivo* measured parameters with the model, we could observe a rectified, less pulsatile, flow in the ISV, as seen in the embryo (Fig. 3A,B; supplementary material Movie 3). To confirm that the constant ISV flow was due to the elasticity of the network, we performed the same simulation without elasticity and found that ISV flow is fully correlated with the DA flow under this condition (Fig. 3C). Thus, features of ISV flow strongly depend on the DA elasticity. The DA is 'inflated' during the contraction phase of the heartbeat, and then more slowly 'deflates' via the ISV flow (Fig. 3B), thus literally acting as a capacitor. Importantly, the model suggests that flow rectification and the additional flow towards the ISV are part of the same biomechanical process.

We next investigated this biomechanical mechanism *in vivo*. The capacitor model presented above simply requires elasticity in elements of the network in order to build up an additional pressure gradient and induce a local net flow near the ISV. In zebrafish, many elements of the vascular network are elastic and could contribute to the capacitor effect. Nevertheless, the most prominent elastic deformation in the network is a drastic change in diameter of the DA during cycles of contraction (Fig. 3D-G; supplementary material Movie 4). Optical sections through 72 hpf *Tg(flk1:eGFP)* zebrafish DA, which expresses GFP in endothelial cells, were reconstructed into four-dimensional data sets (supplementary material Movie 5) to show the extent of the deformation along the

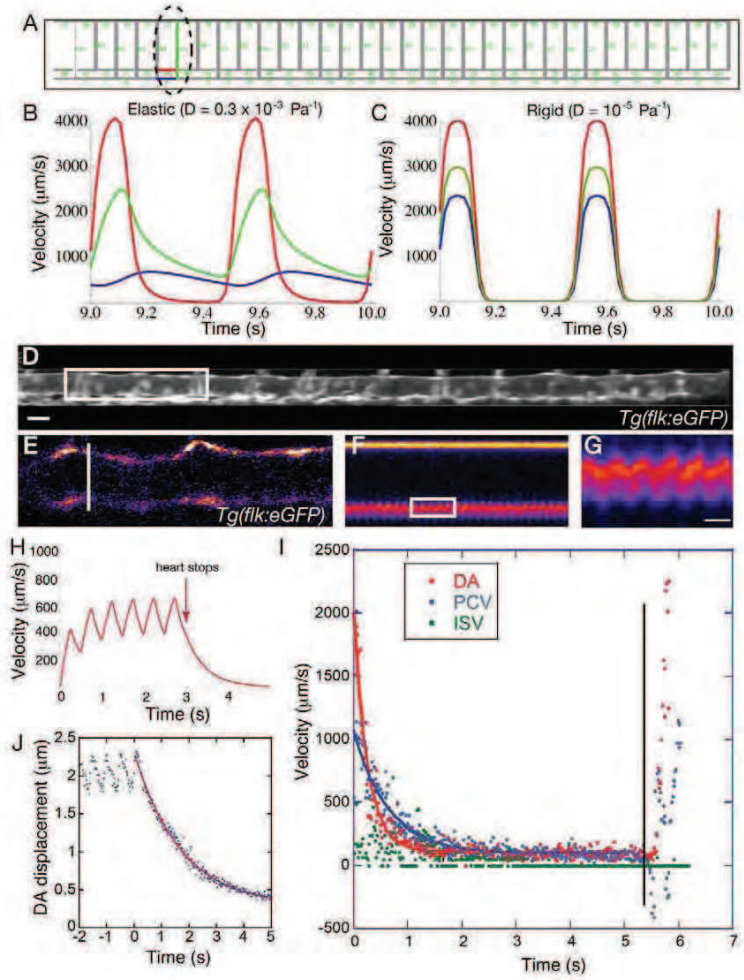

Fig. 3. The dorsal aorta conveys an elastic deformation that is coupled with a capacitive force. (**A**) The overall simulated network, designed to recapitulate the zebrafish vasculature. The numbers label the individual segments. (**B**) Flow patterns calculated at the sixth segment of the network elasticity (outlined with a dotted black line in A) show a strong flow rectification, as well as a delay between the flow velocity peaks when comparing DA and ISV flow. Arterial flow is in red, ISV flow in green and venous flow in blue. (**C**) Calculated flow profile without elasticity shows that the ISV flow directly tracks the DA. (**D**) Side view of the DA using *Tg(flk1:eGFP)* as a label of the endothelial cell walls reconstituted in 3D. Scale bar: 20 µm. (D-G) An elastic deformation is generated in the network at every heart contraction. (**E**) The distance between the dorsal and ventral wall of the DA (white bar) increases upon the heart contraction in synchrony with heartbeat. The box in D outlines the area shown in E. (**F**) Kymograph of the DA wall displacement over time recorded from the white bar in E. (**G**) Zoom of the kymograph boxed in F showing the regular deformation is visible over time and only on the ventral side of the DA. Scale bar: 420 ms. (**H**) Blood cell velocity plotted as a function of time after stopping the heartbeat predicted by the model. The blood cell motion in the DA does not stop immediately but the velocity decreased progressively over several seconds. (**I**) Blood cell velocity plotted as a function of time after stopping the heartbeat *in vivo* using *Tg(E1b:gal4-VP-16)s1011t, Tg(UAS:NpHR-mCherry)s1003t* at 5 dpf for optogenetics experiments. The time between the black lines corresponds to the duration the heart stopped beating after illumination at 488 nm. Motion is seen after heart stops as predicted by the model. (**J**) Movement of the DA ventral wall (DA displacement) following the stop in heart contraction [*t*=0 corresponds to light switch on (heart off)]. The experimental data were fitted to an exponential decay revealing the time constants of the decay after heart stops (*t*=0, when light switches on) showing a fast deflation of the DA when heart stops.

embryonic DA. We next assessed the possibility that the network builds up pressure driving a net flow within the smaller ISV vessels. Overall, such an effect predicts that flow should be possible even out of phase with the heart contraction for a period after the heart is stopped (Fig. 3H). To perform similar experiments *in vivo*, we used light activation of the halorhodopsin in the myocardium to stop the heart suddenly (Arrenberg et al., 2010) at 5 days post-fertilization (dpf), when heart valves are fully mature. As predicted, flow was visible for several seconds after heart contraction stopped (more than 5 seconds after heart stopped, Fig. 3I; supplementary material Movie 6) at 5 dpf. The displacement of the DA wall after the heart stop was measured and displayed a displacement with a similar profile over several seconds (Fig. 3J). As expected, the flow decay was also significant at 3 dpf (Fig. 4). These data indicate that the DA elasticity permits it to contain blood at pressure at each cycle of contraction and demonstrate that the DA acts as a capacitor.

ISVs set the resistivity of the network

A characteristic feature of tubular network, reflecting the R^4 dependence of flow rate on pressure drop in Eqn 3, is that the resistivity of the network is primarily mediated by the tubes of smaller diameter. In the embryonic vascular network, this would correspond to the ISV because they are much smaller than the DA and the PCV. Thus, we hypothesized the biomechanical origins of the flow decay comes from the ISV. To directly demonstrate the effect of decreasing the size of the ISV network on the flow decay, we knocked down *kdrl*, which is known to stop ISV network formation (Habeck et al., 2002). As expected, we found that *kdrl* knock down affects the vascular network structure, in particular ISV length, which is reduced (Fig. 4A,C). Overall, *kdrl* knock down led to a clear decrease in the combined ISV flow in the network at 3 dpf as less than 25% of the ISVs are functional (n=25) (Fig. 4B,D). As a consequence, *kdrl* knock down leads to an increased resistance in the network as a majority of ISVs are blocked. In the model, blocking 85% of the ISV leads to an increase in the relaxation timescale (Fig. 4E). *In vivo*, we found that the flow decay after heart stopping through optogenetics was significantly longer (33% increase, $t_{1/2}$=0.063±0.012 seconds in *kdrl* versus 0.042±0.005 seconds in wild type, n=6, P=0.05) (Fig. 4F). Together, these data demonstrate that the viscous resistance of the ISV flow sets the time scale of the flow decay in the controlled conditions of the model and in the *kdrl* morphants, where the ISV are blocked due to angiogenesis defects. We can set the configuration such that the blocked ISV is the only change with the model. Of course, in the actual *kdrl* morphants, we cannot exclude that other significant developmental changes aside from pronounced ISV blockage, such as changes in the heart pressure-velocity relations, or the network elasticity, so we cannot make a well-characterized point-to-point comparison. However, there is a significant increase in the

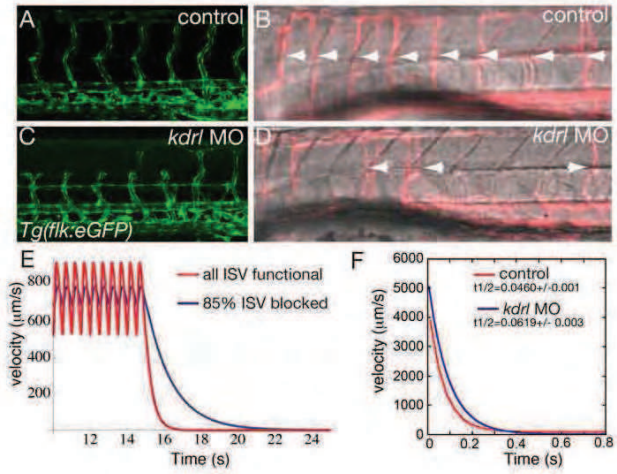

Fig. 4. The viscous resistance of the ISV flow sets the time scale of the flow decay after heart stops. (**A-D**) Visualization of the vascular network shape *Tg(flk1:eGFP)* (A,C) and ISVs with active flow [appearing in pink (false color) after standard deviation projection] (B,D) in controls (A,B) and *kdrl* knock down (C,D) at 3 dpf. White arrowheads indicate active ISVs. (**E**) Plot of the simulated experiment. The heart stops at *t*=15 seconds for both cases. The axes are flow velocity in µm/second versus time for control (red curve), where all the a/vISV are functional and mutants (blue curve) where 85% of the a/vISV are blocked (zero diameter). (**F**) Example of plots observed for the flow decay after heart stop in one control (red) and one *kdrl* knockdown (blue) embryo.

relaxation time in the *kdrl* morphants, which also suggests this behavior. In other words, the results support the expectation that the ISVs are primarily resistive relative to the DA flow.

Embryonic blood flow propagation relies on blood vessel biomechanics

We next addressed the dynamics of the capacitor effect by characterizing blood cell motion towards the ISV in comparison with the movement of the elastic deformation of the DA. We analyzed the motion of trapped blood cells with the deformation of the DA and found a direct correlation between the orthogonal flow towards the ISV and the endothelial cell wall movement (Fig. 5A-C; supplementary material Movie 7). We plotted the time traces in X and Y for a blood cell close to an ISV (Fig. 5B), and extracted the ϕ from the two signals. As expected, the out-of-phase value for these two traces is $\Delta\phi$=38.3°. By comparison with the arterial membrane (Fig. 5C), a strong correlation of motion was seen ($\Delta\phi$=9.2°). Thus, relaxation of the DA at the ISV entry is bounded with the additional pressure gradient, indicating that the DA inward motion observed contributes to ISV flow. Altogether, these data show that the slow deflation of the DA lumen creates an additional flow that drives blood cells towards the ISV (Fig. 5D).

Abnormal vascular elasticity is often associated with vascular diseases in adults where compliance is crucial for optimal vascular functions. This opens the possibility that DA distensibility is involved in embryonic vascular function, specifically in helping propagation of flow forces through the network. As a mechanical pump, the heart must do work to move blood through the network. Deformation of the network can thus significantly impact heart effort and could lead to sub-optimal pumping if not well adjusted. To investigate in more detail whether the DA biomechanical properties can affect flow propagation, we used the physical model to test the effect of the DA

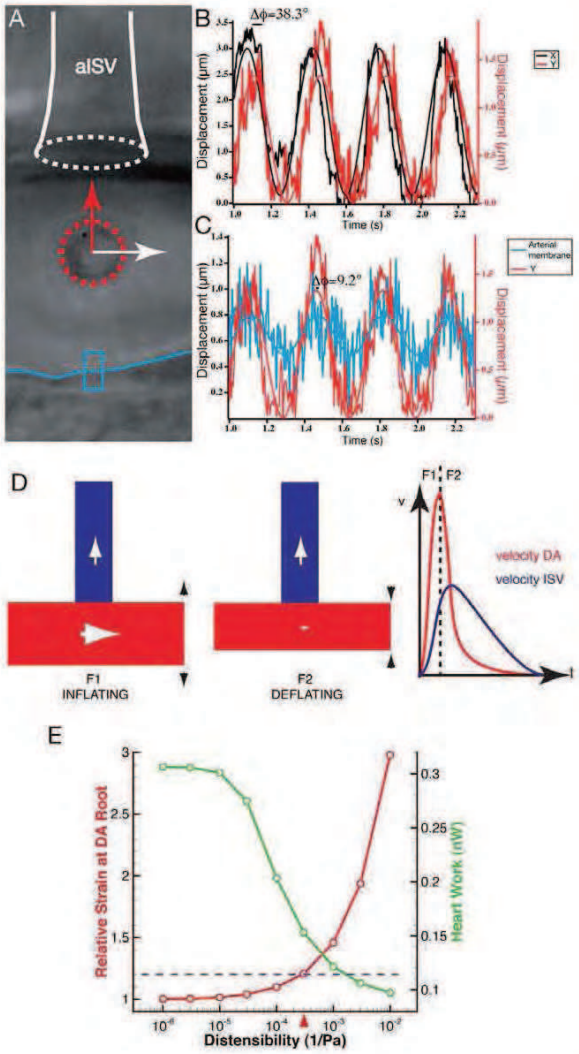

Fig. 5. Dynamic capacitive mechanism in the embryonic vascular network. (**A**) Optical tweezing at the aISV entry in the embryo. The trapped blood cell is outlined by the red dotted circle. The arrows highlight the directions of motion in X (white arrow) and Y (red arrow) of the blood cell. The ISV entry is labeled as a white dotted circle and the blue line labels the ventral DA wall. (**B**) Plot of the oscillations over time in X and Y at the trap point shown in A in the same embryo. (**C**) Plot of the oscillations over time in Y at the trap point shown in A (red line) along with oscillation of the DA cell wall (blue line). The tracked wall corresponds to the blue box in A. The motion towards the ISV is correlated with the DA wall oscillations, showing that the force driving blood cells towards the ISV is coupled with the cyclical deformation of the DA. (**D**) A model for vascular flow at early embryonic stages showing that distensibility of the DA maintains flow in the ISV after heart contraction through its own deflation. The flow direction is labeled with arrows. A first force is needed to inflate the DA (F1) and, as a result of deflation, a second force (F2) is generated that maintains flow steady in the ISV. The observed DA and ISV velocities are plotted according to the force (F1 and F2). (**E**) Heart effort (plotted in green, right *y*-axis) and strain at the DA root (plotted in red, left *y*-axis) as a function of the distensibility. Heart effort decreases as elasticity increases. The horizontal blue bar indicates the theoretical strain limit at which vessel will break. The red arrow indicates the measured distensibility, which corresponds to strain of 20%, which is often considered large but not damaging to tissues, suggesting the DA distensibility is optimized near the rupture limit for lowering heart work.

capacitance on heart effort. Using the collected *in vivo* parameters of distensibility, the model predicts that the network elasticity leads to a decrease in the required pumping effort at its best resistivity (Fig. 5E). Thus, the embryonic vascular network is set to decrease heart work through its distensibility, a situation that despite the dominant role of viscosity is functionally similar to the aorta, pulmonary arteries and the larger vessels of the adult vascular network.

DISCUSSION

By exploiting methods for live imaging, quantitative flow analysis and Poiseuille flow modeling, we have identified highly stereotyped flow propagation in the embryonic vascular network. We characterized three major flow properties of the embryonic DA: (1) a change of flow profile from DA to PCV when traversing the ISV network; (2) a mismatched bi-directional flow direction at the ISV entry; (3) blood cell velocities in the ISV do not follow local DA flow at the low velocity peak. Furthermore, we observed: (1) a local endothelial distension of the DA coupled with flow rectification; and (2) an out-of-phase flow for a period after the heart was stopped. Together, these features highlight a capacitive function for the DA, which is unexpected in the absence of inertia at these early embryonic stages. Overall, our analysis provides compelling evidence that DA capacitance leads to two key functions: (1) flow rectification to dampen flow fluctuations in the network; and (2) pressure storage to minimize heart efforts. It is likely that flow rectification through elasticity is a recurring mechanistic strategy to help propagate flow forces in vertebrate organs.

Low Re systems are particularly susceptible to bradycardia and reversing flows, two features that can be observed in the developing cardiovascular system. The simple biomechanical mechanism we describe here allows blood cell motion in the network to be less dependent on the heart maturation state and its unidirectional pumping efficiency. It only necessitates passive deformability of the DA and does not require any muscular control of the blood vessel function. The presented characterization of the early DA elasticity and function provides the foundation for a dynamic role of the embryonic vascular network in propagating flow forces and should help to revisit the mechanics associated with embryonic and adult angiogenesis. Functionally, the observed behavior is analogous to the standard Windkessel model describing the capacitive function of the large elastic arteries in adults at high Reynolds number (Westerhof et al., 2009). We show here this key feature also applies to embryonic arteries, at near zero Reynolds number. Thus, our work provides evidence of biological continuity for a role of vascular elasticity in both the embryonic and adult cardiovascular network, despite the different fluid mechanics operating at these stages. Studying the mechanical and molecular properties of the embryonic vasculature, therefore, may prove relevant to understanding the numerous cardiovascular diseases affecting arterial elasticity, such as atherosclerosis, as well as in the development of new pharmacological strategies targeting these diseases.

Acknowledgements

We thank Emily Steed, Francesco Boselli, Daniel Riveline for thoughtful comments on the manuscript and Stéphane Roth for excellent technical help. We thank C. Wyart, P. Del Bene and S. Schulte-Merker for providing fish stocks. We thank the Institut de Génétique et de Biologie Moléculaire et Cellulaire (IGBMC) imaging center, in particular Pascal Kessler, Marc Koch and Didier Hentsch and Sandrine Geschier and Sylvie Greidler at the IGBMC fish facility.

Funding

This work was supported by the Human Frontier Science Program (HFSP), Institut national de la santé et de la recherche médicale (INSERM), la ligue contre le cancer, Fondation pour la Recherche Médicale (FRM) and the seventh framework program [MC-IRG256549] to J.V., the United States National Science Foundation [CBET 09-32607] to J.B.F. and the Agence National de la Recherche (ANR) [PCVI-2008-0033] to G.C.

Competing interests statement

The authors declare no competing financial interests.

Author contributions

J.V. conceived the project. J.V. and H.A. designed the experiments. H.A. performed the experiments and collected the data. J.B.F. and J.V. together recognized the rectification mechanism. S.H. performed the tweezing experiments with H.A. S.H. analyzed the tweezing experiments. C.R. and H.A. performed the knockdown experiments. D.W., G.C. and C.P. developed the image processing approaches. F.M. provided technical help with the image analysis. S.B. and M.L. developed the realignment programs necessary for the 3D analysis. J.B.F. developed the mathematical model. J.V. and J.B.F. wrote the paper.

Supplementary material

Supplementary material available online at
http://dev.biologists.org/lookup/suppl/doi:10.1242/dev.096768/-/DC1

References

Adamo, L., Naveiras, O., Wenzel, P. L., McKinney-Freeman, S., Mack, P. J., Gracia-Sancho, J., Suchy-Dicey, A., Yoshimoto, M., Lensch, M. W., Yoder, M. C. et al. (2009). Biomechanical forces promote embryonic haematopoiesis. *Nature* **459**, 1131-1135.

Arrenberg, A. B., Stainier, D. Y., Baier, H. and Huisken, J. (2010). Optogenetic control of cardiac function. *Science* **330**, 971-974.

Boon, R. A. and Horrevoets, A. J. (2009). Key transcriptional regulators of the vasoprotective effects of shear stress. *Hamostaseologie* **29**, 39-40, 41-43.

Buschmann, I., Pries, A., Styp-Rekowska, B., Hillmeister, P., Loufrani, L., Henrion, D., Shi, Y., Duelsner, A., Hoefer, I., Gatzke, N. et al. (2010). Pulsatile shear and Gja5 modulate arterial identity and remodeling events during flow-driven arteriogenesis. *Development* **137**, 2187-2196.

Bussmann, J., Bos, F. L., Urasaki, A., Kawakami, K., Duckers, H. J. and Schulte-Merker, S. (2010). Arteries provide essential guidance cues for lymphatic endothelial cells in the zebrafish trunk. *Development* **137**, 2653-2657.

Bussmann, J., Wolfe, S. A. and Siekmann, A. F. (2011). Arterial-venous network formation during brain vascularization involves hemodynamic regulation of chemokine signaling. *Development* **138**, 1717-1726.

Chen, Q., Jiang, L., Li, C., Hu, D., Bu, J. W., Cai, D. and Du, J. L. (2012). Haemodynamics-driven developmental pruning of brain vasculature in zebrafish. *PLoS Biol.* **10**, e1001374.

Corti, P., Young, S., Chen, C. Y., Patrick, M. J., Rochon, E. R., Pekkan, K. and Roman, B. L. (2011). Interaction between alk1 and blood flow in the development of arteriovenous malformations. *Development* **138**, 1573-1582.

Drobczynski, S., Hébraud, P., Munch, J. P. and Harlepp, S. (2009). Design and realization of a high-stability optical tweezer. *Opt. Eng.* **48**, 113601.

Ellertsdóttir, E., Lenard, A., Blum, Y., Krudewig, A., Herwig, L., Affolter, M. and Belting, H. G. (2010). Vascular morphogenesis in the zebrafish embryo. *Dev. Biol.* **341**, 56-65.

Freund, J. B., Goetz, J. G., Hill, K. L. and Vermot, J. (2012). Fluid flows and forces in development: functions, features and biophysical principles. *Development* **139**, 1229-1245.

Galloway, J. L., Wingert, R. A., Thisse, C., Thisse, B. and Zon, L. I. (2005). Loss of gata1 but not gata2 converts erythropoiesis to myelopoiesis in zebrafish embryos. *Dev. Cell* **8**, 109-116.

Habeck, H., Odenthal, J., Walderich, B., Maischein, H., Schulte-Merker, S.; Tübingen 2000 screen consortium (2002). Analysis of a zebrafish VEGF receptor mutant reveals specific disruption of angiogenesis. *Curr. Biol.* **12**, 1405-1412.

Hahn, C. and Schwartz, M. A. (2008). The role of cellular adaptation to mechanical forces in atherosclerosis. *Arterioscler. Thromb. Vasc. Biol.* **28**, 2101-2107.

Hove, J. R., Köster, R. W., Forouhar, A. S., Acevedo-Bolton, G., Fraser, S. E. and Gharib, M. (2003). Intracardiac fluid forces are an essential epigenetic factor for embryonic cardiogenesis. *Nature* **421**, 172-177.

Jin, S. W., Beis, D., Mitchell, T., Chen, J. N. and Stainier, D. Y. (2005). Cellular and molecular analyses of vascular tube and lumen formation in zebrafish. *Development* **132**, 5199-5209.

Jones, E. A. (2011). The initiation of blood flow and flow induced events in early vascular development. *Semin. Cell Dev. Biol.* **22**, 1028-1035.

le Noble, F., Moyon, D., Pardanaud, L., Yuan, L., Djonov, V., Matthijsen, R., Bréant, C., Fleury, V. and Eichmann, A. (2004). Flow regulates arterial-venous differentiation in the chick embryo yolk sac. *Development* **131**, 361-375.

Lin, Y. F., Swinburne, I. and Yelon, D. (2012). Multiple influences of blood flow on cardiomyocyte hypertrophy in the embryonic zebrafish heart. *Dev. Biol.* **362**, 242-253.
Liu, J., Bressan, M., Hassel, D., Huisken, J., Staudt, D., Kikuchi, K., Poss, K. D., Mikawa, T. and Stainier, D. Y. (2010). A dual role for ErbB2 signaling in cardiac trabeculation. *Development* **137**, 3867-3875.
Nicoli, S., Standley, C., Walker, P., Hurlstone, A., Fogarty, K. E. and Lawson, N. D. (2010). MicroRNA-mediated integration of haemodynamics and Vegf signalling during angiogenesis. *Nature* **464**, 1196-1200.
North, T. E., Goessling, W., Peeters, M., Li, P., Ceol, C., Lord, A. M., Weber, G. J., Harris, J., Cutting, C. C., Huang, P. et al. (2009). Hematopoietic stem cell development is dependent on blood flow. *Cell* **137**, 736-748.
Vermot, J., Forouhar, A. S., Liebling, M., Wu, D., Plummer, D., Gharib, M. and Fraser, S. E. (2009). Reversing blood flows act through klf2a to ensure normal valvulogenesis in the developing heart. *PLoS Biol.* **7**, e1000246.
Weinstein, B. M. and Fishman, M. C. (1996). Cardiovascular morphogenesis in zebrafish. *Cardiovasc. Res.* **31**, E17-E24.
Westerhof, N., Lankhaar, J. W. and Westerhof, B. E. (2009). The arterial Windkessel. *Med. Biol. Eng. Comput.* **47**, 131-141.
Yashiro, K., Shiratori, H. and Hamada, H. (2007). Haemodynamics determined by a genetic programme govern asymmetric development of the aortic arch. *Nature* **450**, 285-288.
Zamir, M. (2000). In *The Physics of Pulsatile Flow* (*Biological Physics Series*), pp 147-185. New York, NY: Springer Verlag.

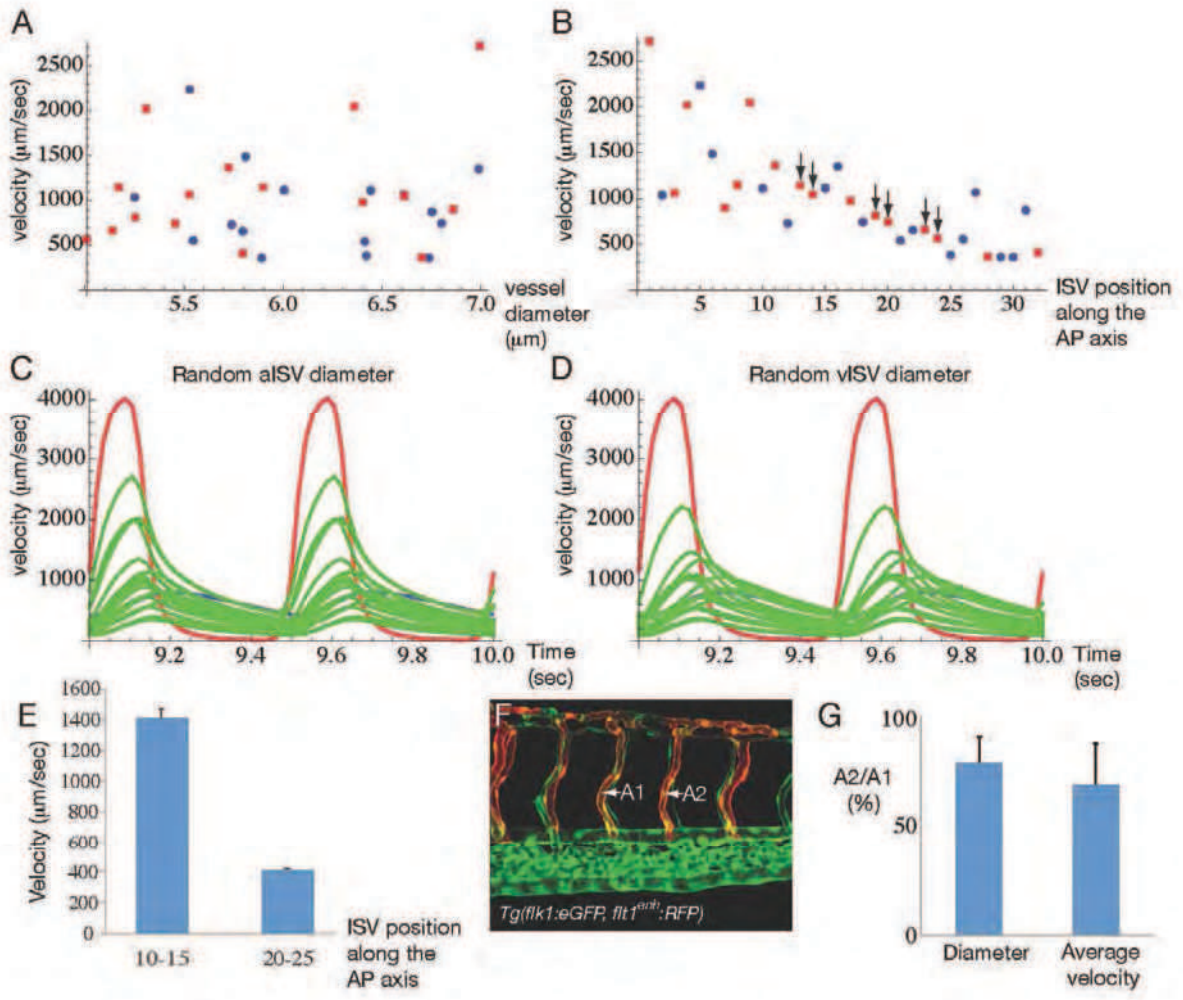

Fig. S1. Validation of the model. (A) Plot showing the ISV peak velocity during cardiac cycle versus lumen inner diameter. (B) Plot showing ISV peak velocity during cardiac cycle versus ISV number from head. Red squares: ISA, blue circles: ISV. (C-D) plot of the DA flow (red), PCV flow (blue), aISV flow (green) (C) vISV flow (green) (D). All the ISVs along the AP axis are represented to show the global variability amongst ISV. Yet the ISV flow in general decrease along the AP axis (see also B). (E) *In vivo* ISV flow measurements showing that posterior ISV flow (ISV 20-25) has lower velocity than anterior (ISV 10-15) as expected from the model (B). (F-G) Flow measured in successive aISV identified by *Tg(flt1^{enh}:RFP)* expression. (F) a1ISV flow is higher than a2ISV when two successive ISVs have an arterial identity. This effect is also observed in the simulation (black arrows in B).

Movie 1: Blood flow in the zebrafish aISV. Related to Fig. 1I-K.

Movie 2: Optical tweezing in the zebrafish DA at the aISV entry shows blood cell motion in the vascular network. The focus of the tweezer is shown as a grey dot at the beginning of the movie. Related to Fig. 2B.

Movie 3: Model of flow (red arrows), pressure (blue circle) and shear stress propagation (bars) using a distensible vascular network that recapitulates zebrafish vascular anatomy. Related to Fig. 3A.

Movie 4: Fast confocal, time-lapse acquisition in one section plan of the DA (side view) over time using the *Tg(flk1:eGFP)*. Note the motion of the ventral part of the DA revealing its distensibility. Related to Fig. 3E-G.

Movie 5: Three D plus time view of the DA showing the inflation and deflation of the DA over time using the *Tg(flk1:eGFP)*. The movie consists of two tiled stacks spanning along the AP axis. It shows the deformation is visible along the whole AP axis of the DA. Related to Fig. 3D.

Movie 6: Movement of the blood cell before illumination (off) and after illumination (on) of the *Tg(UAS:NpHR-mCherry) s1989t* line leading heart to stop beating. Related to Fig. 3I.

Movie 7: Movement of the blood cell in the trap toward the aISV entry. Related to Fig. 5A.

Appendix S1: Elastic-network viscous flow modeling of the zebrafish vascular network (related to Fig. 3A).

II/ Generating a new model of GCN2-induced PVOD in zebrafish

Foreword

GCN2 (EIF2AK4) has been recently identified in WES, by our collaborators from the Soubrier group (La Pitié-Salpetrière, Paris), as a genetic cause of the hereditary form of PVOD, a rare and extremely severe cause of pulmonary hypertension.
In the context of the validation of GCN2 mutation as a cause of PVOD, a collaborative project was set up between the groups of Prof. Florent Soubrier, Prof. Marc Humbert (University Paris-Sud/INSERM), Prof. Pierre Fafournoux (INRA, Clermont-Ferrant) and Dr. Julien Vermot. This project consists of studying cellular and animal models (mice and zebrafish) of GCN2 inactivation and aims to identify the gene expression changes induced *in vitro* and *in vivo* by GCN2 inactivation in pulmonary vascular cells, in order to understand how biallelic mutations of GCN2 lead to specific venous lung vasculature remodeling.

We therefore decided to generate an *eif2ak4* (homolog for GCN2 in zebrafish) KD zebrafish model. Although the zebrafish does not have lungs, this species is a major model for vascular developmental studies and it is of major importance to establish whether GCN2 ablation has an impact on vasculature development.

The aims of this project include:

- knocking-down the GCN2 homolog in zebrafish and assessing modifications in vasculature formation during early embryogenesis,
- determining whether the venous vasculature is preferentially affected as observed in PVOD,
- addressing the cellular mechanism leading to the observed phenotype and which could be implicated in the establishment of PVOD,
- knocking down downstream intermediates of the GCN2 signaling pathway including the ISR activator ATF4, for a better understanding of molecular cascade activated by GCN2 in PVOD.
-

The results obtained are presented in the following manuscript. We plan to submit it in September 2014 after finishing experiments presented in the following preliminary results section.

Manuscript 4: GCN2 (eif2ak4), a gene involved in pulmonary veno-occlusive disease, controls venous angiogenesis in zebrafish

Caroline Ramspacher, Virginie Monceau, Stephane Roth, Charlotte Softley, Caroline Claude, Emily Steed, Florent Soubrier, Julien Vermot

(in preparation)

GCN2 (eif2ak4), a gene involved in pulmonary veno-occlusive disease, controls venous angiogenesis in zebrafish

Caroline Ramspacher[1,2,3,4], Virginie Monceau[5], Stephane Roth[1,2,3,4], Charlotte Softley[1,2,3,4], Caroline Claude[5], Emily Steed[1,2,3,4], Florent Soubrier[5], Julien Vermot[1,2,3,4*]

[1]Institut de Génétique et de Biologie Moléculaire et Cellulaire, Illkirch, France
[2]Centre National de la Recherche Scientifique, UMR7104, Illkirch, France
[3]Institut National de la Santé et de la Recherche Médicale, U964, Illkirch, France
[4]Université de Strasbourg, Illkirch, France
[5]Unité Mixte de Recherche en Santé (UMR_S 956), Université Pierre and Marie Curie Université Paris06 (UPMC) and Institut National de la Santé et de la Recherche Médicale (INSERM), Paris, France.
* To whom correspondence should be addressed: julien@igbmc.fr

Abstract

Pulmonary veno-occlusive disease (PVOD) is a rare form of pulmonary hypertension, characterised by collagen-rich fibrous inclusions in the intima of small pulmonary veins and venules, thickening of venous wall and capillary dilatation as well as hyper-proliferation. PVOD etiology and pathological mechanisms are currently unclear. The serine-threonine kinase GCN2 (or EIF2AK4) has been recently identified in whole-exome sequencing studies as the genetic cause of the hereditary form of PVOD with bi-allelic GCN2-disrupting mutations in all familial cases tested and in 25% of histologically confirmed sporadic PVOD cases (Eyries et al., 2014). In mammals, GCN2 is implicated in amino acid (aa) sensing and triggers Integrated Stress Response (ISR) in response to low aa levels, through phosphorylation of eIf2α and activation of the transcription factor ATF4. Implication of GCN2 in PVOD establishment is not yet known, in particular it remains unclear whether the eif2α/ATF4 pathway is involved or whether other phosphorylation targets of GCN2 participate in the venous-specific pathological remodeling linked with PVOD. To assess this question, we turned to zebrafish and analyzed the effects of the knock-down of GCN2 and ATF4 during zebrafish angiogenesis. We found that *eif2ak4* knock-down triggers a venous-specific phenotype with developmental defects in the caudal vein and the primordial mid-brain channel. These defects are associated with perturbations in the expression of several vascular and venous-specific genes. Moreover, we show that these defects can be rescued by over-expression of human GCN2. Finally, knock down of the two orthologs of ATF4 in zebrafish, *atf4b1* and *atf4b2*, lead to similar venous phenotypes observed in GCN2 morphants suggesting the implication of the ATF4 driven ISR in the establishment of PVOD phenotype.

Introduction

Pulmonary veno-occlusive disease (PVOD) is a rare and extremely severe cause of pulmonary hypertension. PVOD is characterized histologically in the lungs by a thickening of the venous vascular walls, a widespread fibrous intimal proliferation of septal veins and pre-septal venules, frequently associated with pulmonary capillary dilatation and proliferation (Montani et al., 2009). Because PVOD shares several features with pulmonary arterial hypertension (PAH) but also has major differences, PVOD has been categorized into a separate PAH-related group in the current classification of pulmonary hypertension (Montani et al., 2009). PVOD presents either sporadical or as familial cases with a recessive mode of transmission. By whole-exome sequencing, bi-allelic mutations in *GCN2* (also known as *EIF2AK4*) that co-segregated with PVOD were found in all families studied and in 25% of histologically confirmed sporadic PVOD cases. All mutations, either in a homozygous or compound heterozygous state, disrupted the function of the gene. Therefore, these mutations point to GCN2 as being the major gene responsible for PVOD development (Eyries et al., 2014).

GCN2 is a key activator of cell response to amino acid deprivation and encodes a serine-threonine kinase that is present in all eukaryotes. It senses amino acid (aa) availability and induces changes in gene expression in response to aa deprivation at the translational, transcriptional, and chromatin level (Kilberg et al., 2009). It belongs to a family of four kinases which phosphorylate the α-subunit (eIF2α) of the eukaryotic initiation factor-2 (eIF2) (Donnelly et al., 2013). eIF2 functions by directing the binding of initiator methionyl-tRNA to 40S ribosomal subunits in the early stages of protein synthesis. Phosphorylation of eIF2α inactivates eIF2 and this step constitutes a signalization “hub” since different pathways converge towards this step. Indeed, the unfolded response pathway to the endoplasmic reticulum stress involves eIF2 phosphorylation by protein kinase-like ER kinase (PERK). The two other kinases are double-stranded RNA-activated protein kinase (PKR) and the heme-regulated inhibitor kinase (HRI). eIF2 phosphorylation leads to decreased global translation in the cell, induction of ATF4 (CREB-2) and CHOP translation, which in turn induces transcription of ATF5 and the phosphatase DNA damage-inducible 34 (GADD34).

ATF4 represents the major transmitter signal by inducing or inhibiting the transcription of several target genes, mediating what is referred as the Integrated Stress Response (ISR) involved in a few major phenotypic changes of the cell, including resistance to oxidative stress and proangiogenic state (Harding et al., 2003). ATF4 binds to response elements of target genes that are called “CCAAT-enhancer binding protein activating transcription factor (C/EBP-ATF) response element” (CARE). Since ATF4 constitutes the main downstream signaling pathway following eIF2 inactivation, its implication downstream of GCN2 mutation in the context of PVOD remains to be assessed. In particular, ATF4 could provide a link between GCN2 and the observed vascular phenotype. Indeed, bone angiogenesis has been studied in *Atf4*$^{-/-}$ mice (Zhu et al., 2013). In these mice, reduced microvascular density of the bone was associated with decreased expression of HIF1α and VEGF, showing that ATF4 is a key regulator of VEGF in local bone environment, which contributes to

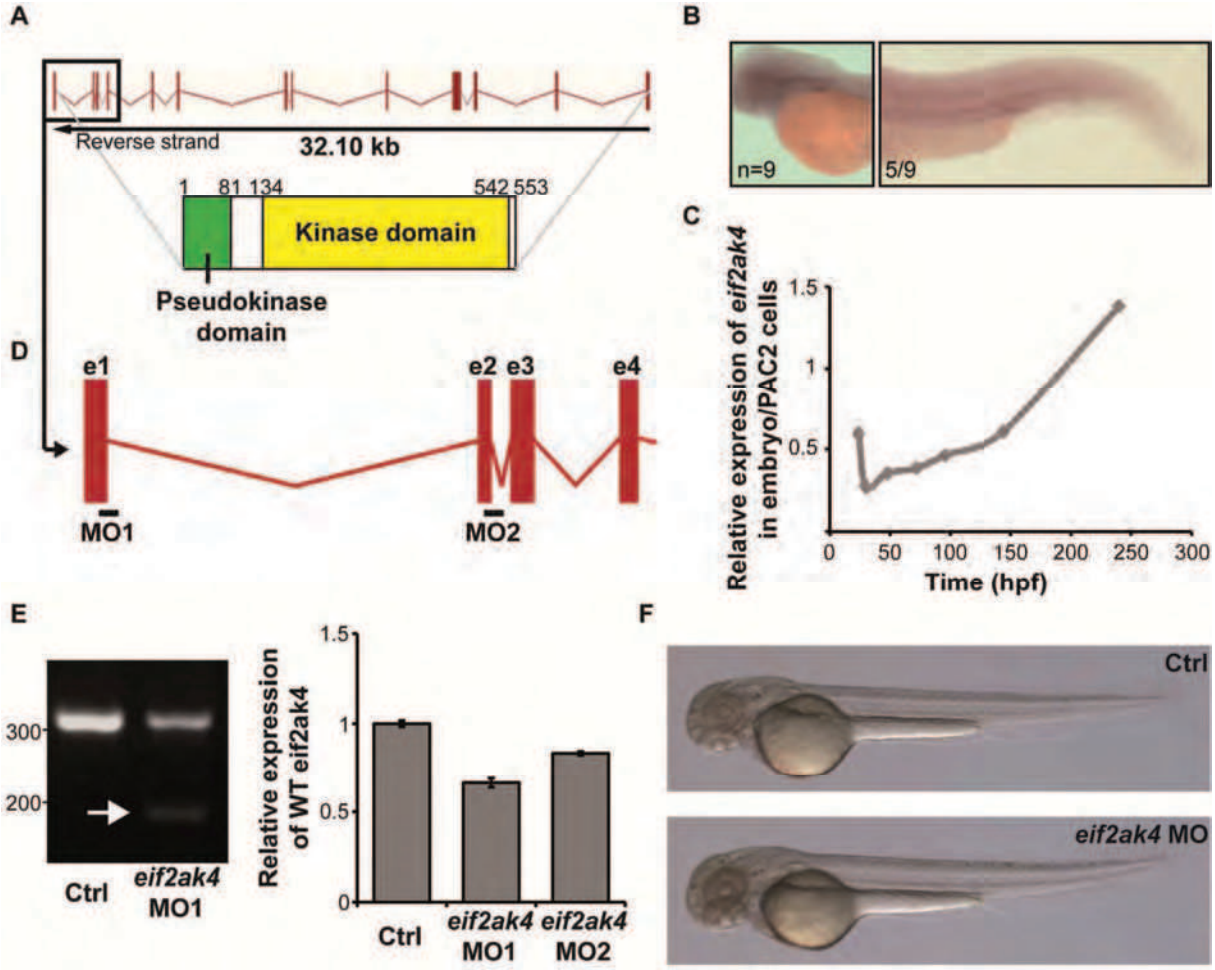

Manuscript 4/ Figure 1: Knock-down of *eif2ak4*, homolog of the human EIF2AK4, was obtained in zebrafish

(A) Schematic representation of the zebrafish *eif2ak4* gene and Eif2ak4 protein. *eif2ak4* is 32.1kb long and counts 13 exons. Putative protein domains include a pseudo-kinase (aa 1-81) and a kinase domain (aa 134-542), homologous to the human GCN2 domains. Nevertheless, no His tRNA synthetase-like domain is present on the zebrafish version of Eif2ak4. (B) Whole mount *in situ* hybridization for *eif2ak4* in 30hpf WT embryos. (C) Quantitative RT-PCR on RNA made from pools of WT zebrafish larvae from 30hpf to 14dpf show the evolution of *eif2ak4* expression over time. Expression levels are given relative to the expression in PAC2 zebrafish cells. (D) Scheme showing the position targeted by the two *eif2ak4* MO used for KD on the *eif2ak4* N-terminal part. (E) Reverse transcription products from RNA extracted from *eif2ak4* morphant and control embryos at 30hpf loaded on agarose gel. A supplementary band of lower size is present in wells loaded with morphant samples, showing the misspliced variants (white arrow). Quantification of the WT band shows the efficiency of the KD for the *eif2ak4* MO1 and MO2. (F) Side views of *eif2ak4* morphant zebrafish embryos and corresponding controls at 48hpf. Scale bar=500µm.

increased bone angiogenesis. However, it is still unclear whether GCN2-/- mice present angiogenesis defects (Anthony et al., 2004) and a formal link between GCN2 and ATF4 in this context remains to be found. Thus addressing the function of both ATF4 and GCN2 in the context of angiogenesis will help to demonstrate whether these genes have common function *in vivo*.

The role of *GCN2* and *ATF4* during angiogenesis and the pathophysiological link between GCN2 mutation and the abnormal vascular phenotype of PVOD patients are still unclear. Zebrafish has become a powerful model to study angiogenesis in recent years. Although zebrafish do not have lungs, this species is a major model for developmental studies and its study is of major importance to establish whether *gcn2* and *atf4* ablation have an impact on vascular development. To study early vascular development in zebrafish embryos, we knocked down *gcn2*, *atf4b1* and *atf4b2*, taking advantage of the transparency of zebrafish embryos, which facilitates live imaging of vascular defects *in vivo*. Our analyses revealed impaired venous development and morphogenesis, which were highly similar in *eif2ak4* and *atf4b1-atf4b2b* knock-down embryos. Furthermore, the venous defects were accompanied by increased sprouting and endothelial cell number in early embryos. Taken together, our results provide insight into the mechanisms by which GCN2 and ATF4 variants induce venous defects.

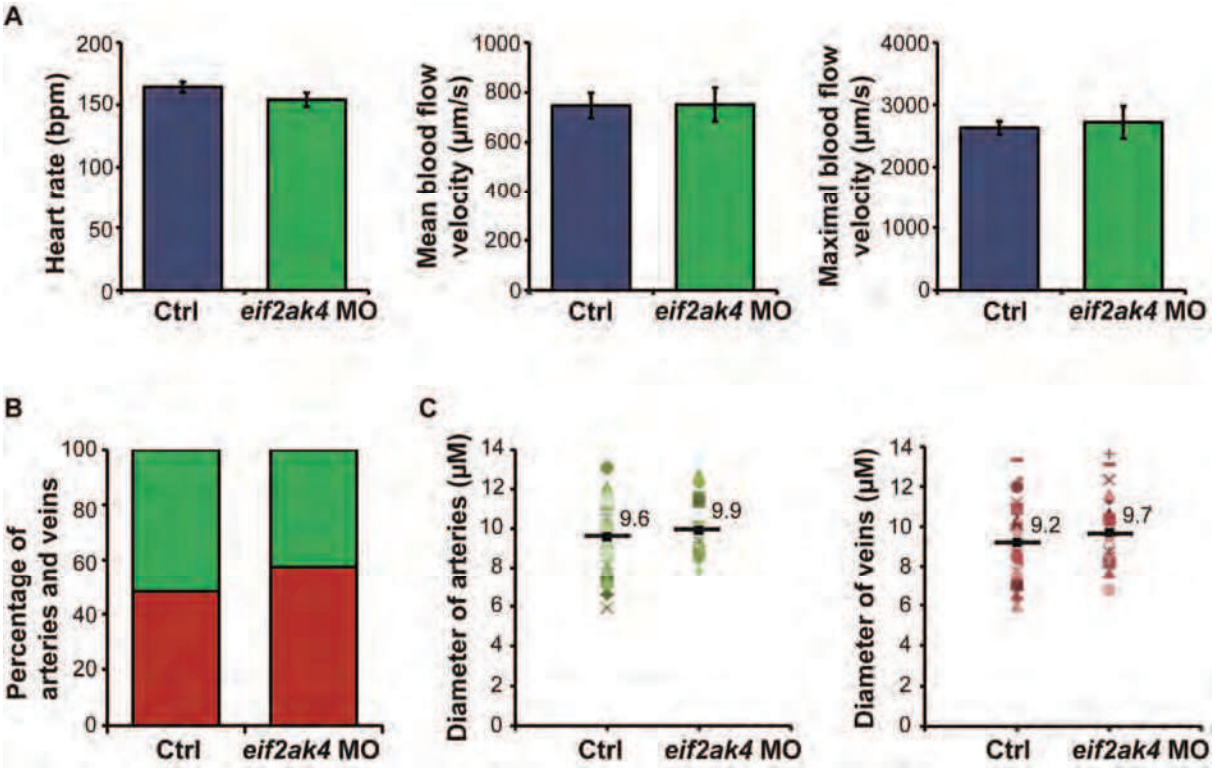

Manuscript 4/ Supplementary Figure S1: The heart pumping efficiency and the ISV repartition is not altered in *eif2ak4* morphants.

(A) Measurement of the heart rate and the blood flow maximum and mean velocity in the DA in 48hpf *eif2ak4* morphants and their corresponding controls. Data were obtained by tracking the red blood cells on videos taken with a bright field microscope and an ultra-fast camera. (B) Number and diameter of arterial *vs.* venous ISVs, obtained from confocal imaging of *Tg(Flk1:EGFP; Flt1enh:td-tomato)* at 55hpf were not perturbed in *eif2ak4* morphants compared to corresponding control embryos.

Results

Generation of a zebrafish knock-down of eif2ak4

The human GCN2 is encoded by the eukaryotic translation initiation factor 2 alpha kinase 4 (*EIF2AK4*) gene has one ortholog in zebrafish: *eif2ak4*. The structure of this ortholog contains highly homologous pseudo-kinase and serine-threonine kinase domains but does not present the His t-RNA synthetase-like domain that confers to mammalian GCN2 its aa sensing function (Figure 1A). To verify expression of *eif2ak4* in zebrafish, we performed whole-mount *in situ* hybridization on 30hpf wild-type (WT) embryos and observed a faint but ubiquitous expression of this gene (Figure 1B). This was confirmed by assessment of the level of expression of *eif2ak4* over time in WT embryos, which were shown to be low at early time-points, but increased linearly over time (Figure 1C). We then performed antisense-morpholino (MO) based knock-down (KD) of *eif2ak4* using two different splice site targeting MOs (exon1-intron1 and exon2-intron2) (Figure 1D). A partial KD was observed, leading to a decrease of 34% and 17% respectively of the *eif2ak4* correctly spliced transcript, as observed by reverse transcription and agarose gel analysis (Figure 2B). Looking at the embryos' overall morphology, we didn't observe differences between *eif2ak4* morphants and WT embryos as shown in Figure 1F presenting 48hpf embryos.

GCN2 morphants present venous-specific developmental vasculature defects

Since EIF2AK4 deficiency in humans affects lung vessels and predominantly the veins, our goal was to detect potential vascular defects in particular affecting venous structures in the zebrafish *eif2ak4* KD model. The two MOs described above were injected in the endothelial-specific *Tg(Flk1: eGFP)* transgenic line in order to assess potential developmental vascular defects. We first verified that blood flow was normal in KD fish. Indeed, it was shown previously that hemodynamic perturbations and modification in the vascular mechanodetection pathway were linked to abnormal vasculature development in zebrafish embryos (Goetz et al., 2014). No significant difference was observed between *eif2ak4* morphants and their uninjected siblings in terms of heart rate, maximal and mean blood flow velocity in the dorsal aorta (DA) at 48hpf (Supplementary Figure S1A), attesting to the blood-flow independence of observed phenotypes. Looking at the overall vasculature, no defects in the intersegmental vessels' (ISVs) structure, distribution or diameter were observed (Supplementary Figure S1B). Nevertheless, we found defects in the caudal vein (CV) and in the cranial vasculature using live confocal microscopy (Figure2). All 30hpf *eif2ak4* KD embryos presented a denser caudal plexus with an important reduction in the number of vascular loops by comparison to the controls (2,3±0,5 loops in morphants *vs.* 8,8±0,5 loops in WT (n=6)) (Figure 2A). From 48hpf, we observed an enlargement of the caudal plexus and dilatation of its vessels. The ratio between plexus and DA width was 1.2 times higher in *eif2ak4* morphants compared to the controls. Finally at 72hpf the presence of a third ectopic vessel of venous identity was observed in the plexus (Figure 2B) (observed in 80% of the morphants (n=5)).

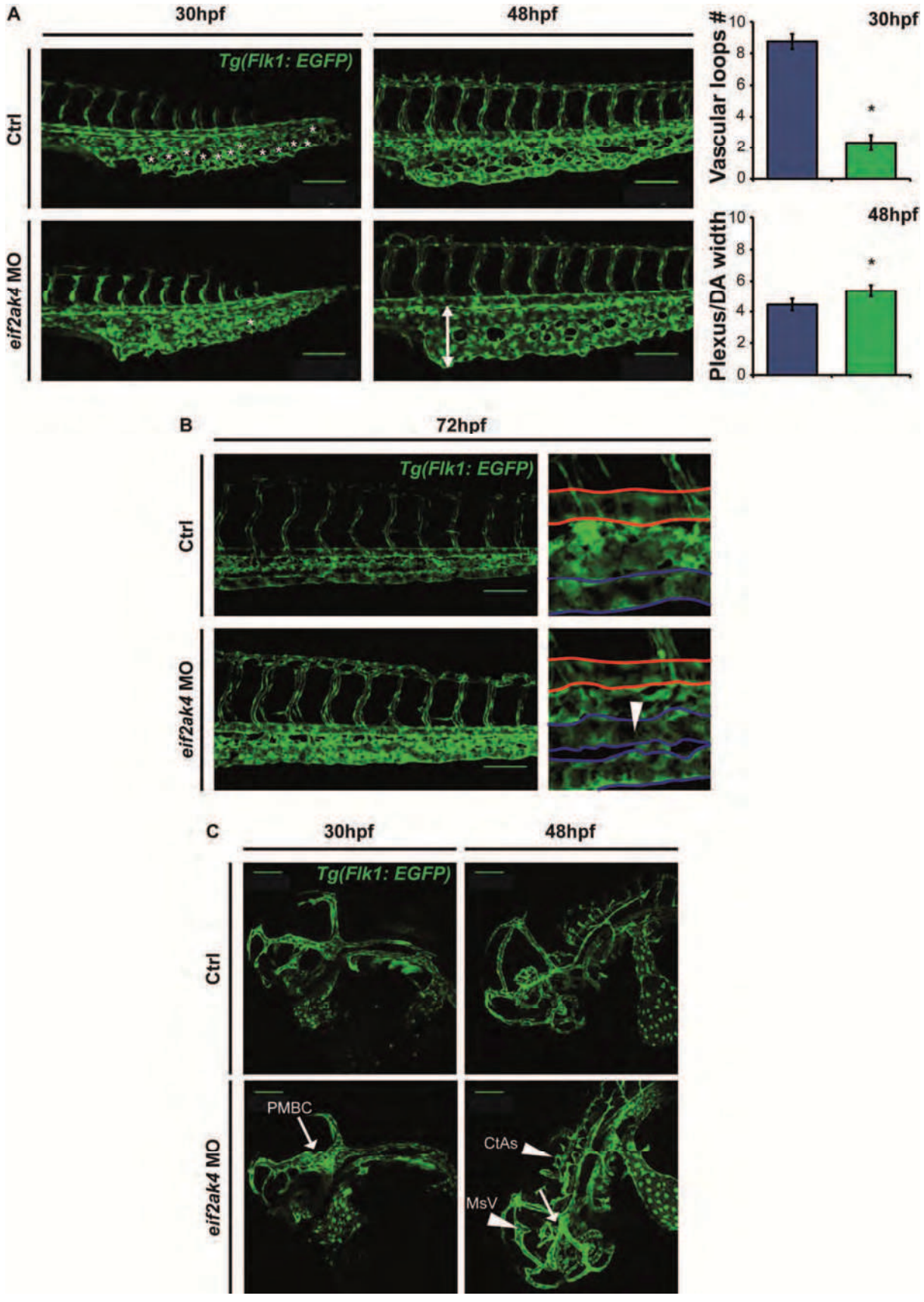
A
30hpf
48hpf
Tg(Flk1: EGFP)
Ctrl
eif2ak4 MO
Vascular loops #
30hpf
Plexus/DA width
48hpf
B
72hpf
C
PMBC
CtAs
MsV

Observing the cranial vasculature, the primordial mid-brain channel (PMBC) was particularly affected at 30hpf (Isogai et al., 2001). We found the PMBC was enlarged in all imaged 30hpf zebrafish embryos (n=5) (Figure 2C). At 48hpf, perturbation of the developing central arteries' (CtAs) architecture, with ectopic branching, was also observed in all imaged embryos (n=4). Additionally, the presence of a developing ectopic vessel from the mesencephalic vein (MsV) was observed in all imaged morphants, but was never present in corresponding control siblings (n=4) (Figure 2B). These observations show that *gcn2* partial loss of function lead to venous specific phenotypes, as observed in PVOD, and validate the *eif2ak4* KD in zebrafish is a good model to study the venous remodeling associated with PVOD.

GCN2 depletion is linked to venous cells proliferation and vessels dilatation in zebrafish embryos

The mechanism linking the mutation in the *eif2ak4* gene to the development of PVOD is currently unclear. No link has been established, until now, between the loss of GCN2 function and venous remodeling. We took the advantage of our zebrafish model to assess more precisely the modifications occurring in veins in the absence of *eif2ak4*. We focused on the CV to assess *eif2ak4* function during venous angiogenesis. Both *eif2ak4* MO were injected in *Tg(Fli1a:lifeact-egfp; Flk1:nls-mcherry)* transgenic line, in order to image endothelial cell (EC) protrusion (with the labeling of actin filaments in the *Fli1a:lifeact-egfp*) and to assess the EC number *in vivo* (with the labeling of nuclear labeling in the *Flk1:nls-mcherry*). We first performed live confocal microscopy of the caudal plexus of both MO-injected and control fish at 28hpf. At this stage, the plexus is still expanding and actin-filament rich sprouts are present in the external part of the plexus, directing migration of endothelial cells in the ventral direction. A significantly lower number of sprouts was found in the plexus of *eif2ak4* morphants compared to their corresponding control embryos (Figure 3A), suggesting that EC have a reduced migration potential when *eif2ak4* expression is reduced. At 30hpf, the caudal plexus presented an increased number of Flk positive nucleus (Figure 3B), suggesting that decreased *eif2ak4* expression lead to an increase in the proliferation of EC. This result was confirmed at 48hpf (Figure 3C), in addition to the previously observed enlargement of the caudal plexus. Taken together, these multiple results show that the remodeling of the CV in zebrafish embryos lacking *eif2ak4* is abnormal and is accompanied by a decrease in the migration properties and increase in proliferation of the EC in the caudal vein.

***Eif2ak4* morphant phenotype can be rescued by overexpression of human GCN2**

To test the specificity of the observed phenotypes and the functional redundancy of the zebrafish and human EIF2AK4 proteins, we injected the human *EIF2AK4* mRNA into the morphant zebrafish and assessed the resulting phenotype. After coinjection of *in vitro* transcribed human *eif2ak4* mRNA with each of the *eif2ak4* MO in single-cell stage embryos in the *Tg(Fli1a:lifeact-egfp; Flk1: nls-mcherry)* transgenic line, all previously observed sprouting and proliferation defects were rescued (Figure 3A, B, C). The number of vascular loops, PMBC width at 30hpf and the caudal plexus width at 48hpf were similar to wild-type levels in the MO + mRNA double injected embryos (data not shown). This confirms

(see figure on the previous page)

Manuscript 4/ Figure 2: Venous-specific phenotypes are observed in *eif2ak4* morphants

(A) Z-stack maximal projection of confocal images of the caudal plexus of *Tg(Flk1:EGFP) eif2ak4* zebrafish morphants at 30 and 48hpf and their corresponding controls. White stars underscore the position of vascular loops at 30hpf and the white arrow shows an enlargement of the plexus at 48hpf. Scale bar = 100µm. Quantifications of vascular loop numbers at 30 hpf and measurements of the ratio between the width of the plexus and the width of the DA at 48hpf are presented in the right panel. (B) Z-stack maximal projection of confocal images of the caudal plexus of *Tg(Flk1:EGFP) eif2ak4* zebrafish morphants and their corresponding controls at 72hpf. Scale bar = 100µm. Zoomed region show the presence of the DA (highlighted in red) and of one caudal vein (highlighted in blue) in the control. An ectopic venous vessel (white arrow head) is observed in *eif2ak4* morphants. (C) Z-stack maximal projection of confocal images of the cranial vasculature of 30 and 48hpf *Tg(Flk1:EGFP) eif2ak4* zebrafish morphants and their corresponding controls. Arrows show enlarged regions (including the primordial mid-brain channel (PMBC)) and arrow heads show regions with ectopic development (including central arteries (CtAs) and the presence of an ectopic vessel from the mesencephalic vein (MsV)).

the specific implication of GCN2 depletion in the observed venous specific phenotypes and validates a functional homology between the human and zebrafish orthologs, in view of the absence of the aa sensing domain in the zebrafish *eif2ak4*.

The *eif2ak4* depletion phenotype is ATF4-dependant

ATF4 increased expression is considered as the major mediator of the effects of GCN2-induced eIF2α phosphorylation. However, GCN2 involvement in venous remodeling could be ATF4-independent and related to GCN2 kinase activity on other substrates than EFI2a, as suggested by some authors (Barrios-Rodiles et al., 2005; Carraro et al., 2010). To address this question, we depleted ATF4 in zebrafish and compared the subsequent phenotype with the *eif2ak4* morphants phenotype. Two orthologs of *ATF4*, *atf4b1* and *atf4b2,* were found in the zebrafish genome. We designed MOs against each of them and co-injected them to achieve a full depletion of ATF4 function. We found that the resulting double *atf4b1-atf4b2* KD recapitulates the venous-specific phenotype observed at the CV (Figure 4A) and PMBC (Figure 4B) in *eif2ak4* morphants. In particular, the PMBC was enlarged at 30hpf, the central arterial disorganization and the ectopic vessel formation were observed at 48hpf in the cranial vasculature. We also found that the CV of the double *atf4* KD presented a reduced number of vascular loops at 30hpf (4 fold reduction, n=6) and appeared to be enlarged at 48hpf in 80% of the imaged embryos (n=5). Increased proliferation was observed at 30hpf as well in the *atf4b* double morphant (232±27 nuclei in the morphants *vs.* 141±9 in the controls (n=6)) and also was rescued by a co-injection of *atf4b1* and *atf4b2* mRNAs at 30hpf (142±12 nuclei in rescued embryos (n=6)). Taken together, these data show that the *atf4* loss of function lead to phenotypes that are similar to *eif2ak4* partial loss of function and suggest that PVOD phenotype establishment depends on *atf4* when *eif2ak4* is not functional.

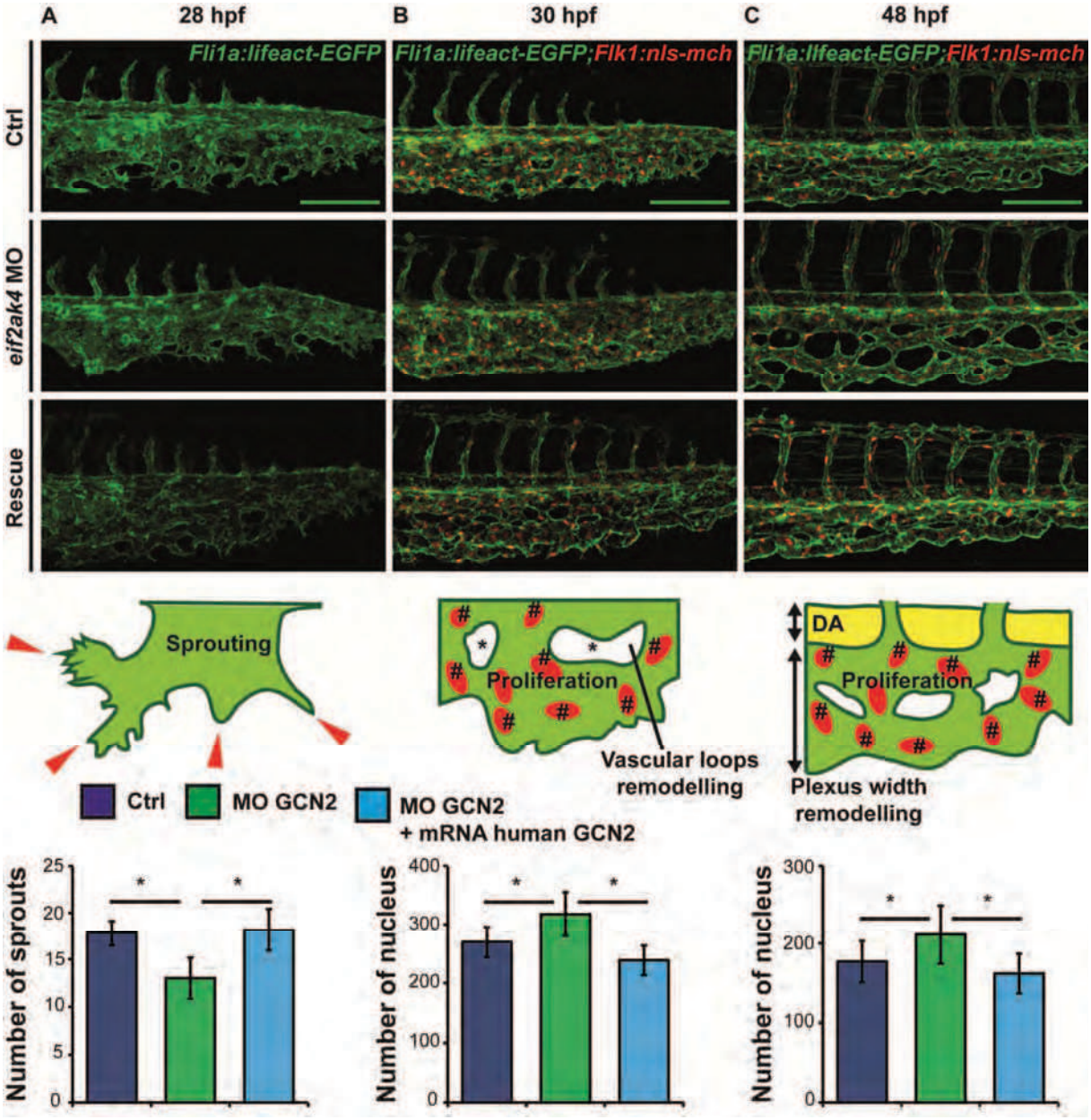

Manuscript 4/ Figure 3: Sprouting and proliferation defects are observed in the caudal plexus of *eif2ak4* morphants.

(A) Z-stack maximal projection of confocal images of the caudal plexus of *Tg(Fli1a:lifeact-EGFP) eif2ak4* zebrafish morphants at 28hpf, their corresponding controls and embryos rescued by coinjection of human GCN2 mRNA and *eif2ak4* MO. The number of sprouts from the caudal plexus was counted. (B) Z-stack maximal projection of confocal images of the caudal plexus of *Tg(Fli1a:lifeact-EGFP; Flk:nls-mcherry) eif2ak4* zebrafish morphants at 30hpf, their corresponding controls and embryos rescued by coinjection of human GCN2 mRNA and *eif2ak4* MO. The number of *Flk* positive nuclei in the caudal plexus was counted. (C) Z-stack maximal projection of confocal images of the caudal plexus of *Tg(Fli1a:lifeact-EGFP; Flk:nls-mcherry) eif2ak4* zebrafish morphants at 48hpf, their corresponding controls and embryos rescued by coinjection of human GCN2 mRNA and *eif2ak4* MO. The number of *Flk* positive nuclei in the caudal plexus was counted.

Discussion

Since there is no known physiological basis allowing the link between *EIF2AK4* bi-allelic loss of function and the development of human PVOD, a disease due to a major remodeling of lung veins and venules, we used the zebrafish as an *in vivo* model for looking at the effects on vessel development of the *EIF2AK4* ortholog gene inactivation by morpholinos. Although the zebrafish does not have lungs, the study of vascular remodeling during development is of major interest for understanding the role of *EIF2AK4*. Indeed, we observed a complex remodeling defect affecting predominantly veins, with a decrease of vein sprouting corresponding to a decrease in vascular cell migration, and an increase in vascular cell proliferation. The specificity of the morpholino's effect was validated by the phenotype rescue by human *EIF2AK4* mRNA injection. In order to identify the signal transduction pathway involved in the EIF2AK4 KD phenotype, we knocked-down the *ATF4* gene, which is considered as the major effector of EIF2AK4. ATF4 is a transcription factor, the translation of which is increased by EIF2AK4-induced phosphorylation of the EIF2α subunit.

Our experiments bring major new insights in the understanding of the link between *EIF2AK4* disruption and vascular remodeling. Firstly, this is the first model that shows an involvement of the zebrafish EIF2AK4 ortholog in the embryo's venous network development, an important finding with regards to the human disease. Indeed, in humans, lungs of the patients are analyzed when the disease has reached its final stages, either at necropsy, or when lung transplantation is performed. The zebrafish model might suggest that vascular abnormalities develop during development and that additional factors are involved to induce the disease at an age that differs between individuals. Two major functions of vascular endothelial cells seem affected - migration capacity, which is decreased, and cell proliferation, which is increased. The increase in cell proliferation is compatible with the endothelial cell and vascular smooth cell proliferation during PVOD.

The major difference in the *EIF2AK4* gene structure between zebrafish and humans is of major importance, because it shows that, in spite of lacking the aa sensor capacity due to the tRNA binding domain, it keeps its role in vessel development. A careful analysis of the zebrafish genome only showed one *EIF2AK4* ortholog, thus eliminating the possibility of other paralogs, including this domain. In zebrafish, EIF2AK4 playing a role in aa availability sensing can be ruled out because it lacks the regulatory domain of the protein. It can therefore be speculated that, in humans, EIF2AK4 does not draw its vascular effects from the aa sensor function, but that another factor induces the activation/expression of *EIF2AK4* and that, in the absence of the gene, abnormal venous remodeling occur.

In spite of this major difference in structure, the ATF4 KD experiments clearly show that this pathway is involved in the signaling pathway leading to venous remodeling. Indeed, ATF4 is a converging step for different stress sensing pathways and represents the major signal transmitter by inducing or inhibiting the transcription of several target genes mediating what is referred to as the ISR (Donnelly et

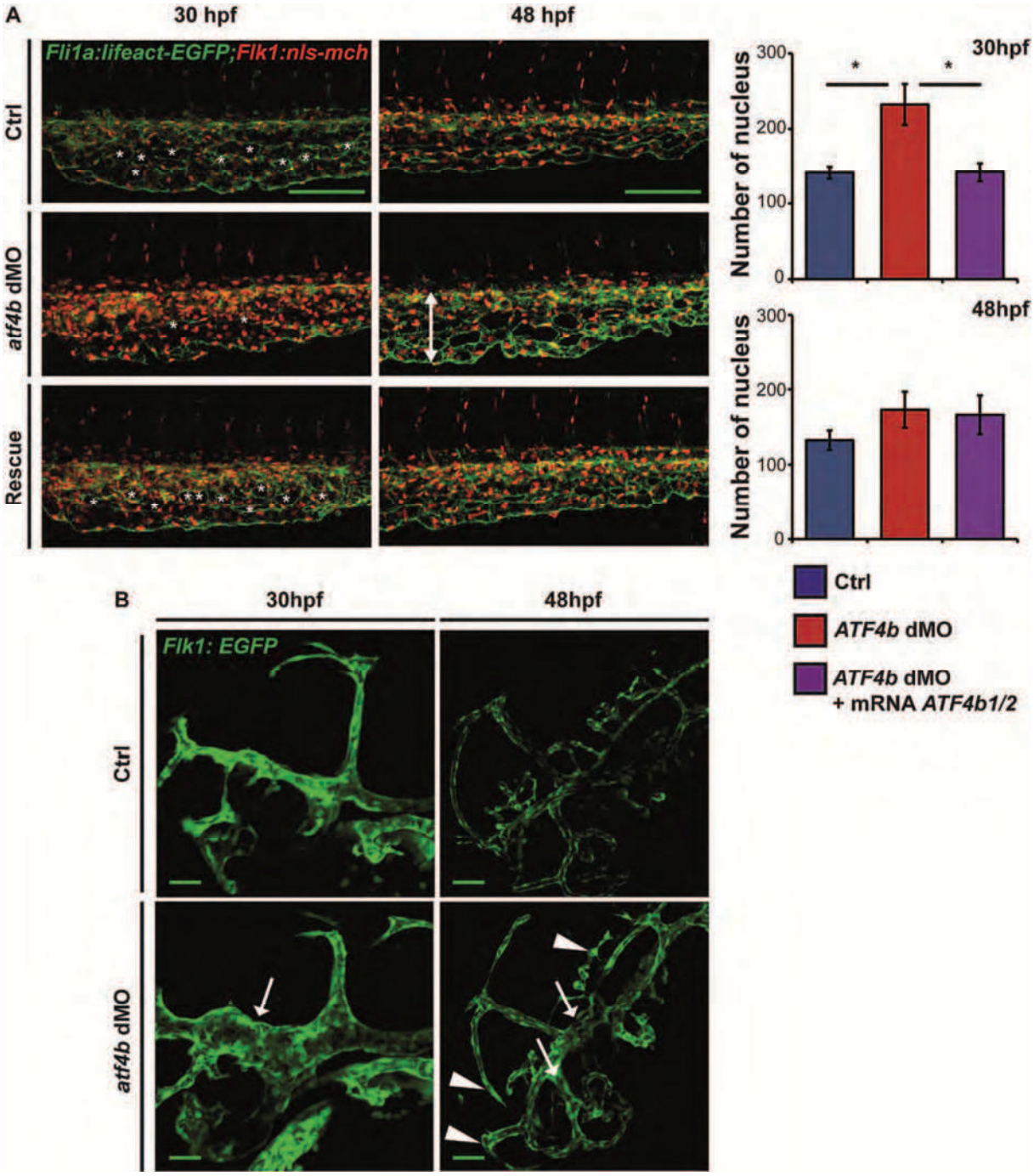

Manuscript 4/ Figure 4: ATF4 double morphants recapitulate the phenotypes observed in eif2ak4 morphants

(A) Z-stack maximal projection of confocal images of the caudal plexus of *Tg(Fli1a:lifeact-EGFP; Flk:nls-mcherry) atf4b1 and atf4b2* zebrafish double morphants at 30 and 48hpf, their corresponding controls and embryos rescued by coinjection of a mix of *atf4b1* and *atf4b2* zebrafish mRNA and the two corresponding MO. The number of *Flk* positive nuclei in the caudal plexus was counted (right panel). White stars show the position and number of vascular loops at 30hpf. A white arrow shows an enlargement of the caudal plexus at 48hpf. (B) Z-stack maximal projection of confocal images of the cranial vasculature of 30 and 48hpf *Tg(Flk1:EGFP) atf4b1 and atf4b2* zebrafish double morphants and their corresponding controls. Arrows show enlarged regions and arrow heads show regions with ectopic development.

al., 2013). These KD experiments tend to rule out the possibility that the *eif2ak4* KD phenotype is related to its kinase activity on other substrates than eIF2α, as also suggested (Barrios-Rodiles et al., 2005; Carraro et al., 2010)

The zebrafish model of *EIF2AK4* loss-of-function during development thus provides important information for guiding the research in humans. As for *BMPR2* heterozygote loss of function, pulmonary hypertension occurs at variable age in life (from early infancy to adult age for PVOD), suggesting triggering factors, either genetic, epigenetic or environmental. Identifying the second factor responsible for the development of the disease would have a major impact for therapy and prevention. The structural difference between the human and the zebrafish *eif2ak4* gene suggests that identification of conditions which normally activate *EIF2AK4*, beside amino acid deprivation, is a key step for understanding the disease.

In summary, our data demonstrate that GCN2 and ATF4 are necessary for venous angiogenesis and CV morphogenesis. They control the level of expression of venous specific markers and modulate the venous cell number. These changes in gene expression, along with changes in expression of yet to be identified genes, serve to dampen angiogenic behavior and to stabilize arterial endothelial cell number. Interestingly, these defects are similar to what observed in the *acvrl1* mutants in zebrafish (Corti et al., 2011), a gene which is also associated with PVOD in patients (Eyries et al., 2012), suggesting a conservation of function in fish. Thus, the use of zebrafish might help to address the cellular and molecular basis of PVOD, as the molecular pathway seems conserved in vertebrates.

Material and Methods

Zebrafish Husbandry and Embryo Treatments

Zebrafish lines used in the study are wild-type AB, *Tg(fli1a:neGFP)*^{y7} (Roman et al., 2002), *Tg(flk1:eGFP)*(Jin et al., 2005), *Tg(flt1enh:RFP)* (Bussmann et al., 2010), *Tg(Fli1a:lifeact-egfp; Flk1: nls-mcherry)* and *Tg(gata1:dsRed)* (Traver et al., 2003) and were described previously. Embryos were staged according to hours (hpf) and days post-fertilization (dpf). They were incubated at 28.5°C in 0.3% Danieau medium supplemented with 0.003% (wt/vol) 2-phenylthiourea to inhibit pigment formation. All zebrafish strains were maintained at the IGBMC under standard husbandry conditions. Animal experiments were approved by the Animal Experimentation Committee of the Institutional Review Board of the IGBMC.

For imaging, embryos were anesthetized with 0.02% Tricaïne (Sigma Aldrich, Saint-Louis, USA) solution and were mounted on the glass bottom Petri dishes embedded in 0.8% low Melting Point agarose (Sigma Aldrich).

Morpholino knockdown and mRNA rescue

Two splice site blocking morpholinos were designed to knockdown zebrafish *eif2ak4* (Gene Tools, Philomath, USA). Their sequences are: *eif2ak4* e1i1 splice MO (exon 1-intron 1): TAGCTGACCCCTGACCTGTTAAGGA, *eif2ak4* e2i2 splice MO (exon 2-intron 2): TATAATGTCAGTCTGACCCTCTGGA. All the presented experiments were performed with both morpholinos and comparable results were obtained, quantifications and images presented here were obtained with *eif2ak4* e1i1 splice MO. Nevertheless, results for *eif2ak4* e1i1 splice MO only were presented in the figures for the sake of space and clarity. Morpholinos against ATF4 orthologs *atf4b1* and *atf4b2* are respectively: *atf4b1* MO (translational): CGTCCCCAACACACAGAGACATGGT and *atf4b2* splice MO (exon 2-intron 2): TCAAATGTCTACACCTCACCTTCAC.

Eif2ak4 Morpholinos were dissolved in water to a concentration of 50µM. A mix 1:2 with final concentrations of 50 µM *atf4b1* MO and 100µM *atf4b2* MO was prepared in water and injected for KD of both forms of Atf4. 2,3nL of MO solutions were injected into embryos at 1 cell stage. For rescue experiments in *eif2ak4* morphants, human EIF2AK4 cDNA obtained in pOTB7 (Source Bioscience, Nottingham, UK) was amplified using SP6-hGCN2 FP: AGCATTTAGGTGACACTATAGACCATGGCTGGGGGCCGTG and hGCN2 RP: CTGTGTCTGGACGTCCTCCT primers. The resulting fragments were transcribed in vitro using mMessage mMachine SP6 Kit (Ambion, Austin, USA). 100ng of the mRNA was injected into embryos at the one-cell stage. *atf4b1* cDNA was obtained in pCMV-SPORT6.1 and *atf4b2* cDNA was obtained in pME18S-FL3 (Source Bioscience, Nottingham, UK). They were amplified respectively with: T3-*atf4b1* FP: ATTAACCCTCACTAAAGGGAACCATGTCTCTGTGTGTTGGGGAC and *atf4b1* RP: CTAGCGTTTGCTCTTGCGCT and T3-*atf4b2* FP: ATTAACCCTCACTAAAGGGAACCATGTCTTTGATGAGCTCACGG and *atf4b2* RP: TTATGTTCTCGAACTTCTGTTCTCTCTTGC primers. The resulting fragments were transcribed in vitro using mMessage mMachine T3 Kit (Ambion, Austin, USA). 2.3µL of a solution containing 50ng/µL

and 100ng/µL of the mRNA of *atf4b1* and *atf4b2* respectively was injected was injected into embryos at the one-cell stage for rescue in atf4 double morphants.

Bright field and confocal imaging

Imaging of whole embryos were performed using a Leica (Wetzlar, Germany) M420 bright field macroscope. Arterial blood velocity measurements were obtained from bright field imaging in transmission configuration using white light illumination. This experiments were performed on a Leica DMIRBE inverted microscope using Photron SA3 high speed CMOS camera. For the blood cell tracking experiments, the time-lapse sequences were acquired at 250fps with a Leica (63x, N.A=1.2) water immersion objective. The velocity of red blood cells was determined by manual tracking using ImageJ. Confocal images were acquired using a Leica SP2 microscope equipped with Leica (20x, N.A=0.7) and (63x, N.A=1.2) water immersion objective. All microscopy setups used were equipped with a heating device that ensured the embryos were kept at 28°C during the imaging.

Quantifications and statistical analysis

Nuclei and sprouts were counted manually using ImageJ (NIH).

Data were statistically analysed in Office Excel (Microsoft) by parametric Student t-test and were considered significant when $P<0.05$. Error bars depict SEM. Values in the text are presented as Mean ± SEM.

ACKNOWLEDGEMENTS

We thank Karim Hnia for thoughtful comments on the manuscript. We thank Salim Abdelilah-Seyfried and Markus Affolter for providing fish stocks. We thank Jean-Marie Garnier for technical help. We thank the IGBMC fish facility (Sandrine Geschier and Sylvie Gredler) and the IGBMC imaging center, in particular Pascal Kessler, Marc Koch and Didier Hentsch. This work was supported by HFSP, INSERM, AFM, FRM and the seventh framework program (MC-IRG256549 (JV)). CR was supported by the AFM.

Genes	Sequence of primers used
Control gene	
Tbp	FP : TCTTCAGCTCGGGGAAGAT RP : TGCCAATCGAGACTGTTCCT
Targets of ATF4	
Ddit3	FP : GACGGTTCCCGACACATC RP : GAGCAGTTTAGAGAAGGCGAAC
Atf5a	FP : CTCACCCACAGGCTAACCAC RP : CCAGTCACTAAGACCATCACCA
Atf5b	FP : ACAAGTCTGCAGCCCACAGT RP : CATGAAGCTCCTCCTCCAAA
Ppp1r15a	FP : GAAGAGCAGTGGGAAGAAGG RP : CTGAACTCTCCTCCTGAAACG
Angiogenesis markers	
Flt4	FP : TGACGTCTGGTCTTTTGGAGT RP : ATGCCGGGGTATGGAGAC
Ephb4a	FP : CTCCGCTCAAAGTCAGCAG RP : TCTTCCTCAAGCCCGAAAC
Dab2	FP : TCCACCTGACATTCATTCTCC RP : GATGCCTGAGACTCATTTTGG
Notch5	FP : CACAGTGACCAGTGGATAGATACAG RP : ACAGAATGCTTGGCTCTTCC
Ephb2a	FP : GGAGTTCTTCAGAGGGAAGGA RP : TTTCATCGACTTGGTTTTACACA
Hey2	FP : ATTGCAGATGACAGTGGATCA RP : GAGAATGAGCGTCGAAATATCC
Etv2	FP : CACAGAAGACTTCAGAACTCAGGA RP : GGACAGGTCTTCACCACTGC
Fli1a	FP : CCATCTCACGCTGACCAGT RP : CAGCATCATAAGACGCATCG
Kdr	FP : CATTCCCCTGGAGCATACC RP : CGTGATAAACCCACTCCACA
Kdrl	FP : CATGTGACCCCAGTGCTAATC RP : TCGGATTTTGAGGAAAATCATC
Flt1	FP : AGTCACGTCCACCCACAATC RP : GCCAACTGTCAGAACTCCAAC
Tbx20	FP : GACTTATGCTGGAGATGAAGAGACT RP : TGCAGTGAACGCTGAACC
Gata1	FP : AACGACATCTTCAATACTACACTTGC RP : GGACACCCAACGAGAAGG
Bmp4	FP : CCCATGCTTTATTTTCTGTCG RP : CTCCCAGTAGGACTTGGCATA
Bmp2b	FP : TAGGAGACGACGGGAACG RP : GCGACCATGATCAGTCAGTTC

Table 5: List of genes probed by qPCR on MO *eif2ak4* and dMO *atf4b* samples and corresponding primers

References

Anthony, T.G., McDaniel, B.J., Byerley, R.L., McGrath, B.C., Cavener, D.R., McNurlan, M.A., and Wek, R.C. (2004). Preservation of liver protein synthesis during dietary leucine deprivation occurs at the expense of skeletal muscle mass in mice deleted for eIF2 kinase GCN2. The Journal of biological chemistry *279*, 36553-36561.

Barrios-Rodiles, M., Brown, K.R., Ozdamar, B., Bose, R., Liu, Z., Donovan, R.S., Shinjo, F., Liu, Y., Dembowy, J., Taylor, I.W.*, et al.* (2005). High-throughput mapping of a dynamic signaling network in mammalian cells. Science *307*, 1621-1625.

Bussmann, J., Bos, F.L., Urasaki, A., Kawakami, K., Duckers, H.J., and Schulte-Merker, S. (2010). Arteries provide essential guidance cues for lymphatic endothelial cells in the zebrafish trunk. Development *137*, 2653-2657.

Carraro, V., Maurin, A.C., Lambert-Langlais, S., Averous, J., Chaveroux, C., Parry, L., Jousse, C., Ord, D., Ord, T., Fafournoux, P.*, et al.* (2010). Amino acid availability controls TRB3 transcription in liver through the GCN2/eIF2alpha/ATF4 pathway. PloS one *5*, e15716.

Corti, P., Young, S., Chen, C.Y., Patrick, M.J., Rochon, E.R., Pekkan, K., and Roman, B.L. (2011). Interaction between alk1 and blood flow in the development of arteriovenous malformations. Development *138*, 1573-1582.

Donnelly, N., Gorman, A.M., Gupta, S., and Samali, A. (2013). The eIF2alpha kinases: their structures and functions. Cell Mol Life Sci *70*, 3493-3511.

Eyries, M., Coulet, F., Girerd, B., Montani, D., Humbert, M., Lacombe, P., Chinet, T., Gouya, L., Roume, J., Axford, M.M.*, et al.* (2012). ACVRL1 germinal mosaic with two mutant alleles in hereditary hemorrhagic telangiectasia associated with pulmonary arterial hypertension. Clinical genetics *82*, 173-179.

Eyries, M., Montani, D., Girerd, B., Perret, C., Leroy, A., Lonjou, C., Chelghoum, N., Coulet, F., Bonnet, D., Dorfmuller, P.*, et al.* (2014). EIF2AK4 mutations cause pulmonary veno-occlusive disease, a recessive form of pulmonary hypertension. Nature genetics *46*, 65-69.

Goetz, J.G., Steed, E., Ferreira, R.R., Roth, S., Ramspacher, C., Boselli, F., Charvin, G., Liebling, M., Wyart, C., Schwab, Y.*, et al.* (2014). Endothelial cilia mediate low flow sensing during zebrafish vascular development. Cell reports *6*, 799-808.

Harding, H.P., Zhang, Y., Zeng, H., Novoa, I., Lu, P.D., Calfon, M., Sadri, N., Yun, C., Popko, B., Paules, R.*, et al.* (2003). An integrated stress response regulates amino acid metabolism and resistance to oxidative stress. Mol Cell *11*, 619-633.

Isogai, S., Horiguchi, M., and Weinstein, B.M. (2001). The vascular anatomy of the developing zebrafish: an atlas of embryonic and early larval development. Developmental biology *230*, 278-301.

Jin, S.W., Beis, D., Mitchell, T., Chen, J.N., and Stainier, D.Y. (2005). Cellular and molecular analyses of vascular tube and lumen formation in zebrafish. Development *132*, 5199-5209.

Kilberg, M.S., Shan, J., and Su, N. (2009). ATF4-dependent transcription mediates signaling of amino acid limitation. Trends Endocrinol Metab *20*, 436-443.

Montani, D., Achouh, L., Sitbon, O., Simonneau, G., and Humbert, M. (2009). Pulmonary venoocclusive disease and failure of specific therapy. Chest *136*, 1181; author reply 1181-1182.

Roman, B.L., Pham, V.N., Lawson, N.D., Kulik, M., Childs, S., Lekven, A.C., Garrity, D.M., Moon, R.T., Fishman, M.C., Lechleider, R.J.*, et al.* (2002). Disruption of acvrl1 increases endothelial cell number in zebrafish cranial vessels. Development *129*, 3009-3019.

Traver, D., Paw, B.H., Poss, K.D., Penberthy, W.T., Lin, S., and Zon, L.I. (2003). Transplantation and in vivo imaging of multilineage engraftment in zebrafish bloodless mutants. Nature immunology *4*, 1238-1246.

Zhu, K., Jiao, H., Li, S., Cao, H., Galson, D.L., Zhao, Z., Zhao, X., Lai, Y., Fan, J., Im, H.J.*, et al.* (2013). ATF4 promotes bone angiogenesis by increasing VEGF expression and release in the bone environment. J Bone Miner Res *28*, 1870-1884.

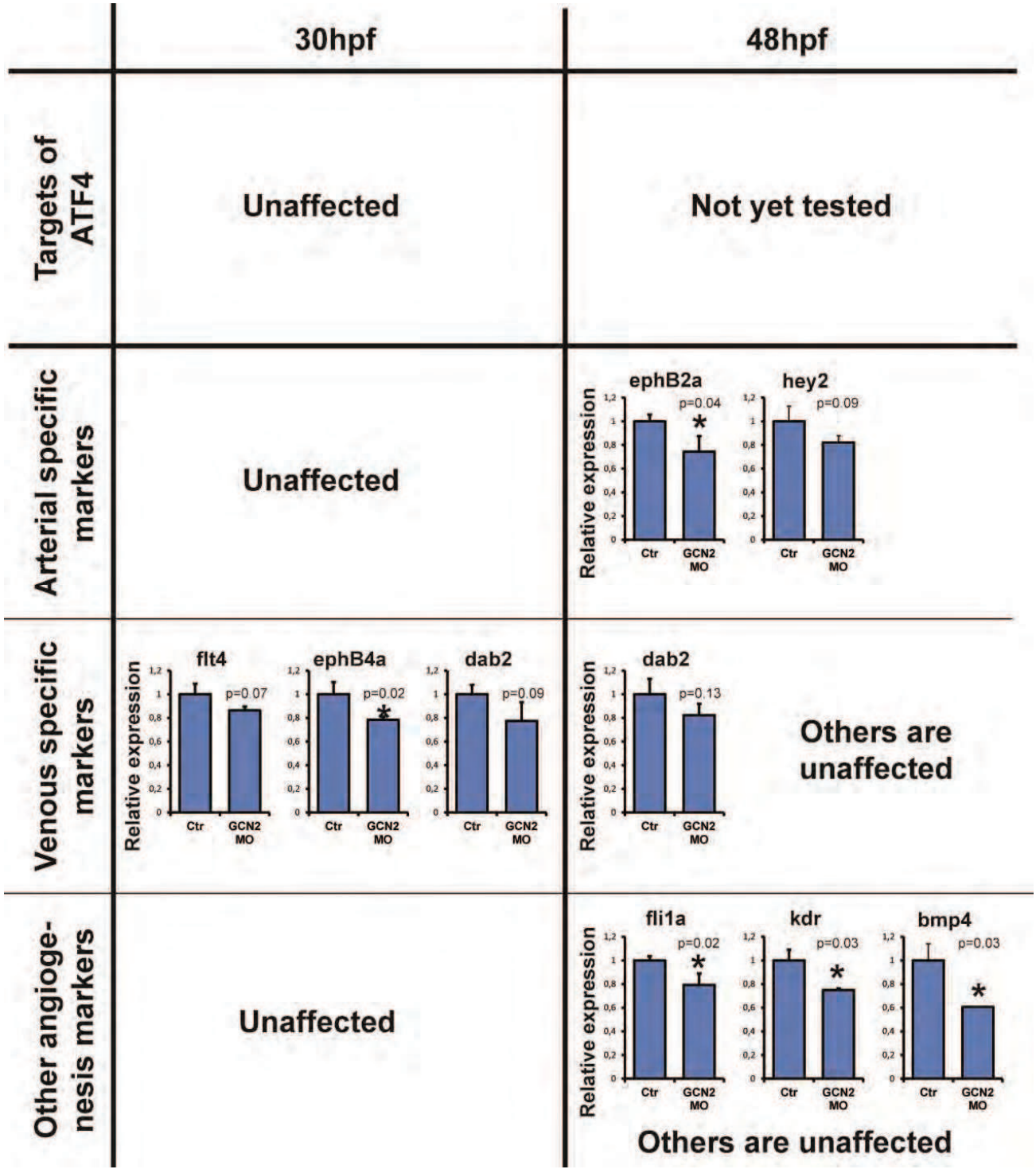

Figure 22: RT-qPCR on mRNA from dissected tails of 30 and 48 hpf MO1 *eif2ak4* (MO GCN2) samples and corresponding controls (n=3, 30 tails per pool).

Supplementary and preliminary results

(to be completed and included in the manuscript before submission)

1) Experimental procedures

RT-qPCR (Caroline Ramspacher and Stephane Roth): RNA was extracted from three pools of 30 dissected tails of 30 and 48hpf fish per condition using Trizol reagent (Invitrogen, Carlsbad, USA) using the manufacturer's instructions. A DNAse step, followed by column purification, was performed using material and instructions from the NucleoSpin RNA XS Kit (Macherey-Nagel, Düren, Germany). cDNAs were synthesized from 1µg of total RNA using SuperScript VILO^{TM} reverse transcriptase (Invitrogen). Quantitative PCR amplification of cDNAs was performed using the Universal Probe Library system (UPL) (Roche Applied Sciences, Basel, Switzerland) on Light Cycler 480 (Roche Applied Sciences). *Tbp* was used as a control, as expression of this gene varies minimally during zebrafish development. The sequences of primers used are presented in Table 5.

Western blotting (Caroline Ramspacher and Virginie Monceau): Zebrafish embryos were deyolked using deyolking buffer (55mM NaCl, 1.8mM KCl, 1.25mM $NaHCO_3$) and washed with 110mM NaCl, 3.5mM KCl, 2.7mM $CaCl_2$, 10mM Tris HCl, pH8.5. They were lysed in buffer containing 10mM Tris HCl, pH 8, 20% Glycérol, 0,4M KCl, 1X protease inhibitor mixture (Complete Mini, Roche Diagnostics), 10 µL/ml VanNa and 20 µL/ ml NaF. Full protein extracts were loaded on SDS-PAGE gel (10%), transferred to nitrocellulose membrane and stained with Ponceau (Biorad, Hercules, USA) to verify equal loading. The blots were probed overnight with rabbit anti-eIF2α (Cell Signalling, Danvers, USA) and rabbit anti-phopho-eIF2α (Ser51) (Abcam, Cambridge,UK) antibodies. Detection was carried out using enhanced chemiluminescence kit (GE Healthcare, Cleveland, USA).

2) Changes in expression of ATF4 targets and venous and vascular-specific markers in *eif2ak4* and *atf4* morphants

After observing morphological differences in the caudal plexus of embryos injected with *eif2ak4* and *atf4* MO compared to control animals, we wondered which molecular changes were implicated in the establishment of the phenotypes. For that, we assessed by qPCR the relative level of expression of genes related to ATF4 according to the literature and known markers of angiogenesis. The last can be subdivised in three categories: the venous markers, including *ephb4a*, *dab2* and *flt4*, the arterial markers with *notch5*, *ephb2a* and *hey2,* and other general angiogenesis markers (see Table 5). The results obtained comparing the expression of these genes in *eif2ak4* morphants (MO GCN2) and their uninjected siblings at 30 and 48hpf are presented in Figure 22. Globally, the venous markers were down-regulated at 30hpf while arterial markers seem to be down-regulated at 48hpf. Generally, angiogenesis markers were not perturbed at 30hpf but showed a down-regulation at 48hpf (*fli1a*, *bmp4* and *kdr*).

We then did the same on samples collected from *atf4* double morphants at 30hpf (the 48hpf time points still needs to be studied). The results obtained are presented in Figure 23. Many angiogenesis markers were shown to be differentially expressed, including both venous and arterial markers. Nevertheless, no clear trend was revealed in terms of up or down-regulation of these genes. Under

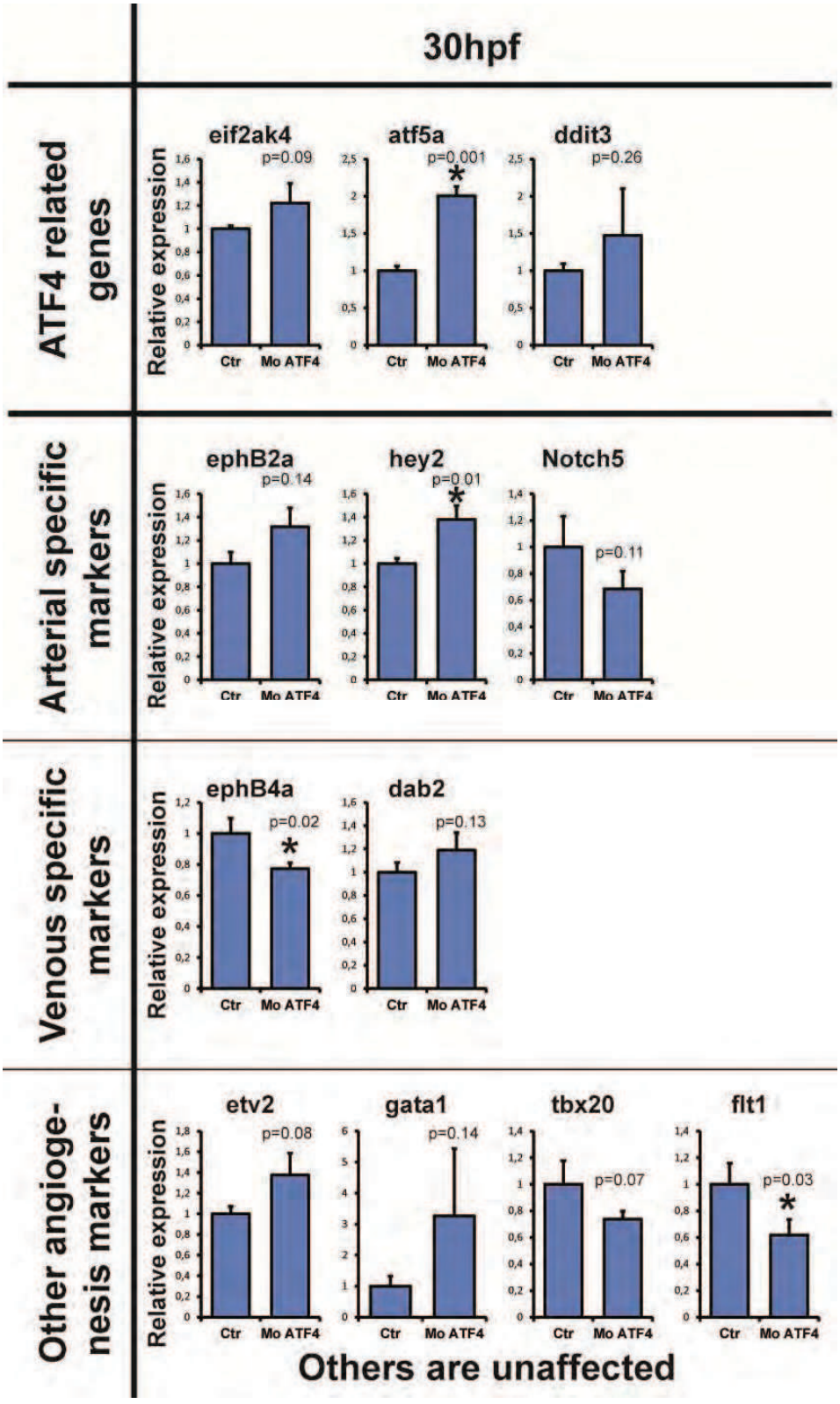

Figure 23: RT-qPCR on mRNA from dissected tails of 30hpf embryos injected with *atf4b1* and *atf4b2* MO (MO ATF4) samples and corresponding controls (n=3, 30 tails per pool).

stress conditions, the translational activation of Atf4 by the phosphorylated EIF2α is known to activate a series of target genes leading to the activation of the ISR pathway (Hardling et al., 2003). Surprisingly, targets of Atf4*,* and in particular *atf5a,* were found to be up-regulated in our morphant zebrafish.

Taken together, these results confirmed dampened angiogenic behaviour, with differences in terms of arterial and venous perturbations. They do not recapitulate exactly our observations, with the down-regulation of venous markers at 30hpf being for example paradoxical with the higher proliferation observed in the caudal plexus. Further qPCR experiments still need to be performed, using a higher number of samples to validate and prove the significance of some of the obtained results and to complete the conditions that are still missing. Moreover, confirmation of results at the protein level or by alternative approaches should be considered in the context of some surprising results like the up-regulation of *atf5a* in the absence of Atf4.

3) Status of the ISR pathway in absence of GCN2

To get a functional insight into the activation status of downstream effectors of GCN2 in response to its lower expression, we evaluated the phosphorylation status of EIF2α in *eif2ak4* morphants. The level of S51-phosphorylated and total EIF2α were probed on Western blot (Figure 24). After quantification, we observed that the level of phosphorylated EIF2α was lower in the context of *eif2ak4* KD as expected. Despite the fact that other kinases target EIF2α, and that no stress condition was applied to the embryos, this results shows the functional impact of GCN2 KO in zebrafish.

In summary, our data demonstrate that GCN2 and ATF4 are necessary for venous angiogenesis and morphogenesis. They control the level of expression of angiogenesis and venous specific markers and modulate the venous cell number. These changes in gene expression, along with changes in expression of yet to be identified genes, serve to dampen angiogenic behavior and to stabilize arterial endothelial cell number.

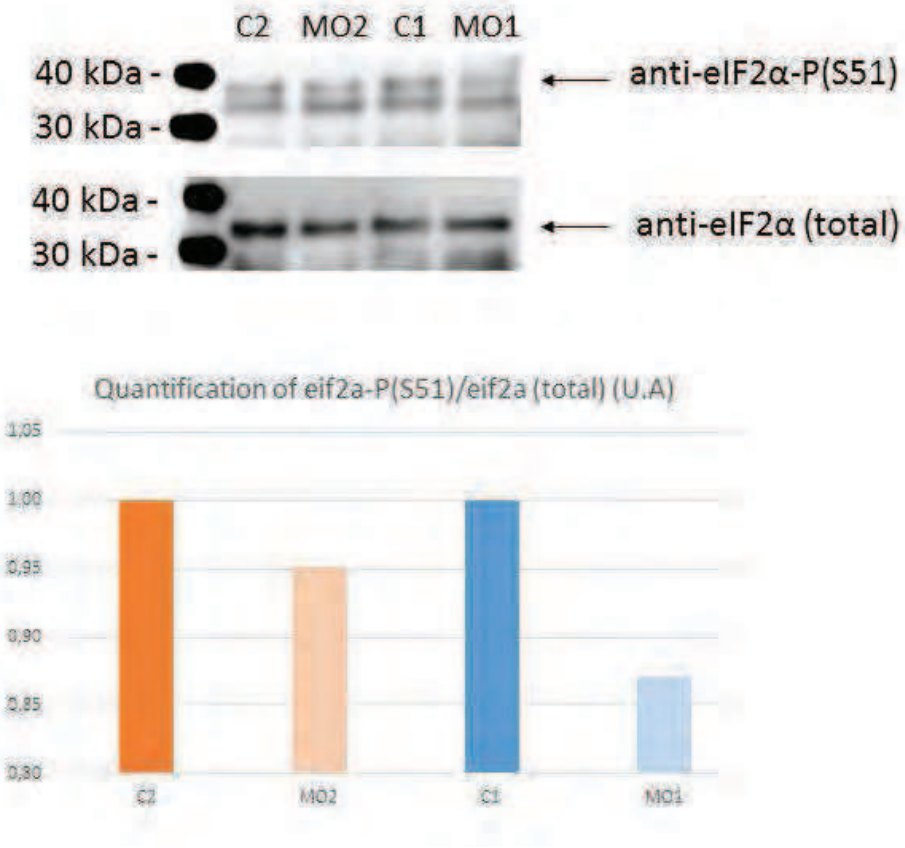

Figure 24: Preliminary results showing the phosphorylation level of Eif2α in 30hpf *eif2ak4* MO embryos and corresponding controls.

Discussion and Perspectives

I/ Discussion on the desminopathy models

A. Function of desmin

1) Studying desmin as a signalling platform in complement to its structural role

As described in our review (Manuscript 1), the role of desmin in signalling is gaining more and more importance relative to its role in the integrity of the myofiber structure maintenance. Most of the novel desmin interactors described so far have homologs in zebrafish. The zebrafish myospryn, *cmya5*, was shown to interact effectively with the type II regulatory subunit of protein kinase A (PKA) clearly demonstrating conservation of the A-kinase anchor protein (AKAP) function of myospryn (Reynold et al., 2007). S100A1 has an ortholog in zebrafish, *s100a1*, but was not showed to be expressed in muscles but in brain, olfactory epithelium and intestine epithelium (Kraemer et al., 2008). No ortholog of S100B1 was found in the fish so far. PEPP2 is orthologous to the zebrafish *plekha5. MTM1* has already been extensively studied in zebrafish, in the context of its implication in centronuclear myopathy (Dowling et al., 2009; Gupta et al., 2013), nevertheless its link with desmin or the role of their interaction remains unclear. ITSN1 ortholog, *itsn1* interaction and regulation were assessed in the zebrafish brain but no evidence exists so far that it is present in muscles (Dergai et al., 2010). Zebrafish MutL Homolog 1 is *mlh1* and seems to have ubiquitous expression in early embryos. It was studied in the context of its implication in meiosis completion and *mlh1* deficient zebrafish males were shown to be sterile, whilst females produced embryos with a high rate of deformities linked with aneuploidy and triploidy (Feitsma et al., 2007; Leal et al., 2008). The effect of these different interactors upon desmin deletion or mutation could be assessed in our model. In particular, their level of expression and subcellular localisation can be tested. In parallel, it would be possible to do systematic MO KD of different desmin partners and observe the effect on the intermediate filament network in WT and desmin mutant conditions. This would bring further insight into the mechanism of interaction between desmin and these interactors, as well as into the implication of these interactions in signalling. In particular, these signalling pathways might be perturbed and could lead to impaired functions in the context of desminopathy.

2) New aspects of desmin loss highlighted by mRNA sequencing

Despite the fact that none of the previously discussed signalling interactors were shown to be misregulated in the context of the mRNA sequencing experiment that we performed, other known interactors of desmin were found, including *caspase b* and ankyrin repeat domain 50 (*ankrd50*). *caspase b,* displayed an 8,1-fold up-regulation, which suggests an increase in apoptosis in *desma* null embryos. *ankrd50* is 2,7-fold up-regulated in the absence of *desma*. Ankyrin participates in the link between desmin and the plasma membrane and probably the sarcoplasmic reticulum (SR). It would be interesting to observe the influence of the presence of mutated desmin on the expression level of these two genes.

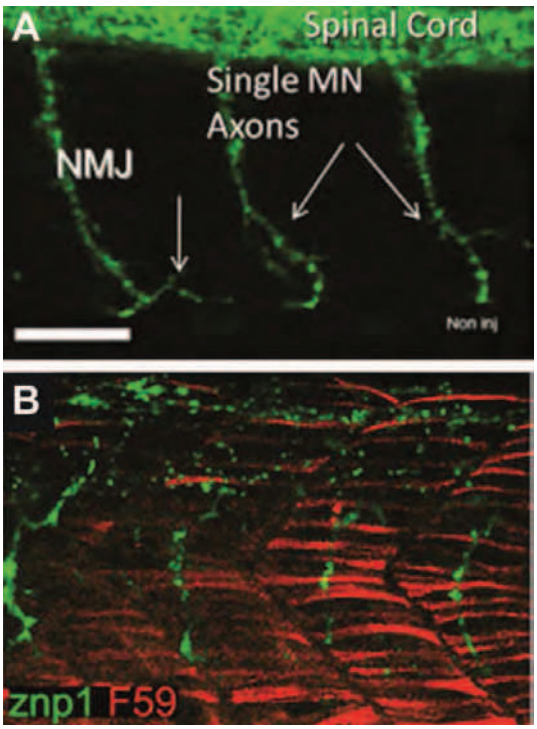

Figure 25: The neuromuscular junction in zebrafish

(A) From Kabashi lab website. Znp1 antibody staining showing motor axons (green) in 48hpf zebrafish embryo (B) From Tallafuss et al., 2008. F59 antibody (red) labeling showing fast muscle fibers and znp1 antibody staining showing motor axons (green) in 48hpf zebrafish embryo.

An important question in the context of desmin KO models is the ability of other intermediate filaments to compensate for the lack of desmin. While neither vimentin nor nestin staining was found in adult Des-/- (Li et al., 1996), this was never assessed at embryonic stages. It is to note that myofibrilogenesis is normal in the absence of desmin, contrary to what observed in cell models (Schultheiss et al., 1991). We therefore looked for other intermediate filaments in our mRNA sequencing results but none of the classical candidates (described in Manuscript 1) were perturbed. Nevertheless, we found that *wu:fb15e04* was 3,1-fold over-expressed. *wu:fb15e04* encodes a "thread keratin", which is a highly specialized IF protein restricted to different fish species and to larval development in an aquatic environment (Schaffeld and Schultess, 2006). *wu:fb15e04* could then partially compensate desmin loss, in particular at early stages, in our *desma*$^{sa5-/-}$ model.

Some immunoglubulin subtypes were found to be down-regulated in the *desma* null embryos. This is probably a readout of a perturbed immune response. This perturbation could be linked with muscle disorganisation and degeneration observed in the absence of desmin. Immune system perturbation is seen in particular in inclusion body myositis, another congenital myopathy that presents protein aggregates and belongs to the group of muscle diseases known as the inflammatory myopathies (Dimachkie et al., 2014). In this disease, T cells appear to be driven by specific antigens to invade degenerating muscle fibers and drive an autoimmune response. In this context, immunoglobulins extracted from isolated single plasma cells directly from IBM-derived muscle tissue sections, were shown to target desmin specifically (Ray et al., 2012). Such manifestations are not reported in desminopathies; however immune response perturbations and related adaptations cannot be excluded.

Clusters of neurotransmitters and receptors were shown to be particularly enriched in the absence of *desma*. With most of the receptors in the cluster being involved in neurotransmission, this result suggests that desmin is involved in the proper maintenance of the NMJ. NMJs were found to be disorganised in Des-/- mice, in particular after the induction of muscle degeneration and regeneration by the myotoxic drug cardiotoxin (Agbulut et al., 2001). The post-synaptic area was particularly affected, with disorganised or absent junctional folds. It was linked with a decrease of the total acetylcholine receptor and Na channel rich area in the NMJ and the staining for cholinesterase activity was lower and more diffuse. Moreover, desmin was found to be directly or indirectly interacting with the nicotinic acetylcholine receptor and was proposed to play a role in the submembranous organization of the motor end plate (Mitsui et al., 2000). Disorganisation of neuromuscular junctions and consequent perturbations in the nerves could explain the presence of neurological signs in 74% of desminopathy patients (van Spaendonck-Zwarts et al., 2011). This currently poorly characterised aspect of desminopathies would be interesting to study further. A potential perspective for our zebrafish model would be to study the structure and function of the NMJ in the absence of desmin and in the presence of desmin aggregates. In zebrafish embryos, one motor neuron per somite arises from the spinal cord and connects the muscular cells, forming NMJs in a central position (Figure 25). Studies of NMJs in zebrafish were extensively performed in the context of neuromuscular diseases

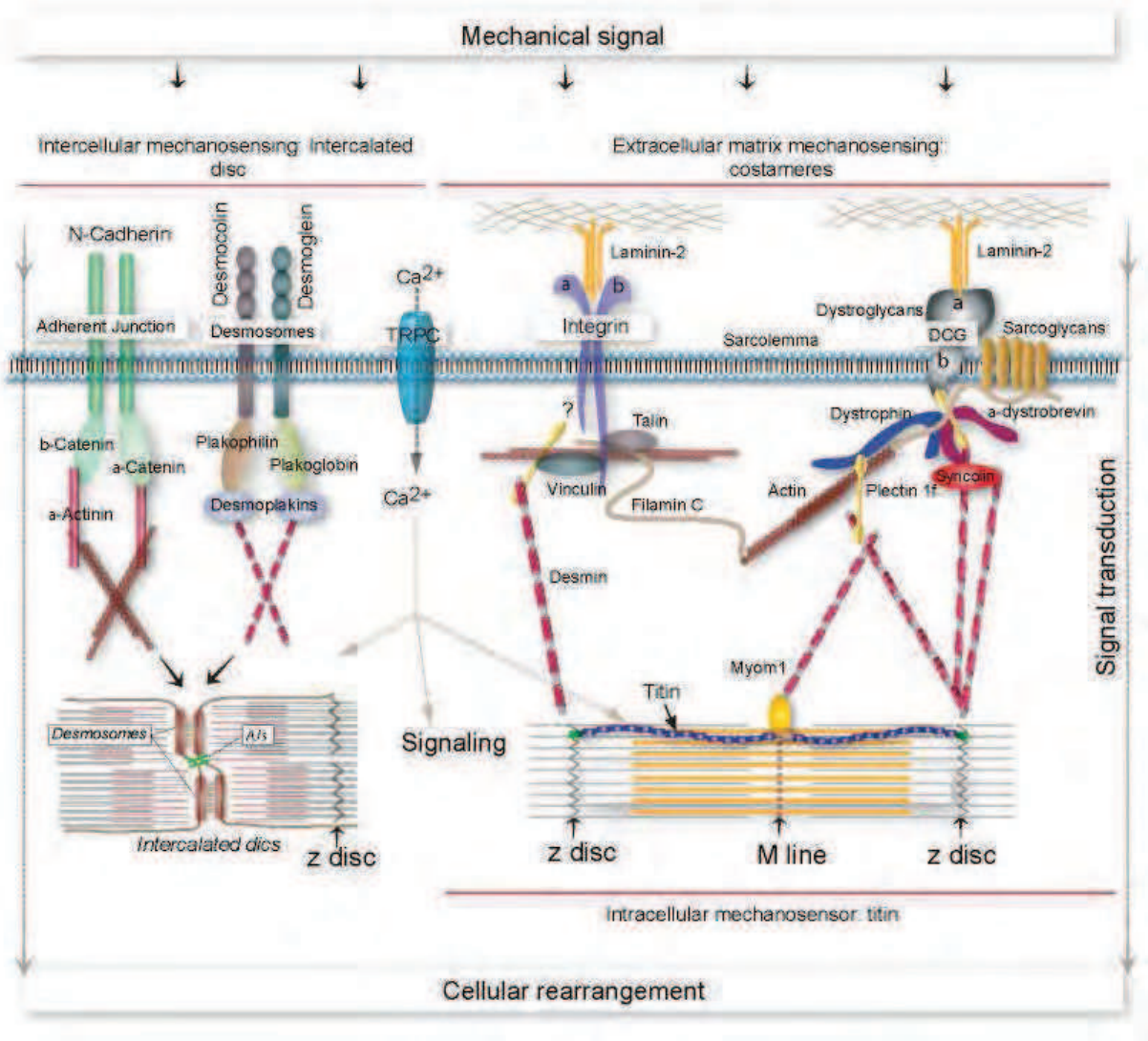

Figure 26: Mechanotransduction in muscle cells

The sensing of a mechanical signal and its transduction to biochemical signal, leading to cellular rearrangement happens through three main components. The intercellular mechanocensing in cardiomyocytes go through the intercalated disks with adherent junctions, desmosomes and TRP channels. Mechanical load from the extracellular matrix is sensed at the costamere by integrins, dystroglycan complex and TRP channels. Finally the intracellular load in sensed through titin in the sarcomere directly. The implication of desmin in these mechanisms is still debated but seems multiple. (design by Karim Hnia)

models including Amyotrophic lateral sclerosis (ALS) models (Kabashi et al., 2010; Armstrong et al., 2013) and include structural characterisation with pre-synaptic (*psv2* antibodies) and postsynaptic (sulforhodamine-conjugated -bungarotoxin (BTX)) markers, motor neurons specific markers (znp1) and transgenic lines (*Tg(Hb9:GFP)*),as well as functional characterisation with touch evoke assays, voltage clamps, pharmacological assays etc. Comparable methods could then be used in our zebrafish desminopathies models.

Finally, lipid-binding protein cluster members were shown to be perturbed but a clear tendency for up- or down-regulation was not seen. Fatty acid binding proteins are thought to facilitate the transfer of fatty acids between extra- and intra-cellular membranes (Weisiger, 2002). Their perturbation can therefore be associated to defects in membrane folding or to the presence of altered vesicular content in desminopathy muscles. Fatty-acid-binding protein levels have been shown to decline with ageing in the mouse brain and this was attributed to a decline in synaptic activity (Pu et al., 1999). Down-regulation of this cluster in our study could then be associated to neuromuscular dysfunction and perturbed folding of the post-synaptic membrane as described above. Moreover, they could participate in the accumulation of adipocytes, which was observed in Des-/- mice in the context of degeneration and regeneration cycles (Agbulut et al., 2001) and reflect the increase in ketone body catabolism, leading to increase in fatty acid oxidation, revealed by proteomic analysis of Des-/- mice heart mitochondria (Fountoulakis et al., 2005).

3) Desmin in mechanosensing and transduction

Mechanotransduction refers to the conversion of a mechanical signal into a biochemical or electrical signal. In muscle cells, three major actors are involved in mechanotransduction. First, the mechanistic forces imposed by the extracellular matrix are sensed, particularly through integrins and mechanosensing channels found at the costameres, which are sarcolemmal structures tightly linked to the Z-disks and M-bands. Then, the intracellular load is sensed directly at the level of the sarcomeres by the extensive and highly elastic titin. Finally, the intercellular load and the mechanistic forces transmitted by neighboring cells in the myocardium is sensed through the participation of intercellular junctions, in particular the cadherins in adherent junctions and through specific mechanosensing channels, particularly enriched at the level of the intercalated disks (McCain et al., 2011). The cytoskeleton plays a pivotal role in both propagating the mechanical stress to sensors and mediating the structural remodeling necessary for the required functional response to stress, within the myocyte. Therefore, the cytoskeleton can be seen as the mechanosensory integrator of the cell. Despite the fact that desmin interacts directly or indirectly with the three main mechanosensor components, the precise role and participation of muscle IFs in mechanotransduction is still debated, as actin and microtubules are themselves interacting with the same components (Figure 26). However it is tempting to speculate that desmin IF could participate actively to particular mechanosensing, when muscle is submitted to extensive contraction (Sjuve et al., 1998).

The major mechanosensing components of the myocyte are the costamere structures. Desmin was found to be enriched at the costameric domains over the Z-disks. In Des-/- mice tibialis anterior, most costameres were lost, showing the importance of desmin filament in the maintenance of these structures (O'Neill et al., 2002). Costameres contain three main complexes considered as the mechanosensor: focal adhesion complexes based on integrins, dystroglycan complexes (DGCs) and their related non-selective stretch-activated cation channels (SACs). Costameres form a link between the extracellular matrix and the cytoskeleton, in particular actin (directly linked to integrins and dystrophin in the DGC) and IFs. Desmin is connected to the beta-dystroglycan and dystrophin through plectin1f (Rezniczek GA et al., 2007) and directly to syncoilin in the DGC (Poon et al., 2002). Mechanical load on the DGC triggers opening of SACs, playing a central role in the cellular response to pressure. Transient receptor potential channels (TRP channels) were found to be putative SACs in higher vertebrates (Patel et al., 2010). Several of them were found to have an important function in muscle cells mechanotransduction. For example, TRPC1 and TRPC6 are non-selective calcium permeable channels involved in muscle diseases, including familial DMD and cardiac hypertrophy (Patel et al., 2010; Wu et al., 2010 PNAS; Eder et al., 2011 Circ Res). No direct link between IFs, including desmin, and the focal adhesions was shown. Nevertheless, loss of vimentin in the fibroblast was recently shown to decrease the activity of the focal adhesion kinase and of its downstream pathway, leading to an abnormal cell response to stretch (Gregor et al., 2014). Tension and integrin-related mechanotransduction was recently shown to imply chaperone-assisted autophagy (CASA) of the filamin C deformed by the mechanical load. Filamin C is a direct integrator of the mechanical stimuli between integrins and actin and undergoes deformation following mechanical stress on integrins. CASA implicates BAG3, which is crucial for the recruitment and coordination of Hsc70, HspB8, the chaperone-associated ubiquitin ligase CHIP and the autophagic ubiquitin adaptor, p62 (Arndt et al., 2010), and recruits the YAP/TAZ signaling pathway in response to mechanical load (Ulbricht et al., 2013). BAG3 interacts tightly with CRYAB forming a chaperone complex crucial for desmin organization. Indeed BAG3 and filamin C mutation leads to secondary desminopathy (Selcen et al., 2009; Vorgerd et al., 2005).

The intracellular mechanical load in myocytes was associated with the giant protein titin. Titin is a highly elastic protein, which spans the sarcomeres and functions as a molecular spring, which is responsible for the passive elasticity of muscles. It is associated with both the thin and thick filaments and connects the Z line to the M line in the sarcomere (Linke, 2008). Titin was shown to regulate gene expression in response to its deformation, by interacting with a large range of molecules implicated in different signaling pathways (Kruger et al., 2009). Desmin was found to interact directly with titin. In this context, it could participate either in the integration of mechanosensing from the DGC to titin, in order to modulate the mechanotransduction signaling cascade, or in the global reorganization of the cytoplasm in response to mechanical load on titin.

In cardiomyocytes, a crucial mechanosensing complex is the intercalated disk, giving both the mechanical and electrical link between adjacent cells. Mechanosensors localized at the intercalated disks consist of cadherins (forming adherent junctions) and TRP channels. Moreover, desmosomes

and hemidesmosomes could participate as well in a mechanotransduction pathway implicating p21-activated kinase (PAK-1), the adaptor GIT-1 and its partner PIX-1 as shown in *C. elegans* epidermis (Zhang et al., 2011). The phosphorylation of IFs is an output of this pathway and triggers the maturation of a hemidesmosome into a junction that can resist mechanical stress. Desmin is not directly linked to cadherins but studies of mouse models of desminopathy showed an important mislocalisation of mechanical junction proteins including N-Cadherin, accompanied by further remodeling of gap junctions and mislocalisation of desmoplakin and plakoglobin (Gard et al., 2005). A recent study showed a critical role of stretch-induced TRPV2 channels at the intercalated disks in the maintenance of cardiac structure and function in a mice TRPV2 conditional KO model (Katanosaka et al., 2014). In this model, desmin expression was perturbed, with a desmin signal no longer observed close to the intercalated junctions (oral communication, Y. Katanosaka, 2014). Desmin was found in the cytoplasmic space, partially aggregated. This study suggests a structural link between desmin and TRP channels and proposes desmin as a member of the "mechanosensitive Ca^{2+}-signalosome" (oral communication, Y. Katanosaka, 2014). The link between desmin and Ca^{2+} mechanosensitive channels could moreover participate in the Ca^{2+} conduction phenotype that we observed in myocardium of both *desma*$^{sa5-/-}$ and *ct122aRGt* zebrafish lines. In zebrafish, the ortholog of TRPV2 is not known. TRPV1 is a good candidate but was not found to be expressed in the myocardium. Nevertheless, the TRPP2 (or Polycystic kidney disease 2: PKD2) member of the TRP channel family was found to be broadly expressed in the heart of zebrafish embryos and to co-localize with SR markers. This well-known mechanotransducer depletion triggers an impaired cardiac function with arrhythmia and aberrant intracellular Ca^{2+} signaling (Paavola et al., 2013). TRPP2 was extensively studied in our lab in the context of cilia-mediated mechanotransduction in the developing vasculature (Goetz et al., 2013), and in the context of blood-flow dependent valvulogenesis (Heckel et al., submitted). We therefore have all the necessary tools in our hands to determine whether there would be a link between PKD2 and desmin function in cardiac mechanosensing and Ca^{2+} wave propagation.

B. Desmin aggregates in desminopathy

1) Desmin aggregates and biomechanical properties of muscle cells

In our zebrafish models, the presence of desmin aggregates was shown to trigger more dramatic phenotypes than the absence of desmin itself. Skeletal muscle phenotypes included degeneration of muscle fibers while disorganization alone was observed in *desma*$^{sa5-/-}$. The origin of the toxicity induced by desmin aggregates remains unclear. It may be due to physical constraints and changes in the mechanism of the beating cells. The biomechanical changes in myoblasts expressing the R350P patient desmin mutation were assessed using magnetic tweezer microrheometry, using fibronectin-coated beads (Bonakdar et al., 2012). This study showed that cells with mutated desmin displayed altered mechanical properties, with an increased stiffness of the myoblasts. It is possible that R350P mutation results in an excessive mechanical stress in response to strain and, consecutively, to increased mechanical vulnerability and damage of muscle cells. Change in tissue stiffness could for example explain the change in ventricle contraction properties observed in our 4D heart beat reconstruction and the consequent squeezing of the tissue, both in the absence of functional desmin and presence of aggregates.

Moreover, the presence of large and condensed protein structures, such as desmin aggregates, in a contractile cell environment could lead to direct cellular damages in the context of the contraction movement. While still speculative and poorly documented, this hypothesis could be verified using a computational model describing the interactions of the aggregates with the cellular components during contraction, or using the injection of nano-beads into contractile muscle cells.

2) Influence of desmin aggregates on mitochondria

Using transmission electron microscopy (TEM), we observed that dilatation of mitochondria and mitophagy was dramatically increased in the *ct122aGt* line, while mitochondria were normal in both *desma*$^{sa5-/-}$ and control embryos at 52hpf. Mitochondrial defects are histological hallmark in desminopathy patients (Schroder et al., 2003; Claeys et al., 2008), in desminopathy mouse models (Kostareva et al., 2008) and in desmin-null mice (Milner et al., 2000). They include extensive mitochondria proliferation, swollen and disintegrating mitochondria (Milner et al., 2000), alteration of mitochondria respiration, lower amount of cytochrome c (Linden et al., 2001), increased permeability of the outer membrane for ADP (Kay et al., 1997), reduced cristae density, circular membranes structures due to vacuolization of their matrix and mitochondrial Ca^{2+} increase (Kostareva et al., 2008). Moreover mitochondrial proteome of Des-/- mice was assessed and showed differences in most metabolic pathways in particular ketone body and acetate metabolism, NADH shuttle proteins and aa metabolism (Fountoulakis et al., 2005).

The absence of mitochondrial defects in *desma*$^{sa5-/-}$ is surprising in contrast to the extensive and early defects reported in Des-/- mice. Later stages embryos should be adressed to determine whether the mitochondrial defects appear only later in this line or if they are really inexistent.

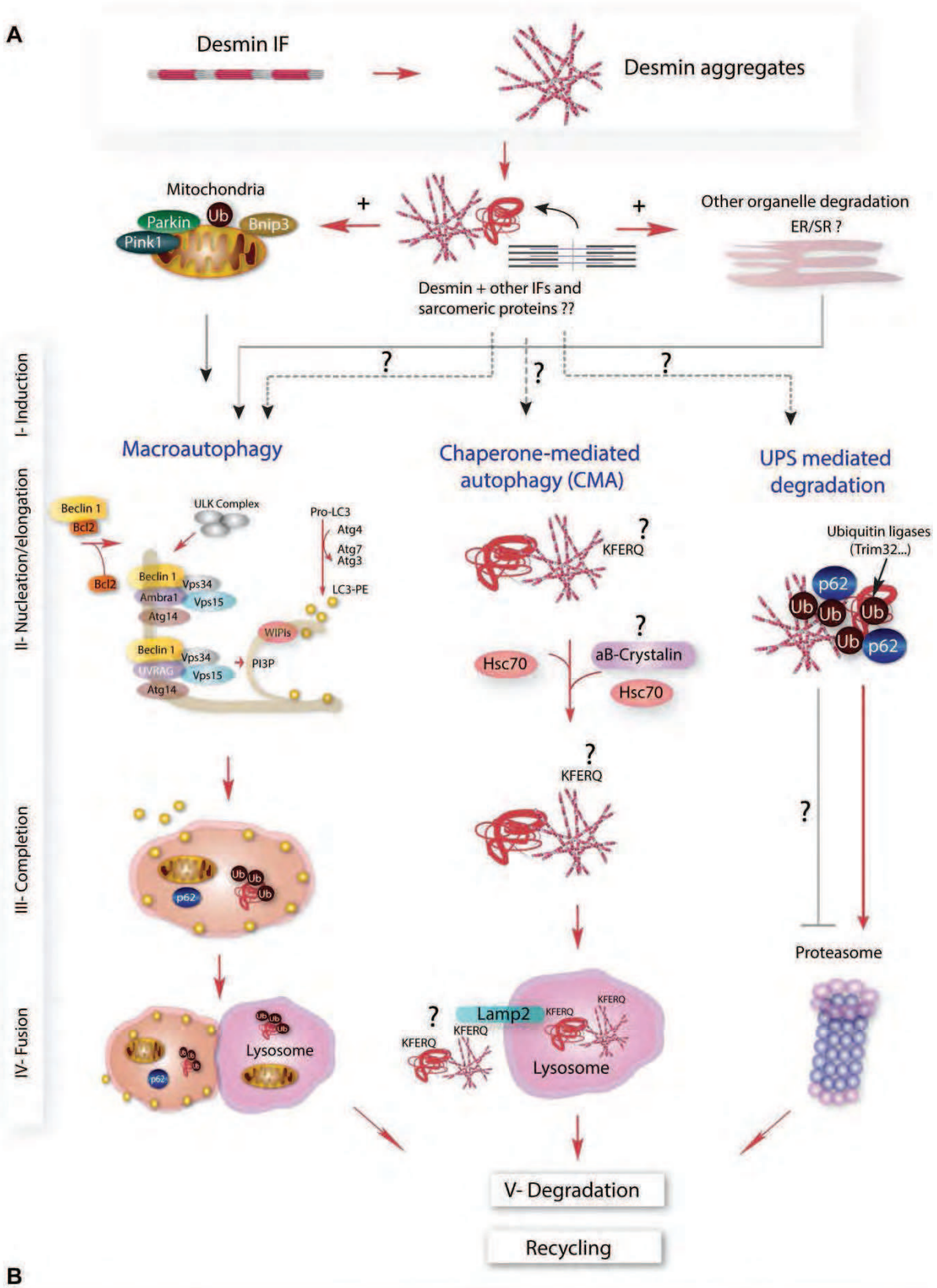
A
Desmin IF
Desmin aggregates
Mitochondria
Parkin
Ub
Bnip3
Pink1
+
+
Other organelle degradation
ER/SR ?
Desmin + other IFs and
sarcomeric proteins ??
I- Induction
II- Nucleation/elongation
III- Completion
IV- Fusion
?
?
?
Macroautophagy
Chaperone-mediated
autophagy (CMA)
UPS mediated
degradation
Beclin 1
Bcl2
ULK Complex
Pro-LC3
Atg4
Atg7
Atg3
LC3-PE
Beclin 1
Vps34
Ambra1
Vps15
Atg14
WIPIs
Beclin 1
Vps34
UVRAG
Vps15
PI3P
Atg14
KFERQ
Hsc70
aB-Crystalin
Hsc70
KFERQ
Ubiquitin ligases
(Trim32...)
p62
Ub
Ub
Ub
Ub
p62
Proteasome
p62
Lysosome
Lamp2
KFERQ
KFERQ
KFERQ
KFERQ
Lysosome
V- Degradation
Recycling
B
Desmin --DVERD--
CMA Pep signal --KFERQ--
180
aB-crystalin --KHEERQ--
--KF-ERQ--
102
Vimentin --SLERQ--
--KFERQ--
338

Desmin was shown to have an important function in protecting mitochondria from high Ca^{2+} levels (Weisleder et al., 2004). Perturbed Ca^{2+} transient in the myocardium of *ct122aGt, Tg(myl7:gcamp3.0)* embryos and observed abnormal sarcoplasmic reticulum by TEM analysis, could then explain mitochondrial defects in the absence of a functional desmin network. The mitochondrial phenotype could also be a consequence of the decrease of *tp53* expression in desmin models. p53 KO mice displayed impaired aerobic capacity and exercise performance, resulting in higher fatigue (Saleem et al., 2009). Indeed, lack of p53 was linked to decreased cytochrome c oxidase activity *via* transcriptional and post-transcriptional control of the subunits I and II, leading to an increase in glycolysis (Saleem et al., 2011). Increased glycolysis was actually observed in studies of Des-/- mice metabolism (Fountoulakis et al., 2005). The results of mitochondrial dysfunction could promote respiratory chain uncoupling, which leads to an increased reactive oxygen species rate promoting oxidative stress and extensive cellular damage.

3) Impact of desmin miss-folding on the quality control machineries

The presence of mutated desmin and aggregates is triggering multiple cellular responses and in particular the protein quality control machinery, in order to clear aggregates content in the cells. The different mechanisms implicated are discussed above and a recapitulative sheme is proposed in Figure 27.

a) Macroautophagy (autophagy) in desminopathy models

As reported in mouse models of desmin-related cardiomyopathy (Zheng et al., 2011), we found accumulation of autophagic vacuoles in our *ct122aGt* model. Indeed, at early stages of muscle and cardiac development, we noted the presence of mitochondrial material triggered for degradation (mitophagy). Large autophagic vesicles were seen in the context of degenerating cells as well. However, we did not observe autophagosomes in the vicinity of aggregates or trapping them in our TEM analysis. These observations are consistent with the hypothesis that desmin aggregates clearance and degradation is not mediated by the autophagosome, as shown in some cell models (Wong et al., 2008). However, previous study on a mouse model carrying the αB-crystallin mutation ($CRYAB^{R120G}$), which leads to desmin aggregation in myocardial cells (Wang et al., 2001b) showed that $CRYAB^{R120G}$ mice displayed decreased autophagy fluxes (Pattison and Robbins, 2011). By enhancing autophagy in $CRYAB^{R120G}$ mice, the authors could show an improvement of mice phenotype and cardiac function (Bhuiyan et al., 2013). Therefore, the effect of desmin aggregation on autophagy seems to be context dependent. While this difference can be explained by the presence of pre-amyloid oligomers (PAO) in the context of CRYAB mutation (as reviewed in McLendon and Robbins, 2011) and by the higher correlation of the disease manifestations with PAO than with the aggregates content (Sanbe et al., 2005), it is still unclear whether autophagy is a direct consequence of desmin aggregates or a secondary reaction to clear-out damaged organelles.

(see Figure on the previous page)

Figure 27: Multiple protein quality control pathways are candidates for the clearing of damaged organelles and aggregates in presence of mutated desmin.

(A) Different quality control pathways are potentially activated in the presence of mutated desmin. For the clearance of damaged organelles, macro-autophagy seems to be a mean of choice. Mechanisms of clearance of desmin aggregates are more debated and could include selective macro-autophagy, chaperone mediated autophagy and clearance by the proteasome. (B) Alignments of the desmin, αB-cristallin and vimentin protein sequences with the KFERQ peptide show a potential implication of chaperone mediated autophagy in the clearance of desmin aggregates.

To better understand the role of autophagy in the *ct122aGt* line, we induced autophagy using the mTOR inhibitor S1555 or AZ. These treatments did not ameliorate the desminopathy phenotype. On the contrary, control embryos treated with this drug presented disorganized and degenerating muscle fibers comparable to what was observed in our mutants. Our preliminary hypothesis would be that an excessive autophagy could perturb muscle integrity. Excessive autophagy causes Danon disease centronuclear myopathy, linked with LAMP-2 deficiency as well as X-linked myopathy with excessive autophagy linked with VMA21 (Tanaka et al., 2000; Ramachandran et al., 2009). In these diseases, reduced lysosomal degradation and the accumulation of autophagic vesicles result in progressive muscle weakness and atrophy. Nevertheless, a more extensive investigation of the impact of autophagy drug enhancers, using several concentrations and treatment time points, could clarify the involvement of autophagy in our model. As we study embryonic stages, the autophagy process might be extremely quick to clear efficiently cellular debris and thereby provide material for the recycling machinery, during this period of extensive growth and remodeling. Finally a potential alternative for autophagy drug enhancers is the use of genetic over-expression of genes that could increase autophagy flux such as Atg7 (Bhuiyan et al., 2013).

Molecularly, we did not observe any significant upregulation of p62 (*sqstm1*), *park2* and *bnip3* in 48hpf *ct122aGt* embryos and a later downregulation of p62 at 96hpf, whereas TEM analysis revealed the presence of mitophagy vesicles at 52hpf. The maintenance of mitochondria shape, size, function and network is critical for the cell metabolism and function in particular in muscle cells (Russell et al., 2014)). Mitochondria quality control mechanism is controlled by autophagy and more specifically by the mitophagy (Zhu et al., 2013a). Mitophagy is a crucial and well controlled pathway, depending on the balance between mitochondria fusion and fission. It is active at a basal level in normal conditions and was shown to be increased in development and under stress conditions (Russell et al., 2014). In the context of desminopathy, the precise targeting of autophagy against mitochondria may happen as a response to their malfunction/permeability and dilatation, as was described in the context of oxidative stress (Rubio et al., 2012).

Moreover, TEM analysis revealed large autophagosomes in the cells showing signs of degeneration. If not linked to p62-dependant activation, this high level of autophagy could be associated with *tp53*. p53 can be either a positive or a negative regulator of autophagy depending on its cellular localization. During basal conditions, p53 is localized in the cytoplasm, where it inhibits autophagy (Tasdemir et al., 2008). During cellular stress, p53 is relocated to the nucleus and promotes the expression of target genes to induce autophagy (Maiuri et al., 2010). Nevertheless, autophagy was found activated in p53 KO mice (Tasdemir et al., 2008), showing a potential link between low *tp53* levels and the induction of autophagy in *ct122aGt*.

The next critical step of our study would be to confirm and follow the autophagy flux in our *ct122aGt* model, using the recently developed *Tg(lc3:egfp)* zebrafish line that labels autophagic vacuoles (He, et

al.,2009) and using primary antibodies directed against LC3 (Dowling, et al.,2010). It would be important to verify the localisation of LC3 and desmin aggregates or LC3 and mitochondria.

b) Role of the proteasome

Study in DesD7 mice showed impairment of the ubiquitin-proteasome system (UPS) (Liu et al., 2006a). An increase in the level of ubiquitinated proteins in both the soluble fraction and the total protein extract of DesD7 mice was observed, suggesting impairment in their degradation by the UPS. This was further confirmed by the use of a transgenic line coding for a marked surrogate substrate of the UPS (dgn-GFP) as reporter of the proteasome activity and was associated to a defect in the entry into the UPS machinery. The 19S complex was finally implicated after the observation of down-regulation of some of its key components such as Rpt3 and Rpt5. This impairment was shown to be cell-autonomous and directly linked with the presence of mutated desmin (Liu et al., 2006b). Independence of cardiac malformation or contraction defect and of the lack of functional desmin was also verified (Liu et al., 2006a). These data and the down-regulation of p62 in *ct122aGt* at 96hpf favor the hypothesis that the proteasome function can be impaired in our zebrafish desminopathy model as well. An important next step for our project is to go towards mechanistic aspects of UPS function in our model. For example, it would be interesting to verify this hypothesis by assessing the global level of total ubiquitinated proteins in the *ct122aGt* embryos, the efficiency of the proteasome (using the dgn-GFP marker) and the expression levels of *rpt3* and *rpt5*.

c) Role of selective autophagy

Selective autophagy, including CASA, was shown to ensure the quality control of cellular components, such as the damaged proteins, the damaged organelles, some pathogens (bacterias (e.g. *Mycobacterium tuberculosis*) or viruses (e.g. mouse hepatitis coronavirus) etc. (Colombo et al., 2005)), and aggregate-prone proteins (such as aggregates of mutant huntingtin, mutant tau, or co-expressing synphilin-1 and alpha-synuclein (Wong et al., 2008)). Specific autophagy of protein aggregates was shown to occur in the context of several proteinopathies and is referred to as aggrephagy (Yamamoto et al., 2011, Hyttinen et al., 2014). After being ubiquitinated, they are recruited into autophagosomes by adaptor proteins including NBR1 and SQSTM1/p62 (Lippai et al., 2014). These proteins are equipped with both an ubiquitin associated domain, with the capability to recognize and attach directly to polyubiquitin chains on the surface of aggregates, and an LC3-interacting region able to directly bind autophagosome membrane proteins (Lippai et al., 2014). The down-regulation of p62 at 96hpf in *ct122aGt* embryos and the fact that the aggregates where not found recruited in the autophagy vesicles did not favor this mechanism. Nevertheless, it can be verified in our model by checking the ubiquitination of aggregates and the phosphorylation status of NBR1 (Nicot et al., 2014).

d) Chaperone-mediated autophagy (CMA)

At this step of our investigation and based on previous study on desmin related models, we cannot exclude that desmin aggregates could activate an ubiquitination-independent selective autophagy pathway, such as chaperone mediated autophagy (CMA). CMA selects specifically damaged or mis-

folded proteins through the recognition of a small peptide sequence (KFERQ) and triggers them to the lysosomes (Cuervo and Wong, 2014). KFERQ peptide signal was not found at high identity in desmin sequence but was found on vimentin sequence (personnal observation). As vimentin could heteropolymerize with desmin during development (Schultheiss et al., 1991), the presence of KFERQ signal on vimentin could trigger desmin for CMA degradation. This hypothesis could be verified first in cells expressing both desmin and vimentin (BHK21) and further confirmed in desminopathy models. The KFERQ motif being based on the charge of the recognition peptide sequence, it is also possible to create a motif out of an incomplete four-amino acid motif through post-translational modifications like phosphorylation or acetylation (Cuervo and Wong, 2014). This was found to be the case for huntingtin clearing (Thompson et al., 2009). CMA could be an efficient way to clear aggregating mutant proteins, whilst autophagy takes in charge damaged organelles. Globally, the implication of different type of autophagy and their potential crosstalk should be further investigated in the context of desmin aggregation and represents a nice future prospect for our zebrafish model.

4) Additional strategies to ameliorate the desminopathy phenotype

a) Doxycycline (Doxy) and chemical chaperones

During my PhD, I showed that Doxycycline (Doxy) decreases the size of aggregates and the overall aggregates number, which leads in an amelioration of the skeletal muscle phenotype of the *ct122aGt* embryos. Doxy is part of the tetracycline family and is used principally for its antibiotic properties. Tetracyclines were showed to have other properties, improving pathological events including amyloid deposit formation, inflammation, oxidative stress, apoptosis and uncoupling of metal homeostasis (Stoilova et al., 2013). The anti-amyloidogenic properties of Doxy were first shown *in vitro* (Forloni et la., 2001). Doxy treatment was then shown to lower the aggregate content in many proteinopathies (like oculopharyngeal muscular dystrophy (Davies et al., 2005)) and can partially rescue the desmin-related cardiomyopathy phenotype in the αB-crystallin mouse model (Wang et al., 2001, Zheng et al., 2010). The function of Doxy to reduce aggregate formation remains unclear, but it has been proposed that Doxy acts as a chemical chaperone or by intervening at other levels for the maintenance of protein quality control (Villarreal et al., 2010) without activating autophagy (Zheng et al., 2010).

The importance of chaperoning desmin in the context of its mutation and aggregation was shown in desmin-related cardiomyopathy mouse-models, breeding DesD7 with CRYAB^{R120G} mice. In this context, increased aberrant desmin aggregates were observed and the mice displayed a stronger cardiac hypertrophic response (Wang et al., 2003). To verify this idea, it is possible to knock-down the CRYAB gene in zebrafish. Zebrafish has two orthologs of CRYAB, namely *cryaba* and *cryabb* but *cryabb* only was shown to be expressed in the heart and in skeletal musculature (Smith et al., 2006). Recently, treatment of plectin-deficient myotubes, as well as plectin-deficient mice presenting myofibrillar myopathy, with a chemical chaperone 4-phenylbutyrate resulted in reduction of desmin aggregation and remarkable amelioration of the pathological phenotypes (Winter et al., 2014). Similarly, the use of geranylgeranylacetone, a potent HSP inducer, in CRYAB mutant mice reduced

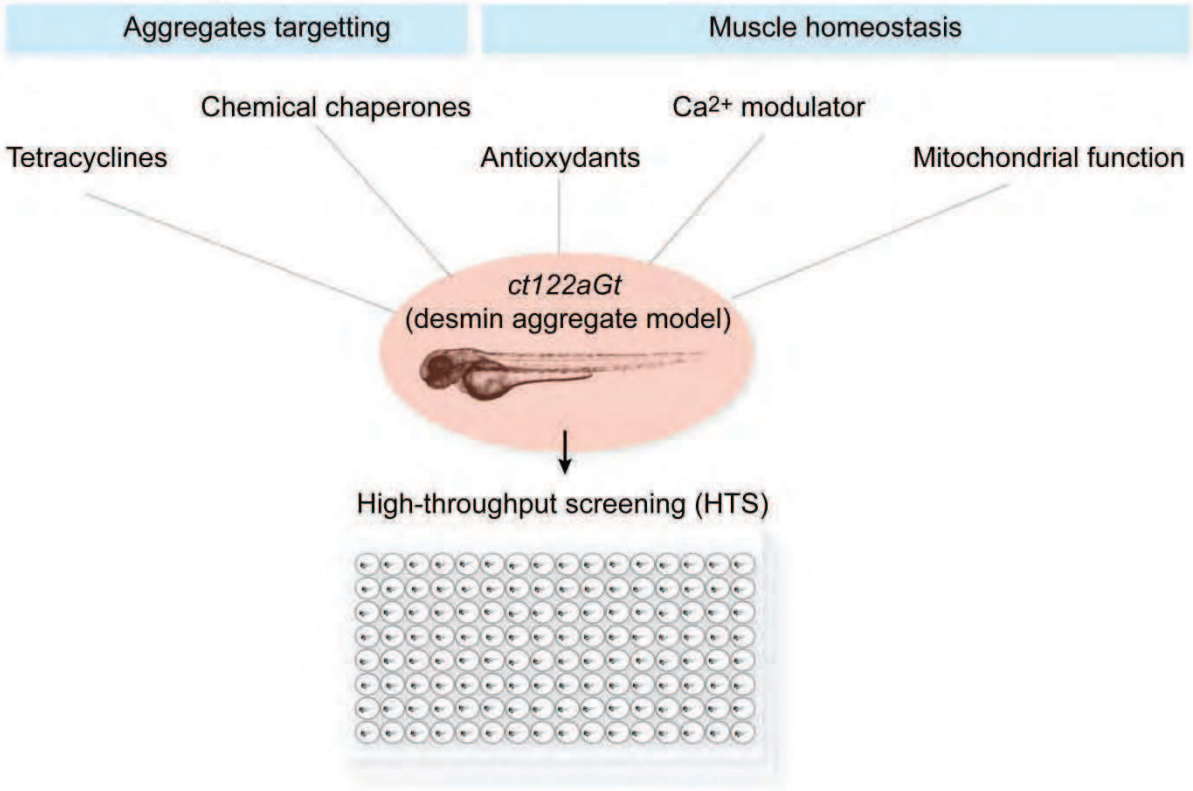

Figure 28: Potential treatments of desminopathies

In complement of testing treatments already proposed in the literature to ameliorate desminopathy conditions, either by targeting the aggregates or ameliorating muscle homeostasis, we propose to perform a high-throughput drug screen i our ct122aGt embryos for the identification of new compounds.

amyloid oligomer levels and aggregates (Sanbe et al., 2009). These drugs could be tested in our model, for example through their capacity to rescue *ct122aGt*, *cryabb* KD phenotypes.

b) Other potential drugs

While the link between a decrease of the aggregates size upon Doxy treatment and an amelioration of the desminopathy phenotype in our zebrafish model fit the result showing that the presence of aggregates in *ct122aGt* exacerbates the skeletal muscle phenotype observed in *desma*$^{sa5-/-}$, other properties of Doxy could also be involved in the amelioration of the phenotype. In particular, its role in reducing oxidative stress and apoptosis seem particularly important in the context of desminopathy.
Antioxidants were shown to have beneficial effects on various muscular disorders (Arbogast et al., 2009; Dowling et al., 2012) and were tested on desminopathy. An example is N-acetyl-L-cysteine (NAC), used primarily as a mucolytic agent, which has been described previously as a promising antioxidant in myopathies linked to selenoprotein N or Ryanodin Receptor (RYR) associated muscle disorders (Arbogast et al., 2009). NAC pre-treatment in DesD399Y expressing myocytes prevented aggregation upon stress induction (Segard et al., 2013).

Another drug proposed in the context of desminopathy is the anti-anginal nicorandil. This drug is known to be an opener of the ATP-sensitive potassium channel and a nitric oxide donor and was shown to protect the heart against ischemia (IONA Study Group, 2005). Upon nicorandil treatment, CRYAB^{R120G} mice showed normalized electrocardiogram parameters, improved ventricular conduction and a rescue of connexin 43 increase. This resulted in a prevention of ventricular tachyarrhythmia in this mouse model of desmin-related cardiomyopathy (Matsushita et al., 2014). Nicorandil would be an interesting drug to test in our zebrafish model, in particular testing its ability to rescue the observed myocardial Ca^{2+} transient defects using live Ca^{2+} imaging.

5) Desminopathies *vs.* other proteinopathies

Proteinopathies form a large group of diseases with well-recognized features, mainly hallmarked by protein aggregation. The spectrum of proteinopathies includes neurodegenerative diseases like Parkinson's disease (PD), Alzheimer Disease (AD), Huntington disease (HD), ALS and various forms of dementia. Additionally, pathological protein aggregation has been established in a broad spectrum of muscle diseases comprising of congenital myopathies, the group of inclusion body myositis, distal myopathies and certain LGMD. They include myofibrillar myopathies and, in particular, desminopathy. A crucial question in the proteinopathy field consists of the role of aggregates in the pathology and in particular how they become toxic and how they contribute in the pathophysiology of the disease. Finally, whether the aggresome functions as a quiescent storage of pathological misfolded protein intermediates, sometimes referred to as PAO, thereby protecting cells from damages and consisting more of a defense mechanism, is another key question in the field (Menzies et al., 2006).

Different parameters have to be taken into consideration while trying to answer these questions. First, the presence of transient toxic forms of the mutated protein is not comparable in all proteinopathies. For example, in the context of desminopathies, the presence of PAO was demonstrated in the context of CRYAB mutation (Sanbe et al., 2004), but was never observed in the context of desmin mutation, neither by immunofluorescence using amyloid-structure specific antibodies (Kayed et al., 2003) nor on TEM images from patients or model animals. The severity of phenotypes in αB-cristallinopathy is not dependent of level of aggregates but correlates directly with the PAO content (Sanbe et al., 2005). On the contrary, we showed that the phenotype in zebrafish containing mutant desmin correlates with the presence of aggregates (Manuscript 2). These two diseases, although both characterized by desmin positive protein aggregates in cardiac muscle cells, present different pathophysiological mechanisms and consequently different response mechanisms (Mc Lendon and Robbins 2011). PAO were found in most proteinopathies including AD, PD, HD, prion diseases etc. (Kayed et al., 2003). Moreover, some other precursor forms can be toxic including soluble oligomeric forms of the mutated protein, as shown for example in the context of HD (Leitman et al., 2013). In the case where PAO or other oligomers are causing the disease, aggregates present quiescent forms of the mutated protein and therefore have a protective role in the cell until their degradation.

Furthermore properties of the aggregates or amyloid formed are not the same. In particular, the quality control mechanisms targeting them are different. Some aggregates, including mutant huntingtin, mutant tau, or synphilin-1, and alpha-synuclein, were shown to be amenable to clearance by autophagy, while those induced by AIMP2 (p38) or mutant desmin seemed to be resistant to autophagic clearance (Wong et al., 2008). Interestingly, changing the composition of aggregates by inclusion of autophagy clearance prone proteins enabled their degradation. Autophagy is considered protective in late-onset neurodegenerative disorders such as Huntington disease and other polyglutamine expansion diseases, and it has been suggested that autophagy up-regulation may be a tractable strategy for the treatment of a wide range of disorders (Sarkar et al., 2008).

Finally the cellular context in which the protein aggregates are present is important. For example, the presence of large and condensed structures in a contractile muscular cell environment can lead to direct cellular damages in the context of the aggregates movement. It seems, therefore, difficult to imagine that aggregates could have a protective function in this context.

Taken together, this comparison shows that our model can help our understanding of features that are similar in other proteinopathies and therefore can have an impact, not only for new insight into desminopathy, but in aggregate diseases more generally. Moreover, the presence of desmin aggregates was found in cardiac stress conditions, without any specific mutation. This is the case, for example, in heart failure, which was linked with post-translational modifications leading to desmin accumulation (Agnetti et al., 2014).

C. Going further with the zebrafish model

1) Desmin filament assembly and aggregation kinetics in live and dynamic conditions

We showed that Desmin aggregate formation is the main triggering event leading to muscle cell defects in our models. *In vitro*, Desmin aggregates form extremely quickly, within minutes (Bar et al., 2005; Hnia, et al., 2011). No model established previously permitted to assess the kinetics of desmin aggregation, in particular in a dynamic physiological context. An idea to answer this question would be to generate a zebrafish line expressing desmin tagged with a photoswitchable fluorescent cassette. Alternatively, and only upon *in vitro* verification that the tag is not itself perturbing desmin assembly, tagged human mutated constructs with photoswitchable cassettes could be used to compare the aggregation kinetics with different disease-causing mutations. An example of usable photoconvertible fluorescent protein is Dendra2. The photoconversion would label a subset of proteins and enable us to quantify their accumulation in the sarcomeres. The protein stability changes and aggregates formation in the mutated version in comparison to Dendra2 alone and the normal human desmin could be precisely assessed by fast confocal imaging. Dendra2-tag expression vectors as well as imaging conditions were already prepared and tested in the context of my summer internship in the Vermot lab in 2009.

2) Contribution of *ct122aGt and desma*$^{sa5-/-}$ mutations in smooth muscle phenotypes in vessels and intestines

We showed that *desma* absence or aggregation affects the biomechanical properties of the cardiac muscle and impacts vascular function and development. Considering that *desma* is not detectable in endothelial cells and the absence of VSMC at this stage, our results suggest that the reported vascular phenotypes could result from indirect impact of blood flow alteration. Although poorly diagnosed or infrequent in human desminopathies, subtle vascular abnormalities should be further investigated and could participate in patient heart and muscle dysfunctions. Desmin-null mouse present arterial defects attributed to alerted smooth muscle cell function where desmin is highly expressed (Li et al., 1996). In zebrafish embryo, smooth muscle cells appear at late embryonic stage (Whitesell et al., 2014). We can then study phenotypes in both the VSMC and intestine smooth muscle cells in zebrafish larvae. Preliminary observations suggest that *desma*$^{sa5-/-}$ present less spontaneous intestinal peristaltic contractions than their corresponding controls at 96hpf (data not shown). This study could therefore bring new insights into desminopathy manifestations that are still poorly characterized.

3) Study of adult phenotypes and of the surprising lack of mortality

Phenotypic and clinical signs of desminopathies are mostly observed in adulthood. The observed defects (in particular pleiotropic muscle weaknesses) progressively become worse with time. To characterize the late functions of desmin and to validate further our model, adult homozygous

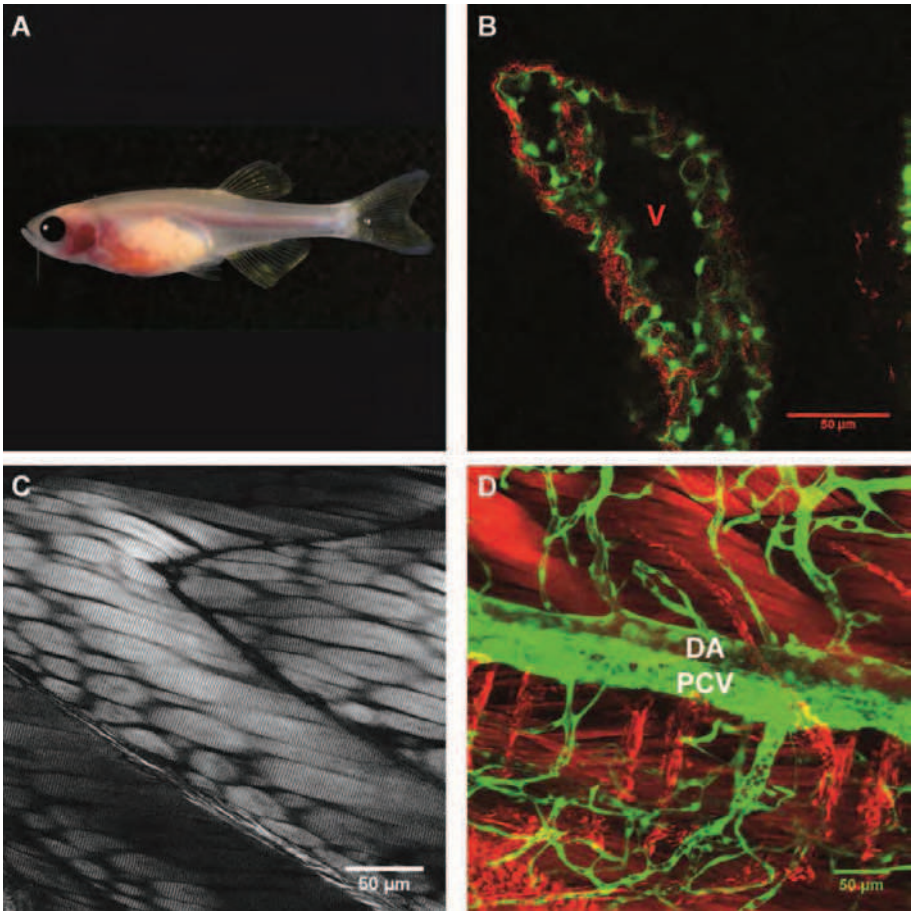

Figure 29: First tests of SHG imaging in 1month old fries

(A) From carolina.com. For fries imaging, the *casper* background is used. *Casper* fish corresponds to double mutants for two genes implicated in pigmentation, *nacre* (corresponding to *mitfa*) and *roy*. (B) Optical section in the ventricle of a 1 month old *Tg(Flk1:egfp)* zebrafish fry. The green signal corresponds to the endocardium labelled with GFP. The red signal corresponds to SHG. (C) Optical section of the tail musculature of a 1 month old fry showing SHG signal. (D) Maximal projection of a z-stack of the tail of a 1 month *Tg(Flk1:egfp)* fry showing SHG signal in red and caudal vasculature in green.

desma$^{sa5-/-}$ and *ct122aGt* mutants can be generated and backcrossed in the *casper* background, which permits analysis of potential late, adult phenotypes. *Casper* fish are suitable for two-photon and SHG imaging, as they do not form pigments and are fully transparent throughout their life (White et al.,2008). To characterize muscular organization in the heart, head and trunk muscles, SHG can be used, allowing direct imaging of muscles, without using labeling. These observations could be performed between 4 days and one month of development in order to follow the progression of the defects in *desma*$^{Sa5-/-}$, *ct122aGt* mutants and control fries. Preliminary SHG studies in 1 month old WT zebrafish fry showed nice signal in both skeletal muscles and heart (Figure 29).

Adult studies would enable to better understand the lack of premature mortality observed in our models. In fact, despite strong skeletal muscle and cardiac phenotypes observed already at early stages, the longevity of the *desma*$^{sa5-/-}$, *ct122aGt* and *ct122aRGt* mutants is comparable to their corresponding control and exceeds three years (data not shown). It would be interesting to study later stages of the establishment of the disease in these fish in order to understand the compensatory mechanisms rescuing the embryonic phenotypes. Hypotheses go towards compensation by another intermediate filaments, (*desmb* would be a candidate, as its expression was shown to increase after 72hpf (Manuscript 2)) or the induction of regeneration pathways. While the regeneration of the myocardium was extensively studied in zebrafish (Gemberling et al., 2013), the skeletal muscle regeneration mechanism is still unclear. Despite the fact that regeneration appears not to occur through dedifferentiation, no clear satellite-cells homologs were identified so far (Siegel et al., 2013).

4) Humanized models

More quantitative studies based on animal models and experimental genetic manipulations are needed to understand and model the variation in phenotype existing in desminopathy patients (Joanne et al., 2013). We showed with *ct122aGt* and *ct122aRGt* fish that the deletion of the tail part of the protein leads to a different aggregate structure. In zebrafish, overexpression of numerous mutated versions of desmin and corresponding phenotype characterization is possible in a quick, automated manner by overexpression of several mutated desmin found in desminopathy patients. This will further our understanding on the genotype-phenotypes correlation. Moreover, on the long run, this project would enable to generate a large number of models of desminopathy aiming to get “personalized” models for each particular mutation.

Upon discussion with the Patrick Vicart team and based on their ability to form aggregates in murine cell models, we selected the most appropriate mutants to be overexpressed in zebrafish (Table 6). This would enable a collaborative exchange of information gathered from both cellular and zebrafish models. The quickest way to generate these humanized models would be by direct mRNAs injection in 1 cell stage WT zebrafish embryos. In case the interaction between human and zebrafish desmin causes a problem, or to have a controlled ratio between WT and mutated alleles to recapitulate patient heterozygous conditions for example, a mix of WT and mutated alleles can alternatively be injected in

Nr	DNA Sequence Variant	DNA Sequence Variant Type	Protein Sequence Variant	Domain	Associated Disease	References
1	c.1109T>C	Substitution	p.Leu370Pro*	2B	DRM	(Dagvadorj, et al.,2003)
2	c.1195G>T	Substitution	p.Asp399Tyr	2B	DRM	(Goudeau, et al.,2006)
3	c.1302C>T	Substitution	p.Arg406Trp	2B	DRM+ **DRCM**	(Park, et al.,2000)
4	c.934G>A	Substitution	p.Asp312Asn	2B	**DRCM**	(Taylor, et al.,2007)
5	c.1353C>G	Substitution	p.Ile451Met	Tail	**DRCM**	(Li, et al.,1999)
6	c.1375G>A	Substitution	p.Val459Ile	Tail	**DRCM**	(Taylor, et al.,2007)

Table 6: Desmin mutations leading to DRM or DRCM that will be used for overexpression in zebrafish embryos through mRNA injection for the generation of humanized models of desminopathy in zebrafish.

the *desma*$^{sa5-/-}$ background. This would further enable us to estimate the limit amount of mutant desmin needed to trigger aggregation.

In case the human desmin mRNA injection is unstable or toxic to the first stages of development, a conditional expression approach (using the GalFF/UAS system (Halpern et al., 2008)) can be used in order to stably express the normal and mutated versions of human desmin alternatively in all muscles cells (using *acta1a* driver line, prepared by our collaborators in the Jocelyn Laporte team) or in the myocardial cell layer (using *cmlc2* promoter) of the zebrafish embryo.

II/ Discussion on vascular diseases models

A. From the verification of the Windkessel effect to the modelling of hypertension and arterial stiffness in zebrafish

1) Limitations of the Windkessel model

Although the Windkessel is a simple and convenient model for pulse propagation and arterial capacitance, it does not take into account modern approaches that describe arterial pressure and flow in terms of wave propagation and reflection (Nichols et al., 2005), although recent attempts have been made to integrate wave propagation in this model (Tyberg et al., 2009). Nevertheless, wave reflections are an inevitable phenomenon of any conduction system with geometric discontinuity, as for example with the decreasing diameter of the aorta, and are of particular importance in the study of arterial stiffness influence in the establishment of hypertension-related clinical signs. As pressure waves propagate through the artery, a reflected wave of energy is generated. In the case of an elastic artery, the reflected wave reaches the heart during late systole to diastole. However, in the case of stiffened arteries, the reduction in artery diameter occurs closer to the heart, changing the propagation of the reflected wave. This wave therefore arrives at the heart closer to systole, applying a greater load on the heart and favoring hypertrophy (Westerhof and Westerhof, 2013).

Moreover, this system does not take into account variations naturally present in the vascular system, including changes in blood flow distribution, changes in aortic compliance, effect of local vessel or flow perturbations, presence of vessels affected by stiffening or obstruction other than the aorta etc. (Westerhof et al., 2009).

The Windkessel model is thus a simplified approach, enabling better insight into arterial function by reflecting a certain number of meaningful parameters. It offers an accurate estimation of hemodynamic parameters in computational approaches for the estimation of the arterial flow propagation. Nevertheless, it does not reflect the overall complexity of the blood dynamics in the aorta and supplementary parameters, including in particular, flow and pressure wave reflections, have to be taken into account for a precise model of related pathological conditions.

2) Going further in the understanding of hypertension using zebrafish

AS and AC are mechanisms principally related to the function of VSMC, which are not present in zebrafish embryos at the early stages we are studying. It would still be possible to generate models of these pathologies in fries or adults using the *casper* line presented above. Figure 29 shows endothelial cells in the vascular network in one-month-old fish. The DA still present the main artery in the fish trunk, similar to the human aorta. KO (and conditional KO) of genes implicated in AS and AC can therefore be proposed for a better understanding of related pathological mechanisms in zebrafish.

They include elastin, extracellular matrix proteins and a variety of proteins involved in bone and mineral metabolism implicated in the conversion of VSMC and pericytes into “osteoblast-like” cells (London, 2013). This phenomenon could also be studied over time in natural aging conditions of the fish.

In zebrafish embryos, changing the capacitance properties of the endothelial cells forming the DA could be achieved through changes in the extracellular matrix content, for example altering the composition of collagen or lamin. As such modifications (either by depletion or overexpression of extracellular matrix genes) could perturb other tissues in the embryo, conditional approaches including the use of photo-MOs for specific activation or deactivation of gene expression in the DA should be considered. Another way of studying the establishment of hypertension in zebrafish embryos is *via* the study of arteriosclerosis-related genes. Indeed, arteriosclerosis was shown to be linked with mechanotransduction of perturbed blood flow. This is one of the major focus in the Vermot group and several projects are now trying to answer this point in particular through the identification of mechanosensors (pkd2, trpv4 etc.) and the illumination of their corresponding mechanotransduction pathways (Ca^{2+} signaling, klf2a pathway etc.). Future perspectives of this project include the study of the endothelial cell response in consequence to the pressure-induced deformation of the DA. For that, membrane markers (like VE-cadherins) and cytoskeletal markers (actin) could be extensively imaged and their deformation analysed in response to different hemodynamic conditions and a computational model of the cellular deformations could be implemented.

B. GCN2 implication in venous angiogenesis and in the establishment of PVOD

In this study, we used the zebrafish model to investigate defects in vascular development in response to KD of *eif2ak4* (GCN2), a gene responsible for hereditary forms of PVOD, which is a rare form of pulmonary hypertension. We found that embryos knocked down for GCN2 displayed abnormalities of venous angiogenesis, similar to the effect of KD of ATF4 (by coinjection of MO against its two zebrafish orthologs *atf4b1* and *atf4b2)*, a known downstream effector of GCN2 in mammals. Our results are consistent with reports showing that PVOD-associated mutations induce lung vascular remodeling in humans. We provide insight into the underlying mechanism, showing defects in endothelial cells migration and cell proliferation in the caudal plexus. The venous defects that we observed in zebrafish embryos are associated with abnormal venous identity and angiogenesis markers. These data suggest that GCN2 and ATF4 are acting in the same genetic pathway in the context of GCN2-driven vascular phenotypes.

1) Through a better understanding of the venous specificity of phenotypes

We focused on the vascular defects in embryos where ATF4 and GCN2 function have been knocked down, found that endothelial cell number and morphogenesis of the vascular plexus is affected in the KD embryos and identified common molecular targets. Together, these experiments indicate the importance of the vascular involvement of the GCN2-ATF4 pathway. Our work suggests that zebrafish can be used to model PVOD and will help to address the cellular function of both GCN2 and ATF4 in the process. Interestingly, these defects are similar to what observed in the *acvrl1* mutants in zebrafish (Roman et al., 2002; Corti et al., 2011), a gene which is also associated with PAH in patients (Eyries et al., 2012), suggesting a conservation of function in fish. Thus, the use of zebrafish might help to address the cellular and molecular basis of PVOD, as the molecular pathway seems to be conserved in vertebrates.

Other genes were implicated in venous angiogenesis and related morphant embryos presented phenotypes with similarities with our observations. For example, *bmpr2a* (Wiley et al., 2011) and *dab2* (Kim et al., 2012) morphants showed defective sprouting in the caudal plexus. Dab2, a venous-specific cargo adaptor protein for clathrin, was identified as a mediator the pro-angiogenic function of BMP2 signaling. Dab2 participates in internalization of BMP receptors for recycling and induces phosphorylation of SMAD-1, 5, and 8 leading to the activation of the SMAD pathway. Thus, Dab2 provides a molecular basis for the venous dependent pro-angiogenic function of BMP2 signaling. Such interactions between the GCN2 pathway and proteins with a venous specific pattern of expression should then be considered.

To study this, a future prospective step of this project is to assess the expression pattern of angiogenesis markers in *eif2ak4* MO fish by *in situ* hybridization. A differential expression between arteries and veins could explain surprising results found assessing the global mRNA level by qPCR. It

may moreover suggest molecular interactions with the GCN2 pathway in a venous-dependent manner. The qPCR results obtained are still preliminary and this molecular approach needs to be continued and confirmed. In parallel with expression patterns, we should be able to better understand the influence of GCN2 and ATF4 depletion on these markers to understand the venous specificity of phenotypes.

2) Creation of a GCN2 KO zebrafish model

An important prospective step of this project is the confirmation of the obtained results in a GCN2 mutant. Indeed, the use of morpholino gene targeting is currently debated in the zebrafish community due to potential off-target and toxicity-linked phenotypes (see paragraph IIIB). The verification of phenotypes in a stable mutant line becomes a necessary step to KD studies. Even if the phenotypes observed in our PVOD models do not resemble a MO toxicity phenotype and successful rescues were obtained, an *eif2ak4* mutant model should be created. Using MO, we optimized the best concentration to be injected in order to guarantee the survival of the fish while being able to detect the phenotype. The KD obtained is thus only partial (34% and 17% respectively for *eif2ak4* MO1 and MO2). Then, despite the fact that human patients present a biallelic disruption of the EIF2AK4 gene, it is possible that a full KO of *eif2ak4* would be detrimental to the zebrafish embryo. If this is the case, the study of the heterozygous fish may already recapitulate the observed phenotypes, according to the low KD necessary to trigger it.

Several nuclease-based technologies were recently developed and applied to zebrafish in order to generate a KO of a specifically targeted gene. They include ZFN, TALEN and CRISPR/Cas9. The principle of these three gene targeting methods is comparable and consists of the engineering of specific DNA-recognition motifs linked to nuclease domains of a restriction enzyme. The so-formed complex binds a specific target site in the gene of interest and induces a double strand break in the selected DNA region. Then the endogenous cellular DNA repair mechanisms act on the break. Mostly, the break will be repaired by the error prone non-homologous end joining (NHEJ) pathway, which triggers mutations including insertions and deletions. Differences between these different technologies reside in the nature of the DNA recognition motif. While ZFN and TALEN are based on a protein-DNA interaction for recognition of the target site, the CRISPR/Cas9 system used a guide RNA and was then showed to be quicker and more efficient in many systems (Cong et al., 2013, Mali et al., 2013), but was also shown to lead to a higher risk of inducing off-targets (Cho et al., 2014). Compared to ZFN, TALEN was shown to have a higher efficiency and an easier method and are now preferentially used except when sterical constraints (for example for viral-vector based delivery) exist, the ZFN complex being smaller (Gaj et al., 2013).

During the first year of my PhD studies, I tried to generate a ZFN-mediated KO of two genes in zebrafish: *desma* and *klf2a*, a transcription factor implicated in mechanotransduction and highly studied in the Vermot group. After obtaining a positive somatic mutation rate for only one ZFN couple

(for *klf2a*) out of 6 tested in total, we never managed to identify mutant founders while genotyping the injected fish after they reached adulthood. We then tested TALEN technology (in collaboration with the group of Jean-Paul Concordet, Museum d'histoire naturelle, Paris) on *klf2a* and *klf2b* and successfully obtained mutants for both of these genes. More recently, we tried the CRIPR/Cas9 system as well in order to create *trpv4* mutants (in collaboration with the group of Bernardo Reina, IGBMC). Nevertheless, no mutant has been identified so far in genotyping fish injected with two out of three of the guides tested. While I was not responsible for these mutagenesis projects anymore, having focused on my actual PhD project, I continued participating in the design of the experiments, the design and optimization of a genotyping strategy and pipeline and in the training of new users. Strong with this experience, we then would choose the TALEN technology to generate a specific mutant of *eif2ak4* in zebrafish.

During the time of generation of this mutant line (approximately a year from now until it is usable, independently of the method used), some other tools can be created including transgenic lines for a more efficient characterization of the *eif2ak4* KO phenotype. In order to follow the expression dynamics of *eif2ak4* expression in live embryo, a transgenic line containing the complete promoter of *eif2ak4* expressing a fluorescent reporter (for example the nuclear marker h2b-cerulean to permit simultaneous imaging with other reporter of different color) could be generated. This would help to characterize the expression pattern of *eif2ak4 in vivo* through time and test the specificity of arterial *vs.* venous expression, which is unclear on *in situ* hybridization results. The h2b tag will enable us to precisely quantify the levels of expression of *eif2ak4* using quantitative scripts we specifically develop in the lab to automatically and precisely measure relative levels of fluorescent reporter expression.

In association with the arterial specific lines *(flt1-enh:redFP)* we possess, we could also generate a venous specific line by using the promoter of mrc1 *(mrc1:redFP)*, a gene which is specifically expressed in the venous network. These lines will be critical to identify the arterial and venous network during angiogenesis and in the adult vascular network. This approach will allow us to follow cell behavior in real time and to follow the onset of *eif2ak4* expression in endothelial cells.

3) Comparison with GCN2 KO mice and cellular systems

The zebrafish model of PVOD that we proposed is part of a large collaborative project set up with the groups of Florent Soubrier (La Pitié Salpetrière, Paris), Marc Humbert (University Paris-Sud/INSERM) and Pierre Fafournoux (INRA, Clermont-Ferrand). The ultimate goal is to compare and contrast data obtained with GCN2 depletion in different models (cell, zebrafish and mouse). Gcn2-/- mice are viable and have apparent normal longevity, although they display several metabolic abnormalities and different responses to TAC (Anthony et al., 2004). Hemodynamic measurements in basal conditions and after nutritional stress will be performed by our collaborators and vascular lung remodeling will be studied. In addition to $GCN2^{-/-}$ mice, the generation of lineage-specific KO mice for inactivating GCN2

in either endothelial or vascular smooth muscle cells, using specific promoter is planned. Mice models could be further challenged with different nutritional and immunological stresses.

In vitro experiments will be achieved for identifying the changes in gene expression induced by Gcn2 inactivation in lung vascular cells. Gene expression profile will be analysed by mRNA sequencing and by proteomic analysis in both basal and stress conditions. These data should allow us to define more precisely the gene networks that are involved in the pathological process.

Taken together, these different approaches should provide new physiopathological data on vascular remodeling, in particular in veins severely involved in the human PVOD. With vascular fibrous intimal proliferation being also observed in other pathologies like atherosclerosis, this project can also have significance for other vascular diseases. The molecular alterations identified at the origin of the vascular remodeling would enable the identification of targets for drugs inhibiting the remodeling and allow the development of biomarkers of the disease, which could constitute general markers of vascular remodeling. Following the discovery that inactivating mutations of the GCN2 gene are responsible for PVOD, the elucidation of the mechanisms leading to the disease would finally enable a more general model of pulmonary hypertension to be elaborated and the genetic architecture of this disease to be clarified.

III/ General discussion

A. Limitation of the zebrafish model in the context of the modelled diseases

While zebrafish has many advantages to model human genetic diseases, some limitations remain. To begin with, the absence of lungs in zebrafish makes the comparison between our model and PVOD patients only partial. Developmentally speaking, the swimbladder is considered as the equivalent of the lung in fish (Winata et al., 2009) but the homology between these structures remain poor and do not allow direct comparison. Therefore, in spite of the highly-conserved nature of angiogenesis mechanisms, the global context of the establishment of the disease is unclear. This is one reason why the collaboration with labs working with mice models, and in particular studying the GCN2-/- mice, is crucial for an overall understanding of the implication of GCN2 mutation in PVOD.

The lack of specific antibodies in zebrafish was often limiting too. In particular, we are still trying to validate the double KD of *atf4b1* and *atf4b2*. While a proof of almost full KD of the splice MO against *atf4b2* was obtained using reverse transcription and agarose gel (data not shown), similarly to the validation of *eif2ak4* KD, the *atf4b1* MO is a translation start site targeting MO and requires testing at the protein level. Our collaborators are still testing new antibodies against ATF4 in zebrafish in order to obtain this crucial validation step before submission of Manuscript 4.

Using the zebrafish embryo to model desminopathy, we were not able to assess smooth muscle phenotypes due to the absence of this tissue at the early stages considered. Visceral smooth muscle cells mRNA begins to be expressed at around 50 hpf and VSMC begin to appear in the ventral part of the DA around 3,5 dpf (Whitesell et al., 2014). As smooth muscle phenotypes are an important manifestation of desminopathy in patients, this aspect is still crucially lacking in our models.

While performing the molecular characterization of the desminopathy phenotype in our models, in particular through qPCR and whole mRNA sequencing, we had troubles with the variability existing between *ct122aGt* embryos, both positive and negative for the *desma* signal, at 48 and 72hpf. This is reflected as well by the variability of phenotypes observed in skeletal muscles at 96hpf. As the KI generated is based on a gene-trap approach, it is unlikely that a supplementary insertion had happened and mutated another gene, as it would be tagged by the cassette and therefore should be detectable. In prospective steps, in particular trying to get more mechanistic insights into desminopathy with our model, it will be crucial to multiply the number of samples used in experiments, trying to get enough statistical power to get significant results.

Taken together, these drawbacks of the zebrafish model underline the necessity to reinforce the study of diseases in zebrafish performing comparative studies in other models.

B. Current mistrust of MO effects

MOs (Summerton et al., 1999) are largely used for gene-targeting strategies both in research and as potential therapeutics (Arora et al., 2000, Warren et al., 2012, Douglas et al., 2013). As discussed previously, the use of MOs is debated in the zebrafish community. Since their first usage MOs have been found to generate some off-target effects leading to well-described characteristic phenotypes including cell death, shortened tail, small head and cardiac oedema (Ekker et al., 2001). Cell death was later associated to an ectopic up-regulation of the *tp53* pathway, leading to apoptosis. MO co-injection with *tp53*-targeting MO is used to reduce that effect (Robu et al., 2007). Although artificial, this approach was considered to ameliorate MO toxicity and has been extensively used (Bill et al., 2009). Other protocols to assess MO toxicity and validate specific KD include the use of two MOs targeting two non-overlapping sequences of the same gene, showing the synergy of co-injection of these two MOs and the injection of mismatch MO (Bill et al., 2009). Despite these precautions, some studies showed the limit of the MO technology in term of toxicity. For example, a first study using MO-based approach suggested zebrafish *prox1b* expression marks lymphatic endothelial cells and that KD of *prox1b* via MO completely abolishes lymphangiogenesis (Del Giacco et al., 2010). Further studies using a combination of proper MO injection and comparison with mutants, later refuted this finding by showing that zebrafish *prox1b* mutants develop a normal lymphatic vasculature and that *prox1b* does not specifically mark lymphatic endothelial cells (Tao et al., 2011). Another example consists in the first published KD of *desma* in zebrafish embryos, showing strong phenotypes including huge cardiac oedema, tail deformity and dramatic effect on heart rate (Vogel et al., 2009). These observations are contradictory with our observations where we both used MO and mutant approaches to address desmin loss of function. It is likely that the phenotypes generated by MO KD in that case are due to some MO toxicity. Anecdotally, this toxicity can lead to good surprises as with, for example, the discovery of the role of pro-apoptotic genes in hindbrain boundary development following unspecific activation of *tp53* upon toxicity of *wnt1* MO (Gerety et al., 2010). In this context, the use of mutants to validate MO phenotypes is more and more appreciated and the future of studies solely relying on MO in zebrafish is nowadays questioned.

C. Use of KIs in zebrafish

For years, targeted engineering of genomic loci was restricted to model organisms whose embryonic stem cells could be manipulated using homologous recombination, in particular mice (Thomas et al., 1987). More recently, the discovery of sequence-specific endonuclease, ZFN, TALEN and CRISPR/Cas9 system, opens new avenues to manipulate genomes in most of the model organisms that was lacking this technology such as *C.elegans*, *D.melanogaster*, *A.thaliana*, *R.Norvegicus* and *D.rerio* (Auer and Del Bene., 2014). In zebrafish, the three systems were employed successfully to generate loss-of-function alleles by generating insertions or deletions in open reading frames or whole chromosomal regions (Doyon et al., 2011, Huang et al., 2011, Sander et al., 2011,Hwang et al., 2013). Moreover the possibility of targeting multiple loci at the same time was shown using CRISPR/Cas9 (Jao et al., 2013). This possibility of generating loss-of-function alleles in zebrafish in a specific and efficient manner was already an important step for the zebrafish community, until then limited through the use of potentially toxic and short-life MOs and the laborious identification of mutants from mutagenesis screens.

In addition, TALEN and CRISPR/Cas9 were recently used to generate KI consisting of the insertion of site-specific mutations, restriction sites, loxP sites, protein tags and even whole donor plasmid vectors (Auer and Del Bene, 2014). For that, different strategies were used, with different efficiency. First, small insertions (<40bp) were obtained using single-stranded DNA oligonucleotides and homology-directed repair after TALEN (Bedell et al., 2012) and CRISPR/Cas9 (Chang et al., 2013) cut. The efficiency of integration was between 0 and 8.3% but integrated sequences were found further modified in the majority of events. This was attributed to an involvement of the error-prone NHEJ pathway (Auer et al., 2014). Further studies demonstrated the possibility of integrating large cassettes by homologous recombination in zebrafish using TALEN and a linear double-stranded (ds) DNA donor (Zu et al., 2013). Finally, dsDNA from an integrator donor vector was inserted specifically into the fish genome using the NHEJ pathway (Auer et al., 2014b). A small “bait” sequence, mimicking the endogenous TALEN or CRIPR/Cas9 target, was integrated upstream of the cassette to be inserted into the donor vector and is cleaved concomitantly. Homologous independent repair is then achieved naturally between the open ends of dsDNA in the cell, leading to an integration of the donor sequence. The frequency of efficiency was found to reach up to 31% but integration was found in both forward and reverse orientation, the junctions were subjected to the error-prone repair and therefore irregular segments and concatemers of the donor plasmid were occasionally inserted. Taken together, these new techniques offer a broad range of possibilities for targeted modifications of endogenous loci in the zebrafish. This new tool-box opening predicts exiting perspectives for the zebrafish community and may be used largely in the years to come. Further applications of targeted mutagenesis may then enable us to generate largely conditional loss-of-function alleles, reporter lines and docking lines (with site-specific recombination (attB) sites) for site directed transgenesis (Auer et Del Bene, 2014).

D. High throughput screens

An exciting perspective of the desminopathy project is the use of the *c122aGt* line to test drugs limiting the aggregation of desmin using a high-throughput drug screening approach. Zebrafish was already used for screening of new drugs in the context of muscular diseases (Kawahara et al., 2011) and is currently the only animal model suitable for drug screening approaches directed toward cardiac function (Wen et al., 2012; Yozzo et al., 2013). Yet, this approach has so far never been used to identify compounds attenuating aggregation or improving survival with proteinopathy. Importantly, the chances of finding a new drug that limits aggregation in our model of desminopathy and that is viable for use in patients to correct genetic diseases at different stages of its progression are quite high. This hypothesis is based on the proof of concept of the feasibility of using simple chemicals to reduce aggregation in a desminopathy phenotype that we proposed in Manuscript 2 using Doxy. Moreover, the libraries available to the zebrafish communities for automated drug screening are composed of FDA approved compounds which proved reduced toxicity in human. Their use in a therapy against a novel disease is then potentially quicker. Technically, further testing and optimizing of the protocol we established with the IGBMC screening platform will be needed, but we are confident of overcoming these limitations and launch a screen rapidly.

Generally, high-throughput drugs screens in zebrafish are a powerful method for new drug discovery. After optimization of screening and analysis techniques, specific screening platforms dedicated to zebrafish were launched by and for the zebrafish community (http://www.ezrc.kit.edu/59.php) and may be more and more popular using disease models.

Références

Adamo, C.M., Dai, D.F., Percival, J.M., Minami, E., Willis, M.S., Patrucco, E., Froehner, S.C., and Beavo, J.A. (2010). Sildenafil reverses cardiac dysfunction in the mdx mouse model of Duchenne muscular dystrophy. Proceedings of the National Academy of Sciences of the United States of America 107, 19079-19083.

Agbulut, O., Li, Z., Perie, S., Ludosky, M.A., Paulin, D., Cartaud, J., and Butler-Browne, G. (2001). Lack of desmin results in abortive muscle regeneration and modifications in synaptic structure. Cell motility and the cytoskeleton 49, 51-66.

Agnetti, G., Halperin, V.L., Kirk, J.A., Chakir, K., Guo, Y., Lund, L., Nicolini, F., Gherli, T., Guarnieri, C., Caldarera, C.M., et al. (2014). Desmin modifications associate with amyloid-like oligomers deposition in heart failure. Cardiovascular research 102, 24-34.

Agullo-Pascual, E., Cerrone, M., and Delmar, M. (2014). Arrhythmogenic cardiomyopathy and Brugada syndrome: diseases of the connexome. FEBS Lett 588, 1322-1330.

Ahrens, M.B., Orger, M.B., Robson, D.N., Li, J.M., and Keller, P.J. (2013). Whole-brain functional imaging at cellular resolution using light-sheet microscopy. Nature methods 10, 413-420.

Anders, S., and Huber, W. (2010). Differential expression analysis for sequence count data. Genome biology 11, R106.

Anderson, J., Li, Z., and Goubel, F. (2001). Passive stiffness is increased in soleus muscle of desmin knockout mouse. Muscle Nerve 24, 1090-1092.

Anthony, T.G., McDaniel, B.J., Byerley, R.L., McGrath, B.C., Cavener, D.R., McNurlan, M.A., and Wek, R.C. (2004). Preservation of liver protein synthesis during dietary leucine deprivation occurs at the expense of skeletal muscle mass in mice deleted for eIF2 kinase GCN2. The Journal of biological chemistry 279, 36553-36561.

Anton, H., Harlepp, S., Ramspacher, C., Wu, D., Monduc, F., Bhat, S., Liebling, M., Paoletti, C., Charvin, G., Freund, J.B., et al. (2013). Pulse propagation by a capacitive mechanism drives embryonic blood flow. Development 140, 4426-4434.

Arbogast, S., Beuvin, M., Fraysse, B., Zhou, H., Muntoni, F., and Ferreiro, A. (2009). Oxidative stress in SEPN1-related myopathy: from pathophysiology to treatment. Ann Neurol 65, 677-686.

Armstrong, G.A., and Drapeau, P. (2013). Loss and gain of FUS function impair neuromuscular synaptic transmission in a genetic model of ALS. Human molecular genetics 22, 4282-4292.

Arndt, V., Dick, N., Tawo, R., Dreiseidler, M., Wenzel, D., Hesse, M., Furst, D.O., Saftig, P., Saint, R., Fleischmann, B.K., et al. (2010). Chaperone-assisted selective autophagy is essential for muscle maintenance. Current biology : CB 20, 143-148.

Arora, V., Knapp, D.C., Smith, B.L., Statdfield, M.L., Stein, D.A., Reddy, M.T., Weller, D.D., and Iversen, P.L. (2000). c-Myc antisense limits rat liver regeneration and indicates role for c-Myc in regulating cytochrome P-450 3A activity. The Journal of pharmacology and experimental therapeutics 292, 921-928.

Arrenberg, A.B., Stainier, D.Y., Baier, H., and Huisken, J. (2010). Optogenetic control of cardiac function. Science 330, 971-974.

Asimaki, A., Kapoor, S., Plovie, E., Karin Arndt, A., Adams, E., Liu, Z., James, C.A., Judge, D.P., Calkins, H., Churko, J., et al. (2014). Identification of a new modulator of the intercalated disc in a zebrafish model of arrhythmogenic cardiomyopathy. Sci Transl Med 6, 240ra274.

Auer, T.O., and Del Bene, F. (2014). CRISPR/Cas9 and TALEN-mediated knock-in approaches in zebrafish. Methods.

Auer, T.O., Duroure, K., De Cian, A., Concordet, J.P., and Del Bene, F. (2014). Highly efficient CRISPR/Cas9-mediated knock-in in zebrafish by homology-independent DNA repair. Genome research 24, 142-153.

Auman, H.J., Coleman, H., Riley, H.E., Olale, F., Tsai, H.J., and Yelon, D. (2007). Functional modulation of cardiac form through regionally confined cell shape changes. PLoS biology 5, e53.

Austin, E.D., and Loyd, J.E. (2014). The genetics of pulmonary arterial hypertension. Circulation research 115, 189-202.

B'Chir, W., Maurin, A.C., Carraro, V., Averous, J., Jousse, C., Muranishi, Y., Parry, L., Stepien, G., Fafournoux, P., and Bruhat, A. (2013). The eIF2alpha/ATF4 pathway is essential for stress-induced autophagy gene expression. Nucleic acids research 41, 7683-7699.

Bai, Q., Garver, J.A., Hukriede, N.A., and Burton, E.A. (2007). Generation of a transgenic zebrafish model of Tauopathy using a novel promoter element derived from the zebrafish eno2 gene. Nucleic acids research 35, 6501-6516.

Bakkers, J. (2011). Zebrafish as a model to study cardiac development and human cardiac disease. Cardiovascular research 91, 279-288.

Balogh, J., Merisckay, M., Li, Z., Paulin, D., and Arner, A. (2002). Hearts from mice lacking desmin have a myopathy with impaired active force generation and unaltered wall compliance. Cardiovascular research 53, 439-450.

Bar, H., Mucke, N., Kostareva, A., Sjoberg, G., Aebi, U., and Herrmann, H. (2005). Severe muscle disease-causing desmin mutations interfere with in vitro filament assembly at distinct stages. Proceedings of the National Academy of Sciences of the United States of America 102, 15099-15104.

Bar, H., Schopferer, M., Sharma, S., Hochstein, B., Mucke, N., Herrmann, H., and Willenbacher, N. (2010). Mutations in desmin's carboxy-terminal "tail" domain severely modify filament and network mechanics. Journal of molecular biology 397, 1188-1198.

Bassett, D.I., and Currie, P.D. (2003). The zebrafish as a model for muscular dystrophy and congenital myopathy. Human molecular genetics 12 Spec No 2, R265-270.

Bedell, V.M., Wang, Y., Campbell, J.M., Poshusta, T.L., Starker, C.G., Krug, R.G., 2nd, Tan, W., Penheiter, S.G., Ma, A.C., Leung, A.Y., et al. (2012). In vivo genome editing using a high-efficiency TALEN system. Nature 491, 114-118.

Beis, D., Bartman, T., Jin, S.W., Scott, I.C., D'Amico, L.A., Ober, E.A., Verkade, H., Frantsve, J., Field, H.A., Wehman, A., et al. (2005). Genetic and cellular analyses of zebrafish atrioventricular cushion and valve development. Development 132, 4193-4204.

Bendig, G., Grimmler, M., Huttner, I.G., Wessels, G., Dahme, T., Just, S., Trano, N., Katus, H.A., Fishman, M.C., and Rottbauer, W. (2006). Integrin-linked kinase, a novel component of the cardiac mechanical stretch sensor, controls contractility in the zebrafish heart. Genes & development 20, 2361-2372.

Benedetti, S., Hoshiya, H., and Tedesco, F.S. (2013). Repair or replace? Exploiting novel gene and cell therapy strategies for muscular dystrophies. The FEBS journal 280, 4263-4280.

Benjamini Y, H.Y. (1995). Controlling the false discovery rate: a practical and powerful approach

to multiple testing. Journal of the Royal Statistical Society 57, 289-300.

Berardi, E., Annibali, D., Cassano, M., Crippa, S., and Sampaolesi, M. (2014). Molecular and cell-based therapies for muscle degenerations: a road under construction. Frontiers in physiology 5, 119.

Berger, Z., Ravikumar, B., Menzies, F.M., Oroz, L.G., Underwood, B.R., Pangalos, M.N., Schmitt, I., Wullner, U., Evert, B.O., O'Kane, C.J., et al. (2006). Rapamycin alleviates toxicity of different aggregate-prone proteins. Human molecular genetics 15, 433-442.

Best, D.H., Sumner, K.L., Austin, E.D., Chung, W.K., Brown, L.M., Borczuk, A.C., Rosenzweig, E.B., Bayrak-Toydemir, P., Mao, R., Cahill, B.C., et al. (2014). EIF2AK4 mutations in pulmonary capillary hemangiomatosis. Chest 145, 231-236.

Bhuiyan, M.S., Pattison, J.S., Osinska, H., James, J., Gulick, J., McLendon, P.M., Hill, J.A., Sadoshima, J., and Robbins, J. (2013). Enhanced autophagy ameliorates cardiac proteinopathy. J Clin Invest 123, 5284-5297.

Biesecker, L.G., and Green, R.C. (2014). Diagnostic clinical genome and exome sequencing. The New England journal of medicine 370, 2418-2425.

Bill, B.R., Petzold, A.M., Clark, K.J., Schimmenti, L.A., and Ekker, S.C. (2009). A primer for morpholino use in zebrafish. Zebrafish 6, 69-77.

Blackburn, J.S., and Langenau, D.M. (2014). Zebrafish as a model to assess cancer heterogeneity, progression and relapse. Disease models & mechanisms 7, 755-762.

Bolivar, J.J. (2013). Essential hypertension: an approach to its etiology and neurogenic pathophysiology. International journal of hypertension 2013, 547809.

Bonakdar, N., Luczak, J., Lautscham, L., Czonstke, M., Koch, T.M., Mainka, A., Jungbauer, T., Goldmann, W.H., Schroder, R., and Fabry, B. (2012). Biomechanical characterization of a desminopathy in primary human myoblasts. Biochemical and biophysical research communications 419, 703-707.

Brodehl, A., Hedde, P.N., Dieding, M., Fatima, A., Walhorn, V., Gayda, S., Saric, T., Klauke, B., Gummert, J., Anselmetti, D., et al. (2012). Dual color photoactivation localization microscopy of cardiomyopathy-associated desmin mutants. The Journal of biological chemistry 287, 16047-16057.

Brouillard, P., and Vikkula, M. (2007). Genetic causes of vascular malformations. Human molecular genetics 16 Spec No. 2, R140-149.

Bryk, J., and Tautz, D. (2014). Copy number variants and selective sweeps in natural populations of the house mouse (Mus musculus domesticus). Frontiers in genetics 5, 153.

Bryson-Richardson, R.J., and Currie, P.D. (2008). The genetics of vertebrate myogenesis. Nature reviews Genetics 9, 632-646.

Bunpo, P., Cundiff, J.K., Reinert, R.B., Wek, R.C., Aldrich, C.J., and Anthony, T.G. (2010). The eIF2 kinase GCN2 is essential for the murine immune system to adapt to amino acid deprivation by asparaginase. The Journal of nutrition 140, 2020-2027.

Cai, C.L., Liang, X., Shi, Y., Chu, P.H., Pfaff, S.L., Chen, J., and Evans, S. (2003). Isl1 identifies a cardiac progenitor population that proliferates prior to differentiation and contributes a majority of cells to the heart. Developmental cell 5, 877-889.

Carraro, V., Maurin, A.C., Lambert-Langlais, S., Averous, J., Chaveroux, C., Parry, L., Jousse, C., Ord, D., Ord, T., Fafournoux, P., et al. (2010). Amino acid availability controls TRB3 transcription in liver through the GCN2/eIF2alpha/ATF4 pathway. PloS one 5, e15716.

Cerletti, M., Negri, T., Cozzi, F., Colpo, R., Andreetta, F., Croci, D., Davies, K.E., Cornelio, F., Pozza, O., Karpati, G., et al. (2003). Dystrophic phenotype of canine X-linked muscular dystrophy is mitigated by adenovirus-mediated utrophin gene transfer. Gene therapy 10, 750-757.

Chablais, F., Veit, J., Rainer, G., and Jazwinska, A. (2011). The zebrafish heart regenerates after cryoinjury-induced myocardial infarction. BMC developmental biology 11, 21.

Chakrabarti, S., Streisinger, G., Singer, F., and Walker, C. (1983). Frequency of gamma-Ray Induced Specific Locus and Recessive Lethal Mutations in Mature Germ Cells of the Zebrafish, BRACHYDANIO RERIO. Genetics 103, 109-123.

Chang, N., Sun, C., Gao, L., Zhu, D., Xu, X., Zhu, X., Xiong, J.W., and Xi, J.J. (2013). Genome editing with RNA-guided Cas9 nuclease in zebrafish embryos. Cell research 23, 465-472.

Chaveroux, C., Lambert-Langlais, S., Parry, L., Carraro, V., Jousse, C., Maurin, A.C., Bruhat, A., Marceau, G., Sapin, V., Averous, J., et al. (2011). Identification of GCN2 as new redox regulator for oxidative stress prevention in vivo. Biochemical and biophysical research communications 415, 120-124.

Chen, H., Pan, Y.X., Dudenhausen, E.E., and Kilberg, M.S. (2004). Amino acid deprivation induces the transcription rate of the human asparagine synthetase gene through a timed program of expression and promoter binding of nutrient-responsive basic

region/leucine zipper transcription factors as well as localized histone acetylation. The Journal of biological chemistry 279, 50829-50839.

Chi, N.C., Bussen, M., Brand-Arzamendi, K., Ding, C., Olgin, J.E., Shaw, R.M., Martin, G.R., and Stainier, D.Y. (2010). Cardiac conduction is required to preserve cardiac chamber morphology. Proceedings of the National Academy of Sciences of the United States of America 107, 14662-14667.

Chi, N.C., Shaw, R.M., De Val, S., Kang, G., Jan, L.Y., Black, B.L., and Stainier, D.Y. (2008). Foxn4 directly regulates tbx2b expression and atrioventricular canal formation. Genes & development 22, 734-739.

Cho, S.W., Kim, S., Kim, Y., Kweon, J., Kim, H.S., Bae, S., and Kim, J.S. (2014). Analysis of off-target effects of CRISPR/Cas-derived RNA-guided endonucleases and nickases. Genome research 24, 132-141.

Claeys, K.G., Fardeau, M., Schroder, R., Suominen, T., Tolksdorf, K., Behin, A., Dubourg, O., Eymard, B., Maisonobe, T., Stojkovic, T., et al. (2008). Electron microscopy in myofibrillar myopathies reveals clues to the mutated gene. Neuromuscular disorders : NMD 18, 656-666.

Clemen, C.S., Herrmann, H., Strelkov, S.V., and Schroder, R. (2013). Desminopathies: pathology and mechanisms. Acta Neuropathol 125, 47-75.

Colombo, M.I. (2005). Pathogens and autophagy: subverting to survive. Cell death and differentiation 12 Suppl 2, 1481-1483.

Cong, L., Ran, F.A., Cox, D., Lin, S., Barretto, R., Habib, N., Hsu, P.D., Wu, X., Jiang, W., Marraffini, L.A., et al. (2013). Multiplex genome engineering using CRISPR/Cas systems. Science 339, 819-823.

Corti, P., Young, S., Chen, C.Y., Patrick, M.J., Rochon, E.R., Pekkan, K., and Roman, B.L. (2011). Interaction between alk1 and blood flow in the development of arteriovenous malformations. Development 138, 1573-1582.

Costa-Mattioli, M., Gobert, D., Harding, H., Herdy, B., Azzi, M., Bruno, M., Bidinosti, M., Ben Mamou, C., Marcinkiewicz, E., Yoshida, M., et al. (2005). Translational control of hippocampal synaptic plasticity and memory by the eIF2alpha kinase GCN2. Nature 436, 1166-1173.

Costa, M.L., Escaleira, R., Cataldo, A., Oliveira, F., and Mermelstein, C.S. (2004). Desmin: molecular interactions and putative functions of the muscle intermediate filament protein. Braz J Med Biol Res 37, 1819-1830.

Coutinho, T. (2014). Arterial Stiffness and Its Clinical Implications in Women. The Canadian journal of cardiology 30, 756-764.

Cuervo, A.M., and Wong, E. (2014). Chaperone-mediated autophagy: roles in disease and aging. Cell research 24, 92-104.

D'Amico, L., Scott, I.C., Jungblut, B., and Stainier, D.Y. (2007). A mutation in zebrafish hmgcr1b reveals a role for isoprenoids in vertebrate heart-tube formation. Current biology : CB 17, 252-259.

Davies, J.E., Wang, L., Garcia-Oroz, L., Cook, L.J., Vacher, C., O'Donovan, D.G., and Rubinsztein, D.C. (2005). Doxycycline attenuates and delays toxicity of the oculopharyngeal muscular dystrophy mutation in transgenic mice. Nature medicine 11, 672-677.

Davis, E.E., Frangakis, S., and Katsanis, N. (2014). Interpreting human genetic variation with in vivo zebrafish assays. Biochimica et biophysica acta.

de Pater, E., Clijsters, L., Marques, S.R., Lin, Y.F., Garavito-Aguilar, Z.V., Yelon, D., and Bakkers, J. (2009). Distinct phases of cardiomyocyte differentiation regulate growth of the zebrafish heart. Development 136, 1633-1641.

Del Giacco, L., Pistocchi, A., and Ghilardi, A. (2010). prox1b Activity is essential in zebrafish lymphangiogenesis. PloS one 5, e13170.

Dergai, M., Tsyba, L., Dergai, O., Zlatskii, I., Skrypkina, I., Kovalenko, V., and Rynditch, A. (2010). Microexon-based regulation of ITSN1 and Src SH3 domains specificity relies on introduction of charged amino acids into the interaction interface. Biochemical and biophysical research communications 399, 307-312.

Detrich, H.W., 3rd, Kieran, M.W., Chan, F.Y., Barone, L.M., Yee, K., Rundstadler, J.A., Pratt, S., Ransom, D., and Zon, L.I. (1995). Intraembryonic hematopoietic cell migration during vertebrate development. Proceedings of the National Academy of Sciences of the United States of America 92, 10713-10717.

Dimachkie, M.M., Barohn, R.J., and Amato, A.A. (2014). Idiopathic Inflammatory Myopathies. Neurologic clinics 32, 595-628.

Donnelly, N., Gorman, A.M., Gupta, S., and Samali, A. (2013). The eIF2alpha kinases: their structures and functions. Cellular and molecular life sciences : CMLS 70, 3493-3511.

Douglas, A.G., and Wood, M.J. (2013). Splicing therapy for neuromuscular disease. Molecular and cellular neurosciences 56, 169-185.

Dowling, J.J., Arbogast, S., Hur, J., Nelson, D.D., McEvoy, A., Waugh, T., Marty, I., Lunardi, J., Brooks, S.V., Kuwada, J.Y., et al. (2012). Oxidative stress and successful antioxidant treatment in models of RYR1-related myopathy. Brain 135, 1115-1127.

Dowling, J.J., Low, S.E., Busta, A.S., and Feldman, E.L. (2010). Zebrafish MTMR14 is required for excitation-contraction coupling, developmental motor function and the regulation of autophagy. Human molecular genetics 19, 2668-2681.

Dowling, J.J., Vreede, A.P., Low, S.E., Gibbs, E.M., Kuwada, J.Y., Bonnemann, C.G., and Feldman, E.L. (2009). Loss of myotubularin function results in T-tubule disorganization in zebrafish and human myotubular myopathy. PLoS genetics 5, e1000372.

Doyon, Y., McCammon, J.M., Miller, J.C., Faraji, F., Ngo, C., Katibah, G.E., Amora, R., Hocking, T.D., Zhang, L., Rebar, E.J., et al. (2008). Heritable targeted gene disruption in zebrafish using designed zinc-finger nucleases. Nature biotechnology 26, 702-708.

Eder, P., and Molkentin, J.D. (2011). TRPC channels as effectors of cardiac hypertrophy. Circulation research 108, 265-272.

Ekker, S.C., and Larson, J.D. (2001). Morphant technology in model developmental systems. Genesis 30, 89-93.

El Chami, H., and Hassoun, P.M. (2012). Immune and inflammatory mechanisms in pulmonary arterial hypertension. Progress in cardiovascular diseases 55, 218-228.

Eyries, M., Coulet, F., Girerd, B., Montani, D., Humbert, M., Lacombe, P., Chinet, T., Gouya, L., Roume, J., Axford, M.M., et al. (2012). ACVRL1 germinal mosaic with two mutant alleles in hereditary hemorrhagic telangiectasia associated with pulmonary arterial hypertension. Clin Genet 82, 173-179.

Eyries, M., Montani, D., Girerd, B., Perret, C., Leroy, A., Lonjou, C., Chelghoum, N., Coulet, F., Bonnet, D., Dorfmuller, P., et al. (2014). EIF2AK4 mutations cause pulmonary veno-occlusive disease, a recessive form of pulmonary hypertension. Nature genetics 46, 65-69.

Feitsma, H., Leal, M.C., Moens, P.B., Cuppen, E., and Schulz, R.W. (2007). Mlh1 deficiency in zebrafish results in male sterility and aneuploid as well as triploid progeny in females. Genetics 175, 1561-1569.

Ferrante, M.I., Kiff, R.M., Goulding, D.A., and Stemple, D.L. (2011). Troponin T is essential for sarcomere assembly in zebrafish skeletal muscle. Journal of cell science 124, 565-577.

Fischer Paul F, L.F., Lee Seung E, Lee Sang-Wook, Smith David S, Bassiouny Hisham S (2007). Simulation of high-Reynolds number vascular flows. Computer methods in applied mechanics and engineering 196, 3049-3060.

Forloni, G., Colombo, L., Girola, L., Tagliavini, F., and Salmona, M. (2001). Anti-amyloidogenic activity of tetracyclines: studies in vitro. FEBS Lett 487, 404-407.

Forouhar, A.S., Liebling, M., Hickerson, A., Nasiraei-Moghaddam, A., Tsai, H.J., Hove, J.R., Fraser, S.E., Dickinson, M.E., and Gharib, M. (2006). The embryonic vertebrate heart tube is a dynamic suction pump. Science 312, 751-753.

Fountoulakis, M., Soumaka, E., Rapti, K., Mavroidis, M., Tsangaris, G., Maris, A., Weisleder, N., and Capetanaki, Y. (2005). Alterations in the heart mitochondrial proteome in a desmin null heart failure model. J Mol Cell Cardiol 38, 461-474.

Fouquet, B., Weinstein, B.M., Serluca, F.C., and Fishman, M.C. (1997). Vessel patterning in the embryo of the zebrafish: guidance by notochord. Developmental biology 183, 37-48.

Fraser, M., Berlin, A., Bristow, R.G., and van der Kwast, T. (2014). Genomic, pathological, and clinical heterogeneity as drivers of personalized medicine in prostate cancer. Urologic oncology.

Freund, J.B., Goetz, J.G., Hill, K.L., and Vermot, J. (2012). Fluid flows and forces in development: functions, features and biophysical principles. Development 139, 1229-1245.

Fu, Y., Foden, J.A., Khayter, C., Maeder, M.L., Reyon, D., Joung, J.K., and Sander, J.D. (2013). High-frequency off-target mutagenesis induced by CRISPR-Cas nucleases in human cells. Nature biotechnology 31, 822-826.

Gaj, T., Gersbach, C.A., and Barbas, C.F., 3rd (2013). ZFN, TALEN, and CRISPR/Cas-based methods for genome engineering. Trends in biotechnology 31, 397-405.

Gard, J.J., Yamada, K., Green, K.G., Eloff, B.C., Rosenbaum, D.S., Wang, X., Robbins, J., Schuessler, R.B., Yamada, K.A., and Saffitz, J.E. (2005a). Remodeling of gap junctions and slow conduction in a mouse model of desmin-related cardiomyopathy. Cardiovascular research 67, 539-547.

Gard, J.J., Yamada, K., Green, K.G., Eloff, B.C., Rosenbaum, D.S., Wang, X., Robbins, J., Schuessler, R.B., Yamada, K.A., and Saffitz, J.E. (2005b). Remodeling of gap junctions and slow conduction in a mouse model of desmin-related cardiomyopathy. Cardiovascular research 67, 539-547.

Gemberling, M., Bailey, T.J., Hyde, D.R., and Poss, K.D. (2013). The zebrafish as a model for complex tissue regeneration. Trends in genetics : TIG 29, 611-620.

Gerety, S.S., and Wilkinson, D.G. (2011). Morpholino artifacts provide pitfalls and reveal a novel role for pro-apoptotic genes in hindbrain boundary development. Developmental biology 350, 279-289.

Gibbs, E.M., Horstick, E.J., and Dowling, J.J. (2013). Swimming into prominence: the zebrafish as a valuable tool for studying human myopathies and muscular dystrophies. The FEBS journal 280, 4187-4197.

Gieger, C., Radhakrishnan, A., Cvejic, A., Tang, W., Porcu, E., Pistis, G., Serbanovic-Canic, J., Elling, U., Goodall, A.H., Labrune, Y., et al. (2011). New gene functions in megakaryopoiesis and platelet formation. Nature 480, 201-208.

Goetz, J.G., Monduc, F., schwab, Y., and Vermot, J. (in press). Using Correlative Light and Electron Microscopy to Study Zebrafish Vascular Morphogenesis. Methods in Cell Biology.

Goetz, J.G., Steed, E., Ferreira, R.R., Roth, S., Ramspacher, C., Boselli, F., Charvin, G., Liebling, M., Wyart, C., Schwab, Y., et al. (2014). Endothelial cilia mediate low flow sensing during zebrafish vascular development. Cell reports 6, 799-808.

Goldfarb, L.G., and Dalakas, M.C. (2009). Tragedy in a heartbeat: malfunctioning desmin causes skeletal and cardiac muscle disease. J Clin Invest 119, 1806-1813.

Goldsmith, J.R., Cocchiaro, J.L., Rawls, J.F., and Jobin, C. (2013). Glafenine-induced intestinal injury in zebrafish is ameliorated by mu-opioid signaling via enhancement of Atf6-dependent cellular stress responses. Disease models & mechanisms 6, 146-159.

Golzio, C., Willer, J., Talkowski, M.E., Oh, E.C., Taniguchi, Y., Jacquemont, S., Reymond, A., Sun, M., Sawa, A., Gusella, J.F., et al. (2012). KCTD13 is a major driver of mirrored neuroanatomical phenotypes of the 16p11.2 copy number variant. Nature 485, 363-367.

Gore, A.V., Lampugnani, M.G., Dye, L., Dejana, E., and Weinstein, B.M. (2008). Combinatorial interaction between CCM pathway genes precipitates hemorrhagic stroke. Disease models & mechanisms 1, 275-281.

Gore, A.V., Monzo, K., Cha, Y.R., Pan, W., and Weinstein, B.M. (2012). Vascular development in the zebrafish. Cold Spring Harbor perspectives in medicine 2, a006684.

Gregor, M., Osmanagic-Myers, S., Burgstaller, G., Wolfram, M., Fischer, I., Walko, G., Resch, G.P., Jorgl, A., Herrmann, H., and Wiche, G. (2014). Mechanosensing through focal adhesion-anchored intermediate filaments. FASEB journal : official publication of the Federation of American Societies for Experimental Biology 28, 715-729.

Griggs, R., Vihola, A., Hackman, P., Talvinen, K., Haravuori, H., Faulkner, G., Eymard, B., Richard, I., Selcen, D., Engel, A., et al. (2007). Zaspopathy in a large classic late-onset distal myopathy family. Brain 130, 1477-1484.

Group, I.S. (2005). Determinants of coronary events in patients with stable angina: results from the impact of nicorandil in angina study. American heart journal 150, 689.

Groves, J.A., Hammond, C.L., and Hughes, S.M. (2005). Fgf8 drives myogenic progression of a novel lateral fast muscle fibre population in zebrafish. Development 132, 4211-4222.

Gupta, V., Kawahara, G., Gundry, S.R., Chen, A.T., Lencer, W.I., Zhou, Y., Zon, L.I., Kunkel, L.M., and Beggs, A.H. (2011). The zebrafish dag1 mutant: a novel genetic model for dystroglycanopathies. Human molecular genetics 20, 1712-1725.

Gupta, V., and Poss, K.D. (2012). Clonally dominant cardiomyocytes direct heart morphogenesis. Nature 484, 479-484.

Gupta, V.A., Hnia, K., Smith, L.L., Gundry, S.R., McIntire, J.E., Shimazu, J., Bass, J.R., Talbot, E.A., Amoasii, L., Goldman, N.E., et al. (2013). Loss of catalytically inactive lipid phosphatase myotubularin-related protein 12 impairs myotubularin stability and promotes centronuclear myopathy in zebrafish. PLoS genetics 9, e1003583.

Gupta, V.A., Kawahara, G., Myers, J.A., Chen, A.T., Hall, T.E., Manzini, M.C., Currie, P.D., Zhou, Y., Zon, L.I., Kunkel, L.M., et al. (2012). A splice site mutation in laminin-alpha2 results in a severe muscular dystrophy and growth abnormalities in zebrafish. PloS one 7, e43794.

Gut, P., Baeza-Raja, B., Andersson, O., Hasenkamp, L., Hsiao, J., Hesselson, D., Akassoglou, K., Verdin, E., Hirschey, M.D., and Stainier, D.Y. (2013). Whole-organism screening for gluconeogenesis identifies activators of fasting metabolism. Nature chemical biology 9, 97-104.

Guyon, J.R., Goswami, J., Jun, S.J., Thorne, M., Howell, M., Pusack, T., Kawahara, G., Steffen, L.S., Galdzicki, M., and Kunkel, L.M. (2009). Genetic isolation and characterization of a splicing mutant of zebrafish dystrophin. Human molecular genetics 18, 202-211.

Hall, T.E., Bryson-Richardson, R.J., Berger, S., Jacoby, A.S., Cole, N.J., Hollway, G.E., Berger, J., and Currie, P.D. (2007). The zebrafish candyfloss mutant implicates extracellular matrix adhesion failure in laminin alpha2-deficient congenital muscular dystrophy. Proceedings of the National Academy of Sciences of the United States of America 104, 7092-7097.

Halpern, M.E., Rhee, J., Goll, M.G., Akitake, C.M., Parsons, M., and Leach, S.D. (2008). Gal4/UAS transgenic tools and their application to zebrafish. Zebrafish 5, 97-110.

Harding, H.P., Zhang, Y., Zeng, H., Novoa, I., Lu, P.D., Calfon, M., Sadri, N., Yun, C., Popko, B., Paules, R., et al. (2003). An integrated stress response regulates amino acid metabolism and resistance to oxidative stress. Molecular cell 11, 619-633.

Hassel, D., Dahme, T., Erdmann, J., Meder, B., Huge, A., Stoll, M., Just, S., Hess, A., Ehlermann, P., Weichenhan, D., et al. (2009). Nexilin mutations destabilize cardiac Z-disks and lead to dilated cardiomyopathy. Nature medicine 15, 1281-1288.

He, C., Bartholomew, C.R., Zhou, W., and Klionsky, D.J. (2009). Assaying autophagic activity in transgenic GFP-Lc3 and GFP-Gabarap zebrafish embryos. Autophagy 5, 520-526.

Hein, S., Block, T., Zimmermann, R., Kostin, S., Scheffold, T., Kubin, T., Klovekorn, W.P., and Schaper, J. (2009). Deposition of nonsarcomeric alpha-actinin in cardiomyocytes from patients with dilated cardiomyopathy or chronic pressure overload. Experimental and clinical cardiology 14, e68-75.

Henderson, M., De Waele, L., Hudson, J., Eagle, M., Sewry, C., Marsh, J., Charlton, R., He, L., Blakely, E.L., Horrocks, I., et al. (2013). Recessive desmin-null muscular dystrophy with central nuclei and mitochondrial abnormalities. Acta Neuropathol 125, 917-919.

Herrmann, H., Strelkov, S.V., Burkhard, P., and Aebi, U. (2009). Intermediate filaments: primary determinants of cell architecture and plasticity. J Clin Invest 119, 1772-1783.

Herwig, L., Blum, Y., Krudewig, A., Ellertsdottir, E., Lenard, A., Belting, H.G., and Affolter, M. (2011). Distinct cellular mechanisms of blood vessel fusion in the zebrafish embryo. Current biology : CB 21, 1942-1948.

Hirata, H., Watanabe, T., Hatakeyama, J., Sprague, S.M., Saint-Amant, L., Nagashima, A., Cui, W.W., Zhou, W., and Kuwada, J.Y. (2007). Zebrafish relatively relaxed mutants have a ryanodine receptor defect, show slow swimming and provide a model of multi-minicore disease. Development 134, 2771-2781.

Hirsinger, E., Stellabotte, F., Devoto, S.H., and Westerfield, M. (2004). Hedgehog signaling is required for commitment but not initial induction of slow muscle precursors. Developmental biology 275, 143-157.

Hnia, K., Tronchere, H., Tomczak, K.K., Amoasii, L., Schultz, P., Beggs, A.H., Payrastre, B., Mandel, J.L., and Laporte, J. (2011). Myotubularin controls desmin intermediate filament architecture and mitochondrial dynamics in human and mouse skeletal muscle. J Clin Invest 121, 70-85.

Hong, C.C., Kume, T., and Peterson, R.T. (2008). Role of crosstalk between phosphatidylinositol 3-kinase and extracellular signal-regulated kinase/mitogen-activated protein kinase pathways in artery-vein specification. Circulation research 103, 573-579.

Howe, K., Clark, M.D., Torroja, C.F., Torrance, J., Berthelot, C., Muffato, M., Collins, J.E., Humphray, S., McLaren, K., Matthews, L., et al. (2013). The zebrafish reference genome sequence and its relationship to the human genome. Nature 496, 498-503.

Huang, C.J., Tu, C.T., Hsiao, C.D., Hsieh, F.J., and Tsai, H.J. (2003). Germ-line transmission of a myocardium-specific GFP transgene reveals critical regulatory elements in the cardiac myosin light chain 2 promoter of zebrafish. Developmental dynamics : an official publication of the American Association of Anatomists 228, 30-40.

Huang da, W., Sherman, B.T., and Lempicki, R.A. (2009). Systematic and integrative analysis of large gene lists using DAVID bioinformatics resources. Nature protocols 4, 44-57.

Huang, P., Xiao, A., Zhou, M., Zhu, Z., Lin, S., and Zhang, B. (2011). Heritable gene targeting in zebrafish using customized TALENs. Nature biotechnology 29, 699-700.

Huang, W., Zhang, R., and Xu, X. (2009). Myofibrillogenesis in the developing zebrafish heart: A functional study of tnnt2. Developmental biology 331, 237-249.

Hwang, W.Y., Fu, Y., Reyon, D., Maeder, M.L., Tsai, S.Q., Sander, J.D., Peterson, R.T., Yeh, J.R., and Joung, J.K. (2013). Efficient genome editing in zebrafish using a CRISPR-Cas system. Nature biotechnology 31, 227-229.

Hyttinen, J.M., Amadio, M., Viiri, J., Pascale, A., Salminen, A., and Kaarniranta, K. (2014). Clearance of misfolded and aggregated proteins by aggrephagy and implications for aggregation diseases. Ageing research reviews.

Isogai, S., Horiguchi, M., and Weinstein, B.M. (2001). The vascular anatomy of the developing zebrafish: an atlas of embryonic and early larval development. Developmental biology 230, 278-301.

Jackson, H.E., and Ingham, P.W. (2013). Control of muscle fibre-type diversity during embryonic development: the zebrafish paradigm. Mechanisms of development 130, 447-457.

Jacoby, A.S., Busch-Nentwich, E., Bryson-Richardson, R.J., Hall, T.E., Berger, J., Berger, S., Sonntag, C., Sachs, C., Geisler, R., Stemple, D.L., et al. (2009). The zebrafish dystrophic mutant softy maintains muscle fibre viability despite basement membrane rupture and muscle detachment. Development 136, 3367-3376.

Jao, L.E., Wente, S.R., and Chen, W. (2013). Efficient multiplex biallelic zebrafish genome editing using a CRISPR nuclease system. Proceedings of the National Academy of Sciences of the United States of America 110, 13904-13909.

Joanne, P., Chourbagi, O., Hourde, C., Ferry, A., Butler-Browne, G., Vicart, P., Dumonceaux, J., and Agbulut, O. (2013). Viral-mediated expression of desmin mutants to create mouse models of myofibrillar myopathy. Skelet Muscle 3, 4.

Jopling, C., Sleep, E., Raya, M., Marti, M., Raya, A., and Izpisua Belmonte, J.C. (2010). Zebrafish heart regeneration occurs by cardiomyocyte dedifferentiation and proliferation. Nature 464, 606-609.

Jungke, P., Hans, S., and Brand, M. (2013). The zebrafish CreZoo: an easy-to-handle database for novel CreER(T2)-driver lines. Zebrafish 10, 259-263.

Jurynec, M.J., Xia, R., Mackrill, J.J., Gunther, D., Crawford, T., Flanigan, K.M., Abramson, J.J., Howard, M.T., and Grunwald, D.J. (2008). Selenoprotein N is required for ryanodine receptor calcium release channel activity in human and zebrafish muscle. Proceedings of the National Academy of Sciences of the United States of America 105, 12485-12490.

Just, S., Meder, B., Berger, I.M., Etard, C., Trano, N., Patzel, E., Hassel, D., Marquart, S., Dahme, T., Vogel, B., et al. (2011). The myosin-interacting protein SMYD1 is essential for sarcomere organization. Journal of cell science 124, 3127-3136.

Kabashi, E., Lin, L., Tradewell, M.L., Dion, P.A., Bercier, V., Bourgouin, P., Rochefort, D., Bel Hadj, S., Durham, H.D., Vande Velde, C., et al. (2010). Gain and loss of function of ALS-related mutations of TARDBP (TDP-43) cause motor deficits in vivo. Human molecular genetics 19, 671-683.

Kabrun, N., Buhring, H.J., Choi, K., Ullrich, A., Risau, W., and Keller, G. (1997). Flk-1 expression defines a population of early embryonic hematopoietic precursors. Development 124, 2039-2048.

Katanosaka, Y., Iwasaki, K., Ujihara, Y., Takatsu, S., Nishitsuji, K., Kanagawa, M., Sudo, A., Toda, T., Katanosaka, K., Mohri, S., et al. (2014). TRPV2 is critical for the maintenance of cardiac structure and function in mice. Nature communications 5, 3932.

Katsanis, S.H., and Katsanis, N. (2013). Molecular genetic testing and the future of clinical genomics. Nature reviews Genetics 14, 415-426.

Kawahara, G., Karpf, J.A., Myers, J.A., Alexander, M.S., Guyon, J.R., and Kunkel, L.M. (2011). Drug screening in a zebrafish model of Duchenne muscular dystrophy. Proceedings of the National Academy of Sciences of the United States of America 108, 5331-5336.

Kawakami, K., Koga, A., Hori, H., and Shima, A. (1998). Excision of the tol2 transposable element of the medaka fish, Oryzias latipes, in zebrafish, Danio rerio. Gene 225, 17-22.

Kay, L., Li, Z., Mericskay, M., Olivares, J., Tranqui, L., Fontaine, E., Tiivel, T., Sikk, P., Kaambre, T., Samuel, J.L., et al. (1997). Study of regulation of mitochondrial respiration in vivo. An analysis of influence of ADP diffusion and possible role of cytoskeleton. Biochimica et biophysica acta 1322, 41-59.

Kayed, R., Head, E., Thompson, J.L., McIntire, T.M., Milton, S.C., Cotman, C.W., and Glabe, C.G. (2003). Common structure of soluble amyloid oligomers implies common mechanism of pathogenesis. Science 300, 486-489.

Keegan, B.R., Feldman, J.L., Begemann, G., Ingham, P.W., and Yelon, D. (2005). Retinoic acid signaling restricts the cardiac progenitor pool. Science 307, 247-249.

Keegan, B.R., Meyer, D., and Yelon, D. (2004). Organization of cardiac chamber progenitors in the zebrafish blastula. Development 131, 3081-3091.

Kelly, R.G., and Buckingham, M.E. (2002). The anterior heart-forming field: voyage to the arterial pole of the heart. Trends in genetics : TIG 18, 210-216.

Kettleborough, R.N., Busch-Nentwich, E.M., Harvey, S.A., Dooley, C.M., de Bruijn, E., van Eeden, F., Sealy, I., White, R.J., Herd, C., Nijman, I.J., et al. (2013). A systematic genome-wide analysis of zebrafish protein-coding gene function. Nature 496, 494-497.

Kilberg, M.S., Shan, J., and Su, N. (2009). ATF4-dependent transcription mediates signaling of amino acid limitation. Trends in endocrinology and metabolism: TEM 20, 436-443.

Kim, J.D., Kang, H., Larrivee, B., Lee, M.Y., Mettlen, M., Schmid, S.L., Roman, B.L., Qyang, Y., Eichmann, A., and Jin, S.W. (2012). Context-dependent proangiogenic function of bone morphogenetic protein signaling is mediated by disabled homolog 2. Developmental cell 23, 441-448.

Kimmel, C.B., Ballard, W.W., Kimmel, S.R., Ullmann, B., and Schilling, T.F. (1995). Stages of embryonic development of the zebrafish. Developmental dynamics : an official publication of the American Association of Anatomists 203, 253-310.

Kinali, M., Arechavala-Gomeza, V., Feng, L., Cirak, S., Hunt, D., Adkin, C., Guglieri, M., Ashton, E., Abbs, S., Nihoyannopoulos, P., et al. (2009). Local restoration of dystrophin expression with the morpholino oligomer AVI-4658 in Duchenne muscular dystrophy: a single-blind, placebo-controlled, dose-escalation, proof-of-concept study. Lancet neurology 8, 918-928.

Kiss, B., Karsai, A., and Kellermayer, M.S. (2006). Nanomechanical properties of desmin intermediate filaments. Journal of structural biology 155, 327-339.

Kiss, B., Rohlich, P., and Kellermayer, M.S. (2011). Structure and elasticity of desmin protofibrils explored with scanning force microscopy. Journal of molecular recognition : JMR 24, 1095-1104.

Knoll, R., Postel, R., Wang, J., Kratzner, R., Hennecke, G., Vacaru, A.M., Vakeel, P., Schubert, C., Murthy, K., Rana, B.K., et al. (2007). Laminin-alpha4 and integrin-linked kinase mutations cause human cardiomyopathy via simultaneous defects in cardiomyocytes and endothelial cells. Circulation 116, 515-525.

Koo, T., Malerba, A., Athanasopoulos, T., Trollet, C., Boldrin, L., Ferry, A., Popplewell, L., Foster, H., Foster, K., and Dickson, G. (2011). Delivery of AAV2/9-microdystrophin genes incorporating helix 1 of the coiled-coil motif in the C-terminal domain of dystrophin improves muscle pathology and restores the level of alpha1-syntrophin and alpha-dystrobrevin in skeletal muscles of mdx mice. Human gene therapy 22, 1379-1388.

Kostareva, A., Sjoberg, G., Bruton, J., Zhang, S.J., Balogh, J., Gudkova, A., Hedberg, B., Edstrom, L., Westerblad, H., and Sejersen, T. (2008). Mice expressing L345P mutant desmin exhibit morphological and functional changes of skeletal and cardiac mitochondria. J Muscle Res Cell Motil 29, 25-36.

Kraemer, A.M., Saraiva, L.R., and Korsching, S.I. (2008). Structural and functional diversification in the teleost S100 family of calcium-binding proteins. BMC evolutionary biology 8, 48.

Kruger, M., and Linke, W.A. (2009). Titin-based mechanical signalling in normal and failing myocardium. J Mol Cell Cardiol 46, 490-498.

Lacolley, P., Challande, P., Boumaza, S., Cohuet, G., Laurent, S., Boutouyrie, P., Grimaud, J.A., Paulin, D., Lamaziere, J.M., and Li, Z. (2001). Mechanical properties and structure of carotid arteries in mice lacking desmin. Cardiovascular research 51, 178-187.

Lang, M.R., Lapierre, L.A., Frotscher, M., Goldenring, J.R., and Knapik, E.W. (2006). Secretory COPII coat component Sec23a is essential for craniofacial chondrocyte maturation. Nature genetics 38, 1198-1203.

Langmead, B., Trapnell, C., Pop, M., and Salzberg, S.L. (2009). Ultrafast and memory-efficient alignment of short DNA sequences to the human genome. Genome biology 10, R25.

Lawson, N.D., Scheer, N., Pham, V.N., Kim, C.H., Chitnis, A.B., Campos-Ortega, J.A., and Weinstein, B.M. (2001). Notch signaling is required for arterial-venous differentiation during embryonic vascular development. Development 128, 3675-3683.

Lawson, N.D., and Wolfe, S.A. (2011). Forward and reverse genetic approaches for the analysis of vertebrate development in the zebrafish. Developmental cell 21, 48-64.

le Noble, F., Fleury, V., Pries, A., Corvol, P., Eichmann, A., and Reneman, R.S. (2005). Control of arterial branching morphogenesis in embryogenesis: go with the flow. Cardiovascular research 65, 619-628.

Leal, M.C., Feitsma, H., Cuppen, E., Franca, L.R., and Schulz, R.W. (2008). Completion of meiosis in male zebrafish (Danio rerio) despite lack of DNA mismatch repair gene mlh1. Cell and tissue research 332, 133-139.

Leitman, J., Ulrich Hartl, F., and Lederkremer, G.Z. (2013). Soluble forms of polyQ-expanded huntingtin rather than large aggregates cause endoplasmic reticulum stress. Nature communications 4, 2753.

Li, Z., Colucci-Guyon, E., Pincon-Raymond, M., Mericskay, M., Pournin, S., Paulin, D., and Babinet, C. (1996). Cardiovascular lesions and skeletal myopathy in mice lacking desmin. Developmental biology 175, 362-366.

Liebling, M., Forouhar, A.S., Gharib, M., Fraser, S.E., and Dickinson, M.E. (2005). Four-dimensional cardiac imaging in living embryos via postacquisition synchronization of nongated slice sequences. J Biomed Opt 10, 054001.

Lieschke, G.J., and Currie, P.D. (2007). Animal models of human disease: zebrafish swim into view. Nature reviews Genetics 8, 353-367.

Lin, Y.Y. (2012). Muscle diseases in the zebrafish. Neuromuscular disorders : NMD 22, 673-684.

Linden, M., Li, Z., Paulin, D., Gotow, T., and Leterrier, J.F. (2001). Effects of desmin gene knockout on mice heart mitochondria. Journal of bioenergetics and biomembranes 33, 333-341.

Lindsay, E.A. (2001). Chromosomal microdeletions: dissecting del22q11 syndrome. Nature reviews Genetics 2, 858-868.

Linke, W.A. (2008). Sense and stretchability: the role of titin and titin-associated proteins in myocardial stress-sensing and mechanical dysfunction. Cardiovascular research 77, 637-648.

Lippai, M., and Low, P. (2014). The Role of the Selective Adaptor p62 and Ubiquitin-Like Proteins in Autophagy. BioMed research international 2014, 832704.

Liu, J., Bressan, M., Hassel, D., Huisken, J., Staudt, D., Kikuchi, K., Poss, K.D., Mikawa, T., and Stainier, D.Y. (2010). A dual role for ErbB2 signaling in cardiac trabeculation. Development 137, 3867-3875.

Liu, J., Chen, Q., Huang, W., Horak, K.M., Zheng, H., Mestril, R., and Wang, X. (2006a). Impairment of the ubiquitin-proteasome system in desminopathy mouse hearts. FASEB journal : official publication of the Federation of American Societies for Experimental Biology 20, 362-364.

Liu, J., Tang, M., Mestril, R., and Wang, X. (2006b). Aberrant protein aggregation is essential for a mutant desmin to impair the proteolytic function of the ubiquitin-proteasome system in cardiomyocytes. J Mol Cell Cardiol 40, 451-454.

Loh, S.H., Chan, W.T., Gong, Z., Lim, T.M., and Chua, K.L. (2000). Characterization of a zebrafish (Danio rerio) desmin cDNA: an early molecular marker of myogenesis. Differentiation 65, 247-254.

London, G.M. (2013). Mechanisms of arterial calcifications and consequences for cardiovascular function. Kidney international supplements 3, 442-445.

Lu, Z., Xu, X., Fassett, J., Kwak, D., Liu, X., Hu, X., Wang, H., Guo, H., Xu, D., Yan, S., et al. (2014). Loss of the eukaryotic initiation factor 2alpha kinase general control nonderepressible 2 protects mice from pressure overload-induced congestive heart failure without affecting ventricular hypertrophy. Hypertension 63, 128-135.

Maiuri, M.C., Galluzzi, L., Morselli, E., Kepp, O., Malik, S.A., and Kroemer, G. (2010). Autophagy regulation by p53. Current opinion in cell biology 22, 181-185.

Majczenko, K., Davidson, A.E., Camelo-Piragua, S., Agrawal, P.B., Manfready, R.A., Li, X., Joshi, S., Xu, J., Peng, W., Beggs, A.H., et al. (2012). Dominant mutation of CCDC78 in a unique congenital myopathy with prominent internal nuclei and atypical cores. American journal of human genetics 91, 365-371.

Mali, P., Yang, L., Esvelt, K.M., Aach, J., Guell, M., DiCarlo, J.E., Norville, J.E., and Church, G.M. (2013). RNA-guided human genome engineering via Cas9. Science 339, 823-826.

Marques, S.R., Lee, Y., Poss, K.D., and Yelon, D. (2008). Reiterative roles for FGF signaling in the establishment of size and proportion of the zebrafish heart. Developmental biology 321, 397-406.

Marques, S.R., and Yelon, D. (2009). Differential requirement for BMP signaling in atrial and ventricular lineages establishes cardiac chamber proportionality. Developmental biology 328, 472-482.

Martins, L.C., Figueiredo, V.N., Quinaglia, T., Boer-Martins, L., Yugar-Toledo, J.C., Martin, J.F., Demacq, C., Pimenta, E., Calhoun, D.A., and Moreno, H., Jr. (2011). Characteristics of resistant hypertension: ageing, body mass index, hyperaldosteronism, cardiac hypertrophy and vascular stiffness. Journal of human hypertension 25, 532-538.

Matsushita, N., Hirose, M., Sanbe, A., Kondo, Y., Irie, Y., and Taira, E. (2014). Nicorandil improves electrical remodelling, leading to the prevention of electrically induced ventricular tachyarrhythmia in a mouse model of desmin-related cardiomyopathy. Clinical and experimental pharmacology & physiology 41, 89-97.

Mavroidis, M., Panagopoulou, P., Kostavasili, I., Weisleder, N., and Capetanaki, Y. (2008). A missense mutation in desmin tail domain linked to human dilated cardiomyopathy promotes cleavage of the head domain and abolishes its Z-disc localization. FASEB journal : official publication of the Federation of American Societies for Experimental Biology 22, 3318-3327.

McCain, M.L., and Parker, K.K. (2011). Mechanotransduction: the role of mechanical stress, myocyte shape, and cytoskeletal architecture on cardiac function. Pflugers Archiv : European journal of physiology 462, 89-104.

McLendon, P.M., and Robbins, J. (2011). Desmin-related cardiomyopathy: an unfolding story. American journal of physiology Heart and circulatory physiology 301, H1220-1228.

Meder, B., Laufer, C., Hassel, D., Just, S., Marquart, S., Vogel, B., Hess, A., Fishman, M.C., Katus, H.A., and Rottbauer, W. (2009). A single serine in the carboxyl terminus of cardiac essential myosin light chain-1 controls cardiomyocyte contractility in vivo. Circulation research 104, 650-659.

Meeker, N.D., and Trede, N.S. (2008). Immunology and zebrafish: spawning new models of human disease. Developmental and comparative immunology 32, 745-757.

Meng, X., Noyes, M.B., Zhu, L.J., Lawson, N.D., and Wolfe, S.A. (2008). Targeted gene inactivation in zebrafish using engineered zinc-finger nucleases. Nature biotechnology 26, 695-701.

Menzies, F.M., Ravikumar, B., and Rubinsztein, D.C. (2006). Protective roles for induction of autophagy in multiple proteinopathies. Autophagy 2, 224-225.

Milan, D.J., Giokas, A.C., Serluca, F.C., Peterson, R.T., and MacRae, C.A. (2006). Notch1b and neuregulin are required for specification of central cardiac conduction tissue. Development 133, 1125-1132.

Milner, D.J., Mavroidis, M., Weisleder, N., and Capetanaki, Y. (2000). Desmin cytoskeleton linked to muscle mitochondrial distribution and respiratory function. J Cell Biol 150, 1283-1298.

Milner, D.J., Taffet, G.E., Wang, X., Pham, T., Tamura, T., Hartley, C., Gerdes, A.M., and Capetanaki, Y. (1999). The absence of desmin leads to cardiomyocyte hypertrophy and cardiac dilation with compromised systolic function. J Mol Cell Cardiol 31, 2063-2076.

Milner, D.J., Weitzer, G., Tran, D., Bradley, A., and Capetanaki, Y. (1996). Disruption of muscle architecture and myocardial degeneration in mice lacking desmin. J Cell Biol 134, 1255-1270.

Mitsui, T., Kawajiri, M., Kunishige, M., Endo, T., Akaike, M., Aki, K., and Matsumoto, T. (2000). Functional association between nicotinic acetylcholine receptor and sarcomeric proteins via actin and desmin filaments. Journal of cellular biochemistry 77, 584-595.

Mojzisova, H., and Vermot, J. (2011). When multiphoton microscopy sees near infrared. Curr Opin Genet Dev 21, 549-557.

Montani, D., Kemp, K., Dorfmuller, P., Sitbon, O., Simonneau, G., and Humbert, M. (2009). Idiopathic pulmonary arterial hypertension and pulmonary veno-occlusive disease: similarities and differences. Seminars in respiratory and critical care medicine 30, 411-420.

Montani, D., O'Callaghan, D.S., Savale, L., Jais, X., Yaici, A., Maitre, S., Dorfmuller, P., Sitbon, O., Simonneau, G., and Humbert, M. (2010). Pulmonary veno-occlusive disease: recent progress and current challenges. Respiratory medicine 104 Suppl 1, S23-32.

Moon, J.Y. (2013). Recent Update of Renin-angiotensin-aldosterone System in the Pathogenesis of Hypertension. Electrolyte & blood pressure : E & BP 11, 41-45.

Mullins, M.C., Hammerschmidt, M., Haffter, P., and Nusslein-Volhard, C. (1994). Large-scale mutagenesis in the zebrafish: in search of genes controlling development in a vertebrate. Current biology : CB 4, 189-202.

Muto, A., Ohkura, M., Kotani, T., Higashijima, S., Nakai, J., and Kawakami, K. (2011). Genetic visualization with an improved GCaMP calcium indicator reveals spatiotemporal activation of the spinal motor neurons in zebrafish. Proceedings of the National Academy of Sciences of the United States of America 108, 5425-5430.

Nichols Wilmer, O.R.M., Vlachopoulos Charalambos (2005). McDonald's Blood Flow in Arteries, Sixth Edition: Theoretical, Experimental and Clinical Principles.

Nicot, A.S., Lo Verso, F., Ratti, F., Pilot-Storck, F., Streichenberger, N., Sandri, M., Schaeffer, L., and Goillot, E. (2014). Phosphorylation of NBR1 by GSK3 modulates protein aggregation. Autophagy 10, 1036-1053.

Niederriter, A.R., Davis, E.E., Golzio, C., Oh, E.C., Tsai, I.C., and Katsanis, N. (2013). In vivo modeling of the morbid human genome using Danio rerio. Journal of visualized experiments : JoVE, e50338.

Niethammer, P., Grabher, C., Look, A.T., and Mitchison, T.J. (2009). A tissue-scale gradient of hydrogen peroxide mediates rapid wound detection in zebrafish. Nature 459, 996-999.

North, T.E., Babu, I.R., Vedder, L.M., Lord, A.M., Wishnok, J.S., Tannenbaum, S.R., Zon, L.I., and Goessling, W. (2010). PGE2-regulated wnt signaling and N-acetylcysteine are synergistically hepatoprotective in zebrafish acetaminophen injury. Proceedings of the National Academy of Sciences of the United States of America 107, 17315-17320.

Norton, N., Li, D., Rieder, M.J., Siegfried, J.D., Rampersaud, E., Zuchner, S., Mangos, S., Gonzalez-Quintana, J., Wang, L., McGee, S., et al. (2011). Genome-wide studies of copy number variation and exome sequencing identify rare variants in BAG3 as a cause of dilated cardiomyopathy. American journal of human genetics 88, 273-282.

Novoa, B., and Figueras, A. (2012). Zebrafish: model for the study of inflammation and the innate immune response to infectious diseases. Advances in experimental medicine and biology 946, 253-275.

O'Callaghan, D.S., Dorfmuller, P., Jais, X., Mouthon, L., Sitbon, O., Simonneau, G., Humbert, M., and Montani, D. (2011). Pulmonary veno-occlusive disease: the bete noire of pulmonary hypertension in connective tissue diseases? Presse medicale 40, e65-78.

O'Neill, A., Williams, M.W., Resneck, W.G., Milner, D.J., Capetanaki, Y., and Bloch, R.J. (2002). Sarcolemmal organization in skeletal muscle lacking desmin: evidence for cytokeratins associated with the membrane skeleton at costameres. Molecular biology of the cell 13, 2347-2359.

Paavola, J., Schliffke, S., Rossetti, S., Kuo, I.Y., Yuan, S., Sun, Z., Harris, P.C., Torres, V.E., and Ehrlich, B.E. (2013). Polycystin-2 mutations lead to impaired calcium cycling in the heart and predispose to dilated cardiomyopathy. J Mol Cell Cardiol 58, 199-208.

Padilla, S., Corum, D., Padnos, B., Hunter, D.L., Beam, A., Houck, K.A., Sipes, N., Kleinstreuer, N., Knudsen, T., Dix, D.J., et al. (2012). Zebrafish developmental screening of the ToxCast Phase I chemical library. Reproductive toxicology 33, 174-187.

Palazzini, M., and Manes, A. (2009). Pulmonary veno-occlusive disease misdiagnosed as idiopathic pulmonary arterial hypertension. European respiratory review : an official journal of the European Respiratory Society 18, 177-180.

Patel, A., Sharif-Naeini, R., Folgering, J.R., Bichet, D., Duprat, F., and Honore, E. (2010). Canonical TRP channels and mechanotransduction: from physiology to disease states. Pflugers Archiv : European journal of physiology 460, 571-581.

Pattison, J.S., and Robbins, J. (2011). Autophagy and proteotoxicity in cardiomyocytes. Autophagy 7, 1259-1260.

Peralta, M., Steed, E., Harlepp, S., Gonzalez-Rosa, J.M., Monduc, F., Ariza-Cosano, A., Cortes, A., Rayon, T., Gomez-Skarmeta, J.L., Zapata, A., et al. (2013). Heartbeat-driven pericardiac fluid forces contribute to epicardium morphogenesis. Current biology : CB 23, 1726-1735.

Peravali, R., Gehrig, J., Giselbrecht, S., Lutjohann, D.S., Hadzhiev, Y., Muller, F., and Liebel, U. (2011). Automated feature detection and imaging for high-resolution screening of zebrafish embryos. BioTechniques 50, 319-324.

Percival, J.M., Whitehead, N.P., Adams, M.E., Adamo, C.M., Beavo, J.A., and Froehner, S.C. (2012). Sildenafil reduces respiratory muscle weakness and fibrosis in the mdx mouse model of Duchenne muscular dystrophy. The Journal of pathology 228, 77-87.

Pickart, M.A., and Klee, E.W. (2014). Zebrafish approaches enhance the translational research tackle box. Translational research : the journal of laboratory and clinical medicine 163, 65-78.

Pierce K. H. Chow, R.T.H.N., Bryan E. Ogde (2008). Using Animal Models in Biomedical Research: A Primer for the Investigator.

Pinol-Ripoll, G., Shatunov, A., Cabello, A., Larrode, P., de la Puerta, I., Pelegrin, J., Ramos, F.J., Olive, M., and Goldfarb, L.G. (2009). Severe infantile-onset cardiomyopathy associated with a homozygous deletion in desmin. Neuromuscular disorders : NMD 19, 418-422.

Pober, J.S., Neuhauser, C.S., and Pober, J.M. (2001). Obstacles facing translational research in academic medical centers. FASEB journal : official publication of the Federation of American Societies for Experimental Biology 15, 2303-2313.

Poon, E., Howman, E.V., Newey, S.E., and Davies, K.E. (2002). Association of syncoilin and desmin: linking intermediate filament proteins to the dystrophin-associated protein complex. The Journal of biological chemistry 277, 3433-3439.

Potente, M., Gerhardt, H., and Carmeliet, P. (2011). Basic and therapeutic aspects of angiogenesis. Cell 146, 873-887.

Proenca, C.C., Stoehr, N., Bernhard, M., Seger, S., Genoud, C., Roscic, A., Paganetti, P., Liu, S., Murphy, L.O., Kuhn, R., et al. (2013). Atg4b-dependent autophagic flux alleviates Huntington's disease progression. PloS one 8, e68357.

Pu, L., Igbavboa, U., Wood, W.G., Roths, J.B., Kier, A.B., Spener, F., and Schroeder, F. (1999). Expression of fatty acid binding proteins is altered in aged mouse brain. Molecular and cellular biochemistry 198, 69-78.

Raats, J.M., Schaart, G., Henderik, J.B., van der Kemp, A., Dunia, I., Benedetti, E.L., Pieper, F.R., Ramaekers, F.C., and Bloemendal, H. (1996). Muscle-specific expression of a dominant negative desmin mutant in transgenic mice. Eur J Cell Biol 71, 221-236.

Ramachandran, N., Munteanu, I., Wang, P., Aubourg, P., Rilstone, J.J., Israelian, N., Naranian, T., Paroutis, P., Guo, R., Ren, Z.P., et al. (2009). VMA21 deficiency causes an autophagic myopathy by compromising V-ATPase activity and lysosomal acidification. Cell 137, 235-246.

Ravikumar, B., Berger, Z., Vacher, C., O'Kane, C.J., and Rubinsztein, D.C. (2006). Rapamycin pre-treatment protects against apoptosis. Human molecular genetics 15, 1209-1216.

Ravindran, R., Khan, N., Nakaya, H.I., Li, S., Loebbermann, J., Maddur, M.S., Park, Y., Jones, D.P., Chappert, P., Davoust, J., et al. (2014). Vaccine activation of the nutrient sensor GCN2 in dendritic cells enhances antigen presentation. Science 343, 313-317.

Ray, A., Amato, A.A., Bradshaw, E.M., Felice, K.J., DiCapua, D.B., Goldstein, J.M., Lundberg, I.E., Nowak, R.J., Ploegh, H.L., Spooner, E., et al. (2012). Autoantibodies produced at the site of tissue damage provide evidence of humoral autoimmunity in inclusion body myositis. PloS one 7, e46709.

Reynolds, J.G., McCalmon, S.A., Tomczyk, T., and Naya, F.J. (2007). Identification and mapping of protein kinase A binding sites in the costameric protein myospryn. Biochimica et biophysica acta 1773, 891-902.

Rezniczek, G.A., Konieczny, P., Nikolic, B., Reipert, S., Schneller, D., Abrahamsberg, C., Davies, K.E., Winder, S.J., and Wiche, G. (2007a). Plectin 1f scaffolding at the sarcolemma of dystrophic (mdx) muscle fibers through multiple interactions with beta-dystroglycan. J Cell Biol 176, 965-977.

Rezniczek, G.A., Konieczny, P., Nikolic, B., Reipert, S., Schneller, D., Abrahamsberg, C., Davies, K.E., Winder, S.J., and Wiche, G. (2007b). Plectin 1f scaffolding at the sarcolemma of dystrophic (mdx) muscle fibers through multiple interactions with beta-dystroglycan. J Cell Biol 176, 965-977.

Robu, M.E., Larson, J.D., Nasevicius, A., Beiraghi, S., Brenner, C., Farber, S.A., and Ekker, S.C. (2007). p53 activation by knockdown technologies. PLoS genetics 3, e78.

Rodino-Klapac, L.R., Janssen, P.M., Montgomery, C.L., Coley, B.D., Chicoine, L.G., Clark, K.R., and Mendell, J.R. (2007). A translational approach for limb vascular delivery of the micro-dystrophin gene without high volume or high pressure for treatment of Duchenne muscular dystrophy. Journal of translational medicine 5, 45.

Roman, B.L., Pham, V.N., Lawson, N.D., Kulik, M., Childs, S., Lekven, A.C., Garrity, D.M., Moon, R.T., Fishman, M.C., Lechleider, R.J., et al. (2002). Disruption of acvrl1 increases endothelial cell number in zebrafish cranial vessels. Development 129, 3009-3019.

Roy, D., Kauffmann, C., Delorme, S., Lerouge, S., Cloutier, G., and Soulez, G. (2012). A literature review of the numerical analysis of abdominal aortic aneurysms treated with endovascular stent grafts. Computational and mathematical methods in medicine 2012, 820389.

Roybal, C.N., Hunsaker, L.A., Barbash, O., Vander Jagt, D.L., and Abcouwer, S.F. (2005). The oxidative stressor arsenite activates vascular endothelial growth factor mRNA transcription by an ATF4-dependent mechanism. The Journal of biological chemistry 280, 20331-20339.

Rubio, N., Coupienne, I., Di Valentin, E., Heirman, I., Grooten, J., Piette, J., and Agostinis, P. (2012). Spatiotemporal autophagic degradation of oxidatively damaged organelles after photodynamic stress is amplified by mitochondrial reactive oxygen species. Autophagy 8, 1312-1324.

Russell, A.P., Foletta, V.C., Snow, R.J., and Wadley, G.D. (2014). Skeletal muscle mitochondria: a major player in exercise, health and disease. Biochimica et biophysica acta 1840, 1276-1284.

Salani, S., Donadoni, C., Rizzo, F., Bresolin, N., Comi, G.P., and Corti, S. (2012). Generation of skeletal muscle cells from embryonic and induced pluripotent stem cells as an in vitro model and for therapy of muscular dystrophies. Journal of cellular and molecular medicine 16, 1353-1364.

Saleem, A., Adhihetty, P.J., and Hood, D.A. (2009). Role of p53 in mitochondrial biogenesis and apoptosis in skeletal muscle. Physiological genomics 37, 58-66.

Saleem, A., Carter, H.N., Iqbal, S., and Hood, D.A. (2011). Role of p53 within the regulatory network controlling muscle mitochondrial biogenesis. Exercise and sport sciences reviews 39, 199-205.

Sanbe, A., Daicho, T., Mizutani, R., Endo, T., Miyauchi, N., Yamauchi, J., Tanonaka, K., Glabe, C., and Tanoue, A. (2009). Protective effect of geranylgeranylacetone via enhancement of HSPB8 induction in desmin-related cardiomyopathy. PloS one 4, e5351.

Sanbe, A., Osinska, H., Saffitz, J.E., Glabe, C.G., Kayed, R., Maloyan, A., and Robbins, J. (2004). Desmin-related cardiomyopathy in transgenic mice: a cardiac amyloidosis. Proceedings of the National Academy of Sciences of the United States of America 101, 10132-10136.

Sanbe, A., Osinska, H., Villa, C., Gulick, J., Klevitsky, R., Glabe, C.G., Kayed, R., and Robbins, J. (2005). Reversal of amyloid-induced heart disease in desmin-related cardiomyopathy. Proceedings of the National Academy of Sciences of the United States of America 102, 13592-13597.

Sander, J.D., Cade, L., Khayter, C., Reyon, D., Peterson, R.T., Joung, J.K., and Yeh, J.R. (2011). Targeted gene disruption in somatic zebrafish cells using engineered TALENs. Nature biotechnology 29, 697-698.

Sanger, J.W., Wang, J., Holloway, B., Du, A., and Sanger, J.M. (2009). Myofibrillogenesis in skeletal muscle cells in zebrafish. Cell motility and the cytoskeleton 66, 556-566.

Sarkar, S., and Rubinsztein, D.C. (2008). Huntington's disease: degradation of mutant huntingtin by autophagy. The FEBS journal 275, 4263-4270.

Sarparanta, J., Jonson, P.H., Golzio, C., Sandell, S., Luque, H., Screen, M., McDonald, K., Stajich, J.M., Mahjneh, I., Vihola, A., et al. (2012). Mutations affecting the cytoplasmic functions of the co-chaperone DNAJB6 cause limb-girdle muscular dystrophy. Nature genetics 44, 450-455, S451-452.

Schaffeld, M., and Schultess, J. (2006). Genes coding for intermediate filament proteins closely related to the hagfish "thread keratins (TK)" alpha and gamma also exist in lamprey, teleosts and amphibians. Experimental cell research 312, 1447-1462.

Scherz, P.J., Huisken, J., Sahai-Hernandez, P., and Stainier, D.Y. (2008). High-speed imaging of developing heart valves reveals interplay of morphogenesis and function. Development 135, 1179-1187.

Schroder, R., Goudeau, B., Simon, M.C., Fischer, D., Eggermann, T., Clemen, C.S., Li, Z., Reimann, J., Xue, Z., Rudnik-Schoneborn, S., et al. (2003). On noxious desmin: functional effects of a novel heterozygous desmin insertion mutation on the extrasarcomeric desmin cytoskeleton and mitochondria. Human molecular genetics 12, 657-669.

Schroder, R., and Schoser, B. (2009). Myofibrillar myopathies: a clinical and myopathological guide. Brain Pathol 19, 483-492.

Schultheiss, T., Lin, Z.X., Ishikawa, H., Zamir, I., Stoeckert, C.J., and Holtzer, H. (1991). Desmin/vimentin intermediate filaments are dispensable for many aspects of myogenesis. J Cell Biol 114, 953-966.

Segard, B.D., Delort, F., Bailleux, V., Simon, S., Leccia, E., Gausseres, B., Briki, F., Vicart, P., and Batonnet-Pichon, S. (2013). N-acetyl-L-cysteine prevents stress-induced desmin aggregation in cellular models of desminopathy. PloS one 8, e76361.

Sehnert, A.J., Huq, A., Weinstein, B.M., Walker, C., Fishman, M., and Stainier, D.Y. (2002). Cardiac troponin T is essential in sarcomere assembly and cardiac contractility. Nature genetics 31, 106-110.

Selcen, D. (2011). Myofibrillar myopathies. Neuromuscular disorders : NMD 21, 161-171.

Selcen, D., Muntoni, F., Burton, B.K., Pegoraro, E., Sewry, C., Bite, A.V., and Engel, A.G. (2009). Mutation in BAG3 causes severe dominant childhood muscular dystrophy. Ann Neurol 65, 83-89.

Shardonofsky, F.R., Capetanaki, Y., and Boriek, A.M. (2006). Desmin modulates lung elastic recoil and airway responsiveness. Am J Physiol Lung Cell Mol Physiol 290, L890-896.

Siegel, A.L., Gurevich, D.B., and Currie, P.D. (2013). A myogenic precursor cell that could contribute to regeneration in zebrafish and its similarity to the satellite cell. The FEBS journal 280, 4074-4088.

Simonneau, G., Robbins, I.M., Beghetti, M., Channick, R.N., Delcroix, M., Denton, C.P., Elliott, C.G., Gaine, S.P., Gladwin, M.T., Jing, Z.C., et al. (2009). Updated clinical classification of pulmonary hypertension. Journal of the American College of Cardiology 54, S43-54.

Sjuve, R., Arner, A., Li, Z., Mies, B., Paulin, D., Schmittner, M., and Small, J.V. (1998). Mechanical alterations in smooth muscle from mice lacking desmin. Journal of muscle research and cell motility 19, 415-429.

Smith, A.A., Wyatt, K., Vacha, J., Vihtelic, T.S., Zigler, J.S., Jr., Wistow, G.J., and Posner, M. (2006). Gene duplication and separation of functions in alphaB-crystallin from zebrafish (Danio rerio). The FEBS journal 273, 481-490.

Smith, K.A., Chocron, S., von der Hardt, S., de Pater, E., Soufan, A., Bussmann, J., Schulte-Merker, S., Hammerschmidt, M., and Bakkers, J. (2008). Rotation and asymmetric development of the zebrafish heart requires directed migration of cardiac progenitor cells. Developmental cell 14, 287-297.

Stainier, D.Y., Fouquet, B., Chen, J.N., Warren, K.S., Weinstein, B.M., Meiler, S.E., Mohideen, M.A., Neuhauss, S.C., Solnica-Krezel, L., Schier, A.F., et al. (1996). Mutations affecting the formation and function of the cardiovascular system in the zebrafish embryo. Development 123, 285-292.

Stainier, D.Y., Lee, R.K., and Fishman, M.C. (1993). Cardiovascular development in the zebrafish. I. Myocardial fate map and heart tube formation. Development 119, 31-40.

Staudt, D.W., Liu, J., Thorn, K.S., Stuurman, N., Liebling, M., and Stainier, D.Y. (2014). High-resolution imaging of cardiomyocyte behavior reveals two distinct steps in ventricular trabeculation. Development 141, 585-593.

Stellabotte, F., Dobbs-McAuliffe, B., Fernandez, D.A., Feng, X., and Devoto, S.H. (2007). Dynamic somite cell rearrangements lead to distinct waves of myotome growth. Development 134, 1253-1257.

Stergiopulos, N., Westerhof, B.E., and Westerhof, N. (1999). Total arterial inertance as the fourth element of the windkessel model. The American journal of physiology 276, H81-88.

Stoilova, T., Colombo, L., Forloni, G., Tagliavini, F., and Salmona, M. (2013). A new face for old antibiotics: tetracyclines in treatment of amyloidoses. Journal of medicinal chemistry 56, 5987-6006.

Sugawara, M., Kato, K., Komatsu, M., Wada, C., Kawamura, K., Shindo, P.S., Yoshioka, P.N., Tanaka, K., Watanabe, S., and Toyoshima, I. (2000). A novel de novo mutation in the desmin gene causes desmin myopathy with toxic aggregates. Neurology 55, 986-990.

Summerton, J. (1999). Morpholino antisense oligomers: the case for an RNase H-independent structural type. Biochimica et biophysica acta 1489, 141-158.

Swift, M.R., and Weinstein, B.M. (2009). Arterial-venous specification during development. Circulation research 104, 576-588.

Takahashi, K., Tanabe, K., Ohnuki, M., Narita, M., Ichisaka, T., Tomoda, K., and Yamanaka, S. (2007). Induction of pluripotent stem cells from adult human fibroblasts by defined factors. Cell 131, 861-872.

Tallafuss, A., and Eisen, J.S. (2008). The Met receptor tyrosine kinase prevents zebrafish primary motoneurons from expressing an incorrect neurotransmitter. Neural development 3, 18.

Tanaka, Y., Guhde, G., Suter, A., Eskelinen, E.L., Hartmann, D., Lullmann-Rauch, R., Janssen, P.M., Blanz, J., von Figura, K., and Saftig, P. (2000). Accumulation of autophagic vacuoles and cardiomyopathy in LAMP-2-deficient mice. Nature 406, 902-906.

Tao, S., Witte, M., Bryson-Richardson, R.J., Currie, P.D., Hogan, B.M., and Schulte-Merker, S. (2011). Zebrafish prox1b mutants develop a lymphatic vasculature, and prox1b does not specifically mark lymphatic endothelial cells. PloS one 6, e28934.

Tasdemir, E., Maiuri, M.C., Galluzzi, L., Vitale, I., Djavaheri-Mergny, M., D'Amelio, M., Criollo, A., Morselli, E., Zhu, C., Harper, F., et al. (2008). Regulation of autophagy by cytoplasmic p53. Nature cell biology 10, 676-687.

Telfer, W.R., Nelson, D.D., Waugh, T., Brooks, S.V., and Dowling, J.J. (2012). Neb: a zebrafish model of nemaline myopathy due to nebulin mutation. Disease models & mechanisms 5, 389-396.

Tennessen, J.A., Bigham, A.W., O'Connor, T.D., Fu, W., Kenny, E.E., Gravel, S., McGee, S., Do, R., Liu, X., Jun, G., et al. (2012). Evolution and functional impact of rare coding variation from deep sequencing of human exomes. Science 337, 64-69.

Tessadori, F., van Weerd, J.H., Burkhard, S.B., Verkerk, A.O., de Pater, E., Boukens, B.J., Vink, A., Christoffels, V.M., and Bakkers, J. (2012). Identification and functional characterization of cardiac pacemaker cells in zebrafish. PloS one 7, e47644.

Thessadori, F., and Bakkers, J. (submitted).

Thomas, K.R., and Capecchi, M.R. (1987). Site-directed mutagenesis by gene targeting in mouse embryo-derived stem cells. Cell 51, 503-512.

Thompson, L.M., Aiken, C.T., Kaltenbach, L.S., Agrawal, N., Illes, K., Khoshnan, A., Martinez-Vincente, M., Arrasate, M., O'Rourke, J.G., Khashwji, H., et al. (2009). IKK phosphorylates Huntingtin and targets it for degradation by the proteasome and lysosome. J Cell Biol 187, 1083-1099.

Tille, J.C., and Pepper, M.S. (2004). Hereditary vascular anomalies: new insights into their pathogenesis. Arteriosclerosis, thrombosis, and vascular biology 24, 1578-1590.

Tobin, D.M., Roca, F.J., Oh, S.F., McFarland, R., Vickery, T.W., Ray, J.P., Ko, D.C., Zou, Y., Bang, N.D., Chau, T.T., et al. (2012). Host genotype-specific therapies can optimize the inflammatory response to mycobacterial infections. Cell 148, 434-446.

Trapnell, C., and Schatz, M.C. (2009). Optimizing Data Intensive GPGPU Computations for DNA Sequence Alignment. Parallel computing 35, 429-440.

Trinh le, A., Hochgreb, T., Graham, M., Wu, D., Ruf-Zamojski, F., Jayasena, C.S., Saxena, A., Hawk, R., Gonzalez-Serricchio, A., Dixson, A., et al. (2011). A versatile gene trap to visualize and interrogate the function of the vertebrate proteome. Genes & development 25, 2306-2320.

Tyberg, J.V., Davies, J.E., Wang, Z., Whitelaw, W.A., Flewitt, J.A., Shrive, N.G., Francis, D.P., Hughes, A.D., Parker, K.H., and Wang, J.J. (2009). Wave intensity analysis and the development of the reservoir-wave approach. Medical & biological engineering & computing 47, 221-232.

Ulbricht, A., Eppler, F.J., Tapia, V.E., van der Ven, P.F., Hampe, N., Hersch, N., Vakeel, P., Stadel, D., Haas, A., Saftig, P., et al. (2013). Cellular mechanotransduction relies on tension-induced and chaperone-assisted autophagy. Current biology : CB 23, 430-435.

van Eeden, F.J., Granato, M., Schach, U., Brand, M., Furutani-Seiki, M., Haffter, P., Hammerschmidt, M., Heisenberg, C.P., Jiang, Y.J., Kane, D.A., et al. (1996). Mutations affecting somite formation and patterning in the zebrafish, Danio rerio. Development 123, 153-164.

van Spaendonck-Zwarts, K.Y., van Hessem, L., Jongbloed, J.D., de Walle, H.E., Capetanaki, Y., van der Kooi, A.J., van Langen, I.M., van den Berg, M.P., and van Tintelen, J.P. (2011). Desmin-related myopathy. Clin Genet 80, 354-366.

Verhoeven, M.C., Haase, C., Christoffels, V.M., Weidinger, G., and Bakkers, J. (2011). Wnt signaling regulates atrioventricular canal formation upstream of BMP and Tbx2. Birth defects research Part A, Clinical and molecular teratology 91, 435-440.

Vermot, J., Forouhar, A.S., Liebling, M., Wu, D., Plummer, D., Gharib, M., and Fraser, S.E. (2009). Reversing blood flows act through klf2a to ensure normal valvulogenesis in the developing heart. PLoS biology 7, e1000246.

Vicart, P., Caron, A., Guicheney, P., Li, Z., Prevost, M.C., Faure, A., Chateau, D., Chapon, F., Tome, F., Dupret, J.M., et al. (1998). A missense mutation in the alphaB-crystallin chaperone gene causes a desmin-related myopathy. Nature genetics 20, 92-95.

Villarreal, F., and Lew, W.Y. (2010). Protein quality control in heart disease: using established drugs to target novel mechanisms. Journal of the American College of Cardiology 56, 1427-1429.

Vogel, B., Meder, B., Just, S., Laufer, C., Berger, I., Weber, S., Katus, H.A., and Rottbauer, W. (2009). In-vivo characterization of human dilated cardiomyopathy genes in zebrafish. Biochemical and biophysical research communications 390, 516-522.

Vogeli, K.M., Jin, S.W., Martin, G.R., and Stainier, D.Y. (2006). A common progenitor for haematopoietic and endothelial lineages in the zebrafish gastrula. Nature 443, 337-339.

Vorgerd, M., van der Ven, P.F., Bruchertseifer, V., Lowe, T., Kley, R.A., Schroder, R., Lochmuller, H., Himmel, M., Koehler, K., Furst, D.O., et al. (2005). A mutation in the dimerization domain of filamin c causes a novel type of autosomal dominant myofibrillar myopathy. American journal of human genetics 77, 297-304.

Walcott, B.P., and Peterson, R.T. (2014). Zebrafish models of cerebrovascular disease. Journal of cerebral blood flow and metabolism : official journal of the International Society of Cerebral Blood Flow and Metabolism 34, 571-577.

Wang, X., Klevitsky, R., Huang, W., Glasford, J., Li, F., and Robbins, J. (2003). AlphaB-crystallin modulates protein aggregation of abnormal desmin. Circulation research 93, 998-1005.

Wang, X., Osinska, H., Dorn, G.W., 2nd, Nieman, M., Lorenz, J.N., Gerdes, A.M., Witt, S., Kimball, T., Gulick, J., and Robbins, J. (2001a). Mouse model of desmin-related cardiomyopathy. Circulation 103, 2402-2407.

Wang, X., Osinska, H., Klevitsky, R., Gerdes, A.M., Nieman, M., Lorenz, J., Hewett, T., and Robbins, J. (2001b). Expression of R120G-alphaB-crystallin causes aberrant desmin and alphaB-crystallin aggregation and cardiomyopathy in mice. Circulation research 89, 84-91.

Wang, X., Wang, G., Kunte, M., Shinde, V., and Gorbatyuk, M. (2013). Modulation of angiogenesis by genetic manipulation of ATF4 in mouse model of oxygen-induced retinopathy [corrected]. Investigative ophthalmology & visual science 54, 5995-6002.

Warp, E., Agarwal, G., Wyart, C., Friedmann, D., Oldfield, C.S., Conner, A., Del Bene, F., Arrenberg, A.B., Baier, H., and Isacoff, E.Y. (2012). Emergence of patterned activity in the developing zebrafish spinal cord. Current biology : CB 22, 93-102.

Warren, T.K., Shurtleff, A.C., and Bavari, S. (2012). Advanced morpholino oligomers: a novel approach to antiviral therapy. Antiviral research 94, 80-88.

Webb, S.E., Cheung, C.C., Chan, C.M., Love, D.R., and Miller, A.L. (2012). Application of complementary luminescent and fluorescent imaging techniques to visualize nuclear and cytoplasmic Ca(2)(+) signalling during the in vivo differentiation of slow muscle cells in zebrafish embryos under normal and dystrophic conditions. Clinical and experimental pharmacology & physiology 39, 78-86.

Webster, S.J., Bachstetter, A.D., Nelson, P.T., Schmitt, F.A., and Van Eldik, L.J. (2014). Using mice to model Alzheimer's dementia: an overview of the clinical disease and the preclinical behavioral changes in 10 mouse models. Frontiers in genetics 5, 88.

Weinberg, E.S., Allende, M.L., Kelly, C.S., Abdelhamid, A., Murakami, T., Andermann, P., Doerre, O.G., Grunwald, D.J., and Riggleman, B. (1996). Developmental regulation of zebrafish MyoD in wild-type, no tail and spadetail embryos. Development 122, 271-280.

Weisiger, R.A. (2002). Cytosolic fatty acid binding proteins catalyze two distinct steps in intracellular transport of their ligands. Molecular and cellular biochemistry 239, 35-43.

Weisleder, N., Taffet, G.E., and Capetanaki, Y. (2004). Bcl-2 overexpression corrects mitochondrial defects and ameliorates inherited desmin null cardiomyopathy. Proceedings of the National Academy of Sciences of the United States of America 101, 769-774.

Wells, D.J., and Wells, K.E. (2005). What do animal models have to tell us regarding Duchenne muscular dystrophy? Acta myologica : myopathies and cardiomyopathies : official journal of the Mediterranean Society of Myology / edited by the Gaetano Conte Academy for the study of striated muscle diseases 24, 172-180.

Wen, D., Liu, A., Chen, F., Yang, J., and Dai, R. (2012). Validation of visualized transgenic zebrafish as a high throughput model to assay bradycardia related cardio toxicity risk candidates. Journal of applied toxicology : JAT 32, 834-842.

Westerhof, N., Lankhaar, J.W., and Westerhof, B.E. (2009). The arterial Windkessel. Medical & biological engineering & computing 47, 131-141.

Westerhof, N., and Westerhof, B.E. (2013). CrossTalk proposal: Forward and backward pressure waves in the arterial system do represent reality. The Journal of physiology 591, 1167-1169; discussion 1177.

White, R.M., Sessa, A., Burke, C., Bowman, T., LeBlanc, J., Ceol, C., Bourque, C., Dovey, M., Goessling, W., Burns, C.E., et al. (2008). Transparent adult zebrafish as a tool for in vivo transplantation analysis. Cell stem cell 2, 183-189.

Whitesell, T.R., Kennedy, R.M., Carter, A.D., Rollins, E.L., Georgijevic, S., Santoro, M.M., and Childs, S.J. (2014). An alpha-smooth muscle actin (acta2/alphasma) zebrafish transgenic line marking vascular mural cells and visceral smooth muscle cells. PloS one 9, e90590.

Whitney, M.L., Jefferson, L.S., and Kimball, S.R. (2009). ATF4 is necessary and sufficient for ER stress-induced upregulation of REDD1 expression. Biochemical and biophysical research communications 379, 451-455.

Wiley, D.M., Kim, J.D., Hao, J., Hong, C.C., Bautch, V.L., and Jin, S.W. (2011). Distinct signalling pathways regulate sprouting angiogenesis from the dorsal aorta and the axial vein. Nature cell biology 13, 686-692.

Winata, C.L., Korzh, S., Kondrychyn, I., Zheng, W., Korzh, V., and Gong, Z. (2009). Development of zebrafish swimbladder: The requirement of Hedgehog signaling in specification and organization of the three tissue layers. Developmental biology 331, 222-236.

Winter, L., Staszewska, I., Mihailovska, E., Fischer, I., Goldmann, W.H., Schroder, R., and Wiche, G. (2014). Chemical chaperone ameliorates pathological protein aggregation in plectin-deficient muscle. J Clin Invest 124, 1144-1157.

Wong, E.S., Tan, J.M., Soong, W.E., Hussein, K., Nukina, N., Dawson, V.L., Dawson, T.M., Cuervo, A.M., and Lim, K.L. (2008). Autophagy-mediated clearance of aggresomes is not a universal phenomenon. Human molecular genetics 17, 2570-2582.

Wu, X., Eder, P., Chang, B., and Molkentin, J.D. (2010). TRPC channels are necessary mediators of pathologic cardiac hypertrophy. Proceedings of the National Academy of Sciences of the United States of America 107, 7000-7005.

Xu, X., Meiler, S.E., Zhong, T.P., Mohideen, M., Crossley, D.A., Burggren, W.W., and Fishman, M.C. (2002). Cardiomyopathy in zebrafish due to mutation in an alternatively spliced exon of titin. Nature genetics 30, 205-209.

Yamamoto, A., and Simonsen, A. (2011). The elimination of accumulated and aggregated proteins: a role for aggrephagy in neurodegeneration. Neurobiology of disease 43, 17-28.

Yoruk, B., Gillers, B.S., Chi, N.C., and Scott, I.C. (2012). Ccm3 functions in a manner distinct from Ccm1 and Ccm2 in a zebrafish model of CCM vascular disease. Developmental biology 362, 121-131.

Yozzo, K.L., Isales, G.M., Raftery, T.D., and Volz, D.C. (2013). High-content screening assay for identification of chemicals impacting cardiovascular function in zebrafish embryos. Environmental science & technology 47, 11302-11310.

Zang, L., Shimada, Y., Nishimura, Y., Tanaka, T., and Nishimura, N. (2013). A novel, reliable method for repeated blood collection from aquarium fish. Zebrafish 10, 425-432.

Zhang, H., Landmann, F., Zahreddine, H., Rodriguez, D., Koch, M., and Labouesse, M. (2011). A tension-induced mechanotransduction pathway promotes epithelial morphogenesis. Nature 471, 99-103.

Zheng, Q., Su, H., Ranek, M.J., and Wang, X. (2011). Autophagy and p62 in cardiac proteinopathy. Circulation research 109, 296-308.

Zhu, J., Wang, K.Z., and Chu, C.T. (2013a). After the banquet: mitochondrial biogenesis, mitophagy, and cell survival. Autophagy 9, 1663-1676.

Zhu, K., Jiao, H., Li, S., Cao, H., Galson, D.L., Zhao, Z., Zhao, X., Lai, Y., Fan, J., Im, H.J., et al. (2013b). ATF4 promotes bone angiogenesis by increasing VEGF expression and release in the bone environment. Journal of bone and mineral research : the official journal of the American Society for Bone and Mineral Research 28, 1870-1884.

Zu, Y., Tong, X., Wang, Z., Liu, D., Pan, R., Li, Z., Hu, Y., Luo, Z., Huang, P., Wu, Q., et al. (2013). TALEN-mediated precise genome modification by homologous recombination in zebrafish. Nature methods 10, 329-331.

Appendix

Appendix 1:

desma knock-out fish mRNA sequencing results

Tables listing the genes found to be down-regulated (red) and up-regulated (green) in the mRNA sequencing experience performed on three *desma*$^{sa5-/-}$ and *desma*$^{sa5+/+}$ embryos pools. (See Results section I/C.1))

Ensembl gene id	Gene name	Description	log2 (KO/Ctrl)	Adjusted p-value
ENSDARG00000070822	cnp	2',3'-cyclic nucleotide 3' phosphodiesterase	-5,23	4,32E-49
ENSDARG00000087345	CABZ01059415.2	Uncharacterized protein	-4,08	1,06E-41
ENSDARG00000052207	c3c	complement component c3c	-2,38	2,99E-32
ENSDARG00000025074	CABZ01059390.1	Uncharacterized protein	-1,66	4,11E-29
ENSDARG00000095643	si:dkey-253d23.3	si:dkey-253d23.3	-4,00	1,16E-22
ENSDARG00000093002	si:dkey-2j6.5	si:dkey-2j6.5	-3,71	3,84E-20
ENSDARG00000017299	fabp11a	fatty acid binding protein 11a	-3,92	1,56E-19
ENSDARG00000059786	CABZ01059408.1	Uncharacterized protein	-3,69	2,69E-19
ENSDARG00000056499	ca6	carbonic anhydrase VI	-1,32	3,81E-17
ENSDARG00000093674	si:dkeyp-80d11.4	si:dkeyp-80d11.4	-3,51	3,08E-16
ENSDARG00000009890	CR936442.1	Uncharacterized protein	-2,84	6,04E-15
ENSDARG00000079762	si:dkey-253d23.4	si:dkey-253d23.4	-3,41	1,66E-14
ENSDARG00000058656	desma	desmin a	-2,79	2,96E-14
ENSDARG00000011410	AADAT	aminoadipate aminotransferase	-2,02	6,94E-14
ENSDARG00000087359	c3b	complement component c3b	-2,59	7,85E-14
ENSDARG00000091235	CABZ01015525.1	Uncharacterized protein	-3,12	3,29E-13
ENSDARG00000095478	si:dkey-70b24.5	si:dkey-70b24.5	-3,07	8,88E-12
ENSDARG00000089749	aqp8b	aquaporin 8b	-2,97	1,03E-10
ENSDARG00000013371	isoc2	isochorismatase domain containing 2	-1,25	1,11E-10
ENSDARG00000093367	si:ch1073-272j17.3	si:ch1073-272j17.3	-2,82	1,96E-10
ENSDARG00000058873	PTPDC1 (2 of 2)	protein tyrosine phosphatase domain containing 1	-1,53	8,19E-09
ENSDARG00000031277	BX005389.1	Uncharacterized protein	-2,08	9,61E-09
ENSDARG00000096222	si:ch211-245n8.4	si:ch211-245n8.4	-2,41	1,93E-08
ENSDARG00000094175	si:dkey-29p23.3	si:dkey-29p23.3	-2,69	1,94E-08
ENSDARG00000096107	si:ch211-187d1.1	si:ch211-187d1.1	-2,52	2,13E-08
ENSDARG00000092349	si:ch211-215p11.5	si:ch211-215p11.5	-2,31	2,13E-08
ENSDARG00000005578	ugp2a	UDP-glucose pyrophosphorylase 2a	-2,49	2,55E-08
ENSDARG00000093019	si:dkey-83k24.5	si:dkey-83k24.5	-2,37	2,60E-08
ENSDARG00000076981	zgc:198329	zgc:198329	-2,59	3,08E-08
ENSDARG00000076953	CR388416.1	Uncharacterized protein	-2,41	1,04E-07

Ensembl gene id	Gene name	Description	log2 (KO/Ctrl)	Adjusted p-value
ENSDARG00000086404	CR524823.2	Uncharacterized protein	-2,02	1,14E-07
ENSDARG00000062263	ARHGAP17 (2 of 3)	Rho GTPase activating protein 17	-2,56	1,35E-07
ENSDARG00000093402	si:dkey-286j17.4	si:dkey-286j17.4	-2,54	1,35E-07
ENSDARG00000076224	si:dkey-11f4.16	si:dkey-11f4.16	-2,37	1,42E-07
ENSDARG00000075951	CABZ01072534.1	Uncharacterized protein	-2,15	3,83E-07
ENSDARG00000092712	si:dkeyp-87e3.3	si:dkeyp-87e3.3	-1,78	3,83E-07
ENSDARG00000095993	si:dkey-29j8.5	si:dkey-29j8.5	-2,12	6,59E-07
ENSDARG00000092243	si:ch211-163b2.2	si:ch211-163b2.2	-2,41	1,06E-06
ENSDARG00000019045	WU:FC32F04	Uncharacterized protein	-2,29	1,62E-06
ENSDARG00000095201	ZNF70 (4 of 6)	zinc finger protein 70	-1,59	1,87E-06
ENSDARG00000086254	HHLA2 (1 of 4)	HERV-H LTR-associating 2	-1,94	4,87E-06
ENSDARG00000096226	si:dkeyp-85d8.6	si:dkeyp-85d8.6	-2,24	5,38E-06
ENSDARG00000090560	mfap5	microfibrillar associated protein 5	-1,72	5,82E-06
ENSDARG00000054447	SLC29A1 (1 of 2)	solute carrier family 29 (equilibrative nucleoside transporter), member 1	-2,08	8,98E-06
ENSDARG00000092620	CR382372.1	Uncharacterized protein	-2,21	1,31E-05
ENSDARG00000045835	si:dkey-14d8.6	si:dkey-14d8.6	-2,16	1,37E-05
ENSDARG00000077405	si:ch211-116m6.3	si:ch211-116m6.3	-1,95	1,55E-05
ENSDARG00000095055	si:ch211-205a14.1	si:ch211-205a14.1	-2,22	1,55E-05
ENSDARG00000087102	CU929175.1	Uncharacterized protein	-1,85	1,63E-05
ENSDARG00000096206	si:ch211-207e19.15	si:ch211-207e19.15	-2,13	1,86E-05
ENSDARG00000071622	CABZ01046433.1	Uncharacterized protein	-2,21	2,04E-05
ENSDARG00000057726	znf185	zinc finger protein 185 (LIM domain)	-2,09	3,39E-05
ENSDARG00000093300	si:dkey-18f7.2	si:dkey-18f7.2	-1,60	3,75E-05
ENSDARG00000096200	si:dkeyp-66a7.1	si:dkeyp-66a7.1	-1,21	4,76E-05
ENSDARG00000089296	si:dkey-240n22.6	si:dkey-240n22.6	-2,05	7,85E-05
ENSDARG00000075524	CABZ01044023.1	Uncharacterized protein	-2,06	1,24E-04
ENSDARG00000091201	CABZ01085626.1	Uncharacterized protein	-1,11	1,63E-04
ENSDARG00000022013	lama2	laminin, alpha 2	-1,98	1,75E-04
ENSDARG00000019318	CR354540.2	Uncharacterized protein	-1,78	1,75E-04
ENSDARG00000095139	si:dkey-178o8.2	si:dkey-178o8.2	-2,04	1,75E-04

Ensembl gene id	Gene name	Description	log2 (KO/Ctrl)	Adjusted p-value
ENSDARG00000087318	zgc:174688	zgc:174688	-1,86	1,75E-04
ENSDARG00000058672	NUGGC (3 of 4)	nuclear GTPase, germinal center associated	-1,77	1,90E-04
ENSDARG00000078114	CFP (2 of 2)	complement factor properdin	-1,04	2,23E-04
ENSDARG00000091715	si:dkey-162h11.2	si:dkey-162h11.2	-1,85	2,45E-04
ENSDARG00000079031	si:ch211-22d5.2	si:ch211-22d5.2	-1,42	2,46E-04
ENSDARG00000092992	si:ch211-204a13.1	si:ch211-204a13.1	-1,94	2,46E-04
ENSDARG00000019808	evpla	envoplakin a	-1,70	2,58E-04
ENSDARG00000086021	si:dkey-20l4.2	si:dkey-20l4.2	-1,76	2,61E-04
ENSDARG00000042909	lifra	leukemia inhibitory factor receptor alpha a	-1,55	2,73E-04
ENSDARG00000096189	si:dkey-54j5.2	si:dkey-54j5.2	-1,95	2,88E-04
ENSDARG00000092284	si:ch211-76m11.3	si:ch211-76m11.3	-1,79	2,94E-04
ENSDARG00000086540	NUMA1 (3 of 4)	nuclear mitotic apparatus protein 1	-1,87	3,30E-04
ENSDARG00000038669	gbp2	guanylate binding protein 2	-1,64	3,56E-04
ENSDARG00000076461	pcdh1g18	protocadherin 1 gamma 18	-1,90	3,59E-04
ENSDARG00000093392	si:ch211-261n11.9	si:ch211-261n11.9	-1,49	3,60E-04
ENSDARG00000069559	muc13a	mucin 13a, cell surface associated	-1,85	3,78E-04
ENSDARG00000003146	si:dkey-27m7.4	si:dkey-27m7.4	-1,86	3,79E-04
ENSDARG00000077078	zgc:173726	zgc:173726	-1,76	4,11E-04
ENSDARG00000095193	si:dkey-23c22.7	si:dkey-23c22.7	-1,83	4,12E-04
ENSDARG00000091355	FP074874.2	Uncharacterized protein	-1,56	4,41E-04
ENSDARG00000035603	dao.2	D-amino-acid oxidase, tandem duplicate 2	-1,23	5,03E-04
ENSDARG00000093153	si:ch73-268e11.2	si:ch73-268e11.2	-1,75	5,41E-04
ENSDARG00000095126	si:dkey-82i20.2	si:dkey-82i20.2	-1,54	5,41E-04
ENSDARG00000038133	zgc:113411	zgc:113411	-1,15	6,15E-04
ENSDARG00000087864	BX511066.2	Uncharacterized protein	-1,58	6,39E-04
ENSDARG00000090769	si:dkey-51d8.6	si:dkey-51d8.6	-1,41	6,39E-04
ENSDARG00000070845	si:dkey-56d12.4	si:dkey-56d12.4	-1,39	6,84E-04
ENSDARG00000039069	slx4ip	SLX4 interacting protein	-1,33	7,34E-04
ENSDARG00000094565	BX511066.4	Uncharacterized protein	-1,86	9,68E-04
ENSDARG00000013022	si:ch211-59h6.1	si:ch211-59h6.1	-1,32	1,03E-03

Ensembl gene id	Gene name	Description	log2 (KO/Ctrl)	Adjusted p-value
ENSDARG00000089734	CABZ01065246.2	Uncharacterized protein	-1,65	1,03E-03
ENSDARG00000093503	RSF1 (1 of 3)	remodeling and spacing factor 1	-1,53	1,16E-03
ENSDARG00000095694	si:dkey-193i10.3	si:dkey-193i10.3	-1,84	1,28E-03
ENSDARG00000086724	CABZ01020207.1	Uncharacterized protein	-1,15	1,30E-03
ENSDARG00000001972	tpst2	tyrosylprotein sulfotransferase 2	-1,38	1,51E-03
ENSDARG00000092658	si:ch211-204c5.6	si:ch211-204c5.6	-1,18	1,72E-03
ENSDARG00000073932	CABZ01049362.1	Uncharacterized protein	-1,68	1,83E-03
ENSDARG00000044326	BX950188.1	Uncharacterized protein	-1,60	1,95E-03
ENSDARG00000042829	si:dkey-30j22.1	si:dkey-30j22.1	-1,24	1,96E-03
ENSDARG00000087999	si:dkey-286j17.3	si:dkey-286j17.3	-1,73	1,96E-03
ENSDARG00000045254	C24H7orf50	chromosome 7 open reading frame 50	-1,46	2,03E-03
ENSDARG00000087597	si:dkey-51d8.3	si:dkey-51d8.3	-1,77	2,13E-03
ENSDARG00000010415	SIRT4	sirtuin 4	-1,16	2,43E-03
ENSDARG00000027938	rad18	RAD18 homolog (S. cerevisiae)	-1,33	2,67E-03
ENSDARG00000092757	CR407594.2	Uncharacterized protein	-1,67	2,82E-03
ENSDARG00000042090	PLA2G4C (3 of 5)	phospholipase A2, group IVC (cytosolic, calcium-independent)	-1,73	2,86E-03
ENSDARG00000088961	zgc:173619	zgc:173619	-1,64	3,03E-03
ENSDARG00000075062	ptpn22	protein tyrosine phosphatase, non-receptor type 22	-1,44	3,13E-03
ENSDARG00000091871	si:ch211-13o20.3	si:ch211-13o20.3	-1,26	3,51E-03
ENSDARG00000007349	dmrt1	doublesex and mab-3 related transcription factor 1	-1,60	3,78E-03
ENSDARG00000094150	si:ch211-127i16.1	si:ch211-127i16.1	-1,27	4,02E-03
ENSDARG00000054290	acin1a	apoptotic chromatin condensation inducer 1a	-1,24	4,09E-03
ENSDARG00000086586	BX323854.3	Uncharacterized protein	-1,37	4,22E-03
ENSDARG00000079770	BX119910.13	Uncharacterized protein	-1,66	4,45E-03
ENSDARG00000035116	CR847941.1	Uncharacterized protein	-1,52	4,57E-03
ENSDARG00000078193	si:ch211-67e16.3	si:ch211-67e16.3	-1,52	4,59E-03
ENSDARG00000096223	si:dkeyp-35e5.9	si:dkeyp-35e5.9	-1,52	4,64E-03
ENSDARG00000096091	si:dkey-29j8.3	si:dkey-29j8.3	-1,10	4,74E-03
ENSDARG00000088640	BX897726.1	Uncharacterized protein	-1,60	4,95E-03
ENSDARG00000094558	si:dkeyp-53e4.1	si:dkeyp-53e4.1	-1,66	5,05E-03

Ensembl gene id	Gene name	Description	log2 (KO/Ctrl)	Adjusted p-value
ENSDARG00000037819	CR759920.2	Uncharacterized protein	-1,24	5,06E-03
ENSDARG00000027851	zgc:92218	zgc:92218	-1,29	5,26E-03
ENSDARG00000095082	BX571811.2	Uncharacterized protein	-1,13	5,27E-03
ENSDARG00000017038	zgc:152670	zgc:152670	-1,62	5,34E-03
ENSDARG00000093612	si:dkey-92i17.2	si:dkey-92i17.2	-1,43	5,43E-03
ENSDARG00000071449	ITFG3	integrin alpha FG-GAP repeat containing 3	-1,13	5,52E-03
ENSDARG00000082928	SNORA63	Small nucleolar RNA SNORA63	-1,65	5,57E-03
ENSDARG00000095727	si:ch1073-47b13.2	si:ch1073-47b13.2	-1,65	5,64E-03
ENSDARG00000074029	CT573248.1	Uncharacterized protein	-1,66	5,79E-03
ENSDARG00000095717	si:dkey-172k15.6	si:dkey-172k15.6	-1,51	5,92E-03
ENSDARG00000094436	si:ch211-82g18.3	si:ch211-82g18.3	-1,65	6,02E-03
ENSDARG00000077721	knop1	lysine-rich nucleolar protein 1	-1,39	6,17E-03
ENSDARG00000075457	si:dkey-3p4.8	si:dkey-3p4.8	-1,61	6,19E-03
ENSDARG00000089198	CABZ01075275.1	Uncharacterized protein	-1,55	6,20E-03
ENSDARG00000079645	sc:d217	sc:d217	-1,63	6,46E-03
ENSDARG00000075115	BX119910.5	Uncharacterized protein	-1,63	6,74E-03
ENSDARG00000093713	si:dkey-256i11.2	si:dkey-256i11.2	-1,61	7,44E-03
ENSDARG00000035602	dao.1	D-amino-acid oxidase, tandem duplicate 1	-1,21	7,44E-03
ENSDARG00000058140	ttc25	tetratricopeptide repeat domain 25	-1,61	7,44E-03
ENSDARG00000087046	si:ch211-222k6.2	si:ch211-222k6.2	-1,30	7,44E-03
ENSDARG00000095208	si:dkey-30j22.3	si:dkey-30j22.3	-1,43	8,64E-03
ENSDARG00000087510	zgc:173708	zgc:173708	-1,20	8,70E-03
ENSDARG00000086970	C13H10orf71 (2 of 2)	chromosome 10 open reading frame 71	-1,34	8,92E-03
ENSDARG00000068857	gbp4	guanylate binding protein 4	-1,53	9,50E-03
ENSDARG00000076108	zgc:194336	zgc:194336	-1,53	1,02E-02
ENSDARG00000063126	GUSB (1 of 2)	glucuronidase, beta	-1,39	1,05E-02
ENSDARG00000086478	si:dkeyp-87d1.1	si:dkeyp-87d1.1	-1,54	1,09E-02
ENSDARG00000075818	dok2	docking protein 2	-1,58	1,09E-02
ENSDARG00000074348	BX119910.4	Uncharacterized protein	-1,50	1,10E-02
ENSDARG00000078399	ACSL6	Uncharacterized protein	-1,28	1,15E-02

Ensembl gene id	Gene name	Description	log2 (KO/Ctrl)	Adjusted p-value
ENSDARG00000041199	alg12	asparagine-linked glycosylation 12 homolog (yeast, alpha-1,6-mannosyltransferase)	-1,01	1,15E-02
ENSDARG00000079729	fbn2a	fibrillin 2a	-1,38	1,21E-02
ENSDARG00000068841	si:dkey-29p23.1	si:dkey-29p23.1	-1,40	1,22E-02
ENSDARG00000054921	wu:fd58b11	wu:fd58b11	-1,43	1,22E-02
ENSDARG00000096703	si:dkey-1h6.8	si:dkey-1h6.8	-1,23	1,24E-02
ENSDARG00000092378	si:ch211-222g23.5	si:ch211-222g23.5	-1,54	1,33E-02
ENSDARG00000088348	BX324210.1	Uncharacterized protein	-1,45	1,36E-02
ENSDARG00000095047	si:dkey-85k15.4	si:dkey-85k15.4	-1,53	1,36E-02
ENSDARG00000078951	BX119910.11	Uncharacterized protein	-1,50	1,36E-02
ENSDARG00000094272	map3k19	mitogen-activated protein kinase kinase kinase 19	-1,28	1,38E-02
ENSDARG00000088069	CR759879.1	Uncharacterized protein	-1,50	1,42E-02
ENSDARG00000075848	si:ch211-267j24.1	si:ch211-267j24.1	-1,44	1,46E-02
ENSDARG00000087327	cbx8a	chromobox homolog 8a (Pc class homolog, Drosophila)	-1,50	1,53E-02
ENSDARG00000091987	CU929205.1	Uncharacterized protein	-1,13	1,64E-02
ENSDARG00000078276	COLGALT1 (3 of 3)	collagen beta(1-O)galactosyltransferase 1	-1,46	1,68E-02
ENSDARG00000079292	CU633740.2	Uncharacterized protein	-1,38	1,79E-02
ENSDARG00000086278	CABZ01050664.1	Uncharacterized protein	-1,24	1,79E-02
ENSDARG00000096246	si:ch73-338a16.3	si:ch73-338a16.3	-1,46	1,81E-02
ENSDARG00000045240	cebp1	CCAAT/enhancer binding protein (C/EBP) 1	-1,35	1,88E-02
ENSDARG00000088432	si:dkey-162h11.3	si:dkey-162h11.3	-1,46	1,89E-02
ENSDARG00000013685	vsig8b	V-set and immunoglobulin domain containing 8b	-1,08	2,01E-02
ENSDARG00000078753	BX571813.1	Uncharacterized protein	-1,46	2,02E-02
ENSDARG00000077539	BX119910.8	Uncharacterized protein	-1,44	2,03E-02
ENSDARG00000037843	TOR4A (1 of 4)	torsin family 4, member A	-1,44	2,10E-02
ENSDARG00000093317	si:ch211-209j10.6	si:ch211-209j10.6	-1,40	2,10E-02
ENSDARG00000096094	si:dkey-222o15.4	si:dkey-222o15.4	-1,49	2,12E-02
ENSDARG00000091951	NUGGC (1 of 4)	nuclear GTPase, germinal center associated	-1,42	2,12E-02
ENSDARG00000032640	PDXK (3 of 3)	pyridoxal (pyridoxine, vitamin B6) kinase	-1,48	2,12E-02
ENSDARG00000094396	si:dkey-202i12.5	si:dkey-202i12.5	-1,35	2,15E-02

Ensembl gene id	Gene name	Description	log2 (KO/Ctrl)	Adjusted p-value
ENSDARG00000088337	wu:fc34e06	wu:fc34e06	-1,45	2,20E-02
ENSDARG00000006372	ugt5c2	UDP glucuronosyltransferase 5 family, polypeptide C2	-1,48	2,23E-02
ENSDARG00000044212	CR385063.1	Uncharacterized protein	-1,46	2,23E-02
ENSDARG00000093099	si:ch211-119c24.1	si:ch211-119c24.1	-1,35	2,23E-02
ENSDARG00000088137	CABZ01049802.1	Uncharacterized protein	-1,09	2,29E-02
ENSDARG00000073985	pctp	phosphatidylcholine transfer protein	-1,13	2,31E-02
ENSDARG00000095215	si:ch1073-525h16.1	si:ch1073-525h16.1	-1,29	2,43E-02
ENSDARG00000089322	GRAMD2 (2 of 2)	GRAM domain containing 2	-1,39	2,54E-02
ENSDARG00000086764	MDC1	mediator of DNA-damage checkpoint 1	-1,35	2,58E-02
ENSDARG00000086215	GPR156	G protein-coupled receptor 156	-1,00	2,59E-02
ENSDARG00000093521	B3GNT3 (1 of 4)	UDP-GlcNAc:betaGal beta-1,3-N-acetylglucosaminyltransferase 3	-1,28	2,61E-02
ENSDARG00000093220	BX571878.2	Uncharacterized protein	-1,44	2,72E-02
ENSDARG00000095872	si:ch211-209l18.5	si:ch211-209l18.5	-1,24	2,78E-02
ENSDARG00000096527	si:dkey-18j14.5	si:dkey-18j14.5	-1,31	2,78E-02
ENSDARG00000071589	ZNF22	zinc finger protein 22	-1,40	2,80E-02
ENSDARG00000092131	si:ch211-219f7.3	si:ch211-219f7.3	-1,31	2,81E-02
ENSDARG00000087195	RORC	RAR-related orphan receptor C	-1,40	2,81E-02
ENSDARG00000091955	BX663613.3	Uncharacterized protein	-1,40	2,81E-02
ENSDARG00000095772	si:dkey-11o1.2	si:dkey-11o1.2	-1,40	2,91E-02
ENSDARG00000095569	CABZ01059309.2	Uncharacterized protein	-1,32	2,98E-02
ENSDARG00000011809	mical1	microtubule associated monooxygenase, calponin and LIM domain containing 1	-1,13	3,05E-02
ENSDARG00000075856	si:dkey-257e4.2	si:dkey-257e4.2	-1,42	3,07E-02
ENSDARG00000093181	si:dkey-95f11.6	si:dkey-95f11.6	-1,43	3,11E-02
ENSDARG00000086897	si:dkey-7i4.1	si:dkey-7i4.1	-1,37	3,24E-02
ENSDARG00000094459	si:dkey-16p19.10	si:dkey-16p19.10	-1,38	3,32E-02
ENSDARG00000078023	mia2	melanoma inhibitory activity 2	-1,29	3,32E-02
ENSDARG00000026359	PBLD (2 of 2)	phenazine biosynthesis-like protein domain containing	-1,01	3,32E-02
ENSDARG00000044380	rbmx2	RNA binding motif protein, X-linked 2	-1,32	3,41E-02

Ensembl gene id	Gene name	Description	log2 (KO/Ctrl)	Adjusted p-value
ENSDARG00000075217	TDRD12	tudor domain containing 12	-1,33	3,44E-02
ENSDARG00000041685	BX663520.1	Uncharacterized protein	-1,24	3,48E-02
ENSDARG00000083266	SNORD12	Small nucleolar SNORD12/SNORD106	-1,29	3,48E-02
ENSDARG00000091965	si:dkey-231p15.1	si:dkey-231p15.1	-1,34	3,53E-02
ENSDARG00000086775	top1	topoisomerase (DNA) I	-1,12	3,63E-02
ENSDARG00000075274	CABZ01090021.1	Uncharacterized protein	-1,30	3,64E-02
ENSDARG00000090947	si:dkey-29j8.1	si:dkey-29j8.1	-1,36	3,72E-02
ENSDARG00000075990	acap3a	ArfGAP with coiled-coil, ankyrin repeat and PH domains 3a	-1,11	3,82E-02
ENSDARG00000095714	si:dkeyp-33e11.2	si:dkeyp-33e11.2	-1,19	4,07E-02
ENSDARG00000094489	si:dkey-58f10.6	si:dkey-58f10.6	-1,38	4,16E-02
ENSDARG00000092551	si:dkey-56e3.2	si:dkey-56e3.2	-1,34	4,26E-02
ENSDARG00000054898	ms4a17a.17	membrane-spanning 4-domains, subfamily A, member 17A.17	-1,32	4,27E-02
ENSDARG00000091087	BX936371.1	Uncharacterized protein	-1,36	4,28E-02
ENSDARG00000089643	MCAM (2 of 3)	melanoma cell adhesion molecule	-1,14	4,29E-02
ENSDARG00000025608	casp6l1	caspase 6, apoptosis-related cysteine peptidase, like 1	-1,11	4,39E-02
ENSDARG00000021149	cbr1l	carbonyl reductase 1-like	-1,11	4,58E-02
ENSDARG00000071667	si:dkey-222f2.7	si:dkey-222f2.7	-1,37	4,58E-02
ENSDARG00000089441	si:ch211-105c13.3	si:ch211-105c13.3	-1,24	4,58E-02
ENSDARG00000018061	neil1	nei endonuclease VIII-like 1 (E. coli)	-1,21	4,66E-02
ENSDARG00000094926	si:dkey-176f19.6	si:dkey-176f19.6	-1,09	4,78E-02
ENSDARG00000076737	CR388013.1	Uncharacterized protein	-1,34	4,85E-02
ENSDARG00000043198	si:rp71-1i20.2	si:rp71-1i20.2	-1,09	4,85E-02
ENSDARG00000053311	TESPA1	thymocyte expressed, positive selection associated 1	-1,09	4,94E-02
ENSDARG00000096708	ZNF70 (2 of 6)	zinc finger protein 70	-1,33	4,94E-02

Ensembl gene id	Gene name	Description	log2 (KO/Ctrl)	Adjusted p-value
ENSDARG00000088959	pdxka	pyridoxal (pyridoxine, vitamin B6) kinase a	2,50	7,05E-29
ENSDARG00000076010	twist1b	twist1b	3,13	5,19E-24
ENSDARG00000088089	BX005073.1	Uncharacterized protein	3,85	1,90E-23
ENSDARG00000057365	zgc:112263	zgc:112263	2,68	5,80E-18
ENSDARG00000093349	si:ch211-141e20.2	si:ch211-141e20.2	3,59	7,48E-17
ENSDARG00000088335	LRRC47 (1 of 2)	leucine rich repeat containing 47	3,44	2,07E-15
ENSDARG00000078302	DBC1	deleted in bladder cancer 1	1,81	1,73E-13
ENSDARG00000052039	caspb	caspase b	3,02	2,60E-11
ENSDARG00000095522	si:dkey-71b5.3	si:dkey-71b5.3	2,89	4,84E-10
ENSDARG00000009850	KIF3A (2 of 2)	kinesin family member 3A	2,85	2,46E-09
ENSDARG00000025468	bnip3la	BCL2/adenovirus E1B interacting protein 3-like a	2,30	1,99E-08
ENSDARG00000038378	sagb	S-antigen; retina and pineal gland (arrestin) b	2,26	2,13E-08
ENSDARG00000016187	cxxc1l	CXXC finger 1, like	1,91	1,99E-07
ENSDARG00000032577	clcn6	chloride channel 6	1,67	2,77E-07
ENSDARG00000052609	si:ch211-274f20.4	si:ch211-274f20.4	2,46	3,59E-07
ENSDARG00000017489	zgc:123068	zgc:123068	2,42	1,06E-06
ENSDARG00000093323	si:ch211-114l13.1	si:ch211-114l13.1	2,44	1,07E-06
ENSDARG00000017799	tgm1	transglutaminase 1, K polypeptide	1,33	1,44E-06
ENSDARG00000028236	COL27A1 (2 of 2)	collagen, type XXVII, alpha 1	1,12	2,14E-06
ENSDARG00000092801	si:dkey-71b5.6	si:dkey-71b5.6	2,36	2,86E-06
ENSDARG00000031046	nr1h5	nuclear receptor subfamily 1, group H, member 5	1,48	2,94E-06
ENSDARG00000029230	pnp4b	purine nucleoside phosphorylase 4b	1,55	4,50E-06
ENSDARG00000068963	zgc:158862	zgc:158862	2,28	8,81E-06
ENSDARG00000089095	MRPS12 (1 of 2)	mitochondrial ribosomal protein S12	1,76	2,65E-05
ENSDARG00000038439	fabp10a	fatty acid binding protein 10a, liver basic	1,88	4,15E-05
ENSDARG00000038974	DPYSL2 (1 of 2)	dihydropyrimidinase-like 2	1,17	4,50E-05
ENSDARG00000067691	MRPS30 (2 of 2)	mitochondrial ribosomal protein S30	1,58	8,08E-05
ENSDARG00000017532	KIF25	kinesin family member 25	1,69	1,24E-04
ENSDARG00000095325	si:dkey-49n23.3	si:dkey-49n23.3	1,57	1,90E-04
ENSDARG00000092373	si:dkey-16n15.3	si:dkey-16n15.3	1,51	2,23E-04

Ensembl gene id	Gene name	Description	log2 (KO/Ctrl)	Adjusted p-value
ENSDARG00000030215	matn1	matrilin 1	1,69	2,85E-04
ENSDARG00000079665	GPR158 (1 of 2)	G protein-coupled receptor 158	1,40	3,65E-04
ENSDARG00000005780	npy8br	neuropeptide Y receptor Y8b	1,54	4,51E-04
ENSDARG00000075676	si:ch1073-154c4.1	si:ch1073-154c4.1	1,13	5,41E-04
ENSDARG00000079443	VIP (1 of 2)	vasoactive intestinal peptide	1,90	6,34E-04
ENSDARG00000002204	hspb11	heat shock protein, alpha-crystallin-related, b11	1,15	7,34E-04
ENSDARG00000092971	KMT2C (2 of 4)	lysine (K)-specific methyltransferase 2C	1,73	1,19E-03
ENSDARG00000059945	SV2A	synaptic vesicle glycoprotein 2A	1,32	1,22E-03
ENSDARG00000090428	ctrb1	chymotrypsinogen B1	1,84	1,26E-03
ENSDARG00000094187	si:dkey-270b7.5	si:dkey-270b7.5	1,50	1,27E-03
ENSDARG00000008849	ptprq	protein tyrosine phosphatase, receptor type, Q	1,63	1,29E-03
ENSDARG00000091408	SOGA2	SOGA family member 2	1,10	1,45E-03
ENSDARG00000018743	scamp5	secretory carrier membrane protein 5	1,01	1,46E-03
ENSDARG00000056248	wu:fb15e04	wu:fb15e04	1,64	1,51E-03
ENSDARG00000012609	hpx	hemopexin	1,56	1,63E-03
ENSDARG00000078674	hspb9	heat shock protein, alpha-crystallin-related, 9	1,59	1,82E-03
ENSDARG00000040435	SLC6A11	solute carrier family 6 (neurotransmitter transporter, GABA), member 11	1,24	2,03E-03
ENSDARG00000016789	zgc:152891	zgc:152891	1,54	2,10E-03
ENSDARG00000094380	zzef1	zinc finger, ZZ-type with EF hand domain 1	1,57	2,38E-03
ENSDARG00000060877	edil3b	EGF-like repeats and discoidin I-like domains 3b	1,48	2,38E-03
ENSDARG00000061040	pum2	pumilio homolog 2 (Drosophila)	1,54	2,39E-03
ENSDARG00000037192	zgc:113364	zgc:113364	1,77	2,42E-03
ENSDARG00000079065	ANKRD50 (2 of 2)	ankyrin repeat domain 50	1,46	2,42E-03
ENSDARG00000044355	CT030712.1	Uncharacterized protein	1,76	2,44E-03
ENSDARG00000069017	elnb	elastin b	1,39	2,86E-03
ENSDARG00000090638	GP9	glycoprotein IX (platelet)	1,53	2,98E-03
ENSDARG00000069603	CR848664.2	Uncharacterized protein	1,37	3,30E-03
ENSDARG00000004291	hecw1	HECT, C2 and WW domain containing E3 ubiquitin protein ligase 1	1,05	3,43E-03
ENSDARG00000091385	zgc:165409	zgc:165409	1,65	3,43E-03
ENSDARG00000093604	si:dkey-242k1.6	si:dkey-242k1.6	1,63	3,55E-03

Ensembl gene id	Gene name	Description	log2 (KO/Ctrl)	Adjusted p-value
ENSDARG00000076640	NFATC2 (1 of 2)	nuclear factor of activated T-cells, cytoplasmic, calcineurin-dependent 2	1,50	3,94E-03
ENSDARG00000077360	zgc:173593	zgc:173593	1,43	4,02E-03
ENSDARG00000007344	tcap	titin-cap (telethonin)	1,58	4,35E-03
ENSDARG00000043902	gabrr1	gamma-aminobutyric acid (GABA) receptor, rho 1	1,61	4,41E-03
ENSDARG00000036619	CABZ01084569.1	Uncharacterized protein	1,15	4,51E-03
ENSDARG00000063362	CABZ01084538.1	Uncharacterized protein	1,26	4,57E-03
ENSDARG00000058987	GGA3 (1 of 2)	golgi-associated, gamma adaptin ear containing, ARF binding protein 3	1,15	4,60E-03
ENSDARG00000092379	si:dkeyp-51b9.3	si:dkeyp-51b9.3	1,69	4,63E-03
ENSDARG00000011113	chrna10	cholinergic receptor, nicotinic, alpha 10	1,67	4,84E-03
ENSDARG00000032820	rxfp2b	relaxin/insulin-like family peptide receptor 2b	1,67	4,95E-03
ENSDARG00000071488	CABZ01041804.1	Uncharacterized protein	1,23	5,47E-03
ENSDARG00000052188	ZNF541	zinc finger protein 541	1,60	5,52E-03
ENSDARG00000087437	crygn1	crystallin, gamma N1	1,26	5,54E-03
ENSDARG00000087082	CNGB3 (2 of 2)	cyclic nucleotide gated channel beta 3	1,45	6,17E-03
ENSDARG00000062661	abca4b	ATP-binding cassette, sub-family A (ABC1), member 4b	1,38	6,82E-03
ENSDARG00000057408	CABZ01067232.1	Uncharacterized protein	1,19	6,82E-03
ENSDARG00000063539	slc25a15a	solute carrier family 25 (mitochondrial carrier; ornithine transporter) member 15a	1,02	6,90E-03
ENSDARG00000036272	gcgrb	glucagon receptor b	1,01	7,38E-03
ENSDARG00000074212	SLC5A10	solute carrier family 5 (sodium/glucose cotransporter), member 10	1,33	7,67E-03
ENSDARG00000095915	col6a3	collagen, type VI, alpha 3	1,24	8,63E-03
ENSDARG00000063715	CR376794.1	Uncharacterized protein	1,06	8,70E-03
ENSDARG00000025428	socs3a	suppressor of cytokine signaling 3a	1,29	8,70E-03
ENSDARG00000074471	vps39	vacuolar protein sorting 39 homolog (S. cerevisiae)	1,31	9,12E-03
ENSDARG00000080018	kif16bb	kinesin family member 16Bb	1,09	9,24E-03
ENSDARG00000011983	zgc:136908	zgc:136908	1,28	9,36E-03
ENSDARG00000079217	bbs9	Bardet-Biedl syndrome 9	1,18	9,50E-03
ENSDARG00000092875	si:dkey-264b2.3	si:dkey-264b2.3	1,32	9,55E-03
ENSDARG00000089063	lactbl1a	lactamase, beta-like 1a	1,52	9,81E-03
ENSDARG00000014745	epd	ependymin	1,29	1,02E-02
ENSDARG00000096240	si:ch1073-299b15.4	si:ch1073-299b15.4	1,34	1,04E-02

Ensembl gene id	Gene name	Description	log2 (KO/Ctrl)	Adjusted p-value
ENSDARG00000088268	OTOS	otospiralin	1,10	1,05E-02
ENSDARG00000089986	TP53INP2	tumor protein p53 inducible nuclear protein 2	1,28	1,09E-02
ENSDARG00000086345	cux2b	cut-like homeobox 2b	1,24	1,09E-02
ENSDARG00000026666	mthfd2	methylenetetrahydrofolate dehydrogenase (NADP+ dependent) 2, methenyltetrahydrofolate cyclohydrolase	1,01	1,20E-02
ENSDARG00000086060	BX548021.2	Uncharacterized protein	1,52	1,24E-02
ENSDARG00000058362	BX649391.1	Uncharacterized protein	1,56	1,24E-02
ENSDARG00000088687	zgc:165347	zgc:165347	1,48	1,24E-02
ENSDARG00000009087	cd74a	CD74 molecule, major histocompatibility complex, class II invariant chain a	1,51	1,24E-02
ENSDARG00000087513	CABZ01048675.1	Uncharacterized protein	1,51	1,29E-02
ENSDARG00000069827	crygm2d11	crystallin, gamma M2d11	1,55	1,32E-02
ENSDARG00000058103	glra4b	glycine receptor, alpha 4b	1,51	1,33E-02
ENSDARG00000093926	si:dkey-71b5.2	si:dkey-71b5.2	1,45	1,33E-02
ENSDARG00000063713	SYNGAP1 (1 of 2)	synaptic Ras GTPase activating protein 1	1,12	1,41E-02
ENSDARG00000058695	ddr2b	discoidin domain receptor tyrosine kinase 2b	1,26	1,53E-02
ENSDARG00000063564	fam168a	family with sequence similarity 168, member A	1,05	1,53E-02
ENSDARG00000007553	opn4.1	opsin 4.1	1,07	1,56E-02
ENSDARG00000076620	BX255969.1	Uncharacterized protein	1,05	1,56E-02
ENSDARG00000074217	si:dkey-188i13.6	si:dkey-188i13.6	1,52	1,62E-02
ENSDARG00000025672	antxr1a	anthrax toxin receptor 1a	1,32	1,69E-02
ENSDARG00000002193	rho	rhodopsin	1,50	1,88E-02
ENSDARG00000070780	rln3a	relaxin 3a	1,48	1,95E-02
ENSDARG00000055014	CR558302.2	Uncharacterized protein	1,18	1,95E-02
ENSDARG00000089035	CABZ01080224.1	Uncharacterized protein	1,48	2,02E-02
ENSDARG00000074441	gp1bb	glycoprotein Ib (platelet), beta polypeptide	1,15	2,06E-02
ENSDARG00000055192	zgc:136930	zgc:136930	1,23	2,10E-02
ENSDARG00000015025	nadl1.1	neural adhesion molecule L1.1	1,40	2,12E-02
ENSDARG00000077537	nudt19	nudix (nucleoside diphosphate linked moiety X)-type motif 19	1,41	2,16E-02
ENSDARG00000004227	pde3a	phosphodiesterase 3A, cGMP-inhibited	1,08	2,20E-02
ENSDARG00000074976	dckl1b	doublecortin-like kinase 1b	1,07	2,21E-02

Ensembl gene id	Gene name	Description	log2 (KO/Ctrl)	Adjusted p-value
ENSDARG00000055518	pygma	phosphorylase, glycogen (muscle) A	1,01	2,33E-02
ENSDARG00000095662	si:dkey-54i3.2	si:dkey-54i3.2	1,41	2,53E-02
ENSDARG00000076632	zdhhc12a	zinc finger, DHHC-type containing 12a	1,31	2,54E-02
ENSDARG00000061909	CU855896.1	Uncharacterized protein	1,36	2,58E-02
ENSDARG00000070543	grin2ab	glutamate receptor, ionotropic, N-methyl D-aspartate 2A, b	1,08	2,59E-02
ENSDARG00000063050	rc3h2	ring finger and CCCH-type domains 2	1,16	2,72E-02
ENSDARG00000045665	FAT4	FAT atypical cadherin 4	1,18	2,76E-02
ENSDARG00000079971	CABZ01080134.1	Uncharacterized protein	1,37	2,77E-02
ENSDARG00000074320	KCNAB3	potassium voltage-gated channel, shaker-related subfamily, beta member 3	1,39	2,80E-02
ENSDARG00000068919	rad51c	rad51 homolog C (S. cerevisiae)	1,02	2,80E-02
ENSDARG00000070894	abhd6b	abhydrolase domain containing 6b	1,17	2,80E-02
ENSDARG00000063182	RC3H1 (1 of 2)	ring finger and CCCH-type domains 1	1,18	2,91E-02
ENSDARG00000057108	serpine3	serpin peptidase inhibitor, clade E (nexin, plasminogen activator inhibitor type 1), member 3	1,35	3,07E-02
ENSDARG00000019532	fads2	fatty acid desaturase 2	1,00	3,32E-02
ENSDARG00000078088	CR339051.1	Uncharacterized protein	1,12	3,32E-02
ENSDARG00000045811	BX897714.3	Uncharacterized protein	1,38	3,32E-02
ENSDARG00000074378	junba	jun B proto-oncogene a	1,40	3,32E-02
ENSDARG00000055331	aldh9a1a.2	aldehyde dehydrogenase 9 family, member A1a, tandem duplicate 2	1,02	3,48E-02
ENSDARG00000027236	rs1	retinoschisis (X-linked, juvenile) 1	1,35	3,55E-02
ENSDARG00000075754	mri1	methylthioribose-1-phosphate isomerase homolog (S. cerevisiae)	1,15	3,66E-02
ENSDARG00000061478	igf2bp1	insulin-like growth factor 2 mRNA binding protein 1	1,21	3,67E-02
ENSDARG00000060202	si:dkey-266h18.3	si:dkey-266h18.3	1,37	3,76E-02
ENSDARG00000093131	si:ch211-57f7.7	si:ch211-57f7.7	1,39	3,78E-02
ENSDARG00000079569	CR385022.1	Uncharacterized protein	1,17	3,79E-02
ENSDARG00000026611	socs3b	suppressor of cytokine signaling 3b	1,12	3,82E-02
ENSDARG00000067507	kctd8	potassium channel tetramerisation domain containing 8	1,21	3,87E-02
ENSDARG00000071871	GLOD5	glyoxalase domain containing 5	1,21	3,90E-02
ENSDARG00000037084	CPNE7	copine VII	1,32	4,27E-02
ENSDARG00000088660	CABZ01075689.1	Uncharacterized protein	1,31	4,28E-02

Ensembl gene id	Gene name	Description	log2 (KO/Ctrl)	Adjusted p-value
ENSDARG00000089534	CU693369.1	Uncharacterized protein	1,24	4,28E-02
ENSDARG00000045979	PTGDS (3 of 3)	prostaglandin D2 synthase 21kDa (brain)	1,02	4,29E-02
ENSDARG00000025920	TIAM1 (2 of 2)	T-cell lymphoma invasion and metastasis 1	1,29	4,36E-02
ENSDARG00000078895	fasn	fatty acid synthase	1,37	4,36E-02
ENSDARG00000087980	CABZ01100973.1	Uncharacterized protein	1,24	4,39E-02
ENSDARG00000057292	si:dkey-228d14.8	si:dkey-228d14.8	1,37	4,39E-02
ENSDARG00000019228	mogat2	monoacylglycerol O-acyltransferase 2	1,34	4,44E-02
ENSDARG00000095751	C20H6orf58 (2 of 2)	chromosome 6 open reading frame 58	1,14	4,50E-02
ENSDARG00000088302	CABZ01048021.1	Uncharacterized protein	1,37	4,59E-02
ENSDARG00000030750	FP236824.1	Uncharacterized protein	1,30	4,63E-02
ENSDARG00000002600	pcsk1	proprotein convertase subtilisin/kexin type 1	1,18	4,63E-02
ENSDARG00000026499	ppm1e	protein phosphatase 1E (PP2C domain containing)	1,24	4,63E-02
ENSDARG00000074376	MDGA1	MAM domain containing glycosylphosphatidylinositol anchor 1	1,12	4,71E-02
ENSDARG00000070216	FANCA	Fanconi anemia, complementation group A	1,05	4,85E-02
ENSDARG00000078438	CABZ01109647.1	Uncharacterized protein	1,35	4,98E-02
ENSDARG00000069973	samd12	sterile alpha motif domain containing 12	1,21	4,99E-02

Appendix 2:

Résumé étendu en français

Résumé étendu en français

Introduction

Le poisson-zèbre (*Danio Rerio*) (Figure 1) est maintenant de plus en plus reconnu comme étant un organisme modèle de choix dans le domaine de la génétique humaine. Il représente, en effet, une bonne alternative aux modèles murins et aux approches in vivo. Les recherches sur le système cardiovasculaire bénéficient particulièrement de l'utilisation du poisson-zèbre, à la fois dans le contexte du développement embryonnaire et des pathologies associées. En effet, l'embryon de poisson zèbre offre la possibilité d'adresser les fonctions cardiaques et vasculaires *in vivo* et de manière non-invasive grâce à sa transparence et à la compatibilité de sa taille pour l'imagerie confocale. En parallèle, l'étude du poisson-zèbre a apporté de nouvelles connaissances dans le domaine du développement musculaire (Chong et al., 2009). Comme les muscles (squelettiques et cardiaques) ont la capacité de se régénérer chez le poisson-zèbre, ce dernier est extensivement utilisé pour étudier la régénération musculaire après une blessure ou d'une insuffisance cardiaque (Zhang et al., 2013).

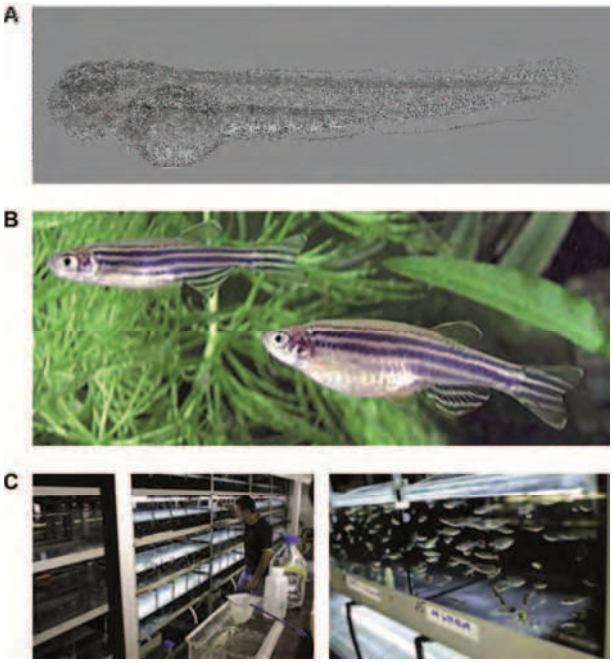

Figure 1: Présentation du poisson-zèbre ou *Danio rerio*
(A) Cliché d'un embryon de poisson-zèbre à 48hpf. (B) Cliché de poissons-zèbre adultes présentant un mâle (en haut) et une femelle (en bas). Source Philippe Mourrain, Stanford Report, 2007. (C) Images de l'animalerie poisson à l'IGBMC. Source: Inserm.

Le poisson-zèbre est désormais de plus en plus utilisé pour l'étude de myopathies et de dystrophies musculaires (Gibbs et al., 2013). Il bénéficie, notamment, de la récente application des technologies de séquençage à haut débit pour l'identification de nouveaux gènes mutés chez des patients

présentant des maladies héréditaires de cause encore inconnue. En effet, ces techniques engendrent le besoin d'un modèle aux modifications géniques rapides pour la validation des gènes candidats. Celles-ci sont possibles dans le poisson grâce à l'utilisation de morpholinos pour la répression de l'expression des gènes candidats, à une mutagénèse et une transgénèse rapides et efficaces et à la possibilité de surexpression de versions humaines mutées de gènes de manière directe dans l'embryon. Ceci permet alors d'étudier, de manière directe et rapide, la pathophysiologie associée à un large panel de mutations génétiques humaines. Enfin, les embryons de poisson-zèbre ont la capacité d'absorber les composants chimiques et les médicaments, de manière directe à partir de leur milieu, ce qui constitue un avantage important pour l'utilisation des animaux modèles générés dans le cadre de criblages chimiques à haut débit.

Dans ce contexte, nous avons alors décidé d'appliquer le large panel d'avantages offert par l'utilisation du poisson-zèbre comme animal modèle pour l'étude de deux maladies génétiques. Dans un premier temps, nous avons décidé d'étudier les myopathies et cardiomyopathies liées à la desmine, qui sont caractérisées par la présence d'agrégats protéiques dans les cellules musculaires des patients. Notre étude se focalise sur les mutations du gène de la desmine lui-même et considère alors deux modèles, de perte et de gain de fonction de la desmine, pour comprendre l'importance respective de la présence des agrégats et de l'absence de desmine fonctionnelle dans l'établissement des phénotypes liés à cette pathologie. Dans un second temps, nous avons généré un modèle de perte de fonction de GCN2 (*eif2ak4*) dans le poisson-zèbre comme modèle de maladie veino-occlusive pulmonaire afin de vérifier la spécificité veineuse des phénotypes associés à la perte de fonction de ce gène.

Projet 1 : Développement de modèles de desminopathies

La desmine fait partie de la famille des filaments intermédiaires et est présente dans les cellules musculaires cardiaques, squelettiques et lisses. Elle y sert d'intégrateur mécanique de la fonction contractile (Boriek, et al.,2001) et son rôle est critique pour le maintien de la structure cellulaire et l'organisation du cytosquelette (Milner, et al.,1996, Li, et al.,1996). La fonction de la desmine a été associée non seulement à un rôle structural, mais aussi à un rôle fonctionnel, servant d'ancrage et participant à de nombreuses voies de signalisation (voir revue, Hnia, Ramspacher et al., 2015, Manuscrit 1 présenté dans le présent manuscrit de thèse). 67 mutations ont été découvertes sur le gène codant pour la desmine (Figure 2) et ont été associées à une myopathie myofibrillaire alors classifiée de desminopathie ou myopathie liée à la desmine.

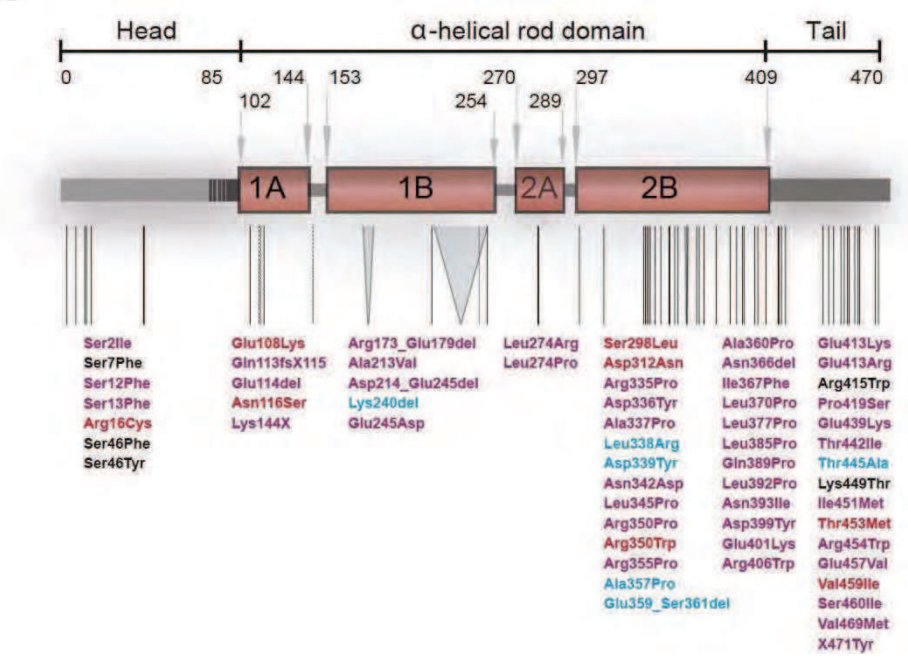

Figure 2: Représentation des mutations identifiées sur le gène de la desmine et à l'origine de desminopathies.

Les mutations identifiées sur le gène de la desmine se trouvent dans tous ses domaines, bien qu'un enrichissement soit visible dans le domaine de l'hélice α 2B et dans la partie C-terminale. Les mutations de la desmine sont présentées en trois groupes, en fonction du phénotype leur correspondant: un phénotype des muscles squelettiques uniquement est représenté en bleu, cardiaque uniquement en rouge et les deux associés, en violet.

La desminopathie fait partie des maladies les plus communes liées aux filaments intermédiaires chez l'homme et se caractérise par la présence d'agrégats intra-sarcoplasmiques contenant de la desmine. Originairement, elle a été caractérisée comme une maladie héréditaire à caractère autosomal dominant ou récessif entrainant une myopathie dilatée des muscles lisses et squelettiques (Goldfarb and Dalakas, 2009). Les phénotypes associés à la desminopathie, sont en fait très variables et comprennent un affaiblissement des muscles squelettiques, généralement d'abord distaux puis proximaux, touchant les membres inférieurs puis supérieurs, des cardiomyopathies, des défauts de conduction cardiaque, une insuffisance respiratoire et des défauts liés aux muscles lisses, en particuliers viscéraux. Une liste grandissante de mutations dans le gène de la desmine a été identifiée pour entrainer spécifiquement des cardiomyopathies liées à la desmine pouvant être de type dilatées, hypertrophiques, restrictives ou arrhythmogéniques du ventricule droit et entrainant des insuffisances cardiaques chroniques. (van Spaendonck-Zwarts, et al., 2011). Les symptômes liés à la desminopathie apparaissent généralement autour de la trentaine.

Les biopsies réalisées sur des patients montrent des fibres musculaires de formes irrégulières contenant des dépôts amorphes ou des inclusions intracellulaires. Une activité enzymatique anormale est souvent observée par coloration et des signes classiques de myopathies, comprenant une variabilité de la taille des fibres, des fibres atrophiées et une localisation centrale des noyaux, peuvent l'accompagner. Des expériences de microscopie électroniques sur biopsies de patients montrent une accumulation de matériel granulo-filamenteux dense dans la région sous-sarcolemmique, inter-

fibrillaire ou péri-nucléaire. Des déformations des disques Z, des structures d'autophagie ainsi qu'un groupement pathologique des mitochondries sont également souvent observés.

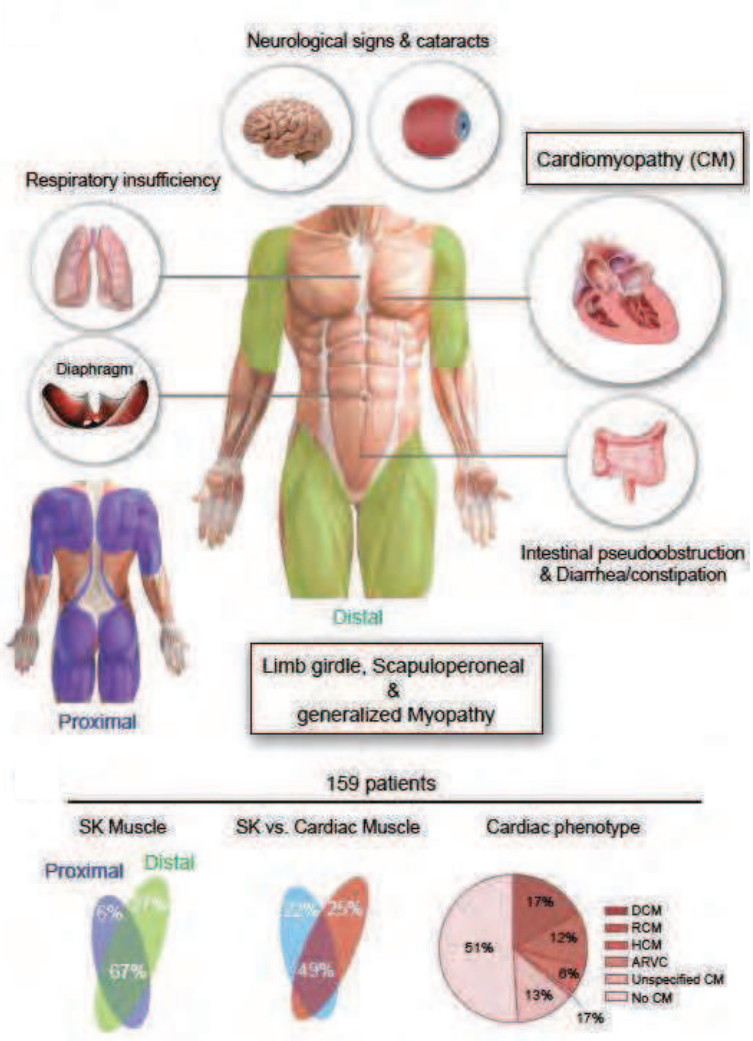

Figure 3 : Pathophysiologie des desminopathies
En parallèle du phénotype musculaire strié, d'autres phénotypes sont présents dans le contexte de la desminopathie, en particulier des signes neurologiques et des problèmes intestinaux. Néanmoins, le phénotype prédominant consiste en un affaiblissement progressif des muscles distaux puis proximaux. Le desminopathie peut également être liée à une dystrophie musculaire des ceintures ou au syndrome scapuloperoneal de type Kaeser. La présence d'un phénotype cardiaque est commune et fréquente, touchant 74% des patients atteints de desminopathie.
Une méta-analyse sur 159 patients permet une approche statistiques aux manifestations de la maladie (van Spaendonck-Zwarts et al., 2011).
CM: cardiomyopathie, DCM: cardiomyopathie dilatée, HCM: cardiomyopathie hypertrophique, RCM: cardiomyopathie restrictive et ARVC : cardiomyopathie arrhythmogénique du ventricule droit.

Outre des études in vitro des propriétés mécaniques des filaments intermédiaires et des études en culture cellulaire des propriétés d'agrégation de la desmine mutée, la souris a été jusqu'à présent le principal animal modèle utilisé pour la compréhension de la fonction de la desmine dans un contexte physiologique. Néanmoins, son rôle dans le contrôle de la fonction musculaire et cardiaque reste peu clair. En effet, l'utilisation de la souris pour l'étude des multiples mutations de la desmine est limitée

par son coût et son incompatibilité avec les techniques d'imagerie dynamique en temps réel. L'utilisation du poisson zèbre dans le domaine de la génétique humaine est maintenant de plus en plus reconnue comme une alternative puissante à l'utilisation de modèles souris et d'approches in vitro, en particulier, pour l'étude du système cardiovasculaire soumis à des conditions hautement dynamiques de par la contraction cardiaque.

Nous avons alors caractérisé le rôle de la *desmine a* (*desma*), homologue de la desmine humaine, chez le poisson-zèbre en utilisant des approches de knock-down et knock-out (Figure 4). Nous avons montré que les larves de poissons-zèbres morphants et mutants de la *desma* présentent des défauts multiples du développement du myocarde et de la fonction cardiaque. Ils présentent également des défauts périphériques affectant le système vasculaire. En parallèle, nous avons développé des outils d'imagerie en temps réel basés sur des techniques de microscopie confocale rapide et de reconstruction des images en 4 dimensions permettant une analyse quantitative du phénotype liée à une cardiomyopathie, tant au niveau tissulaire que cellulaire.

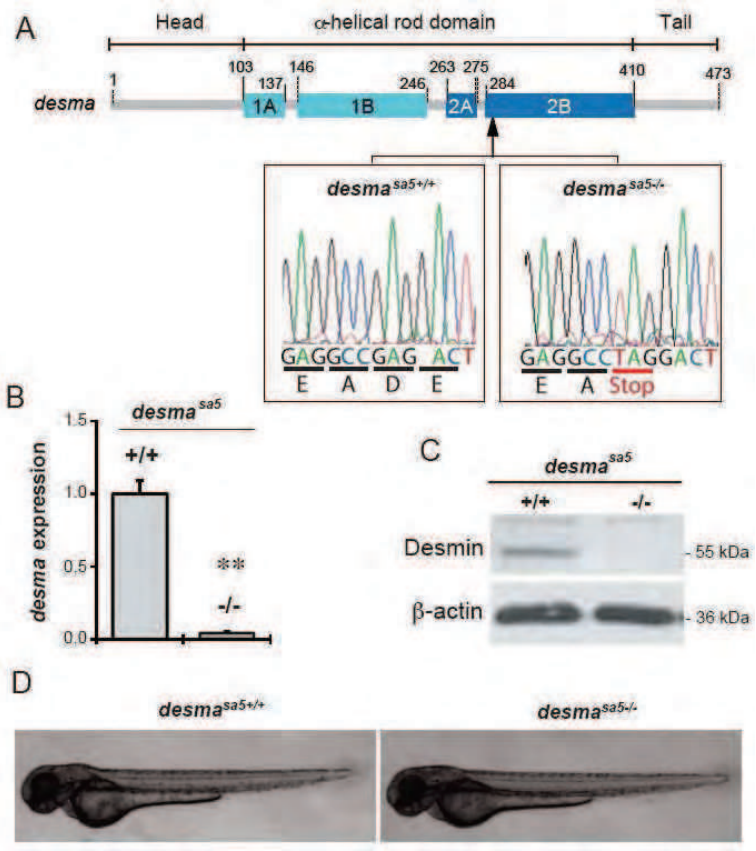

Figure 4 : Présentation du modèle de déplétion du gène de la desmine (*desma*) chez le poisson-zèbre: *desma*$^{sa5-/-}$.
(A) Schémas du gène de la desmin du poisson-zèbre. La flèche indique la position de la mutation présente dans les individus *desma*$^{sa5-/-}$. Le séquençage de la région en question montre la substitution d'un G en un T entre les poissons *desma*$^{sa5+/+}$ and *desma*$^{sa5-/-}$ qui forme un codon stop prématuré et engendre une protéine tronquée. (B) Des expériences de reverse transcription et PCR quantitative montrent l'absence de *desma* au niveau de l'ARN messager suggérant sa dégradation. (C) Par Western blot, l'absence de Desma est confirmée dans des embryons de deux jours par rapport à des embryons sauvages. (D) Des clichés d'embryons à 55 heures montrent qu'ils ne présentent pas de défauts morphologiques dramatiques. Barre de taille=500µm.

De plus, nous avons caractérisé un modèle de gain de fonction de *desma* mutée chez le poisson-zèbre qui permet de visualiser la formation d'agrégats de desmine *in vivo* (Figure 5).

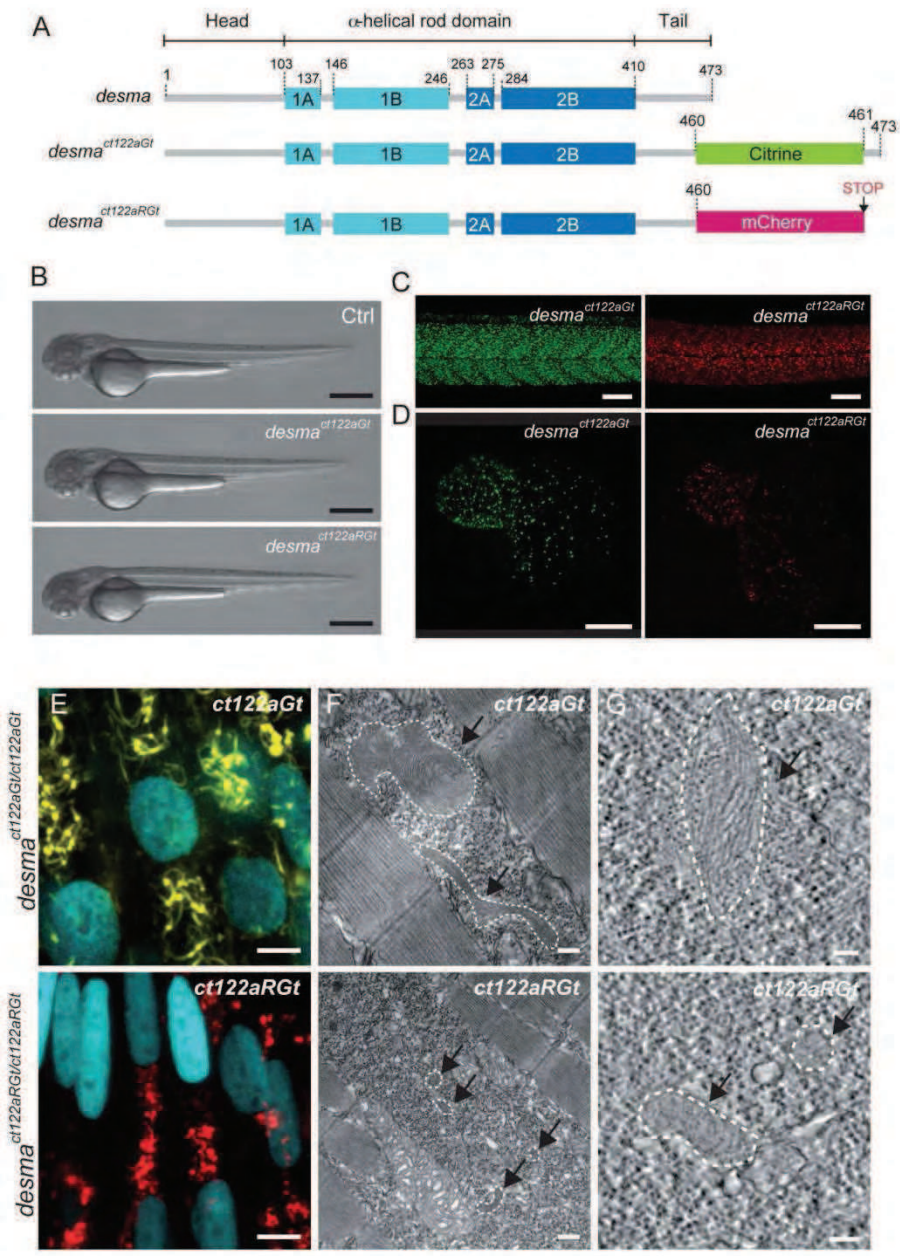

Figure 5 : Présentation du modèle de KI de desma, obtenu grâce à la technologie « Flip-trap » : *desma*^{ct122aGt} and *desma*^{ct122aRGt}
(A) Représentation schématique du gène desma dans les lignées sauvages, *desma*^{ct122aGt} ou *ct122aGt* (avec fusion d'une cassette citrine) and *desma*^{ct122aRGt} or *Ct122aRGt* (avec fusion d'une cassette mcherry). La lignée *ct122aRGt* présente une délétion de 13 acides aminés à la fin du domaine C-terminal, alors que la séquence de *desma* est complète dans la lignée *ct122aGt*. (B) Clichés d'embryons sauvages, *ct122aGt* et *Ct122aRGt à* 55hpf, montrant l'absence de malformation dramatiques. Barre de taille =500µm. (C-D) Des agrégats de Desma sont présents dans les muscles squelettiques de la queue (C) (barre de taille =100µm) et dans le myocarde (D) (barre de taille =50µm) dans les embryons *ct122aGt* et *ct122aRGt* à 48hpf. (E-G) Expériences de microscopie et tomographie semi-corrélatives dans les muscles squelettiques de *ct122aGt* et *ct122aRGt* à 48hpf. (E) Clichés de microscopie confocale. Les noyaux sont marqués en bleu grâce à une construction H2B-Cerulean. (Barre de taille=5µm). (F) Cliché de microscopie électronique montrant la présence d'agrégats cytosoliques (entourés en pointillé et montrés par les flèches) (barre de taille=200nm) (G) Clichés de

tomographie électronique à haute magnification montrant la structure filamenteuse des agrégats dans la lignée ct122aGt et plus compacte et condensée des agrégats dans la lignée ct122aRGt. Les agrégats sont entourés en pointillés et montrés par les flèches (barre de taille=100nm).

L'utilisation de techniques de microscopie multi-photonique (par génération de seconde harmonique), ainsi que des tests fonctionnels, ont permis de montrer que les agrégats augmentent les défauts des muscles squelettiques et cardiaques observés dans le modèle de perte de fonction (Figure 6). En particulier, les muscles squelettiques des poissons *desma*$^{sa5-/-}$ présentent un désalignement des fibres musculaires ainsi qu'un apparent manque de tension dans ces fibres alors que les embryons présentant des agrégats de desma (*ct122aGt*) présentent en plus de ces défaut, des fibres cassées et en dégénérescence.

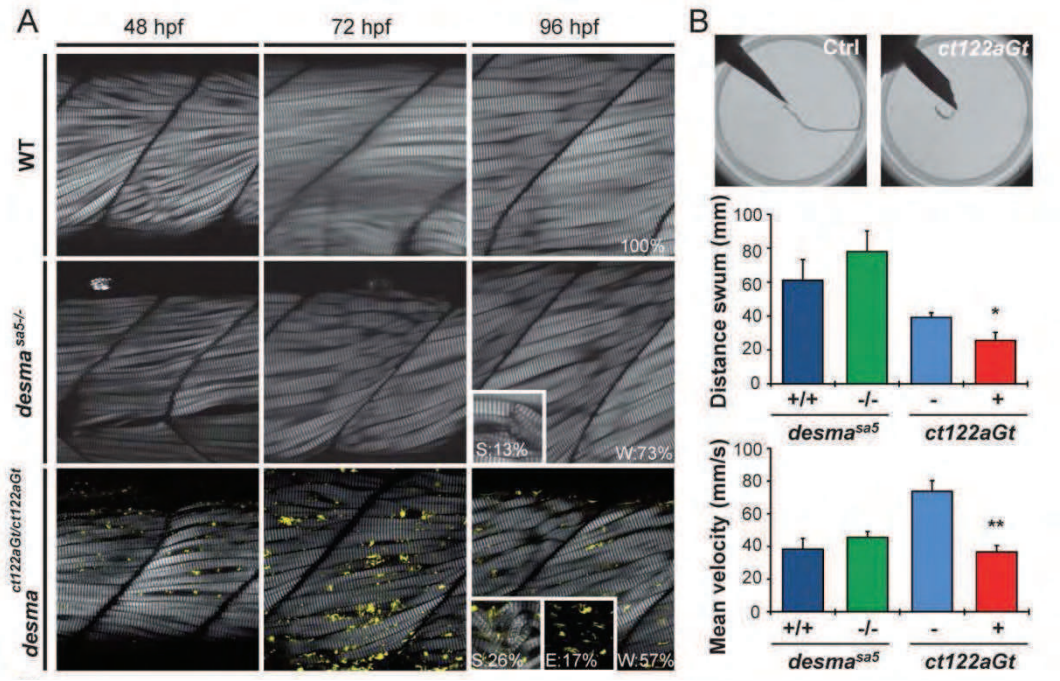

Figure 6 : Une aggravation du phénotype musculaire squelettique est observée dans les embryons ct122aGt par rapport aux embryons *desma*$^{sa5-/-}$.

(A) Sections optiques dans la région caudal d'embryons sauvages, *desma*$^{sa5-/-}$ et ct122aGt à 48, 72 et 96hpf. La génération de seconde harmonique montre que le désalignement des fibres musculaires observé dans les embryons *desma*$^{sa5-/-}$ est souvent accompagné de cassures et de dégénérescences des fibres musculaires dans les embryons *ct122aGt*. A 96hpf, les phénotypes observés ont été catégorisés en trois catégories (faible (W pour weak), fort (S pour strong) et extrêmes (E)). Dans le cas de phénotypes extrêmes, le signal de seconde harmonique est complètement perdu, du à une absence complète d'organisation des structures sarcomériques. (B) Un test fonctionnel de réponse par la fuite a été réalisé sur des embryons sauvages, *desma*$^{sa5-/-}$ et ct122aGt à 52hpf. Les embryons ct122a présentent des capacités de locomotion réduites alors que la réponse des poissons *desma*$^{sa5-/-}$ est similaire à celle des contrôles correspondants.

L'utilisation de microscopie ultra-rapide in vivo a permis de réaliser des reconstructions en 4 dimensions des battements cardiaques et de montrer la présence de phénotypes cardiaques à la fois dans les embryons *desma*$^{sa5-/-}$ et *ct122aGt* à 48hpf. En particulier, nous avons montré la présence

d'un écrasement du ventricule en fin de diastole et un mouvement ondulatoire des battements cardiaques, mis en évidence par l'analyse du mouvement du canal atrio-ventriculaire. (Figure 7).

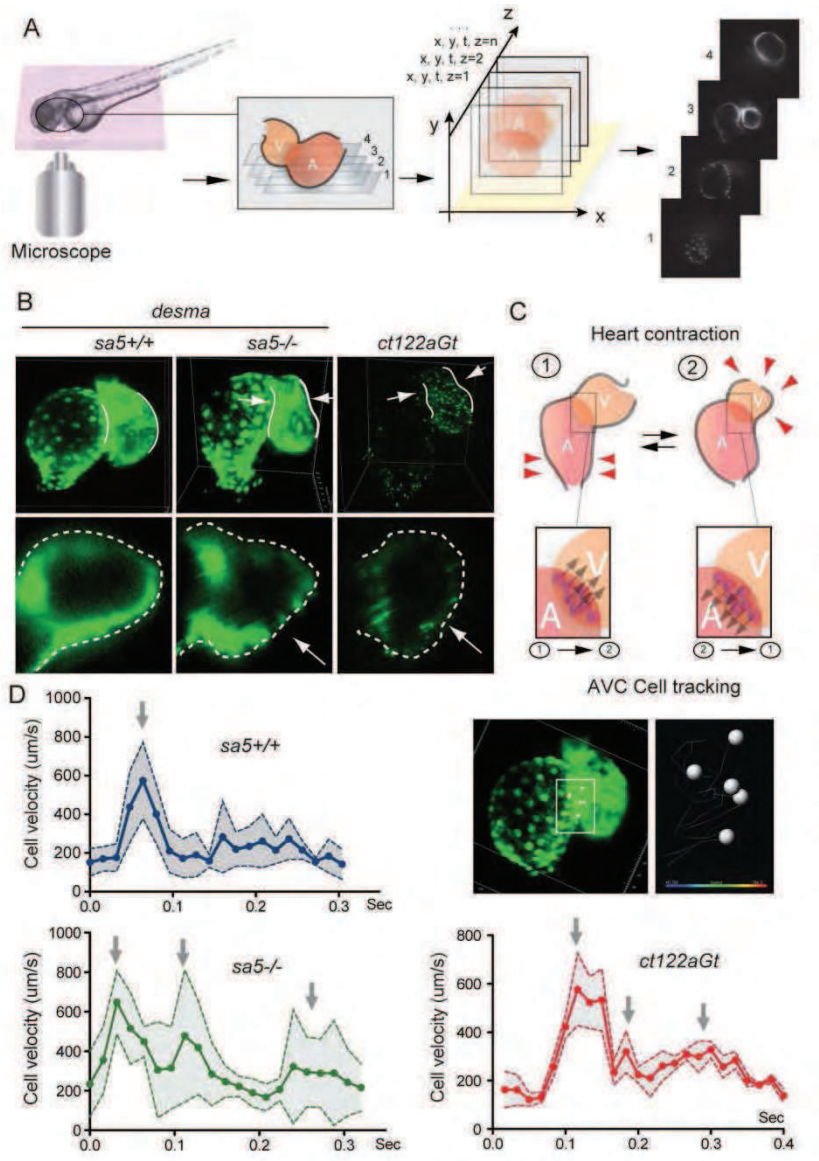

Figure 7 : La biomécanique du cœur des embryons de poisson-zèbre est altérée en absence et en présence d'agrégats de *desma*.

(A) La reconstruction en 4 dimensions (4D) de la dynamique myocardique a été obtenue à partir de vidéos (120fps) en 2D de sections optiques successives sur la totalité du myocarde. La contraction périodique du cœur à ensuite pu être réalignée et synchronisée post-acquisition *in silico*. (B) Sur ces reconstructions en 4D, la comparaison de la forme du myocarde en fin de diastole d'embryons sauvages, *desma*$^{sa5-/-}$ et ct122aGt à 48hpf montre un écrasement du ventricule dans les deux types de mutants. Le panel en dessous montre un zoom sur une section optique transverse du milieu du ventricule au moment de l'écrasement (flèches rouge). (C) Un schémas représente le mouvement du canal atrio-ventriculaire (AVC) lors d'une contraction cardiaque. Les cellules ont été suivies individuellement comme montré dans l'encart et leur vitesse extraite. (D) Graphiques représentant la vélocité des cellules de l'AVC lors d'une contraction cardiaque dans les embryons sauvages, *desma*$^{sa5-/-}$ et ct122aGt à 48hpf. Les flèches grises indiquent les pics de vélocité, caractéristiques du profil de contraction du cœur. Ce profil se trouve modifié dans les poissons mutants.

Une combinaison d'imagerie en temps réel et de microscopie électronique a montré une perturbation de la signalisation calcique dans le myocarde et des dilatations du réticulum sarcoplasmique et des mitochondries dans les muscles squelettiques en absence de desmine fonctionnelle, qui s'intensifient en présence d'agrégats. Ces résultats suggèrent qu'une grande partie des phénotypes observés en présence d'agrégats pathologiques sont liés à la perte de fonction de desmine bien que aggravés par la présence des agrégats.

Finalement, nous avons montré que l'utilisation de la doxycycline et de morpholinos ciblant la desmine permet de réduire à la fois la quantité et la taille des agrégats et de diminuer les phénotypes observés en présence d'agrégats. Ces molécules peuvent alors constituer des candidats potentiels au traitement des desminopathies.

Prises dans leur ensemble, ces données montrent le rôle de la desmine au cours du développement musculaire et cardiaque précoce et la validité de l'embryon de poisson-zèbre comme modèle pour la caractérisation cellulaire de la desmine normale et mutée. Elles procurent également de nouveaux éléments fondamentaux pour la compréhension des mécanismes liés à l'établissement des desminopathies et par extension des protéinopathies.

Projet 2 : Vérification de l'effet Windkessel dans l'embryon de poisson-zèbre pour la validation de son utilisation comme modèle de l'hypertension artérielle.

L'effet Windkessel décrit les propriétés du système vasculaire et en particulier la déformation des artères en les caractérisant par leurs propriétés physiques : leur résistivité et leur compliance. Il compare alors le système sanguin à un système de pompage mécanique dans lequel le cœur est modélisé par une pompe, les vaisseaux périphériques par un tuyau d'évacuation et les artères situé entre les deux par une chambre à air (Figure 8). Cette chambre à air va fonctionner comme un réservoir élastique et permettre la transformation du flux pulsatile sortant du cœur en un flux plus régulier à l'approche des organes.

L'élasticité des artères est alors cruciale. Néanmoins, en conséquence du vieillissement ou de conditions pathologiques comme l'artériosclérose, les artères se rigidifient. En conséquence, les organes vont être soumis à de fortes pressions sanguines et un remodelage du système sanguin va avoir lieu en réponse. Cela s'accompagne alors d'une hypertension artérielle chronique ayant pour conséquence l'hypertrophie cardiaque.

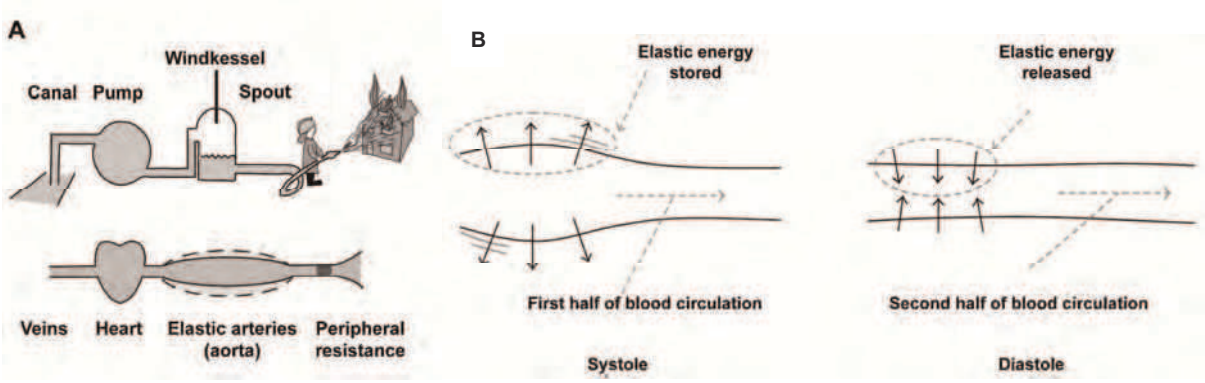

Figure 8 : L'effet Windkessel modèle l'importance de l'élasticité de l'aorte en réponse à la pression.

adaptée de Westerhof et al., 2009. Le « Windkessel » correspond à un réservoir à air d'un système mécanique et va permettre de tamponner l'effet d'une pompe. L'analogie faite avec le système cardiovasculaire, fait correspondre le cœur à la pompe, les vaisseaux périphériques au tuyau et les artères au réservoir à air. Ce modèle permet alors de modéliser le flux sanguin sous forme de paramètre physiques et d'équation mécanistiques. (B) adapté de Roy et al., 2012. Résultat de l'effet Windkessel sur la déformation des artères. Pendant la systole, l'énergie importante accompagnant la pression élevée dans les artères est absorbée et stockée par l'élasticité de l'aorte. Lors de la diastole, l'énergie emmagasinée est libérée et pressurise le flux à basse pression. Ceci permet d'équilibrer les valeurs de pression reçues par les organes. Ceci n'est pas possible dans le cas où la rigidité de l'artère est élevée, soit en conséquence du vieillissement, soit d'une pathologie comme artériosclérose.

L'effet Windkessel se base sur les conditions de pressions dans la vasculature d'un homme adulte. Dans ce système, les conditions sont telles que le nombre de Reynolds, qui définit les conditions de flux dans un système est élevé (autour de 1000). Dans l'embryon de poisson zèbre, le nombre de Reynolds est faible, aux alentours de zéro. Il est donc important de vérifier la conservation de cet effet, et en particulier, la réponse des artères au flux, pour l'utilisation du poisson-zèbre comme modèle de l'hypertension artérielle. En utilisant des techniques de pinces-optiques, de microscopie confocale rapide et de modélisation du flux artériel, nous avons alors étudié la mécanistique du flux sanguin dans le poisson-zèbre et montré l'importance de l'artère dans la modification du profil pulsatile du flux entre le cœur et le reste du circuit vasculaire. Cette étude a alors confirmé que l'élasticité des artères est cruciale dans la gestion des pressions sanguines et que les artères fonctionnent bien comme des condensateurs permettant de réduire le travail du cœur (Figure 9).

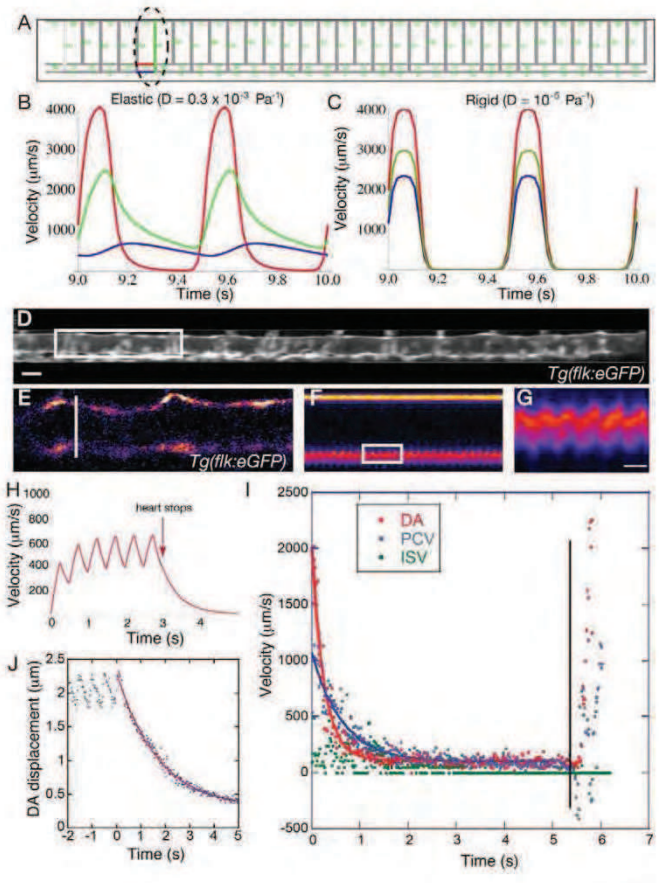

Figure 9 : Dans l'embryon de poisson-zèbre, l'aorte dorsale présente une déformation élastique liée à une fonction de condensateur du flux sanguin.

(A) Représentation du réseau modélisé par une approche *in silico*. (B-C) les profils du flux sanguins calculés par ce modèle en conférant une propriété élastique à l'artère (B) ou non (C) sont différents. La courbe rouge représente le flux dans l'aorte dorsal (DA), la courbe verte dans les vaisseaux inter-segmentaires (ISVs) et la courbe bleu dans la veine caudale (PCV). (D) Vue de coté de l'aorte dorsale dans des poissons contenants un marquage des cellules endothéliales. (Barre de taille = 20µm). (E) La distance entre les parois ventrales et dorsale de l'aorte dorsale (barre blanche) augmente au cours de la contraction cardiaque. (F) Kymographe du déplacement de la paroi ventrale de l'aorte dorsale le long de la barre blanche présentée en E. (G) Zoom sur le précédent kymographe montrant qu'une déformation régulière est visible au cours du temps et seulement au niveau de la paroi ventrale. (Barre de taille=420ms).

Projet 3 : Développement de modèles de maladie veino-occlusive pulmonaire

GCN2 (*eif2ak4*) a été identifié récemment comme étant une des causes génétiques des formes héréditaires de maladie veino-occlusive pulmonaire (MVOP), une forme rare et extrêmement sévère d'hypertension pulmonaire (Eyries et al., 2014). La MVOP est caractérisée, d'un point de vue histologique, par un élargissement de la paroi des veines pulmonaires et une prolifération de tissus

fibreux dans les veines septales et les veinules pré-septales, fréquemment associés à une dilatation et une prolifération des capillaires pulmonaires (Figure 10).

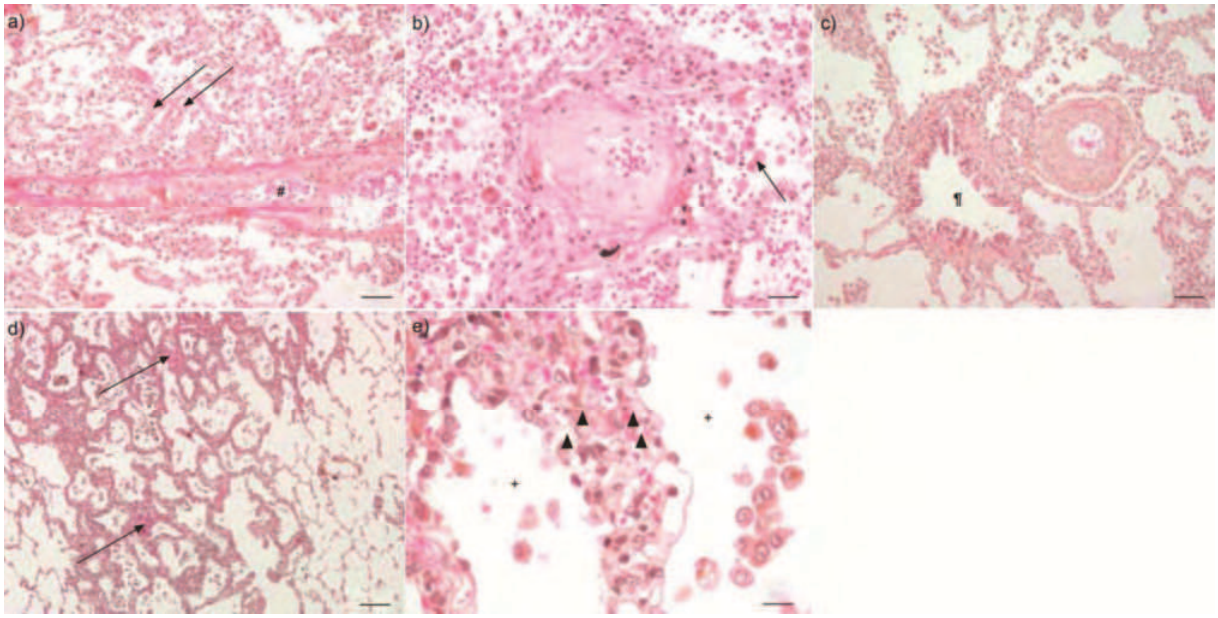

Figure 10 : Lésions vasculaires pulmonaires chez des patients souffrant de MVOP. De Montani et al., 2009. Histologie pulmonaire de patients souffrant de MVOP montrent : a) L'obstruction fibreuse de veines septales (#) et de venules pré-septales (flèches).b) Des venules pré-septales remodelées suite à leur occlusion. La flèche montre une hémorragie intra-alvéolaire. c) Des artères présentant de la fibrose. d) un épaississement irrégulier des alvéoles en présence de micro-vaisseaux occlus. Un septum alvéolaire présentant une prolifération anormale des capillaires.

GCN2 code pour une sérine-thréonine kinase présente chez tous les eucaryotes. Elle fonctionne comme un senseur de la disponibilité des acides aminés et induit des modifications d'expression génique en réponse à la privation en acide-aminés. Elle appartient à une famille de quatre kinases qui phosphorylent la sous-unité alpha (eiF2α) du facteur eucaryote d'initiation de la traduction (eiF2). La phosphorylation d'eiF2α induit une diminution globale de la traduction dans la cellule et active spécifiquement la traduction des facteurs de transcription ATF4 (CREB-2) et CHOP. ATF4 a un rôle central dans le mécanisme de transduction du signal. Il induit ou inhibe la transcription d'une série de gènes cibles qui contrôlent le mécanisme cellulaire de réponse au stress, impliqué dans un remodelage majeur du phénotype cellulaire incluant l'angiogenèse et la résistance au stress oxydatif. Il n'est, jusqu'à lors, pas établi que l'implication de GCN2 dans la MPVO soit liée directement à sa fonction de senseur de la privation en acides aminés et aux changements traductionnels et transcriptionnels qui en découlent ou qu'elle soit liée à l'activité kinase de GCN2 qui pourrait avoir d'autres substrats qu'eiF2alpha.

Dans ce contexte, nous avons alors étudié la perte de fonction de GCN2 dans le poisson-zèbre afin d'identifier les changements en terme d'expression génique induits par l'inactivation de GCN2 dans les cellules vasculaires. (Figure 11) Nous voulons alors, par ce biais, comprendre comment une mutation bi-allélique de GCN2 entraine le remodelage vasculaire pulmonaire et le mécanisme entrainant la spécificité veineuse observée dans la pathologie. L'homologue de GCN2 chez le poisson

zèbre est Eif2aK4. Cette protéine ne possédant pas de domaine senseur de la quantité en acide aminé, comme son homologue humain, l'étude d'Eif2ak4 permet de valider ou de réfuter l'implication de cette fonction dans l'établissement de MVOP.

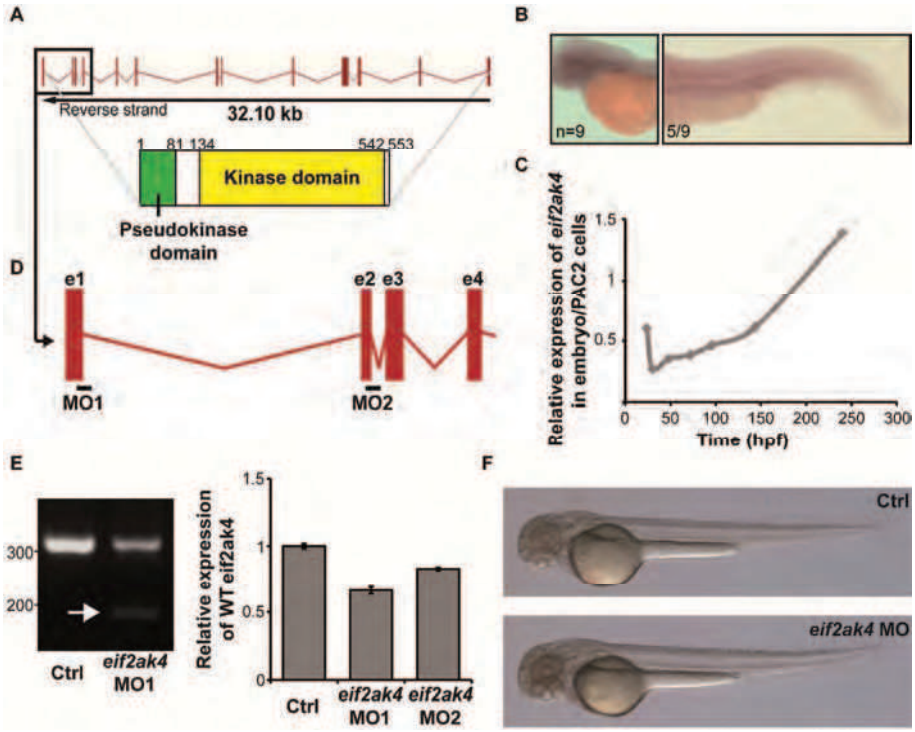

Figure 11 : La diminution de l'expression de eif2ak4, homologue de GCN2 humain chez le poisson zèbre a été obtenue grâce à l'injection de morpholinos anti-sens.

(A) Représentation schématiques du gène de *eif2ak4* chez le poisson-zèbre et de la protéine correspondante. La conservation de cette protéine par rapport à la protéine humaine n'est que partielle. En effet le domaine, His tRNA synthetase-like permettant la fonction de senseur du niveau en acides aminés dans la version humaine de GCN2, n'est pas présent dans le poisson. (B) L-hybridation *in situ* de *eif2ak4* dans des embryons de poissons-zèbre sauvages à 30hpf montrent une expression faible mais ubiquitaire. (C) Des expériences de transcription réverse et PCR quantitative à partir de groupes de 30 embryons de 30hpf à 14 jours montrent l'évolution de l'expression de *eif2ak4* au cours du temps. (D) Deux morpholinos se liant à des séquences d'épissage de *eif2ak4* ont été conçus et testés, afin de diminuer son expression. (E) La transcription réverse d'ARN extrait d'embryons injectés avec le morpholino contre *eif2ak4* à 30hpf montre la présence d'une bande supplémentaire sur gel résultant d'un défaut d'épissage entrainé par le morpholino. Le graphique à droite montre les taux de diminution de l'expression d'*eif2ak4* dans les poissons injectés avec les morpholinos 1 et 2 contre *eif2ak4*. (F) Les clichés de poissons contrôles et injectés avec le morpholino contre *eif2ak4* montrent que les embryons injectés ne présentent pas de malformations dramatiques.

Même si le poisson-zèbre ne possède pas de poumons, ce modèle permet de valider rapidement l'impact de la perte de GCN2 sur le développement vasculaire et l'angiogenèse grâce à l'imagerie *in vivo* du système vasculaire en formation. Nos expériences de knock-down, basées sur l'utilisation de morpholinos dans le poisson-zèbre, montrent d'importantes perturbations de la formation du plexus veineux et du canal mésencéphalique primaire, tous deux d'identité veineuse, lors de l'embryogénèse précoce (Figure 12).

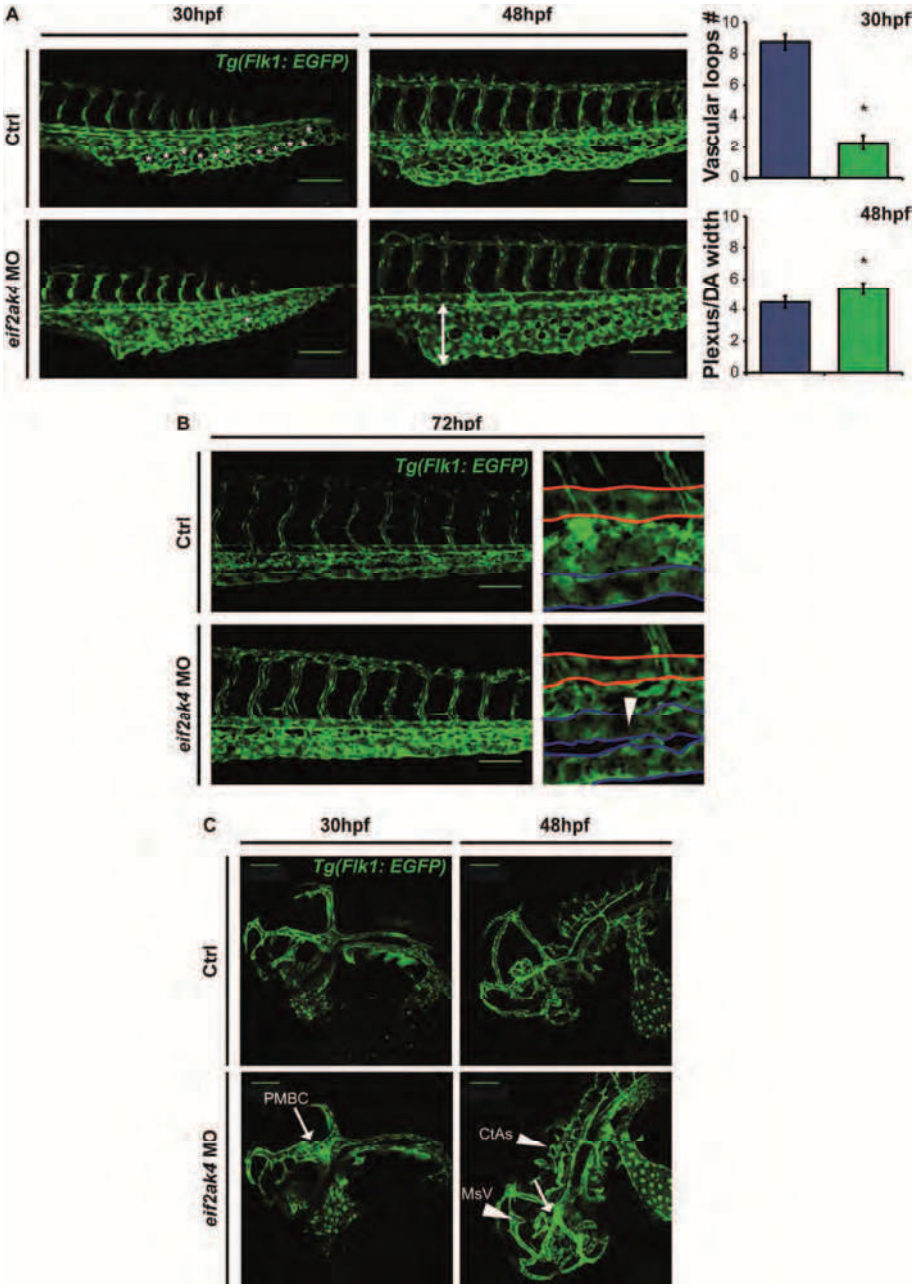

Figure 13 : Des phénotypes spécifiquement veineux sont observés après diminution de l'expression d'*eif2ak4* chez le poisson-zèbre.

(A) Projection maximale d'images de microscopie confocale présentant le plexus caudal d'embryons de poissons zèbre morphants pour *eif2ak4* et leurs contrôles à 30 et 48hpf. Les astérisques montrent la position des boucles vasculaires à 30hpf et la flèche montre un élargissement du plexus à 48hpf. (Barre de taille=100µm). La quantification des boucles vasculaires et les mesures de la largeur du plexus en fonction de la largeur de l'aorte dorsale sont présentées dans le panel de droite. (B) Des projections maximales similaires ont été réalisées à 72hpf.Le zoom montre la présence d'un vaisseau veineux ectopique dans les morphants. (C) Projection maximale d'images de microscopie confocale présentant la vasculature crânienne des poissons injectés avec le morpholino contre *eif2ak4* à 30 et 48hpf. Les flèches montrent les régions ayant subi un élargissement, en particulier le canal mésencéphalique primaire (PMBC) et les têtes de flèche montrent les régions présentant un développement ectopique, en particulier les artères centrales (CtAs) et la veine mésencéphalique (MsV).

De plus, en générant un knock-down d'ATF4b (formes 1 et 2), homologue chez le poisson de l'intermédiaire ATF4 en aval de GCN2 dans la voie de signalisation de la privation en acides aminés, nous avons montré qu'il est possible de récapituler le phénotype observé dans les morphants de GCN2 et prouvons alors par ce biais, la participation de cette voie dans l'établissement du phénotype de la MVOP bien que la fonction de senseur de GCN2 de soit pas impliquée.

Conclusion

L'utilisation du poisson-zèbre pour la modélisation de deux pathologies : les desminopathies et la MVOP, a apporté de nouvelles connaissances quant à l'établissement de leurs phénotypes respectifs et à la fonction de la desmine et de *EIF2AK4* dans le développement précoce. De nouveaux aspects de ces maladies ont été mis en évidence grâce à la simplicité du modèle poisson. En particulier, la simplicité du système vasculaire en cours de développement dans les embryons, encore dépourvu des muscles lisses péri-vasculaires, a permis de découpler les contributions respectives de l'endothélium et du muscle lisse vasculaire et d'attribuer les phénotypes observés à des atteintes liées à l'endothélium. Les techniques récentes d'imagerie *in vivo* ultra-rapide et les techniques d'analyse que nous leur avons associées (génération de seconde harmonique, reconstruction en quatre dimensions d'un battement cardiaque, imagerie calcique etc.) sont pour l'instant principalement utilisées pour des études développementales. Nous avons alors montré que leur utilisation dans des études liées à des problématiques de médecine translationnelle permet encore d'augmenter l'intérêt de l'utilisation du modèle poisson-zèbre dans ce domaine.

Des médicaments candidats ont été proposés dans le contexte de la desminopathie et pourraient être testés désormais dans des modèles mammifères afin de tester leur validité et d'amorcer des études précliniques. Pour amener encore plus loin le potentiel de découverte de médicament à partir de notre modèle de desminopathies, nous proposons de réaliser un criblage moléculaire à haut-débit pour lequel nous avons déjà optimisé les conditions en collaboration avec la plateforme de criblage de l'IGBMC. Le poisson-zèbre est actuellement le seul organisme modèle permettant une telle approche, mais celle-ci n'a pas encore été mise en place pour l'identification de composants capables d'atténuer l'agrégation et d'augmenter la survie dans le contexte de protéinopathies. Elle pourrait alors, à long terme, proposer de nouvelles thérapies à partir de composants connus et rapidement transférables sur le marché.

Caroline RAMSPACHER

Développement de modèles animaux de maladies génétiques des systèmes cardiovasculaire et musculaire chez le poisson-zèbre

Résumé

Le poisson-zèbre est un animal modèle de plus en plus utilisé et reconnu dans le domaine de la médecine translationnelle et pour la modélisation de pathologies humaines. Nous avons alors utilisé les nombreux avantages de ce modèle pour la modélisation de deux maladies héréditaires : la desminopathie et la maladie veino-occlusive pulmonaire (MVOP). La desminopathie est une myopathie myofibrillaire caractérisée par la présence d'agrégats granulofilamenteux riches en desmine, une protéine de la famille des filaments intermédiaires. Deux modèles, de perte et de gain de fonction de la desmin chez le poisson-zèbre, couplés à des techniques d'imagerie électronique et confocale en temps réel, ont permis de mettre en évidence l'importance à la fois de la perte de desmine fonctionnelle et de la présence d'agrégats dans les desminopathies. Les phénotypes observés incluent en particulier des défauts biomécaniques de la contraction cardiaque liés à une perturbation de la propagation calcique myocardique. Des approches thérapeutiques, réduisant la taille des agrégats, ont également été proposées. Après avoir validé l'utilisation du poisson-zèbre comme modèle d'étude de l'hypertension artérielle, en vérifiant l'implication de l'élasticité de la paroi artérielle dans la régulation du flux sanguin, des modèles de MVOP, une forme rare et sévère d'hypertension pulmonaire, ont été générés et étudiés. Ils confirment la spécificité veineuse des phénotypes observés dans la MVOP.

Résumé en anglais

The use of zebrafish in the translational medicine field and for the establishment of novel human disease models is more and more recognized. We used its numerous advantages for the study of two hereditary diseases: desminopathy and pulmonary veno-occlusive disease (PVOD). Desminopathy is a myofibrillar myopathy characterized by the presence of granulofilamentous desmin-positive aggregates in all muscle cell types. Desmin is the muscle specific member of the intermediate filament family. Two models of loss and gain of function of desmin were characterized in zebrafish. In combination with powerful electron and live confocal microscopy techniques, they showed the implication of both loss of functional desmin and presence of desmin aggregates in desminopathy clinical manifestations. Phenotypes observed in these models include in particular a perturbation of the heart contraction biomechanics, which was linked with defects in the propagation of calcium throughout the myocardium. Potential drugs, lowering the aggregate content, were proposed as well. After validating the use of zebrafish as a model of arterial hypertension, by verifying the implication of the elasticity of the dorsal aorta in blood flow regulation, we generated and characterized PVOD models. PVOD is a rare and severe form of pulmonary hypertension. Using morpholino based knock down, we confirmed the venous-specificity of the phenotypes observed in this pathology.